

GEOLOGICA ULTRAIECTINA

Mededelingen van de
Faculteit Aardwetenschappen,
Universiteit Utrecht

no. 197

Faults, Fluids and Friction

*Effect of pressure solution and phyllosilicates on fault behaviour,
with implications for crustal rheology*



Bart Bos

GEOLOGICA ULTRAIECTINA

Mededelingen van de
Faculteit Aardwetenschappen der
Universiteit Utrecht

No. 197

Faults, Fluids and Friction

*Effect of pressure solution and phyllosilicates on fault slip
behaviour, with implications for crustal rheology*

Bart Bos

ISBN: 90-5744-054-7

Faults, Fluids and Friction

Effect of pressure solution and phyllosilicates on fault slip behaviour, with implications for crustal rheology

Breuken, Vloeistoffen en Wrijving

Effecten van drukoplossing en phyllosilicaten op breukgedrag, met implicaties voor de sterkte van de korst

(met een samenvatting in het Nederlands)

PROEFSCHRIFT

**TER VERKRIJGING VAN DE GRAAD VAN DOCTOR AAN DE
UNIVERSITEIT TE UTRECHT, OP GEZAG VAN DE RECTOR
MAGNIFICUS, PROF. DR. H.O. VOORMA, INGEVOLGE HET
BESLUIT VAN HET COLLEGE VOOR PROMOTIES IN HET
OPENBAAR TE VERDEDIGEN OP WOENSDAG 8 NOVEMBER 2000
DES NAMIDDAGS TE 14:30 UUR**

DOOR

BART BOS

GEBOREN OP 27 APRIL 1973 TE HOOGEVEEN

PROMOTOR: PROF. DR. C.J. SPIERS
FACULTEIT AARDWETENSCHAPPEN
UNIVERSITEIT UTRECHT

LEDEN VAN DE BEOORDELINGSCOMMISSIE:

DR. F.M. CHESTER
Texas A&M University, College Station, USA

PROF. M.R. HANDY
Freie Universität Berlin, Duitsland

PROF. T.E. TULLIS
Brown University, Providence, USA

PROF. S.H. WHITE
Universiteit Utrecht

PROF. M.J.R. WORTEL
Universiteit Utrecht

*Varkens beleven meer genoeg aan modder
dan aan zuiver water*

- Heraclitus -

In water dat te zuiver is zit geen vis

- Ts'ai Ken T'an -

*Aan mijn vader,
en in liefdevolle
herinnering
aan mijn moeder.*

TABLE OF CONTENTS

SUMMARY.....11

1. GENERAL INTRODUCTION AND PROBLEM STATEMENT

1.1 General aspects: Faults, fluids and friction 13
1.2 Chemically active fluids and long-term fault strength 15
1.3 Chemically active fluids and seismic fault behaviour 16
1.4 Aims of this research..... 18
1.5 A note on the use of rock analogue materials in rock deformation studies..... 18

2. SLIP BEHAVIOUR OF SIMULATED GOUGE-BEARING FAULTS UNDER CONDITIONS FAVOURING PRESSURE SOLUTION

2.1 Introduction 21
2.2 Experimental method..... 24
2.3 Results..... 28
2.4 Discussion 40
2.5 Conclusions 46

3. FRICTIONAL-VISCOUS FLOW BEHAVIOUR OF SIMULATED FAULT GOUGE DUE TO THE COMBINED EFFECTS OF PHYLLOSILICATES AND PRESSURE SOLUTION

3.1 Introduction 47
3.2 Experiments 49
3.3 Results..... 53
3.4 Discussion 62
3.5 Conclusions 68

4. EFFECT OF STRAIN ON MICROSTRUCTURE AND RHEOLOGY OF SIMULATED, CLAY-BEARING FAULT GOUGE

4.1 Introduction	69
4.2 Experimental method.....	70
4.3 Results.....	72
4.4 Discussion	80
4.5 Conclusions	86

5. FLUID-ASSISTED HEALING PROCESSES IN GOUGE-BEARING FAULTS

5.1 Introduction	87
5.2 Experimental method.....	90
5.3 Results.....	93
5.4 Discussion	100
5.5 Conclusions	108

6. EFFECT OF CLAYS ON FLUID-ASSISTED FAULT HEALING

6.1 Introduction	109
6.2 Experimental method.....	110
6.3 Results.....	112
6.4 Discussion.....	116
6.5 Conclusions	118

7. A MICROPHYSICAL MODEL FOR FRICTIONAL-VISCOUS FLOW AT THE BRITTLE-DUCTILE TRANSITION, WITH IMPLICATIONS FOR CRUSTAL STRENGTH PROFILES

7.1 Introduction:	119
7.2 Previous data on frictional-viscous flow behaviour	121
7.3 Model development	122
7.4 Application to the system halite + kaolinite	130
7.5 Application to natural faults: a strength profile for zones of high strain	132
7.6 Conclusions	140

8 GENERAL CONCLUSIONS AND SUGGESTIONS FOR FURTHER RESEARCH

8.1 Conclusions of this research	141
8.2 Suggestions for further research	142

REFERENCES	145
-------------------------	------------

NEDERLANDSE SAMENVATTING	151
---------------------------------------	------------

DANKWOORD	155
------------------------	------------

CURRICULUM VITAE	157
-------------------------------	------------

Summary

In order to model the mechanics of motion and earthquake generation on large crustal fault zones, a quantitative description of the rheology of fault zones is prerequisite. In the past decades, crustal strength has been modeled using a brittle or frictional failure law to represent fault slip at upper crustal levels, and power law creep equations to describe dislocation creep at lower crustal levels. It has long been argued, however, that such two-mechanism strength profiles may significantly overestimate crustal strength, in particular in zones of high strain. Indeed, geophysical observations (notably heat flow and stress orientation data) indicate that major fault zones are significantly weaker than predicted by classical two-mechanism strength profiles.

Various explanations for the weakness of major faults have been proposed. These include mechanical processes such as the presence of elevated (superhydrostatic) fluid pressures, the transient reduction of friction by a dynamic reduction of normal stress during earthquakes. Apart from this, the inferred weakness of faults may be due to chemically related effects, i.e., due to the operation of fluid-assisted deformation mechanism such as pressure solution. This may act in concert with the growth and alignment of weak phyllosilicate minerals. The explanation for fault weakness remains a source of controversy, since little experimental work has been done which allows rigorous testing of the various hypotheses. The mechanical behaviour of major fault zones accordingly remains poorly understood.

The aim of this thesis is to investigate the effect of solution transfer processes on the mechanical behaviour of fault zones, in order to arrive at a quantitative, mechanism-based understanding of fault slip behaviour under hydrothermal conditions. To this end, sliding experiments were carried out on simulated, gouge-bearing faults. The experiments were performed in a room-temperature ring-shear apparatus. This apparatus allowed control of normal stress and sliding velocity, and in addition allowed high shear strains necessary to achieve significant microstructural modifications. Normal stresses used range from 0.5 to 9 MPa, and sliding velocities of 0.005-10 $\mu\text{m/s}$ were used. The experiments were performed using halite and halite/kaolinite gouge as rock analogue materials. Halite was used because the rates of solution transfer processes in halite are well-constrained and extremely rapid at low-stress conditions. This allowed us to do experiments under conditions where solution transfer processes and cataclasis dominated over dislocation creep processes in halite. Kaolinite was used a phyllosilicate constituent because of its simple chemistry, low ion exchange capacity and absence of interlayer water.

Chapter 2 describes the results of sliding experiments on faults containing monomineralic halite gouge, saturated with mixtures of brine and methanol. Pore fluid composition was varied with the aim of studying the effect of solubility, and hence pressure solution rate, on fault slip behaviour. The results show purely frictional (i.e. rate-insensitive and linearly normal stress-dependent) behaviour under all conditions investigated. No evidence for steady state pressure solution-accommodated fault slip was observed, in spite of the fact that the compaction behaviour and the microstructures clearly demonstrated that pressure solution was active in the gouge. In monomineralic gouge, fluid-assisted healing effects thus dominated over weakening effects.

Chapter 3 deals with the effect of phyllosilicate content on sliding behaviour, focusing on steady state rheology. The results showed that whereas pure kaolinite and pure halite showed rate-insensitive behaviour, halite/kaolinite mixtures showed frictional-viscous behaviour, i.e., behaviour in which shear stress was both normal stress and strain rate sensitive. This was accompanied by the development of a microstructure showing elongate, augen-like halite clasts embedded in a fine-grained, foliated halite/kaolinite matrix. The data suggest that the rate-sensitive behaviour was due to a mechanism involving sliding along kaolinite layers accommodated by pressure solution and

local dilatation. The similarity of the observed microstructures to natural mylonites suggests that solution transfer processes may be important in determining the microstructure and the mechanical behaviour of natural mylonites.

Chapter 4 focuses on the effect of strain on the evolution of microstructure and mechanical behaviour in halite/kaolinite mixtures. To this end, brine-saturated halite/kaolinite mixtures were sheared to various shear strains, at both high and low sliding velocities. At low velocities, the data show a transition in mechanical behaviour from purely frictional behaviour at low strains to frictional-viscous behaviour at higher strains. This transition is accompanied by a microstructural evolution from a typical cataclasite at low strains to a strongly foliated S-C mylonite at high strains. The data show that the mechanical behaviour at high strains is controlled by the fine-grained, foliated halite/kaolinite matrix surrounding the clasts. The experiments demonstrate a mechanism of fault weakening due to grain size reduction by cataclasis, followed by a transition to pressure solution controlled creep behaviour.

Chapters 5 and 6 deal with the effect of solution transfer processes on interseismic fault strength recovery (healing). In Chapter 5 experiments on monomineralic gouge are presented. Fault healing rates in brine-saturated gouge were significantly higher than in gouge saturated with an inert pore fluid. Healing was inferred to be due to pressure solution compaction of gouge, causing packing density increase as well as grain contact area/strength increase during periods of no slip. The behaviour observed is broadly similar to that seen in quartzo-feldspathic gouges at room temperature and described by the widely-used empirical rate-and state-dependent friction (RSF) laws. However, important differences are present in details. In particular, in the experiments reported here friction does not increase log-linearly with time, but instead increases linearly with $t^{1/2}$, consistent with microphysical models for fluid-assisted contact growth. The results imply that models for the seismic cycle based on a log-linear relation calibrated in experiments where healing times are short relative to the natural situation may underestimate fault strength when healing is due to fluid-assisted processes. In Chapter 6, the effect of clays and fault rock microstructure on fault healing is explored. It is shown that fluid-assisted fault healing is strongly retarded by the presence of phyllosilicates, in particular when the phyllosilicates define a foliation. This effect is due to a reduction in the proportion of healing-prone halite-halite contacts due to the presence of phyllosilicates. The results call into question the usage of healing data derived from experiments on monomineralic gouge to modelling of the seismic cycle of natural faults, since these generally contain significant amounts of phyllosilicates.

Finally, in Chapter 7 the thesis returns to the issue of long-term fault strength. Based on our microstructural findings in Chapters 3 and 4, a microphysical model is developed for deformation of phyllosilicate-bearing fault rock by a mechanism of frictional sliding along phyllosilicate foliae, with accommodation of geometrical incompatibilities by pressure solution and dilatation. The model is tested using our data on halite/kaolinite gouge, and shows reasonable agreement with the data. Subsequently, the model is applied to hypothetical quartz-mica shear zones in different tectonic settings, in order to assess the effect of pressure solution controlled fault slip on crustal fault strength. The model shows that frictional-viscous flow behaviour is expected in foliated, phyllosilicate-rich fault rock at depths ranging from 5-20 kilometers, depending on tectonic setting. This is consistent with field observations. The models imply that phyllosilicate-bearing crustal shear zones can be expected to be significantly (up to a factor 4) weaker than predicted by classical two-mechanism strength profiles, in particular in the depth range where the brittle-ductile transition is located according to classical two-mechanism strength profiles. The rheological description used in numerical models for crustal dynamics could be significantly improved by incorporating the pressure solution-controlled fault creep model developed here.

Chapter 1

General introduction and problem statement

1.1 General aspects: Faults, fluids and friction

Deformation of the earth's lithosphere is for a large part concentrated in localised faults or fault zones. Faults occur on all scales. On a global scale faults define plate boundaries as subduction zone megathrusts and continental and oceanic transform faults. However, faults also occur on smaller scales as shear zones accommodating relative movement of tectonic units in orogenic belts, as normal faults accommodating extension in basins, and down to the outcrop scale as discrete brittle faults or thin ductile shear zones. The existence of long-lived, frequently reactivated fault zones is evidence that such zones are significantly weaker than the surrounding rock, and indeed the dynamics of crustal deformation are believed to be largely determined by the rheology of fault zones [e.g. *Sibson, 1977; White et al., 1986; Handy, 1989; Hickman, 1991; Holdsworth et al., 1997*]. A quantitative understanding of the rheology of fault zones is therefore a prerequisite for modelling crustal dynamics. Moreover, fault zones are the primary locus of generation of earthquakes, and thus act as the sources of one of the most destructive natural hazards affecting mankind. Understanding the mechanical behaviour of fault zones is crucial for understanding of the seismic cycle, and associated earthquake hazard assessment. The study of the mechanical behaviour of large fault zones thus forms a subject of major scientific and societal interest.

Field studies of exhumed fault zones show that fault zones generally consist of relatively undeformed blocks separated by a layer of fault rock, which can vary in thickness from a few mm to kilometers. The appearance of fault rocks changes with depth, from loose granular fault gouge at shallow depths, through foliated cataclasites at intermediate depths to fully ductile mylonites at middle-to-lower crustal levels [*Sibson, 1977; Snoke et al., 1999*], probably reflecting an increase with depth of the contribution of ductile processes to deformation at the expense of brittle processes. In most cases, fault rocks are polymineralic and foliated, and have a significantly smaller grain size than the surrounding rock.

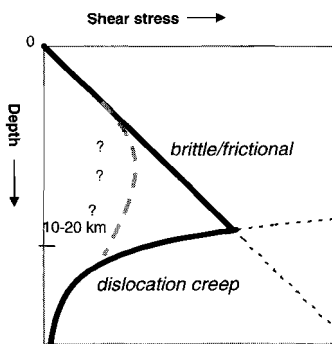


Figure 1.1 Schematic crustal strength profile, showing brittle/frictional behaviour dominating at upper crustal levels, and dislocation creep determining crustal strength at deeper levels (solid lines). The dashed line represents the hypothesized effect of fluid-assisted deformation mechanisms on crustal strength.

Combining field studies and laboratory measurements, attempts have been made in recent decades to place constraints on the deformation mechanisms accommodating crustal deformation, and the stress levels supported by the crust [*Sibson, 1977; Goetze and Evans, 1979; Kirby, 1980; Kirby, 1983; Sibson, 1983; Scholz, 1988; Kohlstedt et al., 1995*]. In general, deformation in the upper crust is approximated in terms of shear strength profiles constructed using a Coulomb-type failure law to represent brittle/frictional behaviour at upper crustal levels, and power law creep equations to describe crystal plastic flow at deeper levels (see Figure 1.1).

Such strength profiles show a maximum at a fairly abrupt brittle-ductile transition, which is inferred to occur at 15-20 km depth. The models imply that crustal strength at the brittle-ductile transition is of the order of hundreds of MPa [*Kohlstedt et al., 1995*]. Assuming hydrostatic fluid pressure and a

direct correlation between brittle behaviour and seismogenesis, these strength profiles account fairly well for the observed depth distribution of seismogenesis [Sibson, 1983; Sibson, 1984; Scholz, 1990]. These laboratory-based strength profiles are widely used in numerical studies of crustal tectonics [Bassi, 1991; Govers and Wortel, 1995; Beaumont et al., 1996; Fernandez and Ranalli, 1997; Buiter et al., 1998].

However, since the first usage of two-mechanism strength profiles it has been argued that the strength profiles possibly overestimate fault strength [Rutter and Mainprice, 1979; Sibson, 1983; Rutter and Brodie, 1991]. Whereas evidence from in-situ stress measurements in boreholes and deep wells indicates that the stress state in intraplate continental crust is generally close to that predicted by laboratory friction experiments [Zoback and Healy, 1992; Brudy et al., 1997; Hickman et al., 1997; Lund and Zoback, 1999; Townend and Zoback, 2000], large intercontinental fault zones seem to be anomalously weak. This point has become particularly concentrated on the San Andreas Fault Zone (although the weakness of this fault was recently questioned by Scholz [2000]), where stress orientations [Mount and Suppe, 1987; Zoback et al., 1987] and heat flow measurements [Lachenbruch and Sass, 1980; Lachenbruch and Sass, 1992] suggest that the apparent friction coefficient in the fault zone is lower than 0.2, and thus far below the value of 0.6-0.9 predicted from laboratory observations. Moreover, observations of stress orientations, heat flow, sea-floor morphology and metamorphic mineral assemblages on other major plate boundary faults (including subduction zone megathrusts and oceanic transform faults) indicate that these may be similarly weak [Lachenbruch and Thompson, 1972; Oldenburg and Brune, 1975; Sibson, 1980; Wilcock et al., 1990; Mount and Suppe, 1992; Magee and Zoback, 1993; Wang et al., 1995]. This casts doubt on the applicability of conventional strength profiles to major fault zones.

The failure of conventional strength profiles to explain the inferred low strength of major fault zones is believed to arise from the fact that the strength profiles present a significant oversimplification of the natural situation, in particular around the brittle-ductile transition, i.e., the region where crustal strength is predicted to be at a maximum. Firstly, strength profiles are based on monomineralic materials, and calibrated in low strain (<20%) experiments, whereas natural fault rocks are usually polymineralic and highly strained. This becomes particularly important when progressive strain leads to microstructural modifications allowing localisation of deformation into the weaker phases, in which case the weaker phases tend to dominate mechanical behaviour [Jordan, 1987; Ross et al., 1987; Ross and Bauer, 1992; Shea and Kronenberg, 1993; Dell' Angelo and Tullis, 1996; Kawamoto and Shimamoto, 1998; Handy et al., 1999]. In many situations, the weakest materials present will be phyllosilicates, either inherited from the host rock or produced during mineral reactions [e.g. Rubie, 1990; Wintsch et al., 1995], many of which are known to have both frictional and plastic strength significantly below that of quartz or feldspars [Shimamoto and Logan, 1981; Logan and Rauenzahn, 1987; Kronenberg et al., 1990; Morrow et al., 1992; Shea and Kronenberg, 1992; Mares and Kronenberg, 1993; Moore et al., 1996; Moore et al., 1997; Morrow et al., 2000].

Secondly, conventional strength profiles essentially ignore the presence of fluids. Fluids may influence the mechanical behaviour of fault zones in two basic ways. First, faults may be weakened due to the presence of superhydrostatic pore fluid pressure in the fault zone, reducing the effective normal stress on the fault [Byerlee, 1990; Blanpied et al., 1992; Rice, 1992; Sleep and Blanpied, 1992; Byerlee, 1993; Sleep, 1995; Miller et al., 1996]. High fluid pressure may arise from the influx of high-pressure fluids from lower levels or from compaction and sealing of porous fault gouge. In addition, high fluid pressures may arise from transient heating of fluids during earthquake rupture.

Alongside effects of increased pore fluid pressure, fault weakness may arise due to the action of fluid-assisted deformation mechanisms such as pressure solution [Rutter, 1976, 1983; Raj, 1982; Lehner and Bataille, 1984/85; Spiers and Schutjens, 1990] and stress corrosion cracking

[Dennis and Atkinson, 1982; Atkinson and Meredith, 1989; Dunning, 1994 #98]. These may allow fault slip at shear stress levels significantly below the frictional strength [Rutter and Mainprice, 1979; Sibson, 1983; Chester and Higgs, 1992; Blanpied *et al.*, 1995; Chester, 1995]. These mechanisms are likely to be important in particular under the hydrothermal conditions pertaining around the brittle-ductile transition, leading to truncation of the strength maximum predicted by conventional strength envelopes (see dashed line in Figure 1.1) [Sibson, 1983; Chester, 1995; Hickman *et al.*, 1995].

Finally, low fault strength might be explained, at least on seismogenic faults, by dynamic reduction in normal stress during earthquake rupture as a result of propagation of dilational elastic waves along the fault [Heaton, 1990; Brune *et al.*, 1993; Mora and Place, 1994; Melosh, 1996; Ben-Zion and Andrews, 1998]. The explanation for the weakness of large fault zones remains a source of controversy, due in part to a lack of systematic experimental work allowing rigorous testing of the above hypotheses. Thus, the mechanical behaviour of major fault zones remains poorly understood.

This thesis deals with the effect of fluid-assisted deformation processes on fault slip behaviour, in both monomineralic and polymineralic systems. Although the notion that fluid-assisted deformation processes are important in fault slip is widespread, the way in which these mechanisms influence fault behaviour is poorly understood and inadequately quantified to allow useful modelling of fault strength and sliding. It should be noted here that the emphasis in this thesis on fluid-assisted deformation mechanisms does not mean that the other weakening mechanisms mentioned are discarded. In fact, none of the above weakening mechanisms is likely to be solely responsible for the weakness of faults such as the San Andreas fault, and fault weakness probably arises from a combination of the mechanisms mentioned. Apart from possibly influencing long-term fault strength, fluid-assisted deformation processes may also be important in seismicity, in particular as mechanisms of interseismic strength recovery. In the following, previous work on the effect of fluids on long-term strength and interseismic strength recovery will be briefly discussed.

1.2 Chemically active fluids and long-term fault strength

It has long been inferred from field observations of natural fault zones that fluid-assisted deformation processes such as pressure solution and subcritical crack growth play an important role in fault zones [Rutter *et al.*, 1986; Wojtal and Mitra, 1986; Power and Tullis, 1989; Chester *et al.*, 1993; Bruhn *et al.*, 1994; Hadizadeh, 1994; Caine *et al.*, 1996]. It is widely believed that these processes may lead to significant weakening, in particular at mid-crustal levels where high confining pressure inhibits brittle failure/frictional sliding and low temperatures inhibit dislocation creep. Microphysically based models for pressure solution-accommodated fault slip have been developed by Rutter and Mainprice [1979] and Lehner and Bataille [1984/1985], assuming all energy dissipation in the fault zone occurs by pressure solution. These models have the disadvantage that they do not incorporate frictional sliding as a dissipative mechanism. The models predict a linear relation between fault strength and sliding rate, and a strong grain size sensitivity of strength. To date, only very few systematic experimental studies allowing these models to be rigorously tested have been undertaken. This is in part because of the difficulty of reproducing fluid-assisted deformation processes under laboratory conditions. Evidence of weakening with respect to frictional strength was obtained in stress relaxation experiments on clay-bearing sandstones [Rutter and Mainprice, 1978; Rutter and Mainprice, 1979; Chester and Higgs, 1992]. However, in these experiments strains were too low to achieve mechanical steady state.

Also, the [Rutter and White, 1979] reported that weakening was absent in clay-free sandstones. Strongly rate-dependent behaviour was also observed in experiments on granite gouge under hydrothermal conditions [Blanpied *et al.*, 1995]. Again, in this case the relative roles of phyllosilicates and pressure solution in producing the observed weakening are unclear. Hence, no reliable basis exists to quantitatively assess the effect of solution transfer processes on fault strength.

It is known from field studies and laboratory investigations that the presence of phyllosilicates at grain contacts strongly increases the rate of pressure solution. This effect is believed to be due to phyllosilicates increasing grain boundary diffusivity [Dewers and Ortoleva, 1991; Hickman and Evans, 1995; Renard *et al.*, 1997; Rutter and Wanten, 2000]. In addition, phyllosilicates tend to form foliations, possibly allowing sliding of grains along foliae because of their relatively low friction. In view of the omnipresence of phyllosilicates in natural faults zones, a quantitative description of solution-transfer accommodated fault slip should include the effect of phyllosilicates.

1.3 Chemically active fluids and seismic fault behaviour

In addition to their effect on long-term fault strength, solution transfer processes may be a mechanism of compacting and welding together of fault asperities or fault gouge, thus increasing the static frictional strength during interseismic intervals [Angevine *et al.*, 1982]. Since the identification of the stick-slip instability as a mechanism for earthquake generation [Brace and Byerlee, 1966], experimental studies of frictional behaviour have focused on transient effects leading to instabilities, culminating in the formulation in the late 1970's of the so-called rate- and state-dependent friction (RSF) laws [Dieterich, 1979; Ruina, 1983; Marone, 1998; Scholz, 1998]. These are empirical equations describing transient effects of rock friction upon sudden changes in sliding velocity. These may be written in the form

$$\mu = \mu_0 + a \ln\left(\frac{V}{V_0}\right) + b \ln\left(\frac{V_0 \theta}{D_c}\right) \quad (1.1)$$

where μ is the friction coefficient, μ_0 is a reference friction value at sliding velocity V_0 , V is the frictional slip velocity, θ is a state variable [Ruina, 1983], a and b are empirical constants, and D_c is a critical slip distance describing the displacement needed to re-establish steady state strength upon a velocity change. Equation (1.1) predicts that upon a sudden increase in sliding velocity friction will show a sudden increase ("direct effect") determined by the second right hand side term of (1.1), after which friction gradually decreases to a new steady steady state level ("evolution effect"). Unstable behaviour can arise only when the evolution effect is larger than the direct effect. The evolution to a new steady state is described by coupling (1.1) with an equation describing the evolution of the state variable. Two basic types of evolution equations or "laws" have been proposed. Here, formulation of Marone [1998] will be used, to allow easy comparison. The first, generally referred to as the Dieterich law, can be written

$$\frac{d\theta}{dt} = 1 - \frac{V\theta}{D_c}. \quad (1.2)$$

Implicit in this law is the view that the state variable represents an average contact lifetime, i.e., strength evolution is an essentially time-dependent process. In contrast to this, [Ruina, 1983] proposed an alternative evolution law, in which it is assumed that any friction change, even during quasi-stationary contact, requires slip. This law can be written

$$\frac{d\theta}{dt} = -\frac{V\theta}{D_c} \ln\left(\frac{V\theta}{D_c}\right). \quad (1.3)$$

Which evolution law is most appropriate is a subject of debate [Beeler *et al.*, 1994; Beeler and Tullis, 1997; Marone, 1998]. The above models are calibrated in laboratory experiments by means of velocity-stepping experiments. Interseismic strengthening is studied by means of so-called slide-hold-slide experiments. In these, sliding at a particular velocity is halted for a given time and resumed at the initial velocity thereafter, and the effect of the hold time on static frictional strength is measured.

The RSF laws have proven very generally applicable, being capable of describing frictional behaviour in almost any material and over a range of conditions (see Marone [1998] and references therein) and are often used to model natural fault behaviour [Cao and Aki, 1986; Tse and Rice, 1986; Okubo, 1989; Sleep, 1995; Sleep, 1997]. However, it should be realized that the RSF laws are empirical in nature. The grain contact scale microphysical mechanisms leading to the observed behaviour are not well understood. Moreover, the RSF laws were developed on the basis of, and calibrated mostly with, experiments at room temperature, where fluid-assisted processes are of relatively little importance. Hence, the applicability of the RSF laws under the hydrothermal conditions pertaining in large parts of the seismogenic zone is as yet unclear. It seems likely that fluid-assisted deformation processes will strongly influence frictional behaviour, by allowing rapid fluid-enhanced compaction and lithification. Indeed, experiments performed under hydrothermal conditions show significantly increased healing rates [Fredrich and Evans, 1992; Karner *et al.*, 1997; Olsen *et al.*, 1998] and increased sliding velocity dependence of steady state friction [Blanpied *et al.*, 1995; Kanagawa *et al.*, 2000], but no clear inferences were made regarding the microscale mechanisms determining the observed behaviour. Hence, there is a need for systematic experiments on fault healing and frictional fault slip under conditions where fluid-assisted processes are known to be important.

Phyllosilicates are likely to influence fluid-assisted healing processes. On the one hand, as mentioned above, phyllosilicates increase the rate of pressure solution compaction, possibly enhancing fault strengthening in this way. On the other hand, clays at grain contacts are inferred to inhibit contact adhesion [Hickman and Evans, 1995], in this way possibly preventing healing. Unfortunately, no systematic experimental data on the effect of phyllosilicates on fault healing presently exist. It seems that to arrive at a realistic description of the seismogenic cycle the effects of phyllosilicates, and their influence on healing processes, need to be taken into account.

1.4 Aims of this research

From the above considerations it is clear that there is a need for systematic experimental investigation into the effects of chemically active fluids on fault slip behaviour, in order to obtain a quantitative, mechanism-based understanding of fault slip behaviour under hydrothermal conditions. These experiments need to be performed in a configuration in which high shear strains, realistic for natural faults, can be reached. For this research, the following specific aims are identified:

1. Experimental verification of the possibility of pressure solution-controlled fault slip in steady state, high strain experiments, testing previously existing models.
2. Assessment of the effect of phyllosilicates on the mechanical behaviour of fault rocks under conditions favouring pressure solution. This involves both the effect of phyllosilicates on steady state fault strength and the effect of microstructural evolution on mechanical behaviour.
3. Development of a realistic, microphysically-based model for fluid-assisted deformation of fine-grained fault rocks, and application of this model to natural faults in order to quantitatively assess the implications of possible pressure solution-controlled fault slip for crustal strength profiles.
4. Investigate the way in which fluid-assisted mechanisms act to influence fault strength evolution, and to what extent the rate- and state-dependent friction laws can be used under conditions where fluid-assisted deformation processes are important.
5. Investigate the effect of phyllosilicate content and spatial arrangement (i.e., microstructure) on fluid-assisted healing processes.

1.5 A note on the usage of rock analogue materials in rock deformation studies

Despite the widespread notion that solution-transfer processes are important in crustal deformation, they are relatively little studied. This is due in part due to the difficulty of reproducing solution transfer processes in natural materials under laboratory conditions, because of their extremely low rates. Due to the fairly low activation energies of solution transfer processes (~20 kJ/mole, see *Nakashima* [1995]), performing experiments at artificially high temperatures, as is often done in studies of dislocation creep, is of little help. A way of solving this problem is to use rock analogue materials, in which the rates of interface reactions and diffusion are much higher at accessible experimental conditions. The experiments reported in this thesis were performed using halite (NaCl) and halite/kaolinite mixtures as rock analogues. The principal assumption underlying the use of analogue materials to study deformation processes is that in these materials the same basic processes occur as in natural materials, albeit at very different rates. For our experiments, the main analogue function is in the fact that halite dissolves in water, similar to quartz or feldspar, but in much higher quantities and at much higher rates. However, the brittle behaviour of halite differs markedly from that of network silicates in the sense that halite cleaves along crystallographic planes, whereas network silicates fracture. A means of assessing to what extent the analogue material may be used to represent natural materials is provided by inspection of microstructures: if

microstructures developed in analogue materials are similar to those in natural rocks, the micro-scale processes leading to the microstructures are likely to be the same as well. Usage of rock analogue materials has yielded important insights into the detailed mechanisms of pressure solution creep [Raj, 1982; Pharr and Ashby, 1983; Rutter, 1983; Tada and Siever, 1986; Spiers and Schutjens, 1990; Hickman and Evans, 1992, 1995; Gratier, 1993; Spiers and Brzesowsky, 1993; Den Brok *et al.*, 1998; Visser, 1999]. However, one should constantly be aware that rock analogue materials can only represent natural materials and phenomena to a limited extent.

It should be noted here that in experimental deformation studies of natural materials the temperatures and differential stresses used are generally much higher than in natural situations. This is necessary in order to achieve measurable deformation rates. However, usage of artificially high temperatures and differential stresses has an important drawback. Because of the fact that the rate of crystal plastic processes is much more strongly dependent on temperature and stress than the rates of solution transfer processes, in experiments on natural materials crystal plastic processes will always be more strongly favoured over solution transfer processes than in natural situations. The only way to avoid this is to use analogue materials in which the relative magnitude of the rates of intercrystalline deformation versus solution transfer processes under experimental conditions is more similar to the relative magnitude in natural situations.

Finally, to avoid confusion it is important to note that rock deformation experiments such as reported in this study are not intended to provide a scaled-down model of (parts of) the earth, as in so-called "analogue modelling" studies [see e.g. Kincaid and Olson, 1987; Shemenda, 1993; Facenna *et al.*, 1999]. Rather, rock deformation experiments aim at understanding the microscale processes leading to the observed behaviour. This allows development of a microphysically based model, which can then be extrapolated to natural conditions and materials and applied in numerical models.

Chapter 2

Slip behaviour of simulated gouge-bearing faults under conditions favouring pressure solution

This chapter was published in modified form as: Bos, B; Peach, CJ; Spiers, CJ.: Slip behavior of simulated gouge-bearing faults under conditions favoring pressure solution, Journal of Geophysical Research 105, pp.16,699-16,717, 2000.

Abstract. Geophysical observations as well as deformation experiments indicate that under hydrothermal conditions crustal faults can be significantly weakened with respect to conventional brittle-plastic strength envelopes. Pressure solution has long been proposed as a mechanism leading to fault weakness. However, pressure solution has also been proposed as contributing to interseismic fault healing, and the competition between the weakening and healing effects of pressure solution is unclear. To investigate this issue, we have conducted rotary shear experiments on synthetic faults containing granular halite (NaCl) gouge using NaCl-saturated mixtures of water and methanol as pore fluid. The NaCl-water-methanol system was chosen as a rock analogue because pressure solution is known to be important in this system at ambient conditions. We explored the influence of varying pore fluid composition (hence pressure solution rate), gouge grain size and wall rock surface roughness, as well as normal stress and sliding velocity on slip behaviour. All experiments were done under drained conditions. An acoustic emission detection system allowed detection of brittle events in the gouge. The results show no evidence for steady state pressure solution controlled fault slip. Frictional, rate-insensitive behaviour was observed, whereas the microstructures and compaction behaviour clearly demonstrated that pressure solution was active in the gouge. Our data show that fluid-assisted healing effects dominated over weakening, causing fault strength to be controlled mainly by brittle-frictional processes. Existing models describing pressure solution controlled fault creep may not be applicable to a porous gouge undergoing compaction as well as slip.

2.1 Introduction

In order to model motion and earthquake generation on large-scale crustal faults, an understanding of the rheology of these faults is necessary. Generally, crustal strength is modeled using a frictional fault-sliding law for the upper, brittle part of the crust, plus power law creep equations describing plastic flow at deeper crustal levels [Goetze and Evans, 1979; Sibson, 1983, 1984; Kohlstedt *et al.*, 1995; Ranalli, 1997]. Experiments have shown that steady state frictional strength under dry conditions is linearly related to normal stress via a coefficient of friction μ of 0.6-0.9, and is to a first approximation insensitive to sliding rate, temperature, mineralogy, and grain size [Byerlee, 1978; Scholz, 1990; Kohlstedt *et al.*, 1995]. This relation is generally referred to as Byerlee's law. In addition, empirical laws describing transient effects of sliding rate changes on friction, the so called rate- and state-dependent friction laws, have been developed and successfully applied to model various earthquake-related phenomena [Dieterich, 1979; Ruina, 1983; Scholz, 1990, 1998; Marone, 1998].

However, it is widely recognized that under diagenetic and hydrothermal conditions, within the upper to middle crust, fault strength may deviate significantly from this. In particular, geophysical observations on the San Andreas Fault, notably stress orientation data and the absence of a significant heat flow anomaly, indicate that large intraplate fault zones may be considerably weaker than predicted by dry frictional sliding experiments [Zoback *et al.*, 1987; Hickman, 1991; Lachenbruch and Sass, 1992]. Several possible explanations for this have been offered. In particular, it has been suggested that the inferred weakness may be due to reduction of sliding

friction by increased pore fluid pressures [Blanpied *et al.*, 1992; Rice, 1992; Sleep and Blanpied, 1992; Byerlee, 1993], presence of materials with low intrinsic friction such as phyllosilicates [Shimamoto and Logan, 1981; Logan and Rauenzahn, 1987; Morrow *et al.*, 1992] or by chemically related effects, i.e. by fluid-assisted deformation processes. In addition, it has been proposed that friction, and associated heat production, could be substantially lowered during earthquakes by a dynamic reduction of normal stress [Heaton, 1990; Mora and Place, 1994; Melosh, 1996; Ben-Zion and Andrews, 1998]. This paper concentrates on the the effect of fluid-assisted deformation processes on fault strength, under conditions where fluid-assisted deformation processes and cataclasis dominate over dislocation creep.

Evidence for fluid-rock interaction and fluid-assisted deformation mechanisms is ubiquitous in exhumed crustal faults [e.g. Chester *et al.*, 1993; Bruhn *et al.*, 1994; Hadizadeh, 1994; Caine *et al.*, 1996; Seront *et al.*, 1998]. Solution transfer processes that are of potentially major importance in fault zones under diagenetic and hydrothermal conditions include pressure solution and capillarity driven neck growth. Pressure solution involves fluid phase diffusional transport of material from stressed grain contacts to pore walls in response to stress-induced gradients in solubility [Raj, 1982; Rutter, 1983; Spiers and Schutjens, 1990; De Meer and Spiers, 1999]. Fluid-assisted neck growth involves fluid phase diffusional transport towards grain contacts in response to gradients in local radius of curvature of the solid-liquid interface [Hickman and Evans, 1992, 1995]. Although solution transfer processes are widely recognized to be important in controlling fault rheology [Chester, 1995; Hickman *et al.*, 1995], views are contradictory regarding their mechanical effect.

For example, both pressure solution and neck growth have been proposed to lead to fault healing and strength recovery in periods of interseismic quiescence [Angevine *et al.*, 1982; Hickman and Evans, 1995], either by cementing grain contacts (by neck growth) or by gouge compaction and contact area increase (pressure solution). This type of effect has been observed in so-called slide-hold-slide experiments on fine grained quartz gouge under hydrothermal conditions [Fredrich and Evans, 1992; Karner *et al.*, 1997]. In these experiments, a temperature dependent increase in peak strength after the "hold" periods was observed. Similar observations were made on quartz-feldspathic gouge [Olsen *et al.*, 1998; Tenthorey *et al.*, 1998], but in these experiments healing was inferred to be due to cementation by a newly formed phyllosilicate phase.

At the same time, pressure solution has been proposed to allow ductile fault creep under conditions where low-to-moderate temperatures inhibit dislocation creep, thus providing a mechanism to truncate the brittle-plastic strength envelope [Rutter and Mainprice, 1979; Chester and Higgs, 1992; Chester, 1995; Hickman *et al.*, 1995; Kohlstedt *et al.*, 1995].

A microphysically based model for steady state fault slip by pressure solution-controlled creep of porous gouge was developed by Rutter and Mainprice [1979], assuming the rate of pressure solution to be diffusion controlled. A similar model has been developed by Lehner and Bataille [1984/85], using a more rigorous non-equilibrium thermodynamics formulation of the pressure solution process and allowing for interfacial reaction control. These models relate shear strain rate $\dot{\gamma}$ to shear stress, τ , via the equation

$$\dot{\gamma} = AZ\tau^n \quad (2.1)$$

where A is a porosity-dependent geometric term specific to individual rate controlling mechanisms. For diffusion controlled pressure solution slip, $n=1$ and Z can be written in the form

$$Z_{diff} = \frac{D\delta C\Omega_s}{RTh^2 d} \quad (2.2a)$$

where D is the diffusion coefficient of the dissolved solid in the intergranular fluid (effective thickness δ), C is the solubility of the solid in the fluid (mass fraction), Ω_s is the molar volume of the solid, R is the gas constant, T is absolute temperature, h is the average diffusion length associated with the diffusion process (i.e. the average distance between sources and sinks), and d is gouge grain size. For interface reaction (dissolution or precipitation) controlled pressure solution, n reflects the order of the interfacial dissolution/precipitation velocity versus driving force relation, and the parameter Z can be written as

$$Z_{int\ erf} = \frac{k^*}{RTd}, \quad (2.2b)$$

where k^* is a kinetic coefficient for the interface reaction. In the derivation by *Lehner and Bataille* [1984/85] for interface reaction control, n is taken to be unity, but in general n can be ≥ 1 depending on the interfacial reaction mechanism [*De Meer and Spiers*, 1997]. As seen from (2.1), these models predict a strong dependence of shear strength on sliding velocity, as well as a strong dependence on grain size. Some experimental evidence has been obtained for fault weakening with respect to the frictional strength towards low sliding rates [*Rutter and Mainprice*, 1978, 1979; *Rutter and White*, 1979; *Chester and Higgs*, 1992]. These data have mostly been obtained from stress-relaxation experiments on simulated faults containing quartz or quartz/clay gouges. However, the strains reached in these experiments are very low, so that the data may not represent steady state pressure solution controlled slip. In a series of slip-rate stepping experiments on granitic gouge, *Blanpied et al.* [1991, 1995] reported similar evidence for weakening and increased rate dependence of the sliding strength of granite gouge under hydrothermal conditions. However, it is not clear whether the observed weakening was due to pressure solution or was related to the generation of weak phyllosilicates during the experiment [*Blanpied et al.*, 1995], or both.

Summarizing, we can say that although there is indisputable experimental evidence for a significant influence of fluids on the mechanical behaviour of simulated faults, the mechanisms causing the observed strengthening and weakening effects, and their relative importance, are poorly understood. It seems useful, then, to investigate the effect of pressure solution and other solution transfer processes on fault slip behaviour in a system under conditions where 1) pressure solution is known to be very rapid, and 2) the rate of pressure solution and the rate determining process are well known. Halite (NaCl) plus saturated solution is such a system. Granular halite deforms rapidly by pressure solution at ambient conditions [*Spiers et al.*, 1990; *Gratier*, 1993; *Spiers and Brzesowsky*, 1993]. In addition, it is well established that pressure solution in halite is diffusion controlled. Moreover, the constitutive parameters (i.e. grain boundary diffusion properties) governing pressure solution creep in halite are well constrained [*Spiers et al.* 1990]. Finally, working at low stresses minimizes the effects of crystal plasticity and recrystallization [*Shimamoto and Logan*, 1986; *Chester and Logan*, 1990; *Spiers and Carter*, 1998]. Accordingly, halite is a highly suitable material for isolating the effect of pressure solution on fault slip behaviour, and for evaluating the importance of pressure solution controlled fault creep in relation to fault gouge compaction and healing.

In this paper, we report rotary shear experiments on simulated, fluid-saturated faults containing granular halite gouge. As pore fluid, NaCl-saturated mixtures of methanol and water were used. As the solubility of NaCl in methanol-water mixtures increases strongly with water content, varying the water content of the pore fluids amounts to varying the solubility of NaCl in the fluid and thus the rate of pressure solution in the gouge. In accordance with the above considerations, the main aim of the experiments was to obtain evidence for pressure solution

controlled fault slip, and to evaluate the importance of this in relation to healing/ strengthening effects. The results show that, although pressure solution was clearly active in the gouge at significant rate, steady state pressure solution controlled fault slip did not occur. Instead, fluid-assisted compaction and healing dominated, and fault slip involved cataclasis and faulting of the gouge.

2.2 Experimental method

2.2.1 Apparatus and sample assembly

The experiments were conducted at room temperature using the rotary shear apparatus shown schematically in Figure 2.1a. The annular sample assembly, described in more detail below, consists of two toothed stainless steel rings with dense halite wall rock pressed onto them (see Figure 2.1b+c), sandwiching a layer of synthetic halite gouge. The stainless steel rings are gripped between two cylindrical forcing blocks. The lower forcing block is rotated at controlled angular velocity by a motor plus gearbox, while the upper block is maintained stationary, thus leading to shear on the synthetic fault. Normal stress is applied and servo-controlled to within 0.01 MPa using an Instron 1362 loading frame and measured using a 100 kN Instron load cell. The shear stress is measured using two strain gauge force gauges mounted in a torque couple which provides the reaction needed to hold the upper forcing block stationary. Shear stress was measured with a resolution of ~10 kPa. The resolution in coefficient of friction μ is 0.015. This is insufficient to study in detail the transient rate-and-state friction effects observed in many experiments and mentioned above (which requires a resolution of ~0.005), but our main focus is on first order effects of pressure solution on sliding strength. Displacement normal to the synthetic fault surface (i.e. gouge compaction/dilatation) is measured using a Linear Variable Differential Transformer (LVDT, 1 mm full scale, 0.01% resolution) located inside the upper forcing block. Angular and hence linear displacement is measured using a potentiometer geared to the rotation of the lower forcing block..

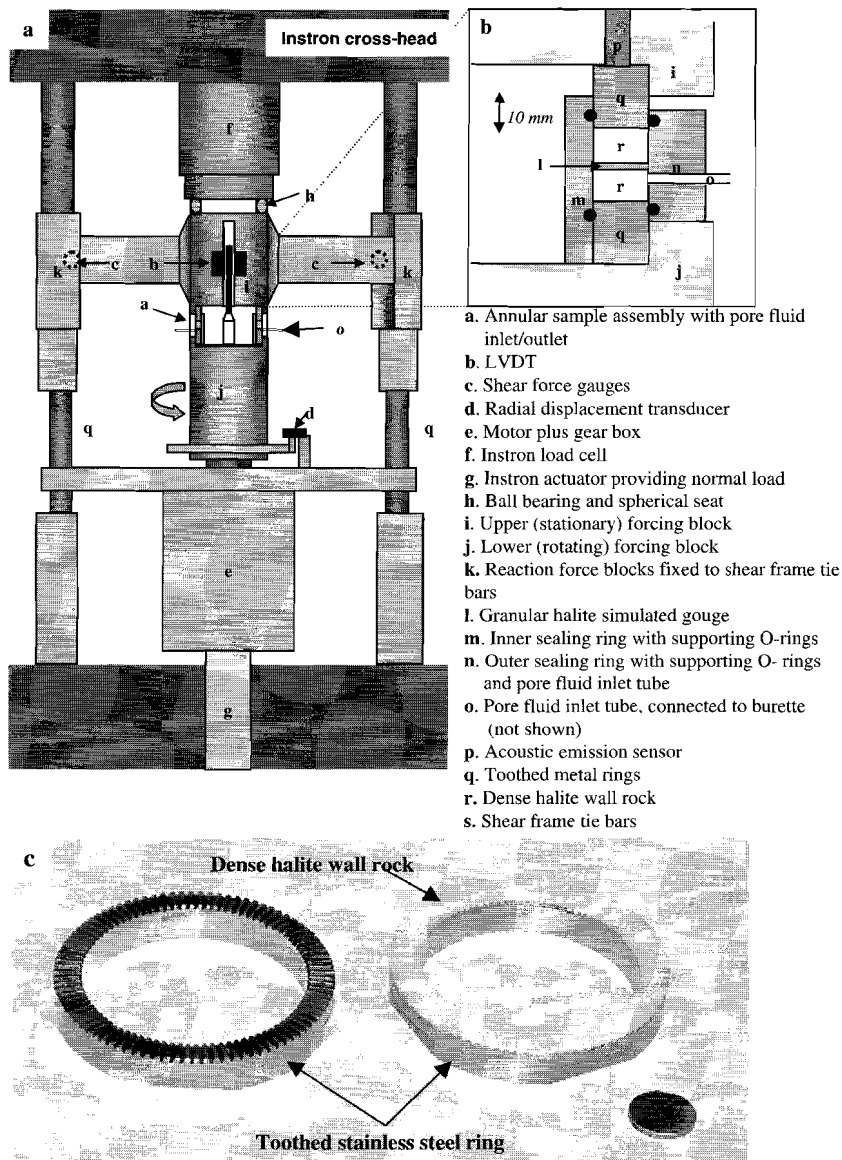


Figure 2.1. Schematic diagram of *a*) the deformation apparatus (not to scale) and *b*) the sample assembly. *c*) Photograph of stainless steel toothed rings with and without halite wall rock (smooth surface) pressed on. The diameter of the coin (for scale) is 23 mm

The details of the sample assembly are depicted in Figure 2.1b and 2.1c. The dense (< 3% porosity) halite wall rock rings (10 cm in diameter and 1 cm in width) were prepared by cold-pressing analytical grade granular halite (Merck) onto the toothed and hardened stainless steel support rings. This was done in an annular compaction die, at 140 MPa applied stress. So-called "smooth" wall rock surfaces were created by pressing dense rings with a flat free surface, and subsequently grinding these surfaces with abrasive paper (grain size ~30 μm). "Rough" surfaces were created by pressing dense wall rock rings with ~0.5 mm high "teeth" in the free surface. In the experiments performed using smooth surfaces, 3.00 g of granular halite was sandwiched between the wall rock rings, yielding a simulated gouge layer of 1 (\pm 0.1) mm thickness. In the rough surface experiments, 5.00 g of halite was used in order to obtain an equivalent gouge thickness. The starting thickness of the gouge layer could be reasonably accurately controlled in the smooth surface experiments. In the rough surface experiments this was more difficult because of the variability of the toothed halite surface. The synthetic fault assembly is sealed using a plastic inner and a stainless steel outer ring, fitted with O-rings (see Figure 2.1b). Pore fluid was introduced through the outer sealing ring using two diametrically mounted tubes (Figure 2.1a), each connected to a burette. Prior to each experiment, one of the burettes was filled with the appropriate pore fluid. The pore fluid was introduced by opening the burette taps, hence allowing the fluid to invade the sample and the second burette. The burettes were capped with rubber membranes to prevent evaporation of pore fluid. The experiments were done under "drained" conditions, i.e. with both burette taps open, hence keeping the pore fluid at atmospheric pressure.

In order to detect microseismic events in the gouge, four equally spaced acoustic emission (AE) sensors are spring-loaded into the upper toothed metal ring of the sample assembly (see Figure 2.1b). The AE system, previously described by *Brzesowsky* [1995], allowed monitoring of the AE event rate. The AE signals were amplified, and filtered to include only the frequency range 100 kHz - 1 MHz. This was necessary for eliminating low frequency interference and resonance effects. The system counts single events by blocking the counters for a controlled period (8 milliseconds) as soon as the signal exceeds a preset threshold. The threshold used in the present experiments was 100 mV, while the typical noise level was < 10 mV. The maximum countable event frequency was 125 events/second. The AE data are presented as AE-rates, in counts/minute.

2.2.2 Experimental procedure

All samples were first subjected to a fixed normal stress of 1 or 3 MPa under dry conditions for 10 minutes, after which no significant further compaction occurred. The sliding velocity was then set to 1 $\mu\text{m/s}$, and the samples were dry-sheared to ~5 mm displacement. The pore fluid was then introduced without interrupting the experiment, and the samples were sheared under wet conditions for typically ~3-5 or ~85-90 mm. In most experiments, the sliding velocity was subsequently stepped at 1 MPa normal stress, and the normal stress was stepped at a sliding velocity of 1 $\mu\text{m/s}$, to determine the influence of these variables on fault shear strength. The velocities used in the stepping procedure were 0.01, 0.2, 1, and 5 $\mu\text{m/s}$, while the normal stresses used were 0.5, 1, 2, and 3 MPa. Sliding displacements of typically 1.5-3 mm were achieved in individual steps. All experiments are listed in Table 2.1, together with relevant experimental details, the amount of displacement prior to stepping, and the sequence of velocity and normal stress steps employed in each experiment.

Table 2.1. Table of All Experiments

Test	Initial Gouge Grain Size, μm	Wall rock Surface Roughness *	Pore Fluid Water/ Methanol Ratio, vol. %	Displacement prior to Stepping, mm	Total Displacement, mm	Normal Stress Sequence, MPa	Sliding Velocity Sequence, $\mu\text{m/s}$
N1	~100	S	100	87.48†	87.48	1	1
N2	~100	S	100	6.79	29.38	1 0.5, 2, 3, 1 1	1, 5, 0.2, 1 1
N3	~100	S	65	86.01†	86.01	1	1
N4	~100	S	65	5.18	32.33	1 0.5, 2, 3, 1 1	1, 0.2, 5, 1 1 0.01
N5	~100	S	35	89.31	100.32	1	1, 0.2, 5, 1
N6	~100	S	35	85.47	98.57	2, 0.5, 3, 1 1	1 1, 0.2, 5, 1
N7	~100	S	10	84.90	101.80	2, 3, 0.5, 1 1	1 1, 5, 0.2, 1
N8	~100	S	dry	90.56	108.18	2, 0.5, 3, 1 1 2, 0.5, 3, 1	1 1, 0.2, 5, 1 1
N9	~100	S	silicone oil	88.37	104.33	1 2, 3, 0.5, 1 1	1, 0.2, 5 1 1
N10	~100	S	100	4.82	4.82	1	1
‡							
N11	~100	R	dry	3.40	29.59	1	1
N12	~100	R	dry	88.14†	88.14	0.5, 1, 2, 3 1	0.2, 1, 5 1
N13	~100	R	100	6.56	28.82	1, 2, 3, 0.5, 1	1 0.2, 5, 1
N14	~100	R	100	92.16†	92.16	1	1
N15	<50	S	35	88.93†	88.93	3	1
N16	~100	S	35	86.56†	86.56	3	1
N17	~200	S	35	86.46†	86.46	3	1

* R = rough surface (roughness ~0.5 mm), S = smooth surface (lapped with SiC paper of roughness 30 μm)

† Experiments at single velocity and normal stress (i.e. without stepping).

‡ Compaction without shear experiment

Three sets of experiments were conducted, respectively exploring the effect of varying pore fluid composition, wall rock surface roughness and initial gouge grain size, in addition to that of sliding velocity and normal stress.

In the first set of experiments (runs N1-10), addressing the effect of fluid composition on sliding behaviour, runs were conducted using gouge with ~100 μm initial median grain size, and smooth wall rock surfaces. Gouge grain size distribution was determined using a Malvern particle sizer, and showed 90% of the grains to lie between 57 and 110 μm . The pore fluids used were NaCl-saturated mixtures of double distilled water and methanol with water contents (volume percentage X) of 100%, 65%, 35%, and 10%. Note that the solubility of NaCl in methanol-water mixtures increases with water content, as shown in Figure 2.2. As the rate of diffusion controlled pressure solution is expected to increase with solubility [Rutter, 1976; Pharr and Ashby, 1983; Gratier and Guiget, 1986], increasing the water content of the pore fluid amounts to increasing the rate of pressure solution in the gouge. In addition, a single dry control experiment (i.e. open to ambient humidity) and an experiment using silicone oil (chemically inert, viscosity ~5 times water viscosity) as pore fluid were conducted. Finally, a "compaction without shear experiment" was

performed (experiment N10). This experiment was first sheared dry, like all others, but after ~4 mm of slip sliding was terminated. Around 15 minutes later, fluid (100% water presaturated with NaCl) was added and the sample was allowed to compact for ~22 hours.

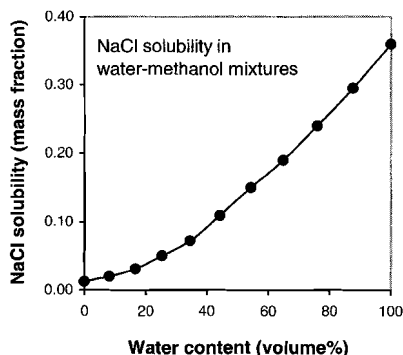


Figure 2.2. Solubility of NaCl in water/methanol mixtures. Data taken from Baykara and Pharr [1991]

The second set of experiments (runs N11-14) comprised four runs with rough surface wall rock, performed under wet (100% water) and dry conditions, again using gouge with an initial grain size of ~100 μm . Under both wet and dry conditions, one experiment was performed at 1 MPa normal stress and 1 $\mu\text{m/s}$ sliding velocity, and one velocity and normal stress stepping experiment was performed. In the third set of experiments (runs N15-17), different initial grain sizes were used. Next to the material used in the first set of experiments (labelled 100 μm), sieved fractions of 37-50 μm and 180-210 μm were used. These were labelled 50 μm and 200 μm , respectively. These experiments were done at a single normal stress (3 MPa) and sliding velocity (1 $\mu\text{m/s}$) and using a pore fluid composition with 35% water.

Experiments were terminated by halting sliding and then removing the normal load. The complete sample assembly was subsequently removed from the loading frame and flushed with hexane and compressed air, while still sealed, to remove the brine from the sample pore space. The sealing rings (m, n in Figure 2.1b) were then removed, and the wall rock and gouge were carefully detached from the stainless steel ring. After macroscopic inspection of the gouge and the wall rock, samples were dried and impregnated under vacuum with blue-stained epoxy resin. Finally, sections were cut normal to the sliding plane and parallel to the sliding direction, and standard thin sections were prepared for microscopic inspection.

2.3 Results

2.3.1 Mechanical data

The results obtained are shown in Figures 2.3-2.9, and are described below. Recall that all experiments started with ~5 mm dry slip, after which the pore fluid was added. During the dry slip period, all smooth surface samples first exhibited a shear stress peak, followed by regular stick-slip behaviour at a shear stress that decayed to a residual value of ~1/2 of the peak stress. Smooth surface samples compacted by ~25-75 μm during the first 3 mm displacement, after which no further compaction was observed until the fluid was added. The rough surface samples showed a stress peak followed by steady sliding at roughly the same shear stress as the stress peak.

Effect of pore fluid composition.

A marked influence of pore fluid composition on sliding behaviour was observed. Figures 2.3a, 2.3b and 2.3c, and 2.3d illustrate the effect of adding the various fluids used on sliding resistance (shear stress), compaction, and AE-rate, respectively, for smooth-surface experiments at

constant imposed sliding rate (1 $\mu\text{m/s}$) and normal stress (1 MPa). Figure 2.3e shows data from the "compaction without shear" experiment, in which sliding was terminated before the fluid was added.

Regarding the shear stress versus displacement plots (Figure 2.3a), two distinct types of behaviour were observed. Stick-slip behaviour was observed in samples slid dry, with oil, and with $X=10\%$ water pore solution. In contrast, experiments with pore fluid water contents $X > 35\%$ exhibited quasi-stable sliding. Experiments performed with $X = 35\%$ showed transitional behaviour, with stable sliding in long term runs at 1 $\mu\text{m/s}$, but with stick-slip occurring at higher stepped velocities. In addition, adding a water-bearing solution caused pronounced strengthening, whereas adding oil had no effect on strength. In the experiments exhibiting stick-slip (N7, N8 and N9), the wet experiment (N7) showed considerably higher stick-slip peak strength compared to the dry experiment. In the stable sliding experiments (N1, N3, N5), the shear stress increased to a stress peak upon adding the fluid, then falling to quasi stable sliding at a shear stress of $\sim 0.9\text{-}1$ MPa, with no systematic dependence of strength on pore fluid water content. In the highest water content experiments (N3, $X=65\%$ and N1, $X=100\%$), stable sliding was accompanied by gradual hardening towards the higher displacements. Examination of the specimen after termination revealed that in these experiments the wall rock had failed. In the "compaction without shear" experiment (see Figure 2.3e), terminating sliding under dry conditions caused a minor increase in shear stress, after which shear stress remained constant until fluid was added. Upon adding the fluid, rapid shear stress relaxation was observed.

Figure 2.3b shows that in the initial dry slip period, samples compacted by 25-75 μm , with no further volume change thereafter. The addition of a water-bearing fluid then led to rapid compaction in all experiments, whereas adding oil produced no effect. After adding the fluid, the stick-slipping experiment performed with $X=10\%$ showed a regular decrease of compaction rate with time. In contrast, the experiments exhibiting stable sliding ($X \geq 35\%$) showed rapid initial compaction upon adding fluid, followed immediately by a burst of dilatation, after which compaction resumed at a more moderate rate (Figure 2.3c). As shown in Figure 2.3c, the maximum dilatation rate coincided with the peak shear stress. The amount of compaction occurring directly after adding the fluid, as well as the amount of dilatation following this compaction showed respectively a positive and negative correlation with pore fluid water content X . The "compaction without shear" experiment (N10) revealed that under wet conditions compaction without shear is much faster than compaction during shear deformation. Finally, it should be noted that the samples that exhibited wall rock failure show dilatation in the final stages of the experiment.

The effect of adding fluid on acoustic emission (AE) rate is shown in Figure 2.3d. The Figure shows AE-data from a representative wet, stable sliding experiment (N1, $X=100\%$), as well as data for the experiment in which oil was added (N9). Adding solution first caused the AE-rate to suddenly drop, after which it recovered to a steady value about one order of magnitude lower than during dry slip. Adding oil had no effect on the AE-rate. In the "compaction without shear" experiment (see Figure 2.3e), terminating shear under dry conditions caused the AE-rate to instantly drop to zero. Directly after adding the fluid, a short burst of emissions was observed, after which no further AE-events were detected.

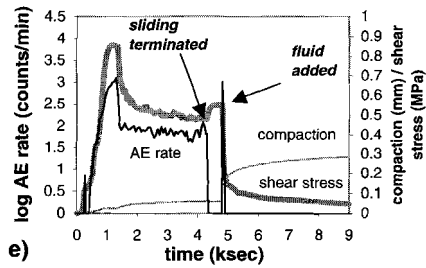
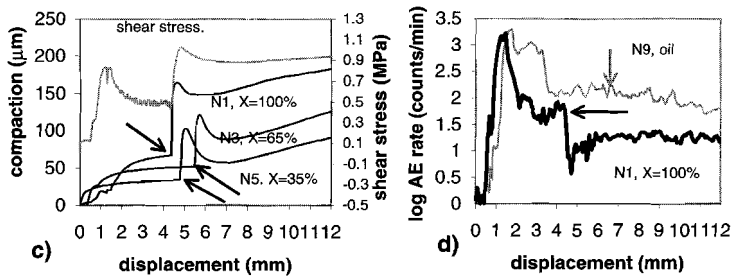
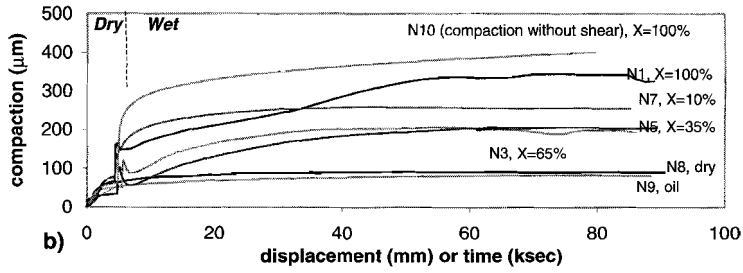
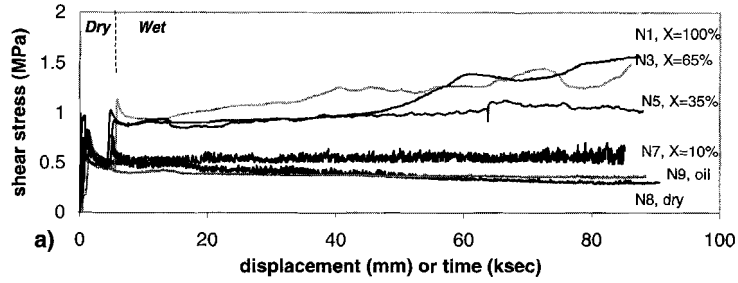


Figure 2.3 (previous page). Shear stress, compaction and acoustic emission data for various fluid compositions, at 1 MPa normal stress and 1 $\mu\text{m/s}$ sliding velocity, for smooth-surface wall rock. Pore fluid composition as indicated. Experiment numbers refer to Table 2.1. a) Shear stress vs. displacement or time. The stick-slip curves are aliased by the logging interval. Data show first ~ 5 mm of dry slip, after which the fluid is added ("wet"). b) Compaction vs. displacement. Note rapid compaction upon adding a water-bearing fluid. c) Detail of response to fluid addition in experiments with $X \geq 35\%$. The grey curve represents shear stress; the black curves represent compaction. Fluid composition is as indicated, the arrows indicate the point of fluid addition. d) Effect of adding fluid on acoustic emission (AE) rate. Arrows indicate point of fluid addition, pore fluids as indicated. e) Shear stress, compaction and acoustic emission data for "compaction without shear" experiment (run N10, $X=100\%$). Note rapid shear stress relaxation upon adding fluid.

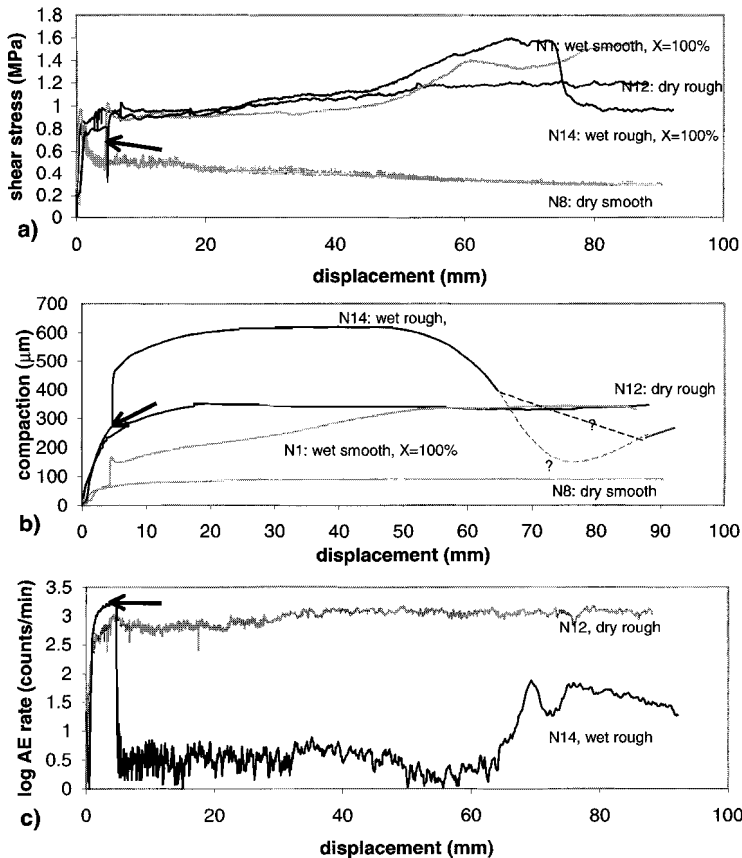


Figure 2.4. Shear stress and compaction data for rough surface experiments. Arrows indicate point of fluid addition. a) Shear stress vs. displacement for rough surface experiments under dry and wet ($X=100\%$) conditions. Smooth surface experiments (also depicted in Figure 3a) are shown in grey for comparison. b) Compaction vs. displacement for rough-surface experiments. No LVDT data are available in the interval between 65 and 88 mm displacement due to a technical error. c) AE-data for rough surface experiments.

Effect of surface roughness

Figures 2.4a, 2.4b and 2.4c illustrate the shear resistance, compaction behaviour and AE-rate in experiments performed with rough wall rock surfaces (runs N12 and N14). Data obtained from smooth-surface experiments (N1 and N8, also depicted in Figure 2.3a) are also shown in Figures 2.4a and 4b for comparison. Under dry conditions, the rough-surface experiments showed first a stress peak, followed by stable sliding, in contrast to the stick-slip behaviour exhibited by the dry smooth-surface experiment. Adding brine fluid led to a drop in shear stress to ~ 0.3 MPa, but after about 0.5 mm stable sliding resumed at slightly higher shear stress than under dry conditions. Note that the stable sliding strength of the wet-smooth, dry-rough and wet-rough experiments (N1, N12 and N14) were similar. At high displacements, both the rough and smooth-surface wet experiments showed significant strengthening, and the samples exhibited wall rock failure. In the dry rough surface experiment, this strengthening was much less pronounced, and the associated wall rock failure was absent.

Figure 2.4b shows the effect of surface roughness on compaction/dilatation behaviour. The dry, rough-surface experiment showed continuous compaction up to 15 mm displacement, after which no significant volume change occurred. The wet, rough-surface experiment showed increased compaction upon adding the fluid, changing to dilatation after about 50 mm displacement. For the displacement interval 65-85 mm no data are available due to a technical error, but at 85 mm displacement, compaction had resumed. It should be noted here that the effective gouge layer thickness in the rough-surface experiments was somewhat higher than in the smooth experiments, but with the current experimental procedure the effective thickness was hard to estimate.

Figure 2.4c shows AE-data for both the wet and dry rough-surface runs. In the dry experiment, the AE-rate was roughly constant throughout the experiment. In the wet experiment, the AE-rate dropped by 2,5 orders of magnitude upon adding the fluid. After ~ 60 mm of slip, the AE-rate rose as the sample dilated and strengthened (compare Figures 2.4a and 2.4b), and slowly fell again after 75 mm displacement, concurrently with a drop in shear stress.

Effect of initial grain size

Figure 2.5 shows the effect of initial grain size on shear strength and compaction behaviour, as observed in experiments (N15-N17) performed with $X=35\%$ water pore fluid, at 3 MPa normal stress, and using smooth wall-rock surface. During the initial dry shear stage, all samples showed a stress peak, followed by rapidly weakening stick-slip behaviour. After addition of the pore fluid, all samples showed a stress peak followed by stable sliding at a shear stress close to the stress peak, although the finest grained sample (run N15) showed a few stick-slip events in the first millimeters of displacement after adding the fluid. The data show no systematic grain size dependence of wet sliding shear strength from sample to sample, although the finest grain size experiment showed more pronounced strengthening in the latter half of the experiment. Inspection of the samples after termination revealed that the wall rock of the finest grain size experiment had failed, whereas the wall rock of the other experiments had remained intact.

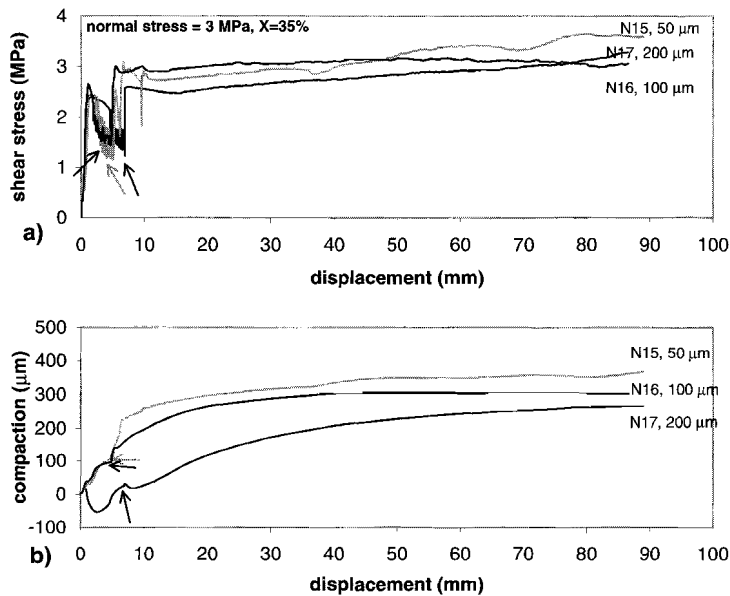
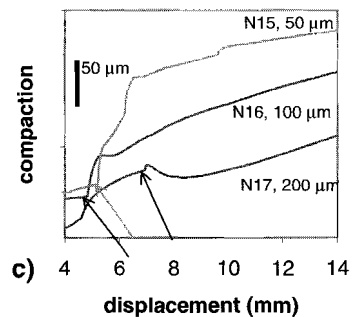


Figure 2.5. Shear stress and compaction vs. displacement for different starting grain sizes. Smooth-surface wall rock, fluid composition $X=35\%$, 3 MPa normal stress, and 1 $\mu\text{m/s}$ sliding velocity. Starting grain size as indicated. Arrows indicate the point of fluid addition. a) Shear stress vs. displacement. No systematic correlation of sliding strength with starting grain size was observed. b) Compaction vs. displacement. Upon fluid addition, compaction was followed by dilatation, the amounts of both correlating with starting grain size c) Detail of compaction behavior after adding fluid, for starting grain sizes as indicated.

In contrast to the above, Figure 2.5b shows a clear effect of grain size on compaction behaviour. In the initial dry stage of the experiments, all samples showed compaction during loading, dilatation during the stress peak, and again compaction as stick-slip sets in. When the fluid was added (see detail in Figure 2.5c), compaction again occurred, as the shear stress increased, with a switch to (minor) dilatation upon reaching the second peak stress. When a steady shear stress was subsequently reached, compaction resumed. The amount of compaction that occurred after adding the fluid increased with decreasing grain size. The amount of dilatation occurring in the neighbourhood of the stress peak increased with increasing grain size. The total amount of compaction achieved in the experiment was higher for smaller initial grain sizes.



Effect of varying sliding velocity

A representative plot of a velocity stepping sequence under wet conditions in stable sliding experiments is shown in Figure 2.6 (run N4, $X=65\%$ water). The behaviour closely resembled conventional rate and state dependent friction behaviour, in exhibiting sudden stress peaks upon stepping the sliding velocity, followed by a gradual decay to a new steady state shear stress. However, the magnitude of the stress peaks produced by stepping the sliding velocity as well as the decay distance were much larger than usually observed in dry friction tests (cf. [Dieterich, 1979; Scholz, 1998]). As illustrated in the inset of Figure 2.6, the shear stress dropped to less than half the steady state strength when sliding velocity was reduced from $1 \mu\text{m/s}$ to $0.01 \mu\text{m/s}$, returning to a steady state value only after $\sim 0.4 \text{ mm}$ of slip. The gouge showed transient dilatation upon increasing slip velocity, and transiently increased compaction rate upon decreasing slip velocity.

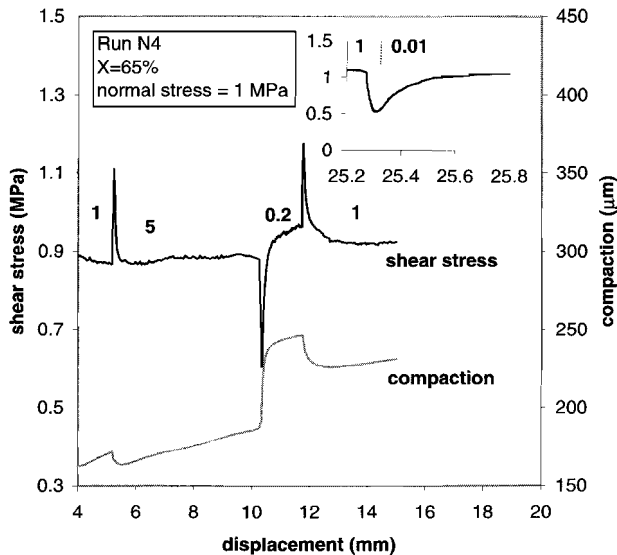


Figure 2.6. Representative data for velocity stepping sequence at 1 MPa normal stress (run N4, fluid composition $X=65\%$). Smooth-surface wall rock, sliding velocity as indicated (in $\mu\text{m/s}$). The black curve represents shear stress; the gray curve represents compaction. The data show only a minor effect of sliding velocity on sliding shear stress, but significant transient effects after stepping the velocity. The inset shows shear stress vs. displacement for a velocity step from 1 to $0.01 \mu\text{m/s}$, showing a large transient effect.

Plots of shear stress vs. sliding velocity for different fluid compositions and wall rock surface roughness are shown in Figures 2.7a and 2.7b. Dotted lines are used to represent data obtained in the stick-slip regime, whereas solid lines indicate stable sliding. For data from the stick-slip regime we plotted the stick-slip peak stress, i.e. the highest stress reached in a "stick" event. For data from the stable sliding regime, we plotted steady state sliding strength. In the experiments with $X=35\%$, a change in sliding behaviour from stable sliding to stick-slip could be induced upon increasing sliding velocity to $5 \mu\text{m/s}$. The behaviour did not return to stable sliding upon decreasing sliding velocity to $1 \mu\text{m/s}$ again. For this fluid composition, data are shown for both stick-slip and

stable sliding behaviour. For the other fluid compositions, this transition could not be induced. From the data it is clear that there was no first order dependence of strength on sliding rate over the $2\frac{1}{2}$ orders of magnitude range investigated. In the stick-slip experiments, stick-slip peak stress increased slightly with decreasing sliding velocity. In the stable sliding experiments, minor weakening with increasing sliding rate was observed, especially at higher velocities. The data clearly show the pronounced effects of pore fluid composition and, in the dry experiments, surface roughness described earlier. The shear stress increased with increasing pore fluid water content in the stick-slip regime, and showed no systematic correlation with pore fluid composition in the stable sliding regime.

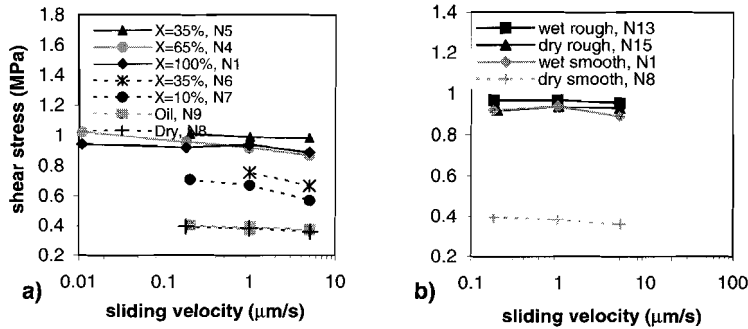


Figure 2.7. Plots of shear stress versus sliding velocity for a) smooth-surface experiments at 1 MPa normal stress and different fluid compositions, and b) smooth and rough surface experiments at 1 MPa normal stress. Fluid composition and experiment numbers as indicated. Stick-slip peak stress data are connected by dotted lines, stable sliding data by solid lines. No major effect of sliding velocity on shear stress is observed.

Effect of varying normal stress

In Figure 2.8, we show a representative plot of a normal stress stepping sequence performed under wet conditions. Increasing normal stress led to an increase in shear stress. Only minor hardening with displacement was observed during stepping. Increasing normal stress led to compaction, whereas decreasing normal stress led to transient dilatation. In Figures 2.9a and 2.9b, we show the shear stress vs. normal stress data obtained for different fluid compositions and surface roughness, respectively. Again, dotted lines denote stick-slip data, whereas solid lines indicate stable sliding. The data show a linear relationship between shear stress and normal stress for all conditions investigated. The data are well described by a Coulomb type failure criterion, relating shear stress τ to normal stress σ_n via a coefficient of friction μ and a cohesion term S , of the form

$$\tau = S + \mu\sigma_n. \quad (2.3)$$

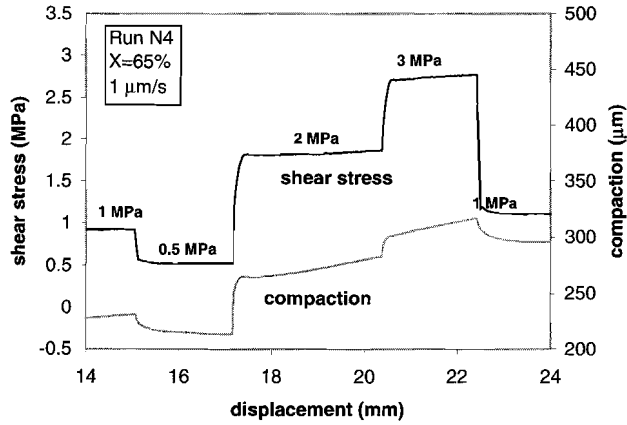


Figure 2.8. Plot of typical normal stress stepping sequence at $1 \mu\text{m/s}$ sliding velocity (Run N4, $X=65\%$ pore fluid). Normal stress as indicated. The black line represents shear stress; the gray line is compaction. A clear effect of normal stress on shear strength is observed.

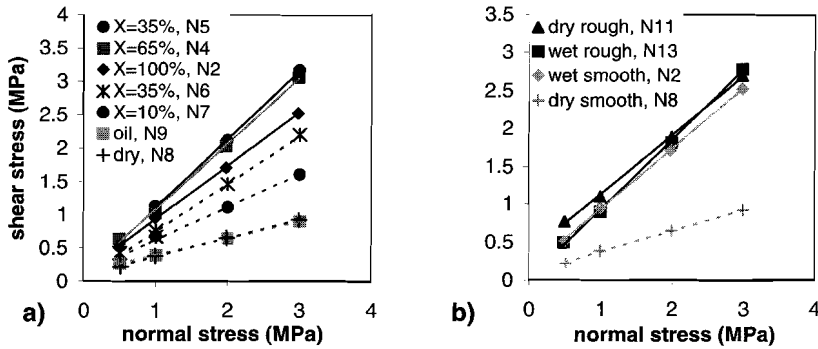


Figure 2.9. Shear stress versus normal stress for a) smooth-surface experiments at $1 \mu\text{m/s}$ sliding velocity and different fluid compositions, and b) smooth and rough surface experiments at $1 \mu\text{m/s}$ sliding velocity and fluid composition $X=100\%$. Dotted lines indicate stick-slip experiments, whereas solid lines indicate stable sliding. Figure 2.9a shows the coefficient of friction (slope of line) increases with water content in the stick-slip experiments, and slightly decreases with water content in the stable sliding experiments. From 2.9b it is clear that the coefficients of friction in both the wet and the dry rough-surface experiments and the wet smooth-surface experiment are roughly equal. The coefficient of friction in the dry smooth experiment is significantly lower.

The values for μ and S obtained in the various experiments are given in Table 2.2. For smooth surfaces, in the stick-slip regime the value for μ increased with increasing brine content from 0.25 for the dry and oil-flooded experiments, through ~ 0.5 for the $X=10\%$ experiment, to ~ 0.7 for the $X=35\%$ experiment. In the stable sliding regime, the value of μ is 0.8-1, and decreased slightly with

increasing pore fluid water content (Figure 2.9a). The data for the wet rough-surface experiment and the dry rough-surface experiment (Figure 2.9b) are very similar, and fall close to the wet smooth experiment.

Table 2.2. Strength Parameters for the Different Experiments

Fluid Composition	Deformation Style	Surface Roughness	μ	S, MPa	Experiment
100% water	stable sliding	S	0.80	0.13	N2
65% water	stable sliding	S	0.98	0.10	N4
35% water	stable sliding	S	1.01	0.10	N5
35% water	stick-slip	S	0.72	0.02	N6
10% water	stick-slip	S	0.50	0.12	N7
oil	stick-slip	S	0.25	0.14	N9
dry	stick-slip	S	0.28	0.10	N8
dry	stable sliding	R	0.78	0.36	N11
100% water	stable sliding	R	0.92	0.02	N13

2.3.2 Sample observations

Starting material. A micrograph of impregnated loose gouge starting material (median grain size $\sim 100 \mu\text{m}$) is shown in Figure 2.10a. Note the subangular grains and the broad grain size distribution. The grains show only a few intragranular cracks.

Samples that exhibited stick-slip. Samples that exhibited on-going stick-slip (i.e. the smooth-surface experiments run dry, with oil, or with $X=10\%$ pore fluid) could easily be separated from the wall rock along the upper gouge wall-rock interface. In the dry sample (N8), this interface was shiny, with numerous grooves several centimeters long developed in the sliding direction. Microstructures of the samples exhibiting stick-slip are shown in Figures 2.10b and 2.10c, for dry (N8) and wet (N7, $X=10\%$) conditions, respectively. Both samples show a very flat upper gouge-wall rock interface, with concentrations of fine-grained material filling up surface roughness (see arrows). The dry deformed sample is characterized by angular grains, and high porosity. Numerous intragranular and transgranular cracks were observed, mostly in the larger grains. In broad terms, the grain size distribution as well as the grain shape resembles that of the starting material. In contrast, the wet-deformed sample shows a compact aggregate, with rounded grains and fewer cracks. This sample could not be impregnated with resin, probably because the connected porosity was too low. In both wet and dry samples there is only minor grain size reduction compared to the starting material, and no fabric or shears were observed in the gouge.

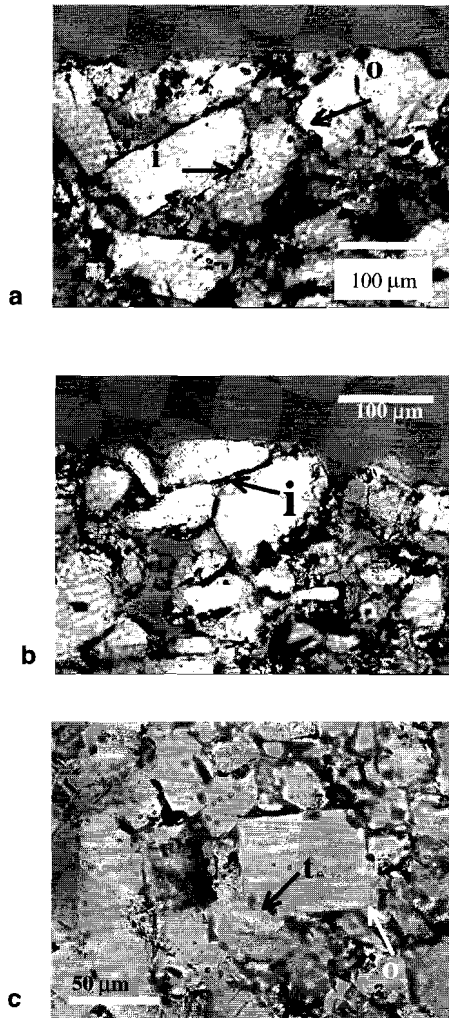


Figure 2.11. Typical truncation (*t*), indentation (*i*) and overgrowth (*o*) microstructures indicative of pressure solution, observed in wet deformed gouge. a) and b) from run N1 ($X=100\%$), c) from run N16 ($X=35\%$).

Samples that exhibited stable sliding.

Samples that exhibited stable sliding could not easily be separated along one of the gouge-wall rock interfaces. The cohesive but still friable gouge preferentially broke along surfaces dipping at an acute angle to the sliding direction. Representative microstructures of samples deformed wet with smooth-surface wall rock are shown in Figures 2.10d (run N3, $X=65\%$) and

10e (run N1, $X=100\%$). As shown in Figure 2.10e, the gouge is transected by low angle R-shears (indicated by arrows), which rotate into the shear zone boundary and which form the breaking surfaces mentioned above. The samples show significant grain size reduction with respect to the starting material. Larger grains often appear rounded. In most places the gouge shows a weak fabric, formed by trains of larger grains aligned at an angle to the shear zone boundary (arrow in Figure 2.10e). As shown in Figure 2.11, the wet samples show classical evidence for the operation of pressure solution, such as long grain contacts, truncations, grain-to-grain indentations, and overgrowths. Figure 2.10f shows a representative micrograph of material deformed wet with rough-surface wall rock. The "teeth" forming the surface roughness are outlined. For the rough-surface experiments, the microstructures of both the wet and dry deformed material were very similar. They show coarse-grained material between the teeth, whereas the zone between the two toothed rings shows isolated, rounded clasts in a fine-grained matrix.

In summary of the above, the samples exhibiting stick-slip behaviour show no fabric or faults, only minor grain size reduction, and a flat gouge to wall-rock interface. In contrast, samples that exhibited stable sliding show grain size reduction and R-shears in gouge. Finally, the wet samples show clear microstructural evidence for the operation of pressure solution in the gouge, both in the stick-slip and stable sliding regimes.

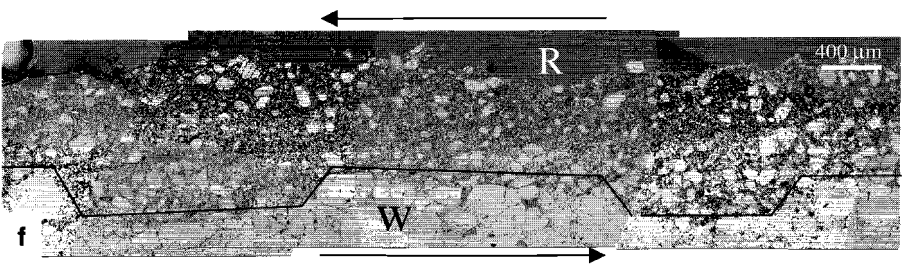
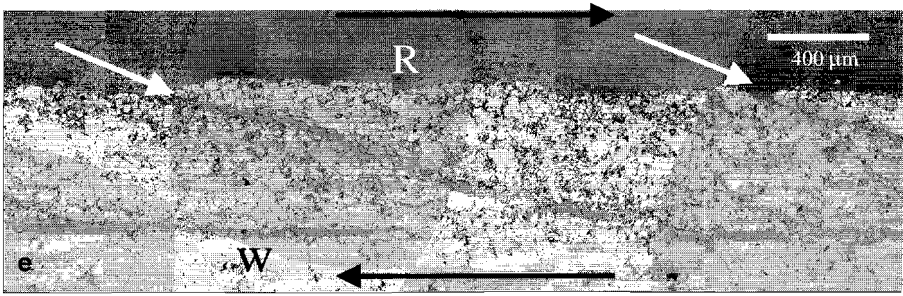
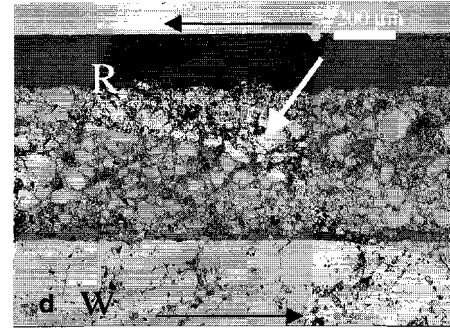
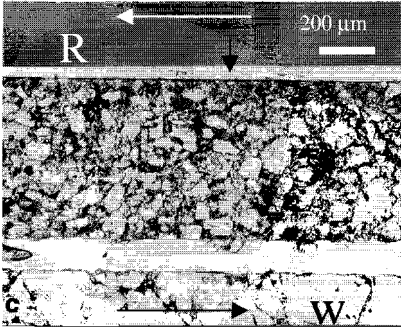
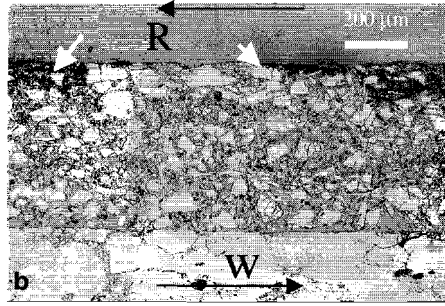
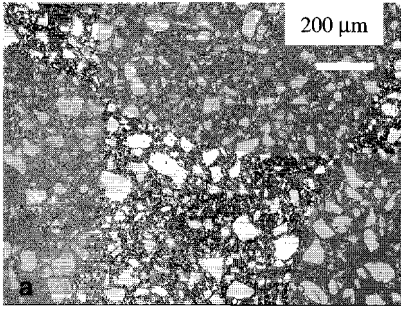


Figure 2.10 (previous page). Transmitted light micrographs of starting material and deformed samples. In all micrographs, "w" denotes the wall rock material, and R denotes the epoxy resin with which samples were impregnated. In most samples, the contact between the gouge and one of the wall rock blocks was lost during sample retrieval after the experiment. In all photographs, halite grains appear white, and the epoxy resin in the pores appears gray. a) Loose gouge starting material. The gray spotted matrix is epoxy resin. Note subangular grains and broad grain size distribution. b) Dry deformed material (Run N8). Note angular grains, absence of fabric, and accumulation of fine-grained material at the gouge-wall rock interface (arrows). c) Material deformed wet, exhibiting stick-slip behavior (Run N7, X=10%). The white material to the top and to bottom of the gouge is glue, which was used to impregnate this sample. Note compact aggregate, low porosity, flat top surface, and absence of any fabric. d) and e) Material deformed wet, exhibiting stable sliding (d: Run N3, X=65%, e: run N1, X=100%). Note grain size reduction with respect to starting material, absence of flat top surface, fabric formed by trains of grains aligned at $\sim 30^\circ$ to the shear zone boundary (see arrow in d), and the presence of R-shears (indicated with arrows in e) transecting the gouge. f) Typical microstructure of samples deformed using rough surface wall rock (run N14, X=100%). The "teeth" forming the surface roughness are outlined. The samples show coarse-grained material between the teeth. The zone above the toothed surface is characterized by isolated rounded clasts in a fine-grained matrix.

2.4 Discussion

2.4.1 Deformation mechanisms

The main aim of this work was to seek evidence for pressure-solution-controlled fault creep, and to evaluate the importance of this in relation to healing and strengthening effects. The absence in wet experiments of a significant slip rate and grain size dependence of shear strength, the considerable AE level (indicating microscale cataclasis) and the absence of persistent fluid-induced weakening leads to the conclusion that steady state, pressure-solution-controlled shear creep did not occur in these experiments. Instead, frictional (i.e. normal stress dependent and sliding rate-insensitive) behaviour dominated under all conditions investigated. The deformation mechanisms determining fault strength, and the effects of fluid on fault slip behaviour will now be discussed.

Dry experiments. In the dry, smooth-surface experiments, the flat and shiny gouge wall-rock interfaces, the absence of significant grain size reduction and the absence of a fabric in the gouge all point towards deformation by localized slip on the gouge-wall-rock interface. In contrast, the dry, rough-surface experiments showed intense grain size reduction within the gouge, suggesting that deformation in these experiments was accommodated by gouge cataclasis. A similar transition from localized to distributed deformation with increasing surface roughness has been reported previously for quartz gouge [Biegel *et al.*, 1989; Sammis and Steacy, 1994]. These authors argued that the transition is caused simply by rough surfaces inhibiting slip along the gouge-wall rock interface, thereby distributing the deformation throughout the gouge. Our data seem consistent with this idea. A change from stick-slip to stable sliding in dry halite gouge was also reported by Chester and Logan [1990], who also observed the associated change from localized to pervasive deformation. In their experiments, the transition could be induced by increasing normal stress and/or decreasing sliding velocity.

Wet experiments. At low pore fluid water contents ($X < 35\%$ water) and high velocities, our wet experiments exhibited stick-slip behaviour, but at higher stress than under dry conditions. The presence of a flat gouge-wall-rock interface, the absence both of significant grain size reduction and of clear fabric in the gouge suggest that most of the imposed displacement was accommodated by slip along the gouge-wall rock interface, as in the dry smooth-surface experiments. The increase

of stick-slip peak stress with increasing brine content and decreasing velocity suggests that the strengthening was caused by fluid-assisted healing of the localized zone during the "stick" periods. This fluid assisted strengthening of the slip surface could be due to pressure solution-induced compaction/cementation [Wong and Wu, 1995; David *et al.*, 1998] or fluid-assisted neck growth and welding or sintering of contact points [Hickman and Evans, 1992, 1995]. Which of these effects dominates is not known. Both the measured compaction upon adding fluid and the observed microstructure provide clear evidence that compaction by pressure solution occurred in the gouge. This does not seem to have had a significant effect on fault strength, however, since no clear correlation between compaction and strength is apparent from our data. Such behaviour is not surprising since most deformation occurred at the gouge-wall rock interface, not in the gouge itself.

Wet experiments performed at high brine contents ($X \geq 35\%$) and lower velocities exhibited quasi-stable sliding. Extensive grain size reduction, as well as the presence of R-shears in the gouge suggests that the deformation was accommodated mainly by cataclasis and faulting of gouge. No continuous boundary-parallel shears (Y-shears), which could accommodate large amounts of deformation, were observed. In the stable sliding regime, fault sliding strength was independent of fluid chemistry. Moreover, the mechanical behaviour of the dry rough-surface, wet rough-surface and wet smooth-surface experiments, all of which exhibited distributed gouge deformation, were very similar (see Figure 2.7b). Therefore, it seems likely that, once deformation was distributed throughout the gouge, fluids did not exert a major influence on fault strength. Rather, the main action of the fluid in the smooth-surface experiments seems to have been to induce pervasive deformation by inhibiting slip on the gouge-wall-rock interface, and on other surfaces of the same orientation. Thus, whereas at low brine contents the deformation was still localized at the gouge-wall rock interface, at high brine contents, healing of this interface led to delocalization of deformation, distributing deformation throughout the gouge. This interpretation is supported by the observation that the a transition from stick-slip to stable sliding could be induced for $X=35\%$ by decreasing sliding velocity, i.e. by increasing the duration of the no-slip period. The striking difference in AE-rate between the wet-rough and dry-rough experiment (see Figure 2.4c) can be explained by the fact that in wet samples contact growth by pressure solution will ensure that the average contact stress is lower in wet samples.

The stick-slip peak strengths observed in our experiments were consistently lower than the stable sliding strengths. The reason for this may lie in the fact that shear requires grain (contact) fracture and dilatation, both contributing to macroscopic fault strength. During localised stick slip only minor dilatation is required because of the low roughness of the interface, so fault strength will be controlled mainly by grain contact strength. In contrast, distributed shear of gouge requires significant dilatation (and hence work against normal stress) in addition to contact fracture, which contributes to macroscopic fault strength. This may explain the above observation, provided the failure strength of the bulk gouge and the contact layer are similar. Furthermore, once the gouge-wall rock interface has failed locally, a dynamic slip pulse may propagate along the interface (which separates two solids of contrasting elastic properties, namely gouge and wall rock) [Weertman, 1980; Ben-Zion and Andrews, 1998], allowing low-friction rupture of the entire fault. This may also contribute to low stick-slip strength. The transition to stable sliding at lower velocities or higher pore fluid brine contents occurs because the fine-grained material accumulating at the gouge-wall rock interface is much more prone to time-dependent compaction and healing than the bulk gouge. Hence, at high brine contents or low velocities the fracture strength of the dense gouge-wall rock contact zone becomes higher than the stress needed to break and dilate the much more porous bulk gouge, thus leading to distributed shear.

The high brine content ($X \geq 65\%$) wet samples tended to show a marked strengthening towards higher displacements and, eventually, wall rock failure. This strengthening was promoted

by smaller initial gouge grain size and by higher brine content of the fluid, and was absent in dry experiments. This suggests that healing and strengthening was a result of a positive feedback between grain size reduction and (grain size sensitive) pressure solution compaction. Although pressure solution did not act to reduce the steady state sliding strength, rapid stress relaxation occurred upon adding fluid in the "compaction without shear" experiment (see Figure 2.3e). This is interpreted as resulting from deviatoric pressure solution creep operating concurrently with compaction. The AE-burst directly after adding the fluid shows that there was also a component of cataclasis involved.

The compaction behaviour recorded during stable sliding is strongly influenced by the presence of fluid. From soil mechanics and fault gouge experiments it is known that pervasive shear deformation of a dry densely packed granular material is generally associated with dilatation upon loading [Mandl *et al.*, 1977; Marone and Scholz, 1989; Marone *et al.*, 1990; Wood, 1990; Marone, 1998]. Experimental data show that the dilatation rate increases upon loading, reaches a maximum at the peak shear stress, and then decreases to near zero as a constant residual shear stress is reached [Mandl *et al.*, 1977; Marone and Scholz, 1989; Marone *et al.*, 1990]. In our wet smooth-surface experiments, pressure solution compaction presumably competes with shear induced dilatation after adding the fluid, as the delocalization of slip from the gouge- wall-rock interface would be accompanied by dilatation under dry conditions. Indeed, the observed behaviour upon adding fluid in our experiments can be explained as a superposition of pressure solution compaction and shear induced dilatation. A typical compaction curve after adding the fluid was characterized by an initial compaction stage, followed by dilatation, which was again followed by compaction (see Figure 2.3c). In view of the above, the initial compaction stage is interpreted as a stage of rapid pressure solution compaction of the gouge, possibility accompanied by subcritical crack growth-enhanced cataclasis. As the porosity, and therefore the compaction rate decreases, the shear-induced dilatation rate outweighs the compaction rate and net dilatation occurs. When the dilatation rate decreases after the peak stress, pressure solution compaction returns to dominate the overall behaviour. Since the dilatation rate changes due to increase in the amount of *slip*, whereas the pressure solution compaction rate decreases with *porosity*, one would expect the amount of initial compaction before dilatation sets in to be larger for higher pressure solution rates, i.e. for smaller grain sizes and higher pore fluid water contents. For the same reason, the amount of dilatation before compaction resumes is expected to be lower for smaller grain size and higher pore fluid water content. The data (Figures 2.3c and 2.5c) show that this is indeed the case.

In summary, we can conclude that no significant pressure solution controlled shear creep of the type hypothesized by Rutter and Mainprice [1979] and Lehner and Bataille [1984/85] occurred in these experiments. Despite the fact that pressure solution was active in the gouge, frictional, rate-insensitive behaviour was observed throughout the conditions investigated. This, together with the microstructures evidencing faulting and cataclasis, suggests that most fault slip was accommodated by brittle mechanisms. Nonetheless, pressure solution strongly affected frictional behaviour. In the stick-slip regime, the action of the fluid was to increase the frictional strength of the fault by fluid-assisted, time-dependent healing of the gouge-wall rock interface. At high rates of pressure solution and low sliding rates (i.e. long duration of the no-slip period), pressure solution induced strengthening of the gouge-wall rock interface eventually resulted in a transition to distributed, stable sliding. In the stable sliding regime, fault strength was independent of the presence or chemistry of the fluid.

2.4.2 Pressure solution controlled fault slip versus cataclasis

It is clear from the above that we found no evidence for fault weakening with respect to frictional strength by steady state pressure solution controlled fault slip. In other experiments under conditions promoting fluid-assisted processes, weakening behaviour has been observed notably in stress relaxation experiments [Rutter and Mainprice, 1978, 1979; Chester and Higgs, 1992]. As the strain attained in those experiments was very low, it is questionable whether the behaviour observed represents a steady state slip process. Moreover, Rutter and Mainprice [1978, 1979] reported weakening only in clay-bearing sandstones. It should be noted here that Dennis and Atkinson [1982] reinterpreted Rutter and Mainprice's [1979] data as being due to stress corrosion cracking, but this does not fit in with the observation by Rutter and White [1979] that phyllosilicates were required to produce the weakening behaviour. Kanagawa *et al.* [2000] recently reported sliding experiments at high-temperature hydrothermal conditions, on both fine-grained (~5 μm) and coarse grained (~100 μm) quartz gouge. Pressure solution is expected to be much more rapid in the fine-grained gouge, because of the strong grain-size dependence of the process. Kanagawa *et al.* reported strain hardening and the presence of R-shears in fine-grained gouge, whereas coarse-grained gouge showed strain softening and localisation of deformation into a boundary-parallel shear. Although in the experiments reported by Kanagawa *et al.* much lower shear displacements were reached than in our samples, the data are broadly consistent with this study in the sense that when pressure solution is rapid, distributed gouge deformation and a high friction coefficient is observed, whereas if pressure solution is less rapid samples show strain localisation into a boundary shear and sliding at a lower friction coefficient. Blanpied *et al.* [1991, 1995, 1998] also observed weakening at high temperatures and lower velocities, but as they used granitic gouge, it is not clear whether this effect was due to pressure solution or to production of weak phyllosilicates during slip. Moreover, in their "weak" experiments, deformation was localized on a boundary shear rich in biotite, which may well have played a role in the observed weakening [Blanpied *et al.*, 1995]. Thus, previously reported fluid-assisted weakening in monomineralic gouges is either limited to low strain relaxation experiments or associated with phyllosilicate-rich layers. It is clear, then, that sound experimental evidence for steady state pressure solution controlled fault creep is lacking. Although pressure solution is clearly active in many experiments, its detailed role is unclear and it may not directly determine the long term shear strength. We will now discuss why pressure solution controlled fault creep did not occur in experiments.

In a gouge-bearing fault, pressure solution slip will occur in preference to brittle failure and/or frictional slip when, at a certain imposed shear strain rate $\dot{\gamma}$ and imposed normal stress σ_n , the shear stress τ_{ps} required for pressure solution slip is lower than the frictional strength of the fault, i.e. when

$$\tau_{ps} < S + \mu(\sigma_n - P_f) \quad (2.4)$$

Here S is the cohesive strength of the fault (i.e. the strength at zero effective normal stress), μ is the coefficient of friction, and P_f is the fluid pressure within the fault. Inserting (2.1) into (2.4) for the case of diffusion controlled pressure solution then yields

$$\frac{RTh^2d}{AD\delta C\Omega_s} \dot{\gamma} < S + \mu(\sigma_n - P_f) \quad (2.5)$$

The relevant kinetic parameters for diffusion controlled pressure solution creep of halite are well constrained [Spiers *et al.*, 1990]. According to (2.1), under the conditions of our experiments and at an imposed sliding rate of 0.01 $\mu\text{m/s}$, the gouge should deform by pressure solution creep at a shear stress of the order of 0.05 MPa. Moreover, because of the grain size dependence of the process, grain size reduction in the gouge should have facilitated pressure solution shear creep. However, our wet experiments show no evidence of this. In deriving (2.1), Rutter and Mainprice [1979] assumed that the diffusion distance h in (2.1) is of the order of the internal roughness of grain contacts. Since this is much smaller than the diffusive length scale for compaction creep, which is of the order of the grain contact size, Rutter and Mainprice [1979] inferred that pressure solution shear creep could occur in porous gouge without significant concurrent compaction. We question this argument, since shear deformation of gouge at constant volume (i.e. without dilatation) requires removal of "mutual grain interference volume" by pressure solution in addition to sliding of grains past each other [Paterson, 1995]. This removal of grain interference volume necessarily involves material transport over distances of the order of the grain contact size. Thus significant pressure solution compaction is expected to accompany shear creep. Compaction will cause hardening during pressure solution shear creep because of a) the decrease in stress concentration at grain contacts due to the increase in grain contact area, and b) the increase in mutual grain interference volume with decreasing porosity. This hardening will stop when the pore fluid pressure balances the normal stress on the fault or when the gouge is completely dense. Only in these situations is fault slip by steady state pressure solution controlled creep of gouge possible.

In a dense material, pressure solution creep can be described by an equation similar to equations for solid state grain boundary diffusional creep (Coble creep) [Raj, 1982; Poirier, 1985]. For the simple shear case, this takes the form

$$\dot{\gamma} = 125 \frac{D\delta C\Omega_s \tau}{RTd^3} \quad (2.6)$$

Inserting the conditions of our experiments into (2.6) yields a predicted creep strength of 80 MPa, far higher than the frictional strength of our samples. This may explain why steady state pressure solution controlled fault creep did not occur in our experiments: compaction caused the material to reach its failure strength before steady state creep set in. The strength drop observed upon adding fluid in the wet rough-surface experiment (Figure 2.4a, experiment N14) is then interpreted to result from the difference between the dry frictional strength and the pressure solution creep strength of the porous gouge. Upon subsequent compaction, the gouge hardened, and eventually deformed by cataclasis.

When the pore fluid pressure balances the normal stress, pressure solution slip is possible at any shear stress lower than the cohesive strength of the gouge (see equation 2.4). It may be possible to attain this situation in an experiment. Whether steady state pressure solution controlled slip is possible in this situation depends on whether grain contact healing also occurs under stress-free conditions, i.e. whether contact healing due to neck growth (driven by gradients in radius of curvature) dominates over pressure solution induced contact enlargement (driven by normal stress).

For natural materials the situation is less clear. Especially in the very fine grained (submicron) silica reported in both natural and experimental faults containing quartz-rich gouge [Power and Tullis, 1989; Yund *et al.*, 1990] pressure solution could potentially be very rapid. However, it is also known that ultrafine grained quartz exhibits rapid neck growth [Maskara and Smith, 1997], thus inhibiting pressure solution. Although there are several reports of fluid-assisted compaction of quartz aggregates [Cox and Paterson, 1991; Schutjens, 1991; Dewers and Hajash, 1995; Lockner and Evans, 1995], microphysical models for pressure solution in quartz have not

been rigorously tested, and the rate controlling process and relevant kinetic parameters are not constrained well enough to be reliably extrapolated to crustal conditions. For example, regarding the grain boundary diffusion coefficient for wet quartz under mid-crustal conditions, it is not clear whether a diffusion coefficient characteristic of fluid phase diffusion (with associated activation energy of ~20 kJ/mole) can be used, or if the empirically determined value of [Farver and Yund, 1991] (with an inferred apparent activation energy of ~110 kJ/mole) is more appropriate (see also [Nakashima, 1995] for discussion on this point). We must conclude that addressing the question whether pressure solution creep of dense gouge can occur in natural faults is hampered by lack of knowledge of the relevant constitutive parameters.

So far, attention has been focused on pressure solution slip involving distributed deformation of a gouge layer. However, pressure solution slip could also be possible by localized deformation, where pressure solution could act as a mechanism to remove asperities on a discrete sliding plane. This is equivalent to the model for diffusion-accommodated grain boundary sliding by Raj and Ashby [1971], with the length scale of diffusive mass transfer determined by the roughness of the localized plane, which may be considerably smaller than the grain size of the material (see also Rutter and Mainprice [1979], Lehner and Bataille [1984/85]). When a mechanism is present to preserve a constant surface roughness, steady state sliding could be possible even under drained conditions. A prerequisite for this kind of mechanism, however, is a continuous plane with low surface roughness on all scales. In our smooth-surface experiments, the shiny flat surface created during the initial stick-slip period would seem an ideal site for such localized pressure solution slip, but our experiments show that the presence of a water-bearing fluid instead causes rapid strengthening. This demonstrates that, at least in our experiments, healing effects dominate.

2.4.3 Implications for natural faults

As outlined in the introduction, our experiments were designed to isolate the effect of pressure solution on fault slip behaviour. The experiments reported here should be viewed as an end member case, where pressure solution and cataclasis dominate over other processes. Moreover, the experiments are conducted on a monomineralic gouge, which excludes any effects of other mineral phases (notably phyllosilicates) on deformation behaviour. This should of course be born in mind when thinking about the consequences for natural fault zones. Nevertheless, we believe that some general conclusions regarding natural faults can be drawn.

Several field studies of exhumed fault zones report a close association between pressure solution microstructures and microstructures evidencing cataclastic deformation [Chester and Logan, 1986; Wojtal and Mitra, 1986; Power and Tullis, 1989; Chester et al., 1993; Hadizadeh, 1994]. These microstructures are often interpreted as evidence of cataclastic frictional behaviour during high strain rates/seismic events, alternating with low strain rate deformation accommodated (at least partly) by pressure solution [Wojtal and Mitra, 1986; Power and Tullis, 1989; Hadizadeh, 1994]. Our data suggest, however, that strain rate variations may not be necessary for producing these microstructures. In our experiments, microstructures evidencing cataclasis and pressure solution developed concurrently, and significant fault compaction and healing, and eventually wall rock failure, was observed during ongoing fault slip. Fault strength was always controlled by cataclasis when deformation was mechanically at (quasi) steady state, leading to frictional behaviour at all sliding rates. On this basis, it seems that microstructural evidence for pressure solution in fault zones should not be taken as evidence that pressure solution is the mechanism determining the long term shear strength at any strain rate. Moreover, the presence of re-ruptured patches of lithified gouge in fault zones need not be evidence of large variations in sliding velocity over time.

As emphasized above, in natural fault zones phyllosilicates (clays, micas) are ubiquitous. It has been proposed that the presence of clays facilitates pressure solution [Rutter, 1983; Tada and Siever, 1989; Dewers and Ortoleva, 1991; Hickman and Evans, 1995; Renard *et al.*, 1997] and inhibits neck growth [Hickman and Evans, 1995]. In addition, clays play an important role in localizing deformation in fault zones [Chester and Logan, 1986; Rutter *et al.*, 1986; Logan and Rauenzahn, 1987; Morrow *et al.*, 1992]. Although the friction of clay-rich fault gouge is probably too high to account for the inferred weakness of the San Andreas Fault [Logan and Rauenzahn, 1987; Morrow *et al.*, 1992; Moore *et al.*, 1996, 1997], the interaction between clays and pressure solution may lead to significant weakening. If clay-rich shears in the gouge inhibit healing, clays could be important in the formation of flat, localized shears of low roughness as discussed above. Indeed, the weakening observed by Rutter and Mainprice [1979] as well as the weakening and increased rate dependence reported by Blanpied *et al.* [1995] are associated with the presence of phyllosilicates. Clearly, the role phyllosilicates in combination with pressure solution deserves further study.

2.5 Conclusions

Experiments have been carried out in order to investigate the importance of fault weakening by pressure solution controlled fault slip in relation to competing fluid-assisted healing effects. The following conclusions can be drawn:

1. Although our experiments were conducted under conditions where pressure solution was clearly active, no evidence was found for steady state pressure solution controlled fault creep. Instead, the mechanical behaviour was frictional under all conditions investigated. The action of the fluid in the stick-slip regime was to cause strengthening by healing of the gouge-wall rock interface. At low sliding rates and high pressure solution rates, this healing inhibited slip on the gouge-wall rock interface, causing distributed gouge deformation and associated stable sliding. In the stable sliding regime, fault strength was independent of the presence or chemistry of the fluid.
2. In our experiments, no pressure solution controlled fault creep occurred. Instead, pressure solution caused densification and strengthening, leading to brittle-frictional behaviour. Existing models for pressure solution controlled fault creep, which do not account for porosity reduction, may not be applicable to undrained conditions, where gouge compaction can occur. However, they may be applicable to completely dense gouge, or to situations where pore fluid is trapped. Unfortunately, evaluating the expected fault strength in natural materials is at present not possible because of incomplete knowledge of the relevant kinetic parameters.
3. Although in our experiments microstructural evidence is found for both pressure solution and cataclasis, steady state strength is always controlled by cataclasis. Thus the presence of microstructures evidencing pressure solution should not automatically be taken as evidence for pressure solution as the strength controlling mechanism. Similarly, the presence of re-ruptured lithified gouge in natural faults need not be evidence for large temporal variations in far-field strain rate.

Chapter 3

Frictional-viscous flow behaviour of simulated fault gouge due to the combined effects of phyllosilicates and pressure solution

Accepted for publication in Tectonophysics, reprinted with permission from Elsevier Science.

Abstract. It is widely believed that conventional brittle-plastic strength envelopes may significantly overestimate crustal strength, in part because they fail to account for the effects of fluid-assisted deformation mechanisms. In particular, pressure solution has been suggested to allow fault creep behaviour at a shear stress well below that predicted by conventional strength envelopes. In addition, many natural fault zones contain significant amounts of phyllosilicates, often defining a foliation. Phyllosilicates are believed to inhibit grain contact healing and increase the rate of pressure solution in quartzose rocks. Hence, the interaction between phyllosilicates and pressure solution may strongly influence fault rheology under the hydrothermal conditions pertaining around the brittle-ductile transition. The aim of this research is to assess the combined effects of pressure solution and phyllosilicates on fault slip behaviour. To this end, we performed high strain, rotary shear experiments on experimental faults containing brine-saturated mixtures of halite and kaolinite as simulated gouge. The experiments were done under conditions where pressure solution and cataclasis dominate over dislocation creep, thus simulating the brittle-ductile transition. Halite was chosen as a rock analogue because of its well-constrained pressure solution kinetics. Experiments were done at room temperature and atmospheric pressure, under drained conditions. In the experiments we explored the effect of varying sliding velocity, normal stress and clay content on fault strength. The results showed frictional-viscous flow behaviour, i.e. shear strength depending on both normal stress and shear strain rate, in brine-saturated halite/kaolinite mixtures. In contrast, purely frictional (i.e. normal stress dependent and shear strain rate insensitive) behaviour was observed when an inert pore fluid (silicone oil instead of brine) or an inert solid (quartz instead of halite) was used. Monomineralic halite and kaolinite gouges showed purely frictional behaviour as well. This demonstrates that the observed frictional-viscous flow behaviour was caused by the combined effects of pressure solution and phyllosilicates. The microstructures, which strongly resemble natural mylonites in many respects, suggest that deformation of the gouge involved sliding along kaolinite-rich foliation planes, accommodated by pressure solution and dilatation/cataclasis, the relative amounts of which varied with sliding velocity. If similar behaviour occurs in natural phyllosilicate-rich fault zones, these can be expected to be significantly weaker than predicted by traditional brittle-ductile strength envelopes. In addition, our microstructures suggest that pressure solution may play an important role next to dislocation creep in microstructural evolution in mylonitic rocks.

3.1 Introduction

In geodynamic modeling, crustal rheology is generally specified using a two-mechanism strength profile. The rheology of the upper part of the crust is regarded as frictional, whereas the lower part of the crust is described using a ductile flow law [e.g. *Goetze and Evans, 1979; Sibson, 1983; Govers and Wortel, 1995; Kohlstedt et al., 1995; Ranalli, 1997*]. In the frictional region, the effect of fluids is assumed to be negligible and deformation is modeled as purely frictional (i.e. the shear strength is taken to be linearly dependent on normal stress and insensitive to strain rate) down to the depth where solid state flow becomes possible. However, it is widely known from field and laboratory studies that under the hydrothermal conditions pertaining near the brittle-ductile transition, fluid-assisted deformation processes such as pressure solution and stress corrosion cracking are operative. It has been suggested that this may lead to frictional-viscous behaviour, i.e. behaviour which is both normal stress and strongly strain rate and temperature dependent [*Rutter and Mainprice, 1979; Chester and Higgs, 1992; Chester, 1995; Hickman et al., 1995; Kohlstedt et al., 1995*], possibly allowing fault slip at shear stress levels well below the strength predicted by dry friction experiments.

Despite widespread acceptance of the notion of fluid-assisted frictional-viscous flow behaviour in the brittle-ductile transition region, experimental evidence for both normal stress and rate-dependent fault slip under hydrothermal conditions is limited. The available evidence includes that obtained in experiments by *Blanpied et al.* [1995], which showed weakening with increasing temperature and decreasing sliding rate in experiments on granitic gouge under hydrothermal conditions. Similarly, *Rutter and Mainprice* [1978, 1979] reported weakening in stress relaxation experiments on faulted clay-bearing sandstone, at temperatures up to 400°C. Although fluids clearly played an important role in these studies, the deformation mechanism leading to the observed weakening, notably the relative contributions of (local) plasticity, pressure solution, brittle fracture, stress corrosion cracking, are unclear. Also, the role of the phyllosilicates present in these experiments is not known.

From studies of exhumed natural fault zones it is known that phyllosilicates (i.e. clays and micas) are ubiquitous in natural fault zones [e.g. *Wu et al.*, 1975; *Rutter et al.*, 1986; *Scholz*, 1990; *Chester et al.*, 1993]). Moreover, experiments on phyllosilicate-bearing gouges have shown that the presence of phyllosilicates causes these gouges to be significantly weaker than phyllosilicate-free materials. The lowest strength is observed in gouges containing swelling clays like montmorillonite [*Shimamoto and Logan*, 1981; *Logan and Rauenzahn*, 1987; *Morrow et al.*, 1992]. The low friction of this clay is probably due to interlayer water, which is lost at higher pressures and temperatures [*Bird*, 1984; *Morrow et al.*, 1992]. In all cases, the strength of phyllosilicate-bearing gouge is reported to be insensitive to sliding velocity. Hence, although phyllosilicates can significantly weaken faults, the presence of phyllosilicates alone does not lead to rate-dependent behaviour.

In addition to the mechanical effect of phyllosilicates in faults, there is evidence from both field studies and experimental work that the presence of phyllosilicates increases the rate of pressure solution in quartzose rocks [*Heald*, 1959; *Rutter*, 1983; *Tada and Siever*, 1989; *Dewers and Ortoleva*, 1991; *Schwarz and Stoeckhert*, 1996; *Rutter and Wanten*, 2000]. *Hickman and Evans* [1995] conducted experiments using convex halite lenses coated with Na-montmorillonite, pressed against fused silica, and observed a five-fold increase in halite-silica convergence rate compared to experiments without clay. Also, pilot compaction experiments on halite + kaolinite aggregates performed by ourselves have shown that adding 10% kaolinite results in a tenfold increase in compaction rate. It is generally thought that the enhancement of pressure solution rates by phyllosilicates is due to enhanced interphase boundary diffusivity [*Rutter*, 1983; *Hickman and Evans*, 1995; *Renard et al.*, 1997; *Farver and Yund*, 1999]. In addition to the proposed effect of phyllosilicates on pressure solution rate, *Hickman and Evans* [1995] suggested that phyllosilicates may inhibit neck growth and associated fault healing processes. In this context, it should be noted that the rate-dependent fault slip behaviour reported by *Rutter and Mainprice* [1979] and *Blanpied et al.* [1995] both involved phyllosilicate-bearing rocks.

The question accordingly arises as to whether the combination of pressure solution and phyllosilicates can lead to frictional-viscous flow behaviour. This paper investigates this issue. To do so, we conducted rotary shear experiments on synthetic halite/kaolinite gouges, in the presence of saturated brine. Both velocity stepping and normal stress stepping experiments were performed. Halite was chosen as a rock analogue because it is known that pressure solution is rapid in the halite + brine system at room temperature conditions, and the rates are well constrained. Kaolinite was chosen as the clay constituent because of its simple chemistry, low ion exchange capacity and absence of interlayer water. To separate the effects of phyllosilicates from those of pressure solution, we also conducted experiments on the system quartz + kaolinite + brine. In this system, the rate of pressure solution is negligible at room temperature.

The results indeed showed frictional-viscous flow behaviour of the wet halite/kaolinite mixtures. Strength increased roughly linearly with normal stress, but the coefficient of friction strongly decreased with decreasing sliding rate, down to values lower than 0.2. This behaviour did

not occur in clay-free gouges or in quartz/kaolinite gouges, which exhibited purely frictional behaviour. The implication of this is that the observed frictional-viscous flow behaviour is due to the combined effects of pressure solution and kaolinite. If similar behaviour occurs in natural materials, significant weakening with respect to the conventional brittle-ductile strength envelope can be expected.

3.2. Experiments

3.2.1 Apparatus and sample assembly

The experiments were conducted using the rotary shear apparatus shown schematically in Figure 3.1a. The annular sample assembly consists of two toothed stainless steel "wall rock" rings 10 cm in outer diameter and 1 cm in width (see Figure 3.1b+c), sandwiching a layer of synthetic gouge. Surface roughness was created by imprinting the stainless steel ring surfaces with closely spaced grooves 100 μm deep, oriented perpendicular to the sliding direction (see Figure 3.1c). This was done in order to prevent slip on the gouge-wall rock interface. The sample is sealed with stainless steel sealing rings, fitted with O-rings. Two diametrically mounted tubes in the outer sealing ring allowed evacuation of the sample and addition of pore fluid. All experiments were conducted at room temperature and atmospheric pore pressure (drained conditions). O-ring friction was measured in sliding experiments performed with water trapped between the wall rock rings, and found to be lower than 0.01 MPa at pore fluid pressures below 3 MPa. The stainless steel rings are gripped between two cylindrical forcing blocks. The lower forcing block is rotated at controlled angular velocity by a motor-driven gearbox, while the upper block is maintained stationary, thus leading to shear on the synthetic fault. Normal stress is applied and servo-controlled to within 0.01 MPa using an Instron 1362 loading frame and is measured using a 100 kN Instron load cell. The shear stress is measured using two force gauges mounted in a torque couple which provides the reaction needed to hold the upper forcing block stationary (resolution ~ 10 kPa). Displacement normal to the synthetic fault surface (i.e. gouge compaction/dilatation) is measured using a Linear Variable Differential Transformer (LVDT, 1 mm full scale, 0.01% resolution) located inside the upper forcing block. Angular and hence linear fault displacement is measured using a potentiometer geared to the rotation of the lower forcing block.

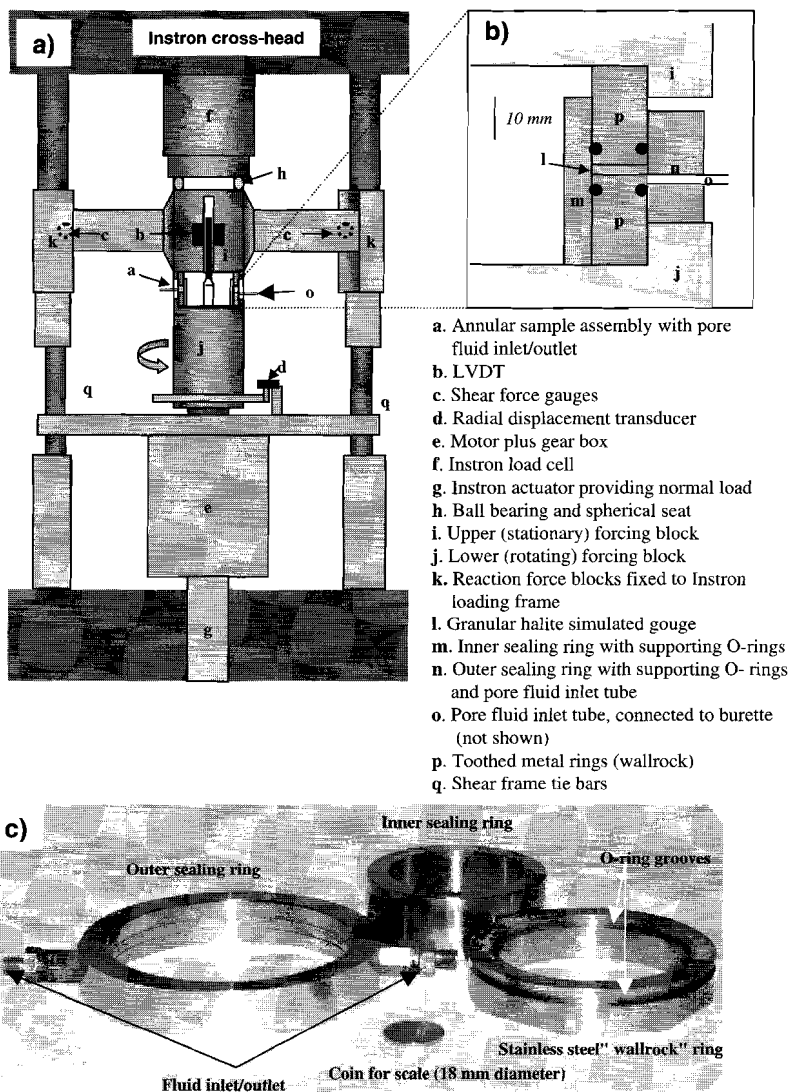


Figure 3.1. Schematic diagram of a) the deformation apparatus (not to scale) and b) the sample assembly. c) Photograph of one of the stainless steel toothed rings and inner and outer sealing rings. The diameter of the coin (for scale) is 18 mm.

3.2.2 Experimental procedure

Synthetic gouges were prepared by mixing various proportions of halite and kaolinite or (for three experiments) quartz and kaolinite. The halite used was sieved granular halite (Merck). The grain size distribution was determined using a Malvern particle sizer, which showed 90% of the grains to have a size between 60 and 110 μm . The median grain size was 104 μm . The quartz powder used was crushed and sieved sand with a grain size distribution similar to the halite. The

kaolinite was supplied by Aldrich, and was mostly submicron. As pore fluid, NaCl-saturated brine was used, except for two experiments (sc20koil and sc50koil), in which silicone oil (inert with respect to halite) was used as pore fluid. The starting gouge thickness used was ~1 mm.

Table 3.1. List of all experiments

Experiment Nr.	Gouge composition (%=weight %)	Pore fluid	Normal stresses (MPa)	Sliding velocities ($\mu\text{m/s}$)
sc00	100% NaCl	brine	5	1, 10, 0.1, 1, 0.03, 1
sc10k	90% NaCl, 10% kaolinite	brine	5	1, 10, 0.1, 1, 0.03, 1
sc20k	80% NaCl, 20% kaolinite	brine	5	1, 10, 0.1, 1, 0.03, 1
sc30k	70% NaCl 30% kaolinite	brine	5	1, 10, 0.1, 1, 0.03, 1
sc40k	60% NaCl 40% kaolinite	brine	5	1, 10, 0.1, 1, 0.03, 1
sc50k	50% NaCl 50% kaolinite	brine	5	1, 10, 0.1, 1, 0.03, 1
sc75k	25% NaCl 75% kaolinite	brine	5	1, 10, 0.1, 1, 0.03, 1
sc100k	100% kaolinite	brine	5	1, 10, 0.1, 1, 0.03, 1
sc20ksn	80% NaCl 20% kaolinite	brine	5, 7, 9, 5, 1, 3, 5 5, 9, 1, 7, 3, 0.03	2 0.03
sc50ksn	50% NaCl 50% kaolinite	brine	5, 3, 7, 1, 9, 5 5, 3, 7, 1, 9, 9	2 0.03 0.005
sc100ksn	100% kaolinite	brine	5, 3, 7, 1, 9, 5 5, 9 9	2 0.03 0.005
sc20koil	80% NaCl 20% kaolinite	silicone oil	5	1, 10, 0.1, 1, 0.03, 1
sc50koil	50% NaCl 50% kaolinite	silicone oil	5	1, 10, 0.1, 1, 0.03, 1
scqtz20k	80% quartz 20% kaolinite	brine	5 9 5 9	1, 10, 0.1, 1 1 0.03 0.03
scqtz50k	50% quartz 50% kaolinite	brine	5 9 5 9	1, 10, 0.1, 1, 1 0.03 0.03
scqtz75k	25% quartz 75% kaolinite	brine	5 9	1, 10, 0.1, 1, 0.03, 1 1, 0.03
sctest5	75% halite 25% kaolinite	dry	5	1

Samples were prepared by sandwiching a pre-weighed amount of granular gouge material between the stainless steel wall rock rings, with the sealing rings in place. All samples were first subjected to a fixed normal stress of 1 MPa under dry conditions for 10 minutes, after which no significant further compaction occurred. The sliding velocity was then set to 1 $\mu\text{m/s}$ and the normal stress to 5 MPa, and the samples were subjected to a "run-in" phase of ~50 mm shear displacement. This was done in order to produce a well-controlled starting microstructure for the wet part of the

experiments. One experiment (scstest5) was terminated directly after the dry run-in period, in order to inspect the microstructure produced during dry sliding. After dry sliding the samples were unloaded, evacuated and saturated with the appropriate pore fluid (brine or silicone oil). The sliding velocity was subsequently set to the desired value and the desired normal stress was applied. All experiments are listed in Table 3.1, together with the experimental conditions and the sequence of velocity and normal stress steps. Two sets of experiments were conducted:

In the first set (experiments sc00 - sc100ksn, see Table 3.1), the behaviour of halite/kaolinite gouge in the presence of NaCl-saturated brine was explored. This was done in a set of velocity stepping experiments at 5 MPa normal stress, as well as in three normal-stress-stepping experiments performed at sliding velocities of 2 $\mu\text{m/s}$ and 0.03 $\mu\text{m/s}$. The velocities used in the velocity stepping experiments were 0.03, 0.1, 1 and 10 $\mu\text{m/s}$. The normal stresses applied in the normal stress stepping experiments were 1,3,5,7 and 9 MPa. In experiments sc50ksn and sc100ksn (see Table 3.1) an additional step was performed: at 9 MPa normal stress and a sliding velocity of 0.005 $\mu\text{m/s}$. In the velocity stepping experiments, gouges with 0, 10, 20, 30, 40, 50, 75 and 100 weight% kaolinite were used. In the normal stress stepping experiments, gouges with kaolinite contents of 20% , 50%, and 100% were used. The amount of slip reached in individual velocity and normal stress steps is typically 2-4 mm.

In experiments sc20koil - scqtz75k (see Table 3.1), the behaviour of wet, clay-bearing gouges was explored under conditions where no pressure solution was expected to occur. Experiments sc20koil and sc50koil were performed using using silicone oil (which is inert with respect to the solids used) instead of brine as pore fluid. Experiments scqtz20k, scqtz50k and scqtz75k were performed using quartz instead of halite, with brine as pore fluid. The rate of pressure solution in quartz is negligible at room temperature. In these experiments we used kaolinite contents of 20% and 50%, and for the quartz/kaolinite gouge also 75%.

The experiments were terminated by halting sliding and then immediately removing the normal load. The complete sample assembly was subsequently removed from the loading frame and flushed with compressed air, while still sealed, to remove the brine from the sample pore space. The sealing rings were then removed, and the gouge was carefully detached from the stainless steel ring. The samples were dried and impregnated under vacuum with blue-stained epoxy resin. Finally, sections were cut normal to the sliding plane and parallel to the sliding direction, and standard thin sections were prepared for microscopic inspection.

3.3 Results

3.3.1 Dry run-in stage: Halite/kaolinite samples

Shear stress versus displacement data obtained for halite/kaolinite gouges with different clay contents during the dry "run-in" period are shown in Figure 3.2. All samples with kaolinite content less than 50% showed an initial stress increase, followed by slip weakening. A transition to stick-slip behaviour occurred thereafter in all of these samples, but at different values of displacement which show no systematic relation to clay content. High kaolinite content samples (i.e. 50%, 75% and 100%) showed a stress increase, followed by stable sliding throughout the dry run-in stage. The 75% and 100% kaolinite experiments showed continuous slip hardening after the initial stress peak. In the experiments with kaolinite content higher than 30%, a clear dependence of strength on kaolinite content was observed in the first 10 mm of shear. For larger displacement, the curves cross and the trend is lost. At 50 mm displacement, the strength (i.e. steady sliding strength or stick-slip peak strength) of all samples fell in the range 2.5-3 MPa, with no systematic dependence on kaolinite content.

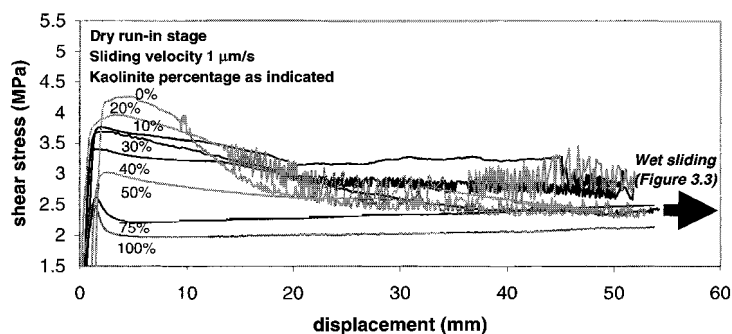


Figure 3.2. Shear stress versus displacement data for the dry "run-in" stage of halite/kaolinite experiments. Kaolinite contents as indicated. Stick-slip data are aliased by the logging interval. Note stick-slip behaviour at kaolinite content of 50% and lower. In the initial part of the experiment, strength correlates with kaolinite content. At higher displacements, this correlation is lost.

3.3.2 Wet stage: Effect of kaolinite content, sliding velocity and normal stress

Shear stress versus displacement data for velocity stepping experiments in halite kaolinite gouges with brine as pore fluid are given in Figures 3.3. All experiments exhibited stable sliding, in contrast to the stick-slip exhibited under dry conditions. Only minor strength evolution with ongoing strain was observed. The data demonstrate a systematic decrease of strength with increasing clay content, at least for sliding velocities above $0.1 \mu\text{m/s}$. All experiments showed a significant effect of changing sliding velocity on shear stress. In general appearance, the data are similar to conventional "rate-and state-dependent" friction experiments [Dieterich, 1979; Ruina, 1983; Marone, 1998; Scholz, 1998] in that upon changing sliding velocity an instantaneous effect was observed, followed by a gradual decay to a new steady state strength. However, both the magnitude of the instantaneous strength change upon changing velocity and the effect of sliding

velocity on steady state strength were much larger than usually reported in literature on friction experiments.

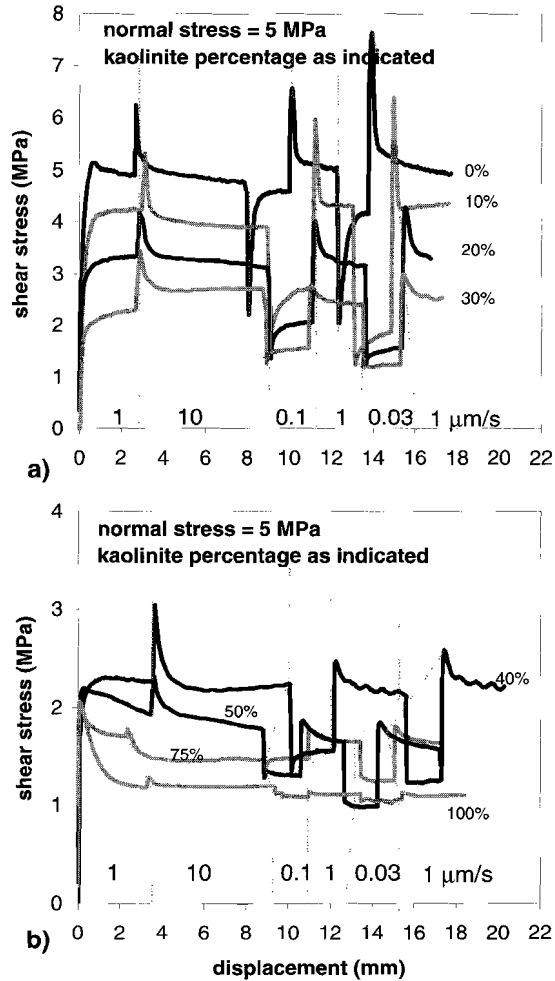
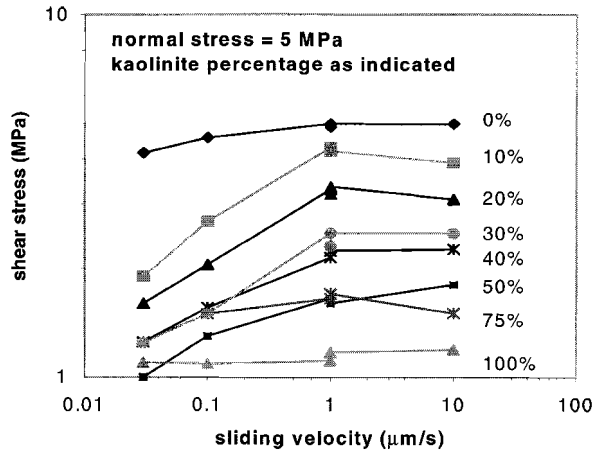


Figure 3.3. Shear stress versus displacement data for the wet phase of the velocity stepping experiments, for halite/kaolinite gouges with kaolinite contents of 0-30% (a) and 40-100% (b). Kaolinite content and sliding velocity steps as indicated. Note the decreasing strength with increasing kaolinite content, and the strong effect of changing sliding velocity in halite/kaolinite mixtures.

Figure 3.4. Shear stress versus sliding velocity data for the experiments shown in Figure 3.3. Note significant sliding rate dependence of shear stress in halite/kaolinite mixtures at sliding velocities below 1 $\mu\text{m/s}$. The maximum slope of a best-fit line (not shown) through the data in the rate-sensitive regime is 0.23.



Data of steady state strength versus sliding velocity for halite/kaolinite gouges at different clay contents are presented in Figure 3.4. Note that more than one data point is shown at sliding velocity of 1 $\mu\text{m/s}$, reflecting minor hardening or weakening in the course of the stepping procedure. Two regimes can tentatively be defined for the halite/kaolinite gouges: At velocities higher than 1 $\mu\text{m/s}$, strength was insensitive to, or slightly decreased with, increasing sliding velocity. At velocities below 1 $\mu\text{m/s}$, however, significant weakening with decreasing sliding velocity was observed.

This rate dependence was strongest for kaolinite contents of 10-30%. The strength of 100% halite was only very weakly decreased with decreasing sliding rate, and the strength of 100% kaolinite gouge was insensitive to sliding rate. Note that, at low velocities, the gouge with 50% kaolinite was weaker than the 75% kaolinite and 100% kaolinite gouge. The maximum observed slope of the logarithmic shear stress versus sliding velocity plot was ~ 0.25 .

Figure 3.5 shows steady state shear strength versus kaolinite content, for sliding velocities of 1 $\mu\text{m/s}$ and 0.03 $\mu\text{m/s}$ and 5 MPa normal stress. It is clear that for both velocities, strength decreased with kaolinite content. In addition, the strength at 0.03 $\mu\text{m/s}$ for the halite/kaolinite experiments was consistently lower than at 1 $\mu\text{m/s}$ for all but the 100% kaolinite experiment.

Compaction data from the halite/kaolinite experiments with 0, 20, 50 and 100% clay are shown in Figure 3.6. Overall, compaction was observed in the course of all experiments. In the pure halite experiment, significant dilatation and compaction was observed when, respectively, increasing or decreasing sliding velocity. In the 20% kaolinite sample, at high velocities significant dilatation was observed (i.e. when stepping from 1 to 10 $\mu\text{m/s}$), but in the rate sensitive regime (see

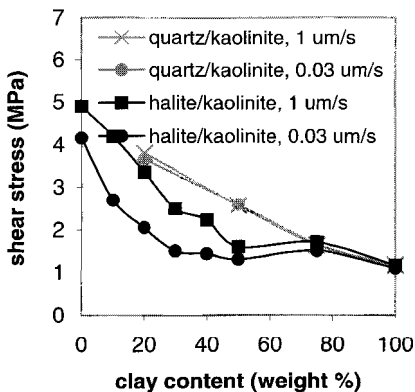


Figure 3.4) the amount of dilatation upon increasing sliding velocity was very small. The 50% sample showed similar behaviour, but here even stepping up to 10 $\mu\text{m/s}$ did not lead to major dilatation. Note that at this composition the rate-sensitive regime extends to 10 $\mu\text{m/s}$ (see Figure 3.4). Finally, the 100% clay sample did not show any volume changes upon stepping velocity.

Figure 3.5. Shear stress versus kaolinite content data for halite/kaolinite samples and quartz/kaolinite samples, at sliding rates of 1 and 0.03 $\mu\text{m/s}$. Note the pronounced effect of velocity on strength in the halite/kaolinite samples.

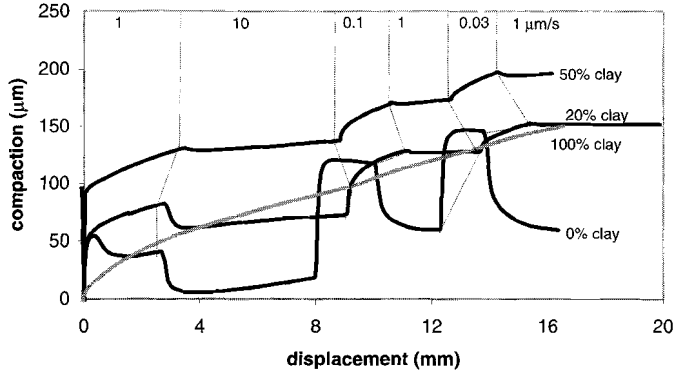


Figure 3.6. Compaction versus displacement for halite/kaolinite experiments with 0, 20, 50 and 100% kaolinite. Sliding velocity as indicated.

The results of the normal stress stepping experiments, plotted as steady state shear stress versus normal stress, are shown in Figures 3.7a, 3.7b and 3.7c for kaolinite contents of 20%, 50% and 100%, respectively. For comparison, data are also shown for quartz/kaolinite gouge (discussed below). The data show that sliding strength was linearly dependent on normal stress in all experiments. The data can be fitted to a Coulomb-type equation of the form

$$\tau = C + \mu\sigma_n \quad (3.1)$$

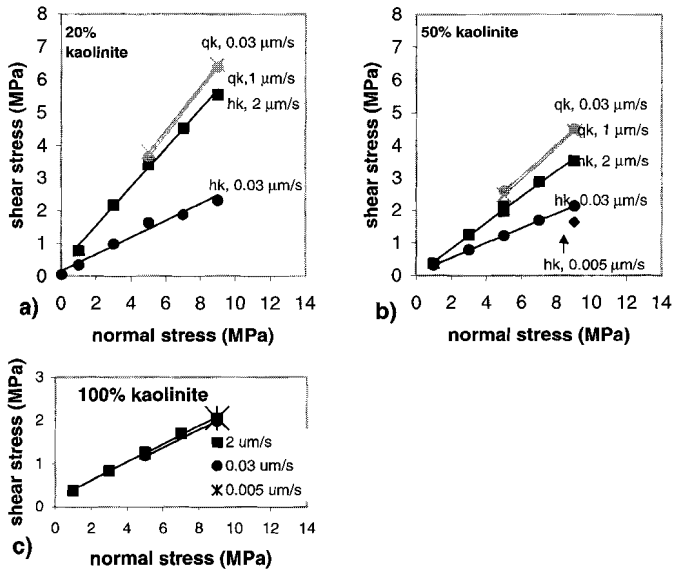


Figure 3.7. Shear stress versus normal stress plots for halite/kaolinite samples (black, denoted hk) and quartz/kaolinite samples (grey, denoted qk), at kaolinite contents of 20% (7a) and 50% (7b). In 7c, data for 100% kaolinite gouge are also shown. Note the pronounced effect of sliding velocity on apparent friction coefficient (i.e. the slope of the plot) in the halite/kaolinite mixtures. This effect is absent in the quartz/kaolinite mixtures and the 100% kaolinite gouge.

where τ is shear stress, σ_n is normal stress, μ is the (effective) coefficient of friction and C is a cohesion term. Values for μ and C from our experiments are given in Table 3.2. Note the strong dependence of μ on sliding velocity in the wet halite/kaolinite samples. The apparent coefficient of friction of the 50% clay sample at 0.03 $\mu\text{m/s}$ was as low as 0.22, and the data point obtained at 9 MPa normal stress and 0.005 $\mu\text{m/s}$ sliding velocity indicates a friction coefficient as low as 0.18. In contrast, the coefficient of friction of pure kaolinite gouge was insensitive to sliding velocity.

Table 3.2. Strength parameters of normal stress stepping experiments

Experiment	Gouge composition	Sliding velocity ($\mu\text{m/s}$)	Effective friction coefficient μ	C (MPa)
scqtz20k	80% quartz, 20% kaolinite " "	1	0.66	0.51
		0.03	0.68	0.27
scqtz50k	50% quartz 50% kaolinite " "	1	0.49	0.36
		0.03	0.48	0.16
sc20k	80% halite, 20% kaolinite " "	2	0.59	0.02
		0.03	0.26	0.19
sc50k	50% halite, 50% kaolinite " " " "	2	0.40	0.03
		0.03	0.22	0.09
		0.005	0.18	
sc100ksn	100% kaolinite " " " "	2	0.21	0.19
		0.03	0.20	0.14
		0.005	0.23	

In summary, synthetic halite/kaolinite gouges deformed under conditions favouring pressure solution of halite showed two distinctive types of behaviour. Purely frictional behaviour was observed at sliding velocities above 1 $\mu\text{m/s}$. At sliding velocities below 1 $\mu\text{m/s}$ frictional-viscous flow behaviour was observed, i.e. shear strength depended strongly on both normal stress and sliding velocity. The data in the strongly rate-sensitive regime (i.e. sliding velocity < 1 $\mu\text{m/s}$ and clay content 10-50%) can be described by an empirical equation of the form

$$\tau = Av^m\sigma_n \quad (3.2)$$

where τ is shear stress, A and m are empirical parameters which depend on kaolinite content, σ_n is normal stress and v is sliding velocity. Fitting this equation to the experimental data for fixed clay contents yields values of m ranging from 0.23 at 10% kaolinite to 0.14 at 50% kaolinite (corresponding to stress exponents of 4.3 to 7.0 in a typical power law creep equation). The product of A and v^m is the apparent friction coefficient, which at a sliding velocity of 0.03 $\mu\text{m/s}$ takes values

of 0.26 in the experiment with 20% kaolinite and 0.22 in the experiment with 50% kaolinite. At a sliding velocity of $0.005 \mu\text{m/s}$ the effective friction coefficient in the 50% kaolinite experiment is as low as 0.18 (see Table 3.2).

3.3.3 Experiments using silicone oil instead of brine and quartz instead of halite

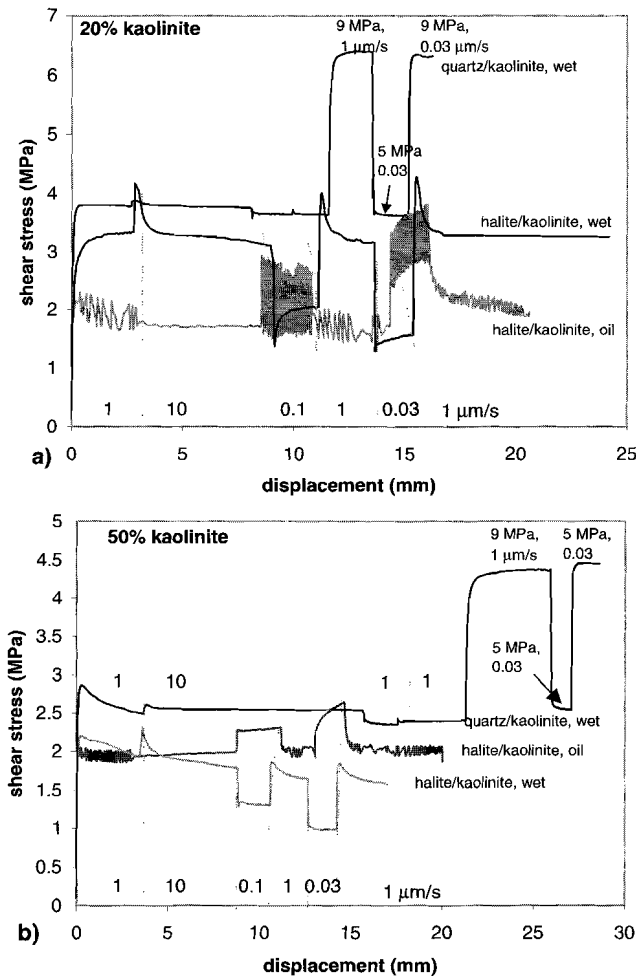


Figure 3.8. Shear stress versus displacement plots of stepping experiments on halite/kaolinite mixtures slid in the presence of brine and oil, and of quartz/kaolinite mixtures slid in the presence of brine. a) Data for 20% kaolinite gouges. b) Data for 50% kaolinite gouges. Sliding velocity and normal stress as indicated.

Data of shear stress versus displacement for experiments on 1) halite/kaolinite gouge using oil as pore fluid, and 2) quartz/kaolinite gouge using brine as pore fluid ("wet") are shown in Figures 3.8. Figure 3.8a and 3.8b show data for gouges with 20 and 50% kaolinite, respectively. Data on wet halite/kaolinite samples are also shown for comparison. In the quartz/kaolinite experiments, normal stress as well as sliding velocity was stepped, whereas in the experiments using oil as pore fluid only velocity was stepped. The 80%halite/20% kaolinite gouge slid with oil showed violent stick-slip behaviour at all velocities, except at 10 $\mu\text{m/s}$ (Figure 3.8a). The 50% halite/50% kaolinite sample slid with oil showed stick-slip at 1 $\mu\text{m/s}$ and stable sliding at all other velocities. The quartz/kaolinite gouges deformed in the presence of brine showed stable sliding. Upon stepping sliding velocity, "rate- and state-dependent" frictional behaviour was observed with amplitudes of the direct and indirect effects comparable to the values usually reported in the literature. In Figures 3.9a and 3.9b, steady state shear stress is plotted against sliding velocity. Again, data for halite/kaolinite gouges are shown as well for comparison. The weakening with decreasing sliding rate observed in the wet halite/kaolinite experiments was absent in the "oil" and the "quartz" experiments. The peak stick-slip stress of the samples slid with oil increased with decreasing sliding rate. The steady state strength of the quartz/kaolinite gouges was insensitive to sliding rate.

Referring to Figure 3.5, where shear stress is plotted against clay content, it can be seen that quartz/kaolinite gouges were slightly stronger than halite/kaolinite gouges deformed wet at all kaolinite contents below 75%. The strength of quartz/kaolinite samples is insensitive to sliding rate at all kaolinite contents, in marked contrast to the halite/kaolinite samples. In Figure 3.7, shear stress is plotted versus normal stress. Referring also to Table 3.2, it can be seen that the effective friction coefficient is insensitive to sliding rate in the quartz/kaolinite experiments, whereas in the wet halite/kaolinite experiments a clear decrease in friction coefficient with decreasing sliding rate observed.

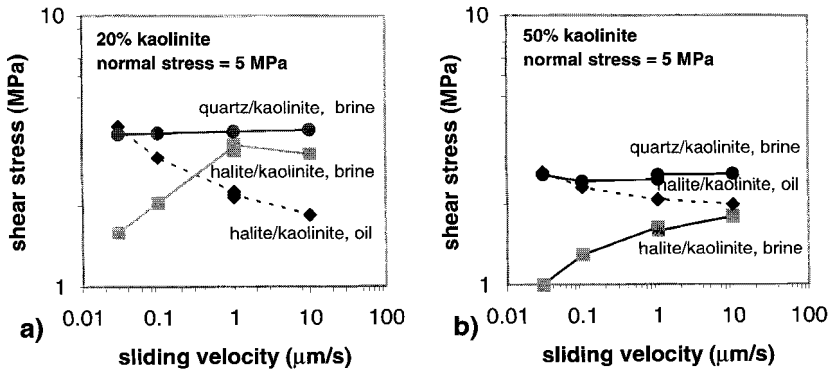
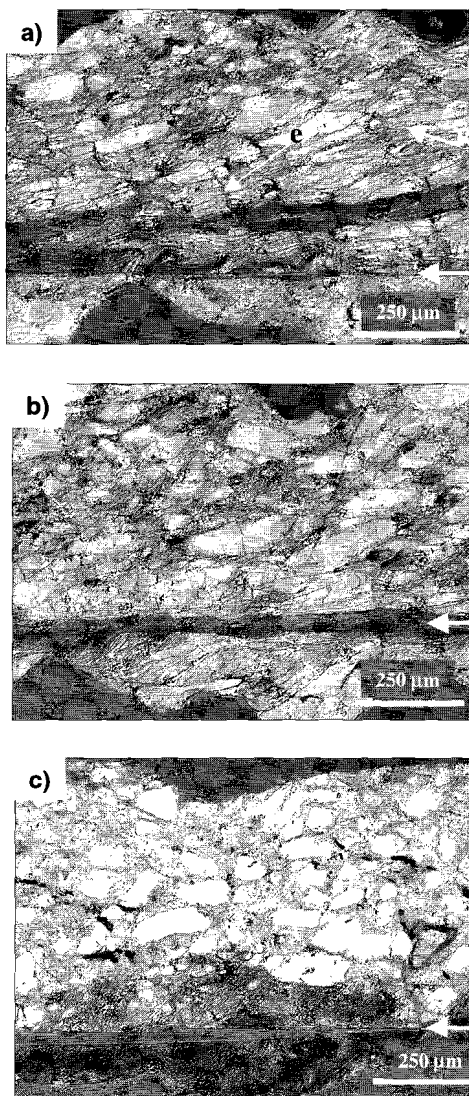


Figure 3.9. Shear stress versus sliding velocity for the experiments shown in Figure 3.8. a) Data for 20% kaolinite mixtures. b) Data for 50% kaolinite mixtures.

In summary, we observed frictional-viscous flow behaviour in faults containing halite/kaolinite gouge using brine as a pore fluid, under conditions where halite is known to undergo pressure solution. When pressure solution is inhibited by using an inert fluid (i.e. silicone oil) instead of brine, or by using a solid of very low solubility (i.e. quartz) instead of halite, no weakening with decreasing sliding rate was observed.

3.3.4 Microstructural observations

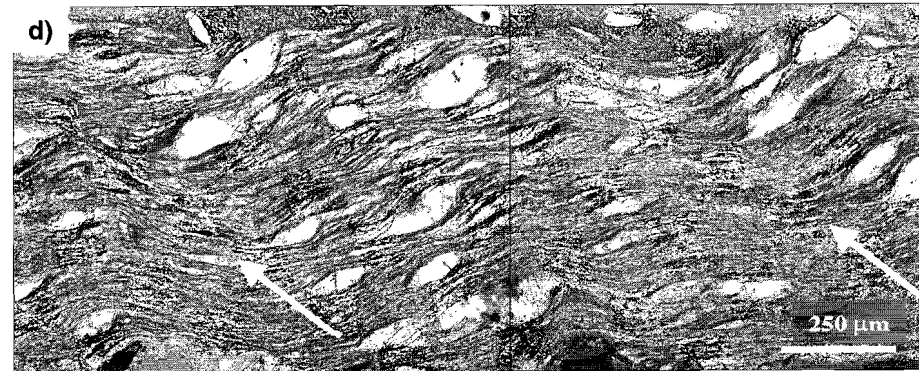
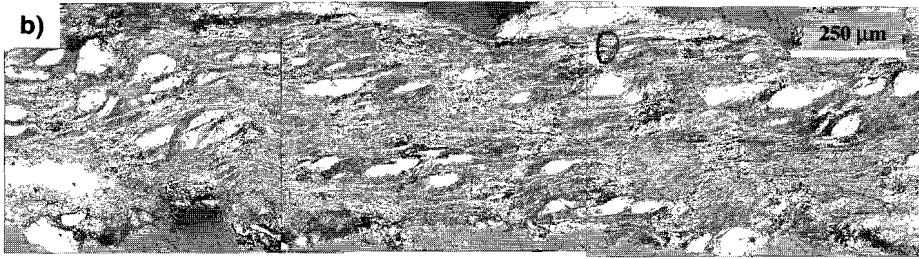
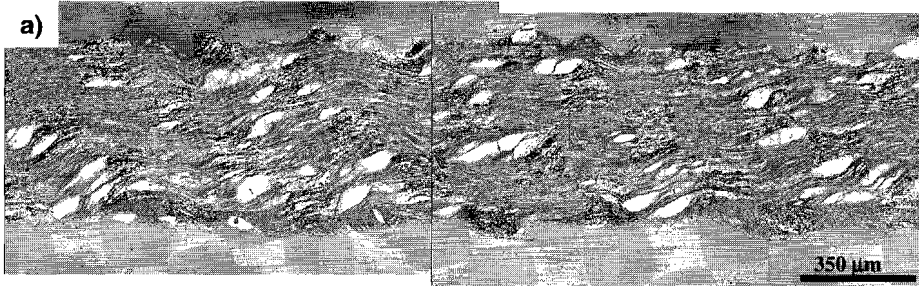


The microstructure of experiment sctest5, which was terminated after the dry "run-in" period is shown in Figures 3.10. The sample shows a continuous, flat, clay-rich boundary parallel fault (Y-shear, see white arrows) located near the shear zone boundary. Most of the gouge is a mixture of clay and halite. The gouge microstructure is spatially heterogeneous. In most regions (~60% of the section), a distinctive foliation was observed (Figure 3.10a), oriented at ~25° to the shear zone boundary. The foliation is formed by aligned kaolinite grains as well as by elongate halite fragments. In places, the foliation is cut by faults in R1 "Riedel shear" orientation (marked "R"), following the terminology described by [Logan *et al.*, 1992]. Some halite grains show extensional fractures (marked "e" in Figure 3.10a). In general, the kaolinite forms an interconnected, anastomosing network. In other areas (~30% of the section) the foliation is weaker (Figure 3.10b), and mostly present near the clay-rich Y-shear. In clay-poor areas (Figure 3.10c), the gouge is porous and no foliation was observed. These regions constitute ~10% of the thin section. Even in the clay-poor areas the region around the Y-shear is rich in clay.

The microstructures of halite/kaolinite mixtures deformed wet are shown in Figures 3.11. Figure 3.11a, b and c show microstructures of samples with different kaolinite contents. In the wet-deformed halite/clay mixtures, no continuous Y-shears were observed. In addition, the strong spatial heterogeneity observed in the samples after the dry run-in is no longer present. Figure 3.11a shows the microstructure of gouge with 30% kaolinite. The gouge consists of asymmetric,

Figure 3.10. Microstructures of experiment sctest5, terminated after the dry run-in phase. In all Figures, the gray material surrounding the gouge is epoxy resin. The white grains are halite, the dark material is kaolinite. Shear sense is dextral in all cases. Note flat boundary or Y-shear (white arrows) in all pictures. a) Foliated region (comprising 60% of the section), showing strong foliation formed by kaolinite layers and elongate halite grains, extensional fractures (e) and R-shears (R). b) Less foliated region (comprising 30% of the section). Note that the foliation is most intense near the Y-shear. c) Microstructure of clay-poor region (comprising 10% of the section). Note absence of foliation, as well as significant porosity and concentration of kaolinite near the Y-shear.

sigmoidal clasts, embedded in a foliated matrix. The clasts are oriented with their long axis at 25-45° to the horizontal. Several clasts show long tails. Most of the clasts appear intact, but some show intragranular fractures. No evidence for recrystallization was observed. The dark matrix consists of a fine scale intercalation of kaolinite layers and elongate halite grains (see Figures 3.11d and 3.11e). All optically visible halite grains are surrounded by a film of kaolinite. The matrix defines a



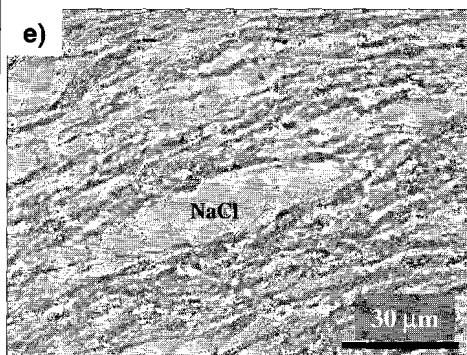


Figure 3.11. Microstructures of clay-bearing samples after wet deformation. Shear sense is dextral in all images. a) sample sc30k (30% kaolinite). Note wavy foliation, asymmetric clasts, and shear bands formed by clast-poor areas. b) sample sc50k (50% kaolinite). Note similarity to Figure 3.11a, but more horizontal foliation and more elongated clasts. c) sample sc75k (75% kaolinite). Note isolated large clasts and fine horizontal halite slivers in kaolinite matrix. d) detail of sample sc30k. Note how the foliation is dragged into the shear bands (white arrows). e) Detail of matrix microstructure of sc30k, showing that the matrix consist of a fine-scale intercalation of halite and kaolinite. Note the absence of halite-halite grain contacts.

distinctive wavy foliation that wraps around the clasts. In areas with many clasts the foliation is generally oriented at 25-35° to the horizontal. In clast-poor regions, shear bands (see white arrows in Figure 3.11d) are developed. In the slip direction these shear bands alternate with more clast-rich regions. Figure 3.11b shows material with 50% kaolinite. Overall, the microstructure is similar to Figure 11a, but the clasts are more elongate, and the foliation is more horizontal than in Figure 3.11a. Also, the shear bands are less prominent. Figure 3.11c shows material with 75% kaolinite. Some large remnant halite clasts are still visible (lower middle side of the image), but most halite is present as thin subhorizontal slivers in a kaolinite matrix. The pure kaolinite sample deformed wet showed a steep, antithetic foliation and the presence of a horizontal, through-going boundary shear.

3.4 Discussion

3.4.1 General aspects

The aim of the experiments reported here was to investigate whether the combination of pressure solution and phyllosilicates can lead to frictional-viscous flow behaviour in simulated gouge-bearing faults. The data clearly show that the strength of faults containing halite/kaolinite gouge deformed in the presence of brine strongly increased with both sliding velocity and normal stress. The increase in strength with increasing strain rate was absent when pressure solution was inhibited using either an inert pore fluid (silicone oil instead of brine) or an inert solid (quartz instead of halite). Also, the strength of the monomineralic gouge (either halite or kaolinite) was relatively insensitive to sliding rate. This leads to the conclusion that the observed frictional-viscous flow behaviour was indeed caused by the combined effects of pressure solution and phyllosilicates. Alternatively, the rate-dependent behaviour could be due to stress corrosion cracking, but this is considered unlikely because if stress corrosion cracking was important one would expect rate-sensitive behaviour in the pure halite samples as well, whereas this was not observed. Moreover, typical stress sensitivity exponents for stress corrosion cracking are of the order 20-30 [Atkinson and Meredith, 1989], in contrast to the 4-7 observed in our experiments. Finally, the presence of elongate, intact halite grains suggests grain elongation by pressure solution rather than cataclasis by stress corrosion cracking.

The halite/kaolinite gouges showed remarkable weakening at low velocities with respect to values typically reported for rock friction. The lowest effective coefficient of friction obtained in our experiments was 0.18, similar to the value for pure kaolinite gouge. This type of behaviour can potentially lead to very weak faults. However, it has rarely been observed before, possibly because only very few experiments have been done on phyllosilicate-bearing gouges under conditions favouring pressure solution. In addition, the strains reached in our experiments (shear strains of 50

in the "run-in", followed by shear strains of ~20 in the stepping experiments) are at least an order of magnitude higher than the strains usually reached in friction experiments under hydrothermal conditions. Sliding experiments on water-saturated quartz + kaolinite gouge at temperatures up to 600°C were reported by *Rutter and Maddock* [1992], but these authors did not observe significant weakening or strong rate dependence of strength. This may be due to the fact that for the grain size and temperature used, pressure solution was not active at a rapid enough rate to produce the effects we observed. In addition, their fixed sliding rate experiments may have been performed at too fast sliding rate to produce a significant rate effect. The stress relaxation tests they used to explore lower sliding velocities may not have produced enough strain to achieve the microstructural modifications necessary for weakening. *Blanpied et al.* [1995] performed sliding experiments on faults containing granitic gouge at both dry and wet conditions, and observed significant weakening as well as a marked rate dependence of strength in wet samples at temperatures above 350°C. This is consistent with the behaviour reported here and may also be due to the combined effects of pressure solution and phyllosilicates.

We can then conclude that the combination of pressure solution and phyllosilicates led to fault weakening and frictional-viscous flow behaviour in our experiments. However, no microphysically based model for this type of behaviour exists. To understand what microscale processes led to the observed mechanical behaviour, close inspection of the microstructures produced during deformation is necessary. In the following, we address the role of phyllosilicates in the present experiments, the strength determining mechanisms, and the implications for natural fault zones.

3.4.2 Deformation mechanisms in the dry run-in stage

In the dry run-in stage of the experiments, kaolinite grains and elongate halite grains formed a foliation inclined at ~25° to the shear zone boundary. Also, a through-going boundary-parallel shear was observed. Since stick-slip behaviour is often associated with localised slip on a boundary-parallel shear [*Chapter 2; Chester and Logan, 1990*], we infer that the fabric was formed in the early stages of the experiment, and deformation concentrated on the Y-shear at the point where stick-slip behaviour started. The initial fabric-forming stage presumably involved cataclasis, grain size reduction and redistribution of material, leading to the formation of an anastomosing clay network in clay-rich regimes (see Figure 3.10a). Coalescence of horizontal segments of the networks subsequently lead to the formation of a through-going horizontal shear (Y-shear), located near the shear zone boundary. All deformation then localised into this Y-shear. In our experiments, the strength of the gouges at high strain in the dry regime is not systematically dependent on clay content, in contrast to reports by *Shimamoto and Logan* [1981] and *Logan and Rauenzahn* [1987]. This apparent contradiction may be due to the fact that much higher strains were attained in our experiments. If the dry experiments had been run to a shear strain of only 5-10, which is the typical shear strain magnitude reached in friction experiments, the data would have shown a clear trend of decreasing strength with increasing kaolinite content, at least for kaolinite contents above 30%. The Y-shear zone formed in our experiments is strongly enriched in clay with respect to the bulk gouge. Hence, the clay content in the region around the Y-shear is not directly related to the clay content of the starting material.

3.4.3 The role of phyllosilicates in wet experiments

In the dry stage of the experiments, anastomosing kaolinite zones formed in the bulk of the gouge, after which deformation localised on a Y-shear. This demonstrates that slip on the Y-shear was easier than deformation of the bulk of the gouge. In contrast, after the wet experiments no through-going Y-shear was present, showing that deformation was transferred to the bulk of the gouge. We infer that upon addition of fluid, compaction as well as healing of clay-poor parts of the Y-shear lead to roughening of the shear plane, transferring deformation to the bulk of the gouge. The surprising observation that no new through-going Y-shear developed in the wet stage can be explained by the fact that under wet conditions the Y-shear (which consists mainly of kaolinite) is velocity-strengthening, in contrast to the velocity-weakening stick-slip behaviour shown under dry conditions. This velocity-strengthening behaviour precludes the maintenance of instabilities needed to form a through-going Y-shear.

The tendency of kaolinite to reside between halite grains may influence the mechanical behaviour of wet gouge in a number of ways: Firstly, the clay-filled halite-halite contacts may provide fast pathways for diffusional transport of solutes [Rutter, 1983; Hickman and Evans, 1995; Renard *et al.*, 1997], thus allowing rapid deformation of halite grains by pressure solution. Secondly, phyllosilicates on grain boundaries may prevent healing of halite-halite contacts [Hickman and Evans, 1995], inhibiting the rapid healing observed in monomineralic halite gouges [cf. Chapter 2] and thus allowing intergranular sliding of halite grains. The observation that after the wet stage neither clast elongation nor foliation orientation tracks the long axis of the finite strain ellipse proves that gouge deformation was not homogeneous on the grain scale. In the absence of recrystallization, this implies that a significant component of intergranular slip on the clay films/foliation must indeed have occurred. We propose that upon adding fluid, pressure solution compaction first destroyed the existing Y-shear, transferring deformation to the bulk of the gouge. In the gouge, pressure solution allowed easy sliding, leading to gouge deformation at a shear stress below that required for the formation of a new Y-shear. This is supported by the fact that in the experiments where silicone oil instead of brine was added stick-slip behaviour was observed, suggesting deformation remained localised on the Y-shear. It also explains why both pressure solution and phyllosilicates were required for the frictional-viscous behaviour we observed in halite/kaolinite mixtures. Phyllosilicates allowed easy sliding along grain boundaries, by forming planes of low friction and inhibiting fluid-assisted grain contact healing. Pressure solution was required as a time-dependent sliding accommodation mechanism, without which no rate-sensitive behaviour is possible.

3.4.4 Microscale processes determining fault strength in wet experiments

As mentioned above, deformation in our experiments involved a significant component of sliding along kaolinite foliae. Since the foliation is oblique and anastomosing, and not flat and horizontal, fault shear involving sliding along foliae requires accommodation of geometrical incompatibilities (such as halite clasts) by pressure solution and/or gouge dilatation or cataclasis. In this scenario, sliding along kaolinite foliae and accommodation of sliding (by pressure solution or dilatation) are series-sequential processes, i.e., all sliding on foliae requires accommodation by either pressure solution or dilatation. This implies that the total strength is the sum of the strength contributions of frictional sliding along foliae and of the accommodative process (either pressure solution or dilatation). In terms of the relative contributions of (rate-insensitive) frictional sliding

along foliae, (strongly rate-sensitive) pressure solution and (rate-insensitive) dilatation/cataclasis to measured shear strength, three regimes of behaviour can be envisaged:

a) At very low sliding velocities pressure solution is negligibly easy and fault strength is controlled by the sliding friction of the kaolinite foliae. This scenario would produce rheological behaviour approaching the behaviour of wet, 100% kaolinite gouge since the strength would be determined by kaolinite-rich planes ideally oriented for sliding. No rate dependence is expected, since the strength of 100% kaolinite gouge is insensitive to sliding rate (see Figure 3.4)

b) At higher sliding velocities, accommodation of sliding on the foliae by pressure solution becomes more difficult, and pressure solution becomes important in controlling fault strength next to the sliding friction of the foliae. In this case, the experiments would show a strong sliding rate dependence of shear strength because the rate of pressure solution depends linearly on driving force stress (i.e. contact stress). Also, sliding strength is expected to be normal stress dependent since due to the contribution of the sliding friction of the foliae to fault strength. In addition, the width of the diffusion path in the solution transfer process (i.e. the fluid-filled halite-kaolinite-halite layer) is likely to depend on normal stress, which may also lead to a normal stress dependence of shear strength. No significant dilatation is expected to accompany deformation, since all sliding is accommodated by diffusive mass transfer.

c) Finally, at still higher velocities, the shear stress becomes so high that accommodation of sliding by dilatation and cataclasis is favoured over accommodation by pressure solution. In this case, purely frictional behaviour is expected since dilatation involves work against normal stress.

To infer whether the above applies to our experiments, we have three sources of information: the microstructures, the shear stress data and the compaction data. Considering the microstructures, two complications arise. The first is that all our experiments are velocity stepping tests, stepping between the purely frictional and the frictional-viscous regime. Hence, it is not surprising that the wet deformed samples show evidence for solution transfer as well as for cataclasis (intragranular cracks, healed microfractures). However, an even more serious complication arises when we consider what microstructural signatures to expect for the different end members: From the microstructures, it is impossible to make a distinction between **a)** and **b)**, since the same processes occur in both. If end member **c)** is dominant and if all sliding is accommodated by dilatation a microstructural signature similar to **a)** and **b)** is again expected. If cataclasis of large grains is important, fractures may be seen. However, in the presence of a chemically active fluid, microstructural evidence for cataclasis may be rapidly obliterated. Fractures will heal rapidly, and sharp corners produced by fracture may be rounded off rapidly by surface-energy driven solution transfer. Hence, in these experiments, where interdependent deformation mechanisms act, microstructures can be used to indicate which deformation mechanisms were operative, but are of limited use for constraining which of the deformation mechanisms determines fault strength.

Regarding the mechanical data, it seems likely that at the higher sliding velocities and low clay contents, where mechanical behaviour is purely frictional, fault strength is controlled by dilatation and cataclasis. The decrease in frictional strength with increasing clay content may be due to the fact that with increasing clay content the amount of large clasts acting as barriers to sliding is lower. Also, our microstructures show that the foliation orientation becomes more horizontal with increasing clay content, so at higher clay contents less dilatation per unit shear strain is required. In the low-intermediate clay content samples and at lower velocities, the strong weakening with decreasing sliding rate suggests that strength is controlled largely by pressure solution. At the very high clay contents ($\geq 75\%$), the rate effect is only minor and behaviour is frictional. In these samples, strength is probably controlled almost entirely by kaolinite friction and dilatation.

This interpretation of the mechanical data is supported by the compaction data. In general, the compaction behaviour of the halite-bearing samples represents the sum of pressure solution

compaction (the rate of which depends on normal stress) and shear-induced dilatation (the rate of which increases with sliding velocity). Upon changing sliding velocity, transient compaction or dilatation may occur to establish a new balance. Hence, under conditions where sliding along kaolinite is accommodated mainly by cataclasis or dilatation, significant dilatation is expected upon increasing sliding velocity. In a regime where pressure solution accommodation is dominant, no significant dilatation is expected upon increasing sliding velocity. Comparing Figures 3.4 and 3.6 it can be seen that the dilatation behaviour correlates well with the mechanical behaviour: Under conditions where sliding is frictional (i.e. pure halite at all velocities and the 20% kaolinite mixture at velocities above 1 $\mu\text{m/s}$), increasing sliding rate is accompanied by significant dilatation. In contrast, under conditions where sliding is rate sensitive (i.e. 50% kaolinite at all sliding velocities and 20% kaolinite at velocities below 1 $\mu\text{m/s}$) only minor dilatation was observed upon increasing sliding velocity. This supports the above conclusion that in the rate-sensitive regime strength is mainly controlled by pressure solution. Similarly, the dilatation occurring in the rate-insensitive regime confirms that dilatation and cataclasis determine fault strength in this regime.

The interpretation that deformation in our samples was due to sliding along kaolinite foliae accommodated by pressure solution and dilatation implies that the fault strength cannot drop below the frictional strength of kaolinite foliae. Indeed, our data show that the strength of pure kaolinite gouge presents a lower bound to observed fault strength. The friction coefficient measured in our kaolinite samples is lower than that measured in other experiments on wet kaolinite gouge, performed at higher pressures, in which values of 0.4-0.6 were measured [Rutter, 1979; Rutter and Maddock, 1992; Morrow *et al.*, 2000]. The low friction coefficient measured in our experiments cannot be due to overpressurized fluids (i.e. an undrained fault due to low permeability), since in this case increasing the normal stress would amount to increasing the fluid pressure as well. Thus, the effective normal stress would stay the same and no normal stress dependence of shear stress would be expected, in contrast to our data (cf. Figure 3.7). It should be noted that the friction coefficient measured in experiments on gouge layers is determined by grain boundary friction as well as by gouge microstructure, and hence is not an intrinsic material property. The kaolinite-rich gouges that yielded the friction values of 0.4-0.6 show distributed deformation and the formation of a steep foliation and R-shears [Rutter, 1979; Rutter *et al.*, 1986]. Unfortunately, Morrow *et al.* [2000] did not show any microstructures of deformed samples. In contrast, in our pure kaolinite experiments deformation was localised on a horizontal Y-shear. This could well explain the lower friction coefficient, since sliding along a horizontal shear requires only overcoming of the boundary friction, whereas sliding along the foliation in an obliquely foliated gouge requires dilatation in addition to overcoming grain boundary friction, both contributing to the measured shear stress. The experiments of Morrow *et al.* [2000] showed a significant lubrication effect of water in various phyllosilicate minerals. The weakening/lubrication effect kaolinite due to the presence of water measured in our experiments is similar to that reported by Morrow *et al.* (i.e., a reduction in μ of ~ 0.25). Since it is the grain boundary friction coefficient, and not the microstructure, that is likely to be instantaneously influenced by the presence of the lubricant, this observation again suggests that the difference between our measured friction and other studies may be attributed to microstructural factors.

As already mentioned, no microphysical model for the frictional-viscous flow behaviour observed in our experiments exists to date. However, in existing microphysical models for fault slip controlled by pressure solution [Rutter and Mainprice, 1979; Lehner and Bataille, 1984/85], shear strength depends linearly on sliding rate, since the rate of (diffusion controlled) pressure solution depends linearly on driving force. Also, no significant normal stress dependence of shear stress is predicted. This is in contrast to our experiments, where a strongly non-linear relation between shear stress and sliding velocity, and significant normal stress dependence of strength were observed. We

believe this is due to the fact that these models do not incorporate frictional sliding along grains as a dissipative process. Incorporating frictional sliding as process acting series-sequentially with pressure solution will introduce a normal stress dependence of strength due to the normal stress dependence of the sliding strength of the foliae/grain boundaries. Also, the stress sensitivity of strain rate will be higher than the linear relation predicted by a model only incorporating pressure solution, since in general deformation behaviour is a mixture of (linear viscous) pressure solution and (rate-independent) frictional sliding behaviour.

Finally, it must be mentioned that the microstructures developed in our experiments are probably not steady state microstructures; the microstructures evolve during deformation. This may have implications for the mechanical behaviour. For example, it is likely that fault strength can develop from being controlled by dilatation and cataclasis to being controlled by pressure solution by continuous deformation, since with increasing deformation 1) the average grain size will be reduced and 2) the porphyroclasts will become more elongated, thus lowering their ability to act as barriers to sliding. Surprisingly, the strength evolution with strain in the wet part of our experiments was minimal. This is probably due to the fact that a foliation was already present at the start of the wet part of the experiments.

3.4.5 Implications for natural faults

In our experiments we obtained evidence for frictional-viscous flow behaviour in halite/kaolinite gouges by the combined effects of pressure solution and phyllosilicate phase. On this basis, it seems reasonable to suppose that frictional-viscous behaviour occurs in natural rocks containing phyllosilicates, under conditions favouring pressure solution. Field studies suggest that in quartzose rocks pressure solution occurs at significant rate at depths of a few kilometers [Tada and Siever, 1989]. Clay minerals are ubiquitous in natural fault rocks, either as component of a sediment or as alteration product of igneous and metamorphic rocks [Wu *et al.*, 1975; Wu, 1978; Chester and Logan, 1986; Rutter *et al.*, 1986; Wintsch *et al.*, 1995]. At higher metamorphic grades, micas are present instead. While the strength of micas is somewhat higher than that of clay minerals, they do have a platy morphology and, like clays, allow easy slip (either frictional or plastic) along their basal plane orientation [Shea and Kronenberg, 1992; Mares and Kronenberg, 1993; Shea and Kronenberg, 1993]. In addition, it appears from both field studies as well as experiments that the presence of phyllosilicates increases the rate of pressure solution [Tada and Siever, 1989; Schwarz and Stoeckert, 1996; Rutter and Wanten, 2000]. Hence, it is expected that in natural fault zones there is a significant range of conditions where frictional-viscous behaviour may be important, and where crustal strength will be significantly lower than predicted by simple two-mechanism strength profiles. Indeed, field studies of phyllosilicate-rich fault zones show evidence of deformation by diffusional mass transfer at stress levels below those needed to activate dislocation creep [Schwarz and Stoeckert, 1996; Imber *et al.*, 1997; Stewart *et al.*, 2000]. Quantification of this weakening effect is hampered by 1) absence of a microphysical model describing frictional-viscous flow behaviour and 2) insufficient knowledge of the relevant constitutive parameters that would enter into such a model, such as grain boundary diffusion coefficients and grain contact friction coefficients.

Many of the microstructural features observed in the wet experiments (such as sigmoidal clasts with tails, subhorizontal foliation, small-scale intercalation of phyllosilicates and soluble solid layers, shear bands) are very much reminiscent of the microstructures observed in natural mylonites [Platt and Vissers, 1980; White *et al.*, 1980; Lister and Snoke, 1984; Passchier and Trouw, 1996]. In natural mylonites these structures are attributed, at least in part, to crystal plasticity. In our experiments, however, the stresses were an order of magnitude too low for any significant plasticity to occur in halite [Carter *et al.*, 1993; Spiers and Carter, 1998]. This shows that crystal plasticity is

not required to form these microstructures; they can be formed by pressure solution and cataclasis as well. In natural mylonites, however, microstructural evidence for dislocation creep is generally present in the form of, amongst others, subgrains, undulatory extinction and a crystallographic preferred orientation. From our experiments it seems likely that in natural faults both pressure solution and dislocation creep plus recrystallization contribute to microstructural evolution and strength. Assessment of the relative contributions of pressure solution and dislocation creep may in general be very difficult, since diagnostic evidence for pressure solution is easily overprinted.

In our experiments, the sliding strength of the weak sliding mineral(s) in the rock presents a minimum level for the strength, towards which the strength of the fault can evolve with strain, provided that 1) the strain rate is low enough (i.e. the contribution to fault strength by accommodative solution transfer processes is negligible) and 2) enough of the weak material is present to form a contiguous foliation. Crustal deformation around the brittle-ductile transition is largely accommodated in shear zones, where high strains are common and significant microstructural readjustments take place. Crustal strength is usually modeled using rheological creep laws describing low strain behaviour of homogeneous, isotropic materials, calibrated in low strain experiments where only very limited microstructural rearrangements are possible. The pronounced effect that microstructural rearrangements have on rock strength casts serious doubt on this approach, as previously put forward by others [Rutter and Brodie, 1991; Shea and Kronenberg, 1992; Kawamoto and Shimamoto, 1998]. It may be more appropriate to model the rheology of high strain shear zones using the strength of the weakest material. Under the conditions pertaining at the brittle-ductile transition, these will usually be clays (if present) or micas [Shea and Kronenberg, 1992; Wintsch *et al.*, 1995]. Since the activation energy for slip on basal planes in mica's are significantly lower than the activation energy for dislocation creep of quartzite, quartz can be expected to become the weaker phase with increasing depth. In order to construct a crustal strength profile including these considerations, a microphysical model for frictional-viscous flow behaviour is needed.

3.5 Conclusions

We performed sliding experiments on synthetic halite + kaolinite fault gouges, in order to investigate whether the combination of pressure solution and phyllosilicates could lead to frictional-viscous flow behaviour. The following conclusions can be drawn:

1. We observed frictional-viscous flow behaviour in wet halite/kaolinite gouges. This behaviour was not observed in clay-bearing gouges using an inert pore fluid (silicone oil instead of brine) or an inert solid (quartz instead of halite).
2. Frictional-viscous flow behaviour occurred by a mechanism involving sliding along kaolinite-rich foliation planes, accommodated by pressure solution. Phyllosilicates prevented halite-halite contact healing and allowed easy sliding, whereas pressure solution acted as a time-dependent accommodation mechanism. On this basis we infer that the *combination* of pressure solution and phyllosilicates leads to frictional-viscous behaviour.
3. Frictional-viscous flow behaviour in faults as reported here may lead to significant weakening with respect to conventional brittle-plastic strength envelopes. A quantitative assessment of its effect is hampered by lack of a microphysical model, as well as by incomplete knowledge of the relevant constitutive parameters.
4. The microstructures observed in our experiments strongly resemble natural mylonites. This suggests that, in natural phyllosilicate-rich fault rocks pressure solution may play an important role next to dislocation creep in allowing microstructural evolution and controlling fault strength.

Chapter 4

Effect of strain on microstructure and rheology of simulated, clay-bearing fault gouge

Submitted to J. Struct. Geol. as: B. Bos and C.J. Spiers, Experimental investigation into the microstructural and mechanical evolution of phyllosilicate-bearing fault rock under conditions favouring pressure solution

Abstract. Mature crustal fault zones are known to be zones of persistent weakness. This weakness is believed to result from microstructural modifications during deformation, such as grain size reduction and foliation development. Around the brittle-ductile transition, phyllosilicates are expected to have a significant effect on fault strength, in particular under conditions favouring pressure solution. To study such effects, we performed rotary shear experiments on brine-saturated halite/kaolinite mixtures, aimed at investigating the relation between microstructural and mechanical evolution in a system where pressure solution and cataclasis dominate. The results show significant strain weakening, and a transition with progressive strain from purely frictional to frictional-viscous behaviour. This was accompanied by a microstructural evolution from a purely cataclastic microstructure to a mylonitic microstructure consisting of elongate, asymmetric clasts in a fine-grained, foliated matrix. The results demonstrate that strain weakening and the development of a typical 'mylonitic' microstructure can occur as a consequence of grain size reduction by cataclasis, and a transition to pressure solution accommodated deformation, even in the absence of dislocation creep. The data raise questions regarding the reliability of microstructures as rheology indicators, as well as on the use of low strain, monomineralic rheology based flow laws for modelling crustal dynamics.

4.1 Introduction

It has long been recognized that mature crustal fault/shear zones are persistent zones of weakness, exerting a strong influence on crustal dynamics. The cause of the persistent weakness of such fault zones relative to the surrounding rock lies in microstructural changes during shear leading to strain weakening [Etheridge and Wilkie, 1979; White *et al.*, 1980]. These changes include grain size reduction by processes such as cataclasis, dynamic recrystallization and mineral reactions, as well as the development of a foliation.

At depths below the brittle-ductile transition, grain size reduction by dynamic recrystallization is widely thought to lead to weakening and localisation as a result of a switch in deformation mechanism from dislocation creep to diffusion creep [Rutter and Brodie, 1988]. However, the feasibility of major weakening by this has recently been questioned, at least for monomineralic materials [De Bresser *et al.*, 1998]. Moreover, recent numerical modelling studies show that permanent localisation of deformation by this mechanism is possible only for very specific conditions, i.e. specific values of strain rate and cooling rate [Braun *et al.*, 1999]. In the case of brittle/frictional faulting and cataclasis, grain size reduction, microcrack damage, cohesive strength loss and localisation are inherent in the faulting process. In addition, grain size reduction by cataclasis can lead to enhanced production of weak phyllosilicate minerals, in particular under the hydrothermal conditions of the brittle-ductile transitional region.

Especially in phyllosilicate-bearing rocks the formation of a foliation may strongly influence the evolution of fault strength with strain. In crustal fault zones, phyllosilicates are ubiquitous [e.g. Wintsch *et al.*, 1995; Passchier and Trouw, 1996; Snoke *et al.*, 1999], either inherited from the host rock or formed as an retrograde alteration product. Under the conditions pertaining around the brittle-ductile transition, phyllosilicates are expected to be the weakest phase present [Logan and Rauenzahn, 1987; Shea and Kronenberg, 1993], and hence the presence and

alignment of phyllosilicates may have a significant influence on fault strength. Related to this, phyllosilicates are believed to increase grain boundary diffusion rates [Rutter, 1983; Hickman and Evans, 1995; Renard *et al.*, 1997; Farver and Yund, 1999], enhancing diffusional mass transfer processes and further foliation development [Means and Williams, 1972]. In addition, the presence of phyllosilicates at grain boundaries inhibits grain growth, thus stabilizing fine grain sizes [Etheridge and Wilkie, 1979; Olgaard and Evans, 1988] and promoting on-going diffusional creep and grain boundary sliding. This may enhance deformation of fine-grained fault rock by pressure solution-accommodated grain boundary sliding [Rutter and Mainprice, 1979; Lehner and Bataille, 1984/85; Paterson, 1995], allowing ductile deformation at temperatures too low for dislocation creep to be important. Despite this perceived importance of phyllosilicates in determining fault rheology in the brittle-ductile transitional region, there have been few experimental studies on their influence on fault constitutive behaviour under hydrothermal conditions.

In a previous study (cf. Chapter 3) we reported rotary shear experiments performed on simulated, gouge-bearing faults under conditions favouring pressure solution. These experiments were carried out using brine-saturated mixtures of halite (NaCl) and kaolinite as a rock analogue. At high slip velocities the experiments showed purely frictional behaviour, but at low velocities frictional-viscous flow behaviour was observed, i.e. behaviour in which the shear stress is both normal stress and shear strain rate dependent. Apparent friction coefficients down to 0.18 were recorded at the lowest sliding velocities. The microstructures observed after deformation showed asymmetric, sigmoidal halite clasts embedded in a strongly foliated, very fine grained halite/kaolinite matrix. However, since all experiments involved slip rate and/or normal stress stepping sequences, it was not possible to directly relate microstructural development to mechanical behaviour. The microscale mechanisms leading to the observed behaviour therefore remained unclear to some extent, as did the applicability to natural fault zones.

The aim of the present work is to examine the relation between microstructural evolution and mechanical behaviour of simulated fault rock under conditions where pressure solution and cataclasis dominate over dislocation creep, thus simulating the brittle-ductile transition. We present mechanical data and microstructures obtained in a series of rotary shear experiments on simulated halite/kaolinite gouge. Samples were sheared to different strains, at velocities corresponding to both the frictional and the frictional-viscous regime as observed by us (cf. Figure 3.4). The results show significant strain weakening, in particular at low sliding velocities. With increasing strain, a transition from purely frictional to frictional-viscous behaviour occurred. This was accompanied by microstructural evolution from a typical cataclasite at low strain to a strongly foliated, mylonitic fault rock at high strain. The result show localisation and fault weakening due to cataclasis and pressure solution, i.e., without the need for dislocation creep processes. The weakening is accompanied by the formation of microstructures in many ways similar to those of natural mylonites, suggesting that pressure solution and cataclasis may be of greater importance in mylonitization than previously thought.

4.2 Experimental method

Synthetic gouges were prepared by mixing analytical grade, granular halite with very fine-grained kaolinite, in proportions of 3:1 by weight. This composition was chosen because the effect of sliding rate on strength observed in previous experiments was strongest at this composition. The grain size distribution of the halite was determined using a Malvern particle sizer. This showed the median grain size to be 104 μm , with 90% of the grains in the range 57-110 μm . The kaolinite was mostly sub-micron, with occasional grains of ~ 10 μm . Saturated brine (i.e., saturated with respect to

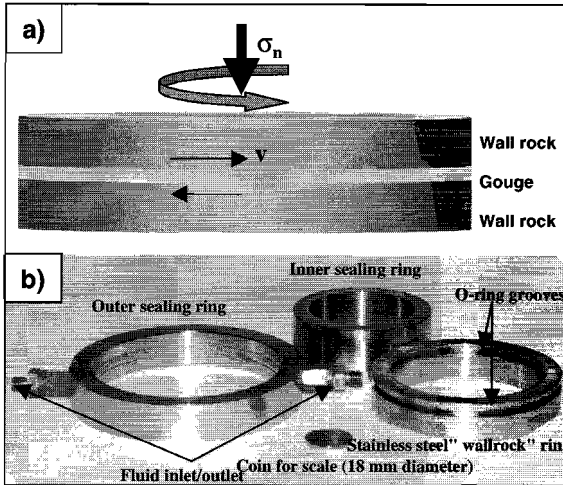


Figure 4.1. a) Schematic diagram of the ring-shear configuration used in this study. Granular fault gouge is sheared between annular stainless steel wall rock rings at controlled velocity v and normal stress σ_n . b) Photograph of the wall-rock rings and the sealing rings. See Chapter 3 for further details of the apparatus.

the gouge material) was used as a pore fluid, maintained at atmospheric pressure during the experiments.

The experiments were performed at room temperature, using the rotary shear apparatus illustrated in Figure 4.1 and described in detail in section 3.2. The annular sample is sheared between two stainless steel "wall rock" rings at controlled normal stress and sliding

velocity (i.e. shear strain rate). The toothed stainless steel "wall rock" rings of 10 cm outer diameter and 1 cm width sandwich a layer of granular gouge (starting thickness after dry compaction $\sim 750 \mu\text{m}$). The sample is sealed with inner and outer stainless steel sealing rings, fitted with O-rings. Two diametrically mounted tubes in the outer sealing ring allow evacuation of the sample and addition of pore fluid. The stainless steel rings are gripped between two cylindrical forcing blocks. While the upper block is held fixed, the lower forcing block is rotated at controlled angular velocity by a motor plus gearbox, thus leading to shear on the synthetic fault. An Instron 1362 loading frame is used to apply and control normal stress to within 0.01 MPa. Shear stress on the fault is measured (resolution 0.005 MPa) using two strain gauge force gauges mounted in a torque couple which provided the reaction needed to hold the upper forcing block stationary. A Linear Variable Differential Transformer (LVDT, 1 mm full scale, 0.01% resolution) located inside the upper forcing block perpendicular to the sliding direction allows measurement of gouge compaction/dilation normal to the shear plane. Rotary displacement is measured using a potentiometer geared to the rotation of the lower forcing block. O-ring friction was measured in a calibration experiment performed with water trapped between the wall rock rings (so the fluid pressure equalled the normal stress), and found to be <0.01 MPa at fluid pressures below 3 MPa.

Experiment	Gouge composition (halite/kaolinite ratio)	Normal stress (MPa)	Sliding velocity ($\mu\text{m/s}$)	Total displacement (mm)	<i>Table 4.1. List of experiments</i>
str1	3:1	5	5	5.67	
str2	3:1	5	5	12.34	
str3	3:1	5	5	51.48	
str4	3:1	5	0.2	0.87	
str5	3:1	5	0.2	3.87	
str6	3:1	5	0.2	17.41	
str7	3:1	5	0.2	52.26	
str8	3:1	5	0.2	536.38	
str9	3:1	5	0.05	15.36	
str10	3:1	2.5	0.2	14.69	
str11	3:1	7.5	0.2	14.84	

The experiments performed are listed in Table 4.1. In setting up individual tests, the granular halite and kaolinite were mixed manually, and a pre-weighed quantity of gouge was evenly applied to the lower wall rock ring. The upper wall rock rings and the sealing rings were then assembled, thus completing the sample assembly which was next located between the forcing blocks. All samples were then compacted dry at 1 MPa for 10 minutes, to produce a gouge with a reproducible starting microstructure. Subsequently, the samples were unloaded and evacuated, and the saturated brine pore fluid was added. The required normal stress and sliding velocity were then imposed. Eight experiments (str1 to str8, see Table 4.1) were performed with the primary purpose of investigating the evolution of microstructure with strain. Three of these were performed at 5 $\mu\text{m/s}$ sliding velocity ("fast" experiments), which is well inside the frictional regime as reported in Chapter 3. The remaining five were performed at 0.2 $\mu\text{m/s}$ ("slow" experiments), which is well inside the strain-rate sensitive regime. All of these experiments were performed at 5 MPa normal stress, reaching displacements given in Table 1. In addition, three experiments were performed in order to provide additional data on the evolution of mechanical behaviour (i.e., the strain rate and normal stress dependence of shear strength) with progressive strain. Two of these (experiments str10 and str11) were performed at a sliding velocity of 0.2 $\mu\text{m/s}$ and a normal stress of 2.5 MPa and 7.5 MPa, respectively. Finally, experiment str9 was performed at 5 MPa normal stress and at 0.05 $\mu\text{m/s}$ sliding velocity.

The experiments were terminated by halting sliding and removing the normal load. The sample assembly was then removed from the forcing rings, and the samples were carefully extracted from the stainless steel wall rock rings. Subsequently, the samples were dried and impregnated with a transparent epoxy resin. Standard thin sections were cut normal to the sliding plane and parallel to the sliding direction, and inspected using an optical microscope. In one sample (str7), the orientation distribution of crystallographic axes was measured by means of Electron Backscatter Diffraction (EBSD). EBSD patterns of halite grains were determined on a Philips XL30FEG scanning electron microscope (SEM).

4.3 Results

4.3.1 Mechanical data

Figure 4.2a shows the shear stress versus displacement data obtained from the microstructural evolution experiments (experiments str1-8, see Table 4.1). The termination point of each experiment is marked with an arrow plus the number of the micrograph illustrating the corresponding microstructure. The experiments performed at 5 $\mu\text{m/s}$ ("fast" experiments, rate-insensitive regime) showed an initial shear stress peak, followed by minor weakening towards a steady state value of ~ 3.25 MPa (apparent friction coefficient μ of 0.65). The experiments run at 0.2 $\mu\text{m/s}$ ("slow" experiments, rate-sensitive regime) show a shear stress peak at ~ 3 mm displacement, after which significant strain weakening was observed. The weakening rate decreased with increasing displacement, the shear stress reaching a value of ~ 2.4 MPa at 10-20 mm displacement. The approach to this steady state was accompanied by an evolution from stable sliding to behaviour showing regular strength oscillations. These oscillations were characterized by a time period of ~ 15 minutes and an amplitude of up to 0.1 MPa. Although a quasi-steady state was reached after ~ 10 -20 mm displacement, minor weakening continued throughout the experiment. The mechanical data obtained in the experiment to 538 mm displacement (str8) were affected beyond 70 mm displacement by misalignment of the forcing rings, leading to increased O-ring friction and unreliable shear stress measurements. For this reason the data from this experiment are not shown beyond 60 mm displacement.

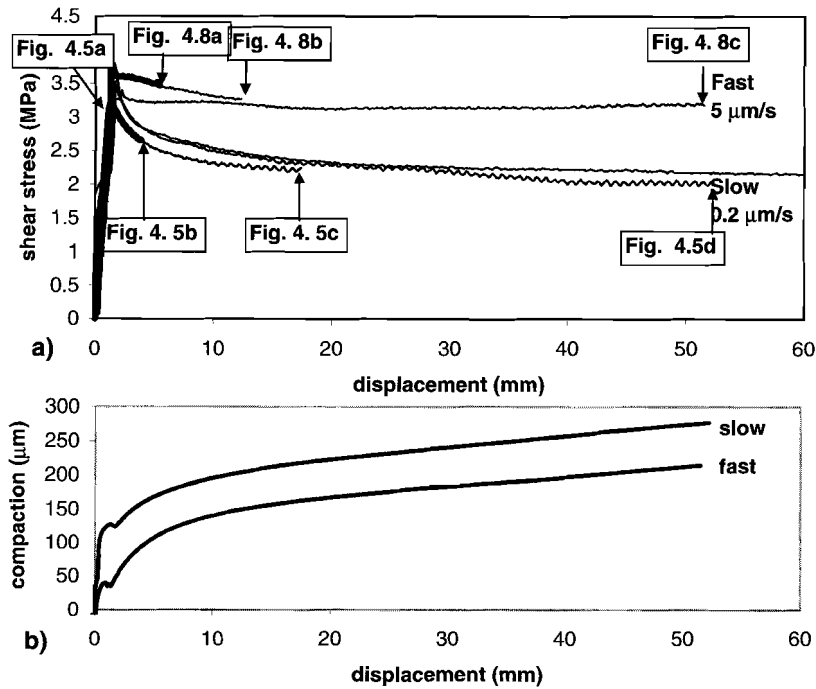


Figure 4.2. a) Shear stress versus displacement for experiments *str1-str8*, conducted to investigate the microstructural evolution. The points at which the respective experiments were halted are denoted with arrows, and the figure showing the corresponding microstructure is indicated. Note the significant strain weakening in the slow experiments, and relatively minor strain weakening in fast experiments. b) Representative compaction versus displacement data (curves shown for experiments *str3* and *str7*).

Figure 4.2b shows representative curves of compaction versus displacement for the fast and slow microstructural evolution experiments run to 50 mm displacement. All curves showed an initial rapid compaction stage, followed by a period of minor dilatation, corresponding to the peak stress in Figure 4.2a. After this, compaction resumed. The total amount of compaction for a given displacement was always larger in the "slow" experiments.

Figure 4.3 shows the mechanical data obtained from experiments *str10* and *str11* performed at a normal stress of 2.5 and 7.5 MPa at 0.2 $\mu\text{m/s}$ sliding velocity, as well as from experiment *str9*, performed at 5 MPa normal stress and at 0.05 $\mu\text{m/s}$ sliding velocity. All of these conditions fall in the rate-sensitive regime. Data from experiment *str6* (2 $\mu\text{m/s}$ sliding velocity, 5 MPa normal stress), which was also shown in Figure 4.2a, are shown for comparison. These experiments all show an initial stress peak, followed by on-going strain weakening, although quasi-steady state was reached after ~ 10 mm displacement. The data indicate that fault strength increased with increasing normal stress and sliding velocity at all strains.

In Figure 4.4, the data presented in Figure 4.3 have been used to illustrate the evolution of rheological behaviour with strain. Figure 4.4a shows shear stress versus normal stress at given shear displacement. The data show a significant normal stress dependence of shear stress at all shear displacements. From Figure 4.4a, the apparent friction coefficient, defined as the slope of a best fit line through the data at a given shear displacement, was calculated. The term "apparent" is used because the mechanical behaviour is not purely frictional, but also sliding rate-dependent. Figure 4.4b shows the calculated apparent friction coefficient as a function of displacement. The data

clearly show that the normal stress sensitivity was highest immediately after the peak stress was reached, and gradually dropped off with increasing displacement. The largest change in apparent friction coefficient occurred in the first 10 mm of the experiment, i.e. during the strong strain weakening phase. In addition, Figure 4.4c shows shear stress versus sliding velocity. These data show that shear stress increases with sliding rate at all displacements, with the dependence being strongest at higher displacements. The sliding rate sensitivity exponent m , defined as the slope of a linear best-fit line through the data shown in Figure 4.4c for a given displacement, is shown in Figure 4.4d. It is evident from this that for the first 2 mm displacement the fit of a linear relation through the shear stress vs. log sliding rate data is poor. Nevertheless, the sliding rate sensitivity gradually increases with increasing shear displacement. Overall, the data of Figure 4.4 show an evolution from almost purely frictional behaviour just after the peak stress to frictional-viscous (i.e. both normal stress and strain rate dependent) behaviour with increasing strain, the change being most rapid in the initial 10 mm of the experiments.

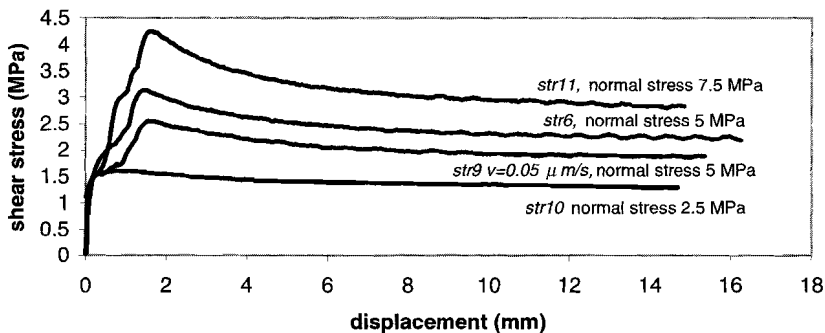


Figure 4.3. Shear stress versus displacement for the experiments str9-str11 conducted to investigate mechanical behaviour evolution. Experiment str6 is shown again for comparison. Note evidence for clear dependence of shear stress on both normal stress and sliding velocity.

4.3.2 Microstructural evolution

Slow experiments. The microstructural evolution with progressive strain in the "slow" experiments (i.e. at $0.2 \mu\text{m/s}$) is shown in Figures 4.5a-e. Also indicated in each Figure is the total shear strain, defined as the ratio of final displacement and final sample thickness. Additional details are shown in Figures 4.6. Figure 4.5a shows the microstructure of a sample from an experiment that was halted at the stress peak (experiment str4). The sample shows numerous intragranular fractures in the halite grains. No preferred alignment of clay particles was observed, but the halite particles seem to define a weak subhorizontal grain shape fabric. Also, most of the intragranular fractures are subvertical.

The microstructure observed midway through the rapid strain weakening stage following the peak stress is shown in Figure 4.5b (experiment str5). A strong foliation has developed at $\sim 35\text{-}40^\circ$ to the imposed shear plane (rotations are measured counter-clockwise). The foliation is defined by elongated halite clasts, separated by anastomosing kaolinite bands. Several large halite clasts show intragranular fractures normal to the foliation. The foliation is transected by clay-rich synthetic shear bands (see white arrow in Figure 4.5b), oriented at -35° to the imposed shear plane. These shear bands have an apparent right lateral shear sense, similar to the macroscopic fault.

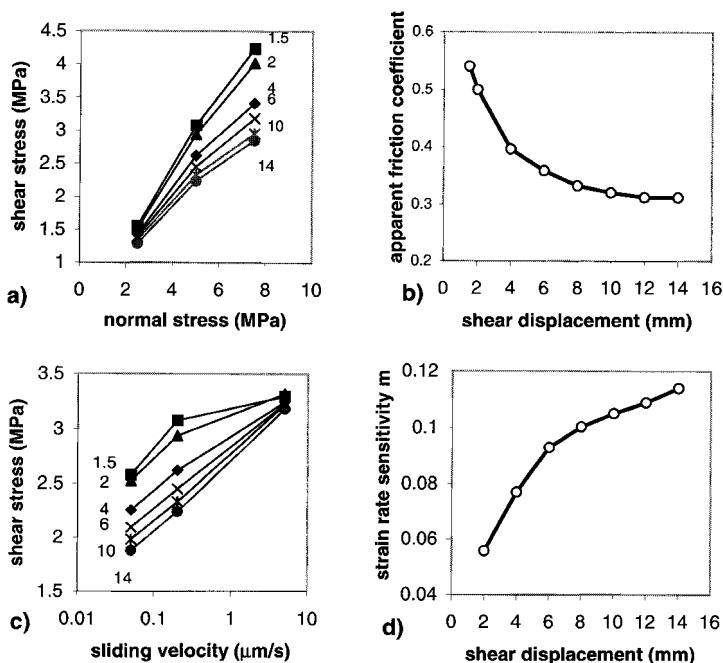
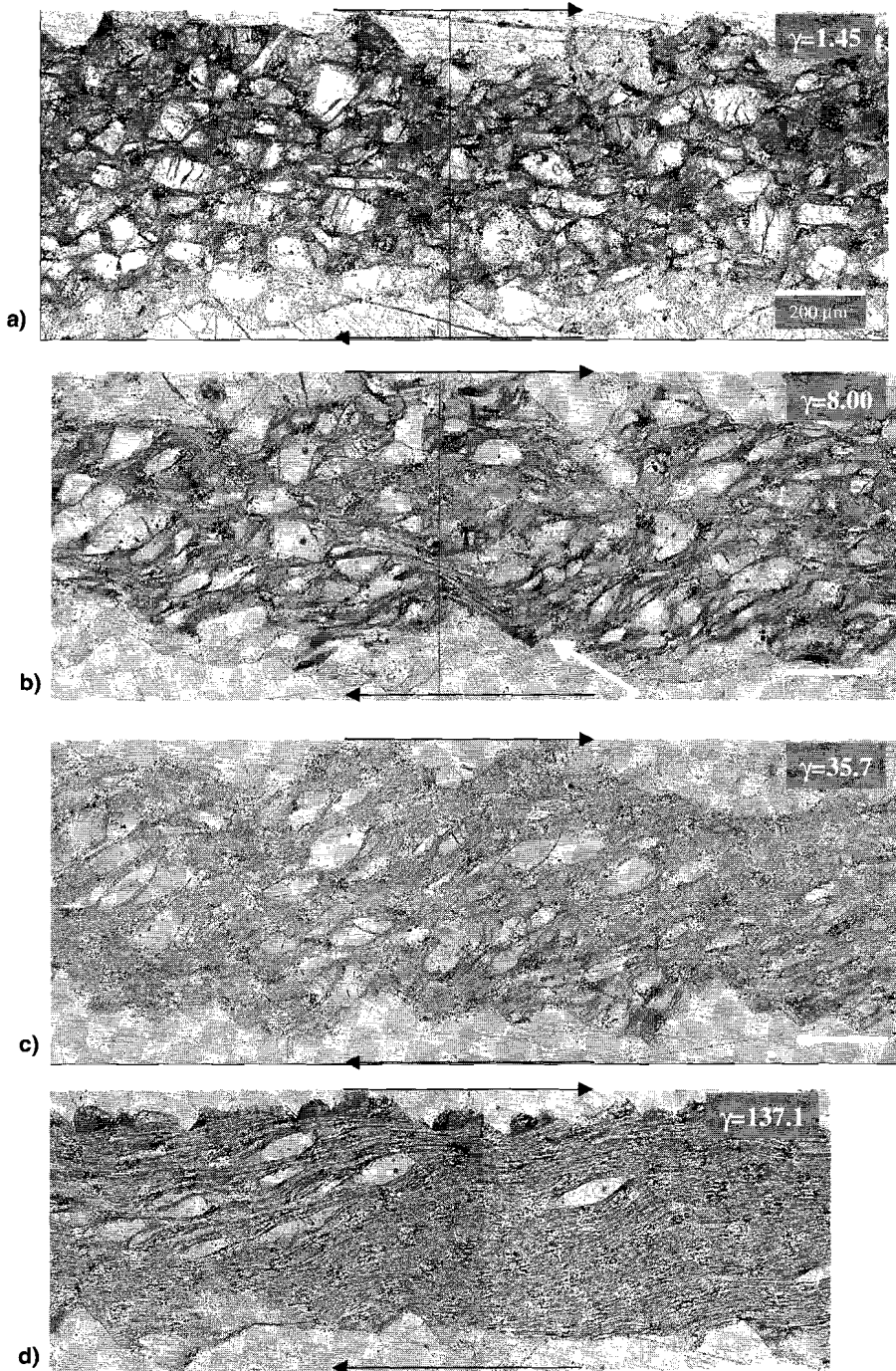


Figure 4.4. Data showing mechanical evolution. a) Shear stress versus normal stress, shear displacement as indicated. b) Apparent friction coefficient μ (i.e., the slope of a linear fit through data of Figure 4.4a at a given displacement) as a function of shear displacement. c) Shear versus shear strain rate, shear displacement as indicated. d) Strain rate sensitivity m (i.e. the slope of a linear fit through data of Figure 4.4b at a given displacement).

Figure 4.5c was taken after the rapid strain weakening stage (experiment str6), immediately after the onset of shear stress oscillations (cf. Figure 4.2a). Strong grain size reduction has occurred with respect to Figure 4.5b. The gouge material now consists of asymmetric remnant clasts in a fine-grained, foliated halite/kaolinite matrix. The sigmoidal clasts are generally oriented with their long axis at $25\text{-}35^\circ$ to the shear zone boundary. In the clasts, intragranular fractures are again common. The foliated matrix, of which a detail is shown in Figure 4.6a, consists of elongate "ribbon-like" halite grains separated by interconnected kaolinite bands. Measuring the area fraction occupied by clasts (i.e., halite grains with smallest axis larger than $10\ \mu\text{m}$) and matrix, by box-counting, showed about 15% of the sample volume consist of clasts. Along the slip direction, regions rich in clasts were found to alternate with clast-poor regions. In the clast-rich regions the foliation is oriented at $\sim 45^\circ$ to the shear zone boundary, whereas in the clay-poor regions the foliation tends to horizontal. The microstructure obtained after $\sim 52\ \text{mm}$ (experiment str7) displacement is shown in Figure 4.5d. This microstructure is similar to that shown in Figure 4.5c in that the material consists of halite clasts in a fine-grained matrix. However, with accumulating strain the proportion of clasts has decreased to 4.4%. The clasts (see Figure 4.6b for details) are now elongate, stair-stepping sigma-objects [Passchier and Trouw, 1996], showing long tails. Most clasts appear free of intragranular cracks, but some are fractured, as shown in Figure 4.6c. In such cases, although the clast shape is still discernible, the fractures between the different fragments are already filled with kaolinite. The

foliation, as defined by the matrix, shows a wavy trend, being more inclined to the shear plane in clast-rich regions than in clast-free regions.



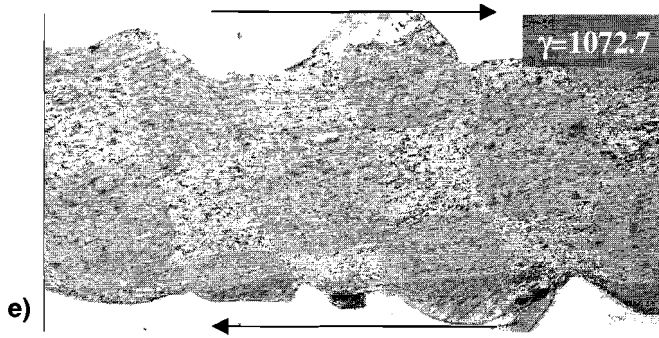


Figure 4.5. Microstructures of samples deformed at 0.2 $\mu\text{m/s}$ ("slow"). Shear sense is dextral, the scale bar is 200 μm in all Figures. The accumulated shear strain is indicated top right. In all figures, the large light grains are halite, the darker material is kaolinite, of which the individual grains are too small to be seen. At the top and bottom of the samples, the teeth forming the surface roughness can be visible. a) Microstructure at the shear stress peak. Note numerous intragranular fractures in halite and absence of fabric. b) Microstructure during pronounced strain weakening. Note strong foliation, transected by clay-rich shear band (arrow), with dextral shear sense. c) Microstructure after the strong weakening. Halite clasts are embedded in a fine-grained matrix (see detail in Figure 4.5a). d) Microstructure after 50 mm displacement. Note isolated asymmetric clasts with long tails, embedded in a fine-grained matrix. e) microstructure after 500 mm displacement. Note oblique foliation and absence of clasts.

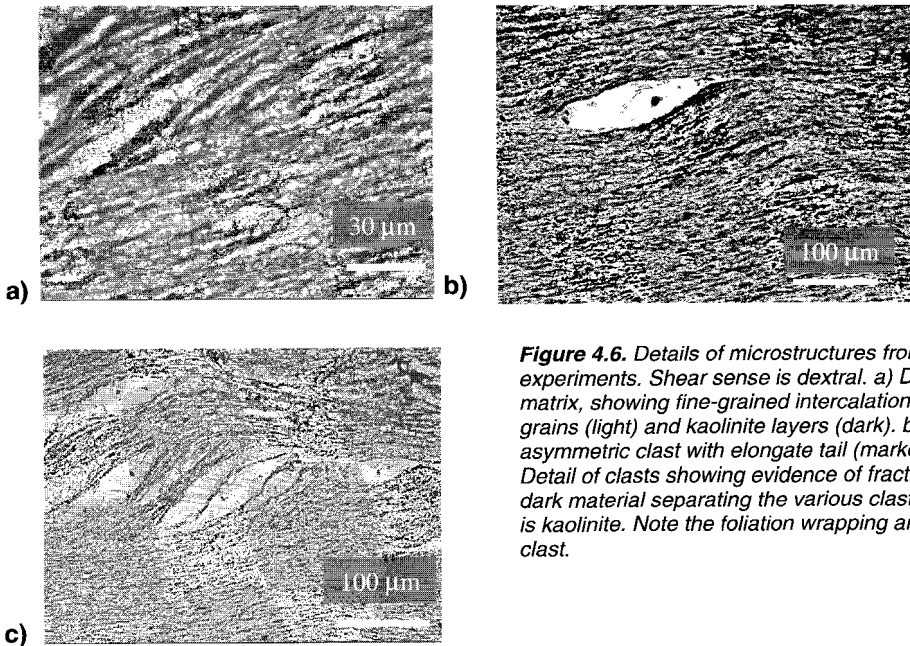


Figure 4.6. Details of microstructures from the "slow" experiments. Shear sense is dextral. a) Detail of matrix, showing fine-grained intercalation of halite grains (light) and kaolinite layers (dark). b) example of asymmetric clast with elongate tail (marked t) c) Detail of clasts showing evidence of fracture. The dark material separating the various clast fragments is kaolinite. Note the foliation wrapping around the clast.

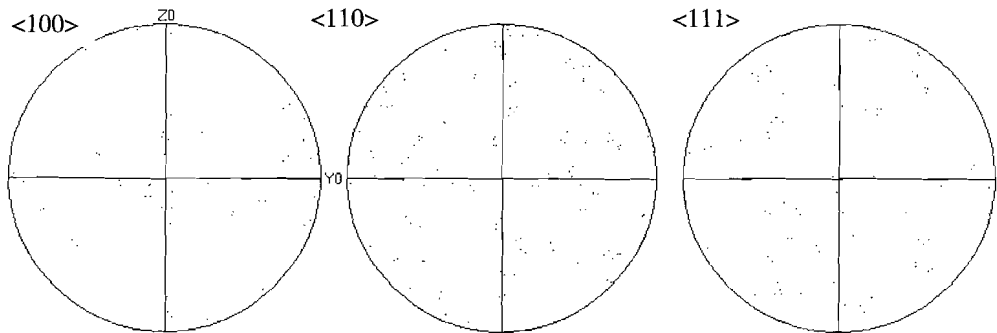


Figure 4.7. Crystallographic preferred orientation plots, obtained using EBSD. A total of 40 matrix halite grains were measured. Pole figures are shown for the $\langle 100 \rangle$, $\langle 110 \rangle$ and $\langle 111 \rangle$ poles. The z-axis (vertical) and y-axis (horizontal) are perpendicular to the shear direction, the x-axis is the shear direction. No significant lattice preferred orientation is present.

Finally, Figure 4.5e shows the microstructure obtained after ~ 500 mm displacement (experiment str8). The entire sample now consists of the fine-grained matrix described above, and no clasts are present. Note that the matrix grain size has not become significantly reduced compared to Figure 4.5c. The foliation still shows a wavy trend. Regions in which the foliation is oriented at an angle of $\sim 20^\circ$ to the shear zone boundary, alternate with shear-band like regions with subhorizontal foliation.

Electron Backscatter Diffraction was used to determine the crystallographic orientation of the halite ribbons in the matrix of sample str7 (cf. Figure 4.5d). Figure 4.7 shows equal area pole figures of $\langle 100 \rangle$, $\langle 110 \rangle$ and $\langle 111 \rangle$. The distribution of crystallographic axes is essentially random in this sample, i.e., no significant preferred orientation was observed.

"Fast" experiments. The microstructural evolution in the "fast" experiments (i.e. those performed at $2 \mu\text{m/s}$ and therefore in the frictional or rate-insensitive regime) is illustrated in Figures 8a-c. Figure 8a shows a sample arrested just before the peak stress (experiment str1). Some intergranular cracks are visible in the halite grains, which are blocky in appearance. No foliation or grain shape fabric was observed. Figure 4.8b shows the sample after ~ 12 mm displacement (experiment str2), i.e. after minor strain weakening had occurred. The microstructure looks similar to Figure 4.8a in that no foliation or grain shape fabric is present, but the average grain size is decreased significantly. Intragranular cracks are common in halite grains. Figure 4.8c shows the sample after ~ 51 mm displacement (experiment str3). As in the "slow" sample after 12 mm displacement (see Figure 4.5c), large rounded halite clasts are now embedded in a fine-grained foliated matrix, but in general the grains are less elongate than in the slow experiment and lack the distinctive tails observed in the slow experiments. In all "fast" samples, imprints of the teeth of the wall rock rings are still clearly visible at the top of the samples, but not at the lower side. The lower side shows a flat, subhorizontal surface where the sample came apart during sample retrieval from the apparatus. Figure 4.9 shows a detail of the fine-grained matrix from sample str3. The microstructure is very similar to that observed in the "slow" experiments (see Figure 4.6a), in showing elongate, ribbon-like halite clasts surrounded by kaolinite. However, the foliation defined by the matrix is much more wavy in character than in the slow experiments, with orientations varying from subhorizontal to $\sim 50^\circ$ to the shear plane.

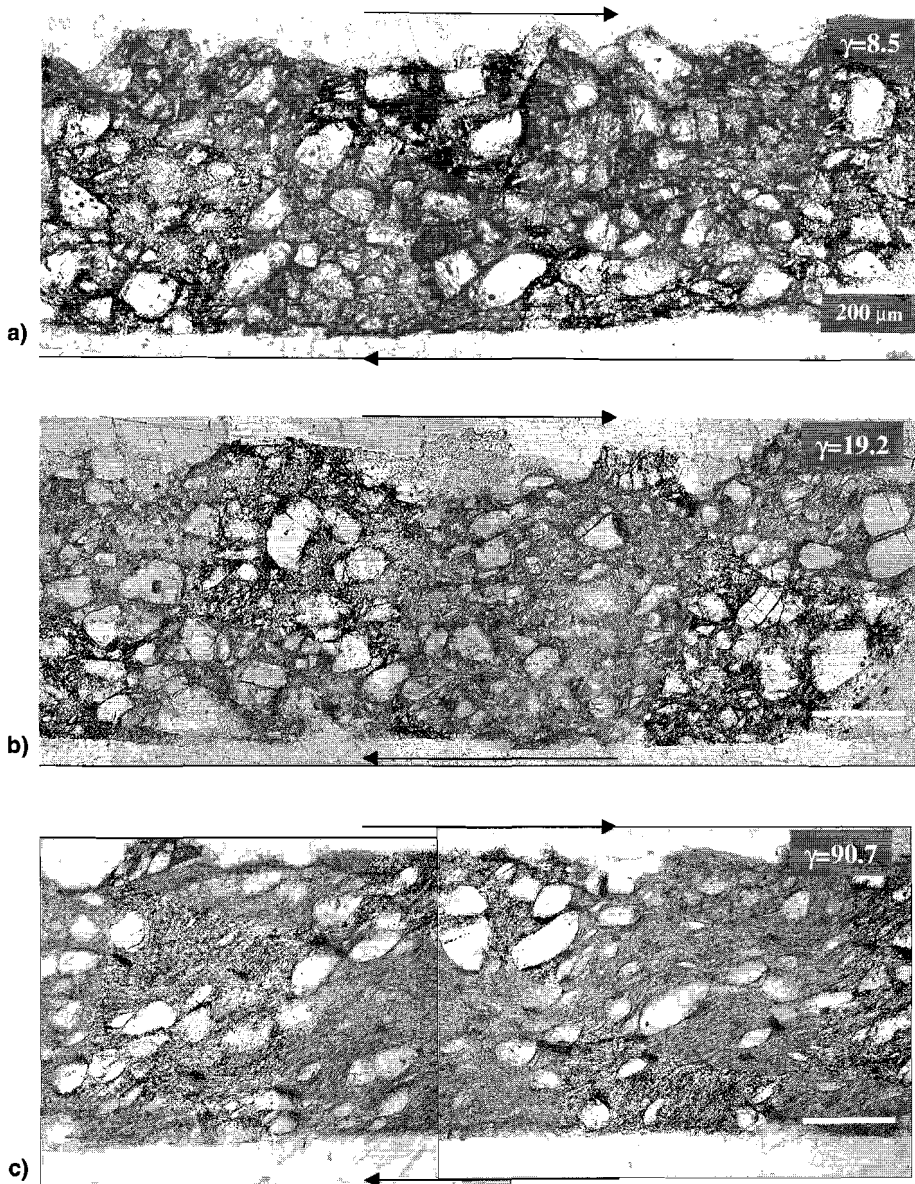


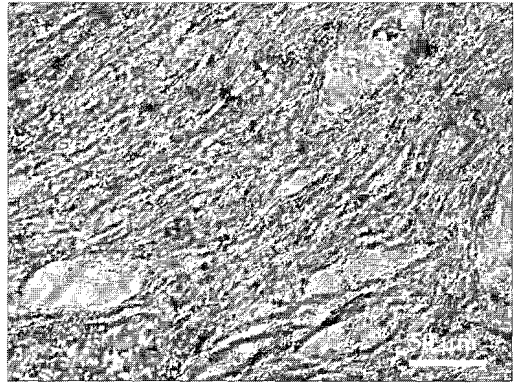
Figure 4.8. Microstructures of samples deformed at 5 μm/s ("fast"). Note fractures in halite in Figures 4.8a (str1) and 4.8b (str2), and foliation in Figure 4.8c (str3).

4.4 Discussion

4.4.1 Deformation mechanisms in our experiments

In this section, we will first discuss the mechanisms controlling fault strength at mechanical quasi-steady state in our experiments. Subsequently, we will address the mechanisms leading to the development of steady state and causing the observed transition in mechanical behaviour from predominantly frictional (rate-independent) to frictional-viscous behaviour.

4.4.1.1 Deformation mechanisms versus microstructures at quasi-steady state



Slow experiments. We have shown above that in the slow experiments (i.e. the experiments performed in the rate-sensitive regime), the attainment of a quasi-steady state strength coincides with the development of a microstructure consisting of isolated sigma clasts embedded in a fine-grained, foliated matrix (see Figure 4.5c and 4.5d). This microstructure is similar to that of natural S-C mylonites developed in natural rocks [White *et al.*, 1980; Lister and Snoke, 1984; Passchier and Trouw, 1996] in that the orientation of the elongated matrix grains defines a mylonitic S-foliation, and the elongate tails of the clasts define a horizontal C-foliation (see Figure 4.5d). The shape fabric of the clasts clearly does not track the finite strain ellipse (since this would be oriented at 1.7° and 0.4° to the shear plane in Figures 4.5c and 4.5d, respectively). This implies that shear deformation was not homogeneously distributed over the clasts and the matrix. The fact that only minor weakening occurred in the slow experiments from 18 mm to 50 mm displacement, while the volume of remnant clasts was reduced by more than a factor 2 (cf. Figures 4.5c and 4.5d) suggests that the matrix, and not the clasts, controlled fault strength. Indeed, in this displacement interval, the relative proportion of matrix increased from 80 to 95%, leading to a factor 1.2 decrease in average matrix strain rate. Since gouge strength at this velocity is known to be roughly proportional to strain rate to the power 0.2 (see Chapter 3), this should have resulted in weakening by a factor 1.04. This is in good agreement with our present data, which show weakening by a factor of 1.10 in the same displacement interval.

Focusing now on the matrix, it was observed that in most places the foliation defined by the matrix also does not track the finite strain ellipse: the foliation was still at $\sim 20^\circ$ to the shear zone boundary at shear strain of 1072 (see Figure 4.5e), rather than the 0.05° of the finite strain ellipse. This shows that within the matrix strain was not accommodated homogeneously, i.e., deformation did not simply involve grain flattening and rotation. In view of the expected relatively low friction coefficient of kaolinite layers, especially in the presence of fluids, deformation might be envisaged to involve passive sliding along through-going foliation planes. However, for this to produce a foliation that is steeper than the orientation of the finite strain ellipse requires overall dilatation of the material (just as compaction would cause further flattening), whereas our data show compaction (cf. Figure 4.2b) during the experiment. It should be noted, however, that the foliation in our

materials is not defined by through-going kaolinite planes, but rather by the long axes of elongate halite grains which are surrounded by an anastomosing network of kaolinite, as depicted schematically in Figure 4.10.

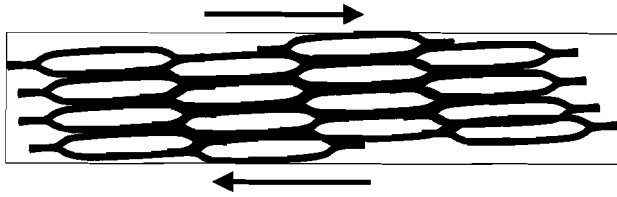


Figure 4.10. Schematic depiction of microstructure of matrix, showing contiguous, anastomosing network of kaolinite layers (black) surrounding halite grains (white).

In this situation, no flat, through-going kaolinite planes are present. Rather, the kaolinite planes form interconnecting sinuous layers, and sliding along kaolinite layers must be accommodated on the grain scale to overcome local irregularities (i.e. the sinuosity of the kaolinite layers). We propose that shear deformation of the matrix involved sliding along kaolinite layers, accommodated locally by pressure solution and/or dilatation. If all sliding is accommodated by pressure solution, the envisaged deformation process is similar to diffusion-controlled sliding along a sinuous surface as modelled by *Raj and Ashby* [1971]. Alternatively, shear can be accommodated by local dilatation, i.e. the halite grains "hopping over" each other. In this case, macroscopic dilatation is expected, but this may be counteracted by concurrent pressure solution compaction. In a general case, sliding may be accommodated by a combination of pressure and dilatation. In this scenario, grain boundary sliding and accommodation of sliding by pressure solution and/or dilatation are serial processes, i.e., the slowest determines the rate of deformation. The observed mechanical behaviour, which showed that shear strength is both normal stress and sliding rate dependent, is consistent with this interpretation: in a situation where pressure solution and frictional grain boundary sliding and dilatation operate at the same time, pressure solution may give rise to the sliding rate dependence, whereas the normal stress dependence is due to sliding and dilatation. Alternatively, the rate-dependence may be due to cataclasis by stress corrosion cracking. However, the fact that no significant grain size reduction took place in the matrix in the shear strain interval 137 to 1072 shows that cataclasis by stress corrosion cracking in the matrix is of little importance. A lower limit for fault strength is attained when accommodation by pressure solution is negligibly easy: in this case the sliding friction of the kaolinite layers will determine fault strength.

Fast experiments. At the high sliding velocity (5 $\mu\text{m/s}$) only minor strain weakening occurred, with quasi-steady state established after ~ 10 mm displacement. The microstructures suggest that at least up to 25% strain the main deformation mechanism was cataclasis. At high strains (Figure 4.7c), a foliation developed, in many respects similar to the low velocity experiments. The fact that the mechanical behaviour was purely frictional, coupled with the absence of weakening compared to the situation at 25% strain suggests that shear deformation involved mainly time-independent, brittle/frictional processes. We propose that shear deformation occurred by sliding along/within kaolinite layers, accommodated mainly by dilatation and cataclasis, and that with increasing foliation development the relative proportion of dilatation vs. cataclasis increased. Also, the subhorizontal lower surface of the sample suggests a component of localized sliding along this surface. Although the microstructure changed significantly with strain, the mechanical behaviour did not. This may be explained by the fact that cataclasis and dilatation both produce frictional, rate-insensitive behaviour.

4.4.1.2 Evolution of mechanical behaviour with increasing strain

As discussed above, only minor strength evolution was observed in the fast experiments, in spite of the fact that, there was significant microstructural evolution in these samples. Moreover, it is known from our previous experiments that sliding at the conditions of the fast experiments is characterized by purely frictional sliding behaviour (cf. Chapter 3).

In contrast, the present slow experiments showed significant strain weakening after the initial stress peak, especially in the first 10 mm displacement. The data for these experiments show a transition with strain from almost purely frictional to strongly rate-dependent (i.e., viscous) behaviour. The microstructures show that around the peak stress deformation must have occurred mainly by cataclasis, which explains the almost purely frictional behaviour observed. After the peak stress, deformation became partitioned between in clay rich shear bands (Figure 4.5b) and a developing oblique "S-foliation". The shear bands are similar to the C'-type shear bands, also termed extensional crenulation cleavage often observed in natural mylonites [Platt and Vissers, 1980; White *et al.*, 1980; Lister and Snoke, 1984; Platt, 1984; Passchier and Trouw, 1996]. The sequence in which the S and C' foliation developed in our "slow" experiments, and the partitioning of strain between them, remains unclear. Our experiments seem to support the idea that these shear bands are associated with strain weakening [Platt and Vissers, 1980; Platt, 1984], but the actual weakening could also have been due to the development of the S-fabric.

Shimamoto and co-workers [Shimamoto, 1986; Shimamoto and Logan, 1986; Shimamoto, 1989] reported microstructures from deformation experiments on pure halite aggregates deformed in the semi-brittle field. These showed aligned trains of statically recrystallized grains forming an S-foliation, transected by discrete faults in the C' orientation. Shimamoto compared these to natural S-C mylonites (notably to the C'-variety) and claimed that natural S-C mylonites may represent late stage localisation and a transition from viscous to frictional behaviour, which he observed in his experiments. Our results are direct contradiction with this interpretation. In our experiments, C'-type shear bands develop during strain weakening and a transition from frictional towards more viscous behaviour. Several explanations for this contradiction can be put forward. The main differences between our experiments and those reported by Shimamoto are that 1) Shimamoto's experiments are in a regime where (limited) dislocation creep is possible, and 2) Shimamoto's experiments were done on dry, clay-free samples. Given the fact that natural C'-type shear bands develop exclusively in phyllosilicate-bearing rocks, it seems that our samples would provide a better analogue for natural materials. However, this remains speculative.

Returning to our own experiments, sliding along the S-foliation can be accommodated either on the grain scale, by dilatation or pressure solution, or on a larger scale, by the formation of sample-scale shear bands. The fact that shear bands were observed during the weakening phase indicates that at this stage accommodation of sliding by shear bands was easier than accommodation by grain scale mechanisms. With progressive displacement, cataclasis and intergranular sliding led to significant grain size reduction and phase mixing, as illustrated in Figure 4.6c. Also, pressure solution led to strong elongation of halite grains, especially in the shear bands (note in this respect the strongly elongate halite grains in the shear band in Figure 4.5b). This allowed formation with progressive strain of the fine-grained, foliated halite/kaolinite matrix. A fine grain size is expected to favour pressure solution creep processes, since these are strongly grain size sensitive. Thus, as soon as an interconnected network of this matrix material had formed, it could start to accommodate a steadily increasing proportion of the sample-scale deformation by a mechanism such as described in the previous section. We propose that with increasing matrix proportion, accommodation of sliding on wavy planes forming the S-foliation by local pressure solution and dilatation became more favourable than the formation of sample-scale shear bands. This explains why the shear bands become less prominent at high strains. Nevertheless, shear bands never totally disappear, which

suggests that even at high strains they may play some role in accommodating sliding along the S-foliation.

In summary, we conclude that in our "slow" experiments the gradual transition in mechanical behaviour from purely frictional behaviour to frictional-viscous behaviour with progressive strain was caused by a progressively decreasing role of cataclasis and an increasing role of pressure solution-accommodated intergranular sliding of halite clasts along kaolinite foliae. In the fast experiments, a similar transition in mechanism took place, but the accommodation of sliding occurred mainly by dilatation, leading to frictional behaviour throughout the experiment.

4.4.2 Implications for natural fault rock

4.4.2.1 Fault weakening and localisation by cataclasis plus solution transfer

Generally, microstructures like tailed porphyroclasts, ribbon grains, grain shape foliations and S-C fabrics are considered indications that crystal plastic deformation and dynamic recrystallization was dominant in the evolution of mylonites, and in bringing about shear localisation. Our experiments show that S-C fabrics can be formed also under conditions where cataclasis and solution transfer are dominant over dislocation creep. The crystallographic preferred orientation patterns, which showed that the crystallographic axes were randomly oriented even in a sample that was deformed to a shear strain of 137, confirm that dislocation creep is unimportant in our experiments. Hence, crystal plastic deformation is not a necessary requirement for the formation of S-C fabrics, in spite of the fact that evidence for crystal plasticity is ubiquitous in natural S-C mylonites. The typical "mylonitic" microstructures we observed did not develop in samples deformed under dry conditions (see Chapter 3), suggesting that solution transfer mechanisms play an important role in their formation (see also *Means and Williams [1972]*).

The present experiments provide an experimental account of a mechanism for the formation of weak fault rocks by a switch in deformation mechanism from frictional behaviour to grain size sensitive diffusional creep following grain size reduction by cataclasis. This mechanism is distinct from the often envisaged scenario of grain size reduction by dynamic recrystallization, and is not subject to the criticisms regarding the possibility of a clear-cut mechanism switch from dislocation creep to diffusion creep and the limitations regarding the amount of weakening possible by such a switch [*Etheridge and Wilkie, 1979; De Bresser et al., 1998; Ter Heege et al., 1999*]. The mechanism presented here is expected to be particularly important around the brittle-ductile transition, where both brittle processes and solution transfer processes are important. It can effectively lead to a shallowing of the brittle-ductile transition in zones of high strain, allowing deformation of the hydrated, fine-grained shear zone by a ductile mechanism whereas the country rock is still in the brittle field, as also proposed by *Stewart et al. [2000]* from field observations on the Great Glen Fault Zone, Scotland. Since diffusional processes will rapidly obliterate microstructural evidence of cataclasis (such as angular grains and microcracks), the cataclastic nature of grain size reduction may not always be apparent in natural rocks. Also, evidence for deformation by pressure solution may be easily overprinted by small amounts of dislocation creep. Hence, microstructures of fault rocks formed by a mechanism of cataclasis, followed by pressure solution creep accompanied by some dislocation creep may be very similar to those of mylonites formed purely by dynamic recrystallization.

4.4.2.2 Microstructure as a rheology indicator

Continuing on the previous point, an important use of microstructural observations in natural rocks is to constrain the operative deformation mechanisms, and thus the rheology of the deformed material [e.g. Schmid and Handy, 1991; Passchier and Trouw, 1996]. Our experiments suggest that this may be much more problematic than frequently thought.

As an example, compare our figure 4.5c and 4.8c. In both Figures, the material consists of rounded, elongate clasts in a fine-grained halite/kaolinite matrix. In general, the microstructures look very similar, although in Figure 4.8c the clasts are more rounded than in Figure 4.5c. Also, the close-ups of the matrix (Figures 4.6a and 4.9) show much similarity. However, the mechanical behaviour displayed by these samples is very different: Figure 4.5c represents material deforming by a strongly strain rate sensitive mechanism, whereas the mechanical behaviour of the material depicted in Figure 4.8c was purely frictional. Thus, very different rheologies are represented by very similar microstructures.

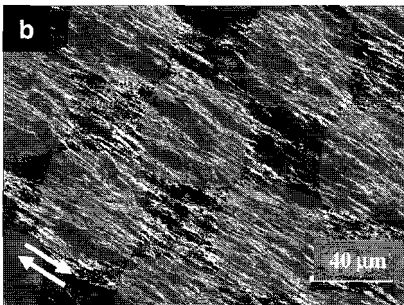
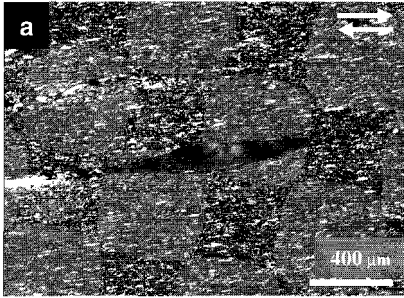


Figure 4.11. Microstructures from mica-rich bands in a shear zone from the Barthelémy massif, French Pyrenees. Shear sense is dextral in both images, and images were taken with crossed polarizers. a) Asymmetric clast in fine-grained, mica-rich matrix b) Fine-grained mixture of mica grains (light) and elongate quartz grains (dark). Note that in Figure 4.11b the shear zone boundary is oblique to the horizontal of the image (see shear sense arrows at bottom left).

Furthermore, compare Figures 4.8b and 4.8c. Although the microstructures are very different, the mechanical behaviour was purely frictional in both cases, and no significant strength change occurred in the strain interval between from Figures 4.8b to 4.8c (cf. Figure 4.2a). As argued above, the mechanism of deformation evolves from behaviour dominated by cataclasis in Figure 4.8a to behaviour dominated probably sliding and dilatation in Figure 4.8c. Both these mechanisms produce frictional behaviour. Thus, very similar macroscopic fault rheologies may be associated with very different internal microstructures.

Lastly, Figure 4.11a and 4.11b show microstructures from mica-rich bands in a natural shear zone from the Barthelémy massif, French Pyrenees. On thin-section scale, this shear zone shows an alternation of mica-rich and essentially mica-free bands. Figure 4.11a shows an asymmetric clast in a fine-grained matrix mica-rich matrix. Figure 4.11b shows a detail of a mica-rich band in the mylonite. Comparing these to our sample microstructures, (in particular comparing Figures 4.11a to 4.6b and Figures 4.11b to 4.6a), the similarity in geometry is striking. In both cases, asymmetric clasts are embedded in a fine-grained, polyphase matrix, which consists of elongate grains separated by an anastomosing network of phyllosilicates. In our samples, deformation occurred by a combination of intergranular sliding, local dilatation, and pressure solution, as argued above. In the natural material, undulatory extinction evidences the operation of dislocation creep. Whether pressure solution and sliding also occurred in these samples is difficult to assess. Evidence for the operation of pressure solution may have been obliterated by concurrent operation of other processes.

In addition, it is impossible to deduce from the microstructure to what extent sliding along mica grains has occurred, since the local finite strain is not known. Our experimental data show that dislocation creep is not a requirement for producing this type of microstructure. Hence, in these natural samples the relative contributions of dislocation creep, intergranular sliding, and pressure solution creep to the total strain and to the rheology of the material are unclear, as is an appropriate rheological description, despite the easily recognized dislocation creep features.

We conclude that, especially in polyphase, phyllosilicate-bearing materials, where mixed deformation processes can occur, the microstructure may not be a very reliable tool for constraining rheology. Also, microstructure can not be used for strain analysis in these materials, because of the large amount of intergranular sliding possibly involved.

4.4.2.3 Implications for crustal strength

A general feature observed in the experiments reported here and in Chapter 3 is that if significant strain is accumulated for microstructural evolution to take place, the strength of the samples approaches the strength of the weakest phase present. The evolution of the strength of a polymineralic aggregate towards the strength of the weaker phase has also been observed in experiments on aplite [Dell' Angelo and Tullis, 1996], orthopyroxene granulite [Ross and Wilks, 1996], calcite/halite mixtures [Price, 1982; Jordan, 1987; Kawamoto and Shimamoto, 1997], halite/anhydrite mixtures [Ross and Bauer, 1992], mica-bearing schists [Shea and Kronenberg, 1993] and many others. In modeling crustal tectonic processes, a strength profile is generally used with brittle behaviour represented by Byerlee's friction law and ductile/plastic behaviour represented by a flow law for pure quartz or feldspar [Goetze and Evans, 1979; Govers and Wortel, 1995; Ranalli, 1997], calibrated in low strain experiments.

However, crustal tectonic processes are for a large part controlled by the behaviour of high strain faults and shear zones (either newly formed or inherited from earlier deformation), which often contain a significant proportion of phyllosilicates. These shear zones are likely to be significantly weaker than predicted using flow laws for monomineralic quartz or feldspar, and also significantly weaker than their undeformed counterparts. Also, by comparison with our experiments, it may very well be that the rheology of phyllosilicate-rich shear zones is both normal stress- and strain rate-sensitive. From the above, we suggest that instead of using a classical brittle-plastic strength profile based on low strain, monomineralic materials, crustal rheology in strongly deformed zones could be modeled by using the strength of the weakest major phase present. This idea has been put forward earlier by Shea and Kronenberg [1992], who also pointed out that around the brittle-ductile transition, the weakest phase will usually be mica. With increasing depth (and hence temperature), quartz will become weaker than mica because the activation energy for creep is higher for quartz than for mica [Mares and Kronenberg, 1993]. One way of taking into account strain weakening would be to allow the rheology in a model to develop, in a realistically prescribed manner, from a quartz rheology to a mica rheology with increasing strain. Admittedly this is a very simplified approach, but it is surely more realistic than the strength envelopes now used, particularly in zones of high strain.

4.5 Conclusions

1. We observed a transition in mechanical behaviour from purely frictional behaviour at low strains to more viscous behaviour at high strains. This transition was caused by the development with progressive strain of a fine-grained halite + kaolinite matrix, which accommodated deformation by a pressure solution-controlled mechanism.
2. Deformation of the halite + kaolinite matrix involved sliding of halite grains along kaolinite layers, accommodated by local pressure solution and dilatation. The combination of frictional sliding along kaolinite layers and pressure solution probably gave rise to the both normal stress and strain rate dependent strength observed.
3. The data suggest a mechanism of weakening and localisation of deformation by grain size reduction due to cataclasis, followed by a transition from brittle behaviour to pressure solution accommodated creep of fault rock.
4. Our microstructures suggest that although microstructural evidence for crystal plasticity may be ubiquitous in natural mylonites, dislocation creep is not a necessary requirement for their development, and the relative contributions of dislocation creep and cataclasis + solution transfer to strain accumulation and fault strength are in general unclear.
5. Although microstructure may be useful as an indication for which deformation processes were active in a rock, using microstructure as rheology gauge is problematic, especially in phyllosilicate-bearing rocks where combined deformation mechanisms occur.
6. Crustal strength in strongly deforming regions may be modelled more realistically by using the strength of the weakest phase present, instead of applying the strength of quartz or feldspar throughout the strength envelope. At the brittle-ductile transition, the weakest phase will usually be mica.

Chapter 5

Fluid-assisted healing processes in gouge-bearing faults.

Submitted to Pure and Applied Geophysics as: B. Bos and C.J. Spiers, Fluid-assisted healing processes in simulated, gouge-bearing faults: Insights from experiments on a rock-analogue material.

Abstract. On the basis of both experimental and field studies, solution transfer processes are expected to be important in contributing to fault strength recovery (healing) under the hydrothermal conditions pertaining in large parts of the seismogenic zone. However, most experimental work on healing effects in faults has been done using quartzo-feldspathic sliding surfaces or fault gouges, under conditions where solution transfer processes are very slow. Mechanisms of fluid-assisted fault healing are accordingly rather poorly understood. We have performed slide-hold-slide fault healing experiments on simulated faults containing brine-saturated granular halite as a fault rock analogue. Halite was used because solution transfer processes are known to be rapid in this system under easily accessible conditions. We studied the effects of hold time duration, shear stress during hold, pre-hold sliding velocity and pore fluid composition on strength evolution. The results show rapid fluid-assisted compaction and stress relaxation during hold periods, and a significant hold time-dependent strengthening upon re-shear. The data show that healing resulted from both a packing density increase and a contact area/strength increase during hold periods. The general type of behaviour observed is similar to that observed in quartzo-feldspathic gouges at room temperature, but important differences were observed as well. Notably, the time-dependence of healing deviates from the log-linear trend observed in gouges where solution transfer processes are absent. This means that if pressure solution is an important healing mechanism in natural faults, applying a log-linear trend will underestimate natural fault healing rates.

5.1. Introduction

From both field studies and experimental work, it is well established that faults show strength recovery (healing) during interseismic periods [Dieterich, 1972; Beeler *et al.*, 1994; Marone *et al.*, 1995; Marone, 1998b]. Fault healing processes are important in determining many aspects of fault behaviour, such as earthquake recurrence and rupture dynamics. Time-dependent fault strengthening forms an essential component of the empirical rate- and state-dependent friction (RSF) laws (see [Marone, 1998b] for review), often used in theoretical models of seismic fault behaviour [e.g. Cao and Aki, 1986; Rice, 1993; Sleep, 1995].

Until recently, fault healing in the laboratory is often studied so-called slide-hold-slide experiments [Beeler and Tullis, 1997]. In such experiments, the simulated fault gouge is typically sheared at a constant rate, reaching a steady state shear stress. Then sliding is halted (the "hold"-period) for a prescribed time. After the hold period, sliding is re-started (re-shear). Fault healing in the laboratory has been studied mostly at room temperature, often under dry conditions. However, increased healing rates observed in experiments performed under hydrothermal conditions [Fredrich and Evans, 1992; Karner *et al.*, 1997; Olsen *et al.*, 1998] suggest that fluid-rock interaction processes are important mechanisms of fault healing under the hydrothermal conditions pertaining in much of the seismogenic zone. Moreover, typical experimentally determined healing rates for dry fault gouge seem to be about an order of magnitude too low to explain the (positive) dependence of seismic stress drop upon earthquake recurrence interval observed for natural faults [Kanamori and Allen, 1986], again suggesting that fluid-assisted mechanisms may play an important role in seismicity [Karner *et al.*, 1997; Olsen *et al.*, 1998]. Apart from a quantitative assessment of the rate of fault healing by fluid-assisted mechanisms, it is important to assess whether the functional form of the strength versus time relation is similar to the logarithmic relation observed in dry experiments and implicit in the rate- and state-dependent friction laws, since this is important in controlling theoretical models.

Using the first law of thermodynamics, a general expression for the energy balance in a volume of fault zone during deformation can be written

$$\tau\dot{\gamma} + \sigma_n\dot{\epsilon} = \int_V \sum_m \dot{\Delta}_m dV \quad (5.1)$$

where τ is shear stress on the fault, $\dot{\gamma}$ is shear strain rate, σ_n is the normal stress on the fault (compression positive), $\dot{\epsilon}$ is the normal strain rate (compaction positive), V is the volume and $\dot{\Delta}_m$ denotes the specific energy dissipation rate by process m . The right-hand side of (5.1) thus represents the sum of the energy dissipation rates by all microscale processes operating in a unit volume of fault zone. These processes include grain fracture and frictional sliding of grain contacts, but also processes such as pressure solution and crystal plasticity. Note that energy terms related to increase in internal energy due to increased surface area, for example, are neglected. Rewriting (5.1) in terms of the shear stress τ (which is the quantity measured in experiments) and expressing strain in incremental terms yields

$$\tau = \tau_x - \frac{d\epsilon}{d\gamma} \sigma_n \quad (5.2)$$

where τ_x is defined

$$\tau_x = \int_V \sum_m \frac{d\Delta_m}{d\gamma} dV. \quad (5.3)$$

From (5.2), strength recovery along a gouge-bearing fault may occur for two basic reasons. On the one hand, gouge compaction during no-slip periods can lead to strengthening because the increased packing density requires dilatancy upon re-shear, and hence work against normal stress as described by the second term of (5.2). On the other hand, strengthening may occur via an increase in contact area and/or contact bonding between particles in the gouge, hence increasing the average contact strength (fracture strength, frictional strength, plastic yield strength or the resistance to deformation by pressure solution or other mechanisms) in the gouge. In general, the observed fault healing will reflect a combination of these two contributions.

Currently envisaged fault healing phenomena are summarized schematically in Figure 5.1. The best studied is the healing effect observed in at room temperature often termed "Dieterich healing", first described by *Dieterich* [1972]. In this case, shear stress is characteristically observed to increase linearly with the logarithm of hold time, with healing rates (defined as the increase in friction coefficient per decade of hold time) typically of the order of 0.009-0.05, and the displacement required to re-establish steady state friction (termed D_c) of the order of 10-100 μm [*Dieterich*, 1972; *Beeler et al.*, 1994; *Marone*, 1998a]. The microscopic and/or contact-scale mechanisms causing Dieterich healing are not well understood. However, the fact that

Name	Driving force	Characteristics
1. "Dieterich"-healing	??	- $D_c=10-100 \mu\text{m}$ - Strength increases linearly with $\log(t)$
2. Pressure solution	Effective normal stress at contact	- t-dependent - T-dependent - Compaction - Stress relaxation during hold
3. Neck growth	Interfacial energy reduction	- t-dependent - T-dependent - No compaction, no stress relaxation
4. Precipitation/cementation	Solute supersaturation in advecting pore fluid	- can occur at $\sigma_n=0$

Figure 5.1. Schematic summary of fault healing phenomena. D_c is the characteristic displacement required to re-establish steady state strength, t is time, T is temperature.

Dieterich healing requires the presence of a humid atmosphere [Dieterich and Conrad, 1984] implies that healing is caused by some kind of water-assisted process.

The other processes represented in Figure 5.1 require the presence of a pore fluid phase for diffusional material transport. Pressure solution [Raj, 1982; Rutter, 1983; Lehner and Bataille, 1984/85; Spiers and Schutjens, 1990], which involves fluid phase diffusional transport of material from stressed grain contacts to pore walls, is expected to cause both compaction and contact area increase, and possibly also an increase in contact bonding, depending on the evolution of the grain contact structure with time [Hickman and Evans, 1992; Schutjens and Spiers, 1999]. Since pressure solution is a deformation mechanism, it is expected to allow shear stress relaxation during periods of no slip. The driving force for this process is essentially mechanical: pressure solution is driven by solubility gradients related to gradients in effective normal stress between grain contacts and pore walls. In contrast, neck growth [Hickman and Evans, 1992; De Meer and Spiers, 1999] is driven by gradients in solubility between pore walls and contact margins caused by surface curvature gradients, leading to cementation of grain contacts in a manner similar to crack healing [Smith and Evans, 1984]. Neck growth is not a deformation mechanism, and hence no significant stress relaxation or gouge compaction is expected when this mechanism dominates healing. Nonetheless, strengthening is expected to occur due to increasing contact area and evolving grain contact structure. Note that pressure solution and neck growth are mutually exclusive processes, which dominate under different conditions [De Meer and Spiers, 1999; Visser, 1999]. Their relative importance is determined by the relative magnitudes of their driving force (contact normal stress vs. surface energy gradients) and of the corresponding kinetic coefficients governing mass transport (e.g. grain boundary diffusion vs. pore fluid diffusion coefficients). Finally, healing has been inferred to occur by cementation through authigenic mineral precipitation at grain contacts. In general, the precipitating minerals may originate from advecting supersaturated pore fluids, as well as from local mineral transformations. This process is essentially driven by pore fluid

supersaturation, but may be promoted by the presence of deviatoric stress, as reported by *Olsen et al.* [1998].

To date, in modelling fault behaviour the RSF laws based on Dieterich healing are mostly used. However, since the microscale mechanism controlling Dieterich healing are not well understood, it is unclear whether the same process will determine the behaviour of faults under natural conditions, or if other healing processes will dominate. To date, experimental work on fluid-assisted fault strength recovery is limited, and the microscale mechanisms are too poorly understood for reliable extrapolation to natural conditions. Laboratory investigation of solution transfer processes in natural materials is difficult because of the extremely low rates. Increasing the rates by increasing temperature is of limited help because of the low activation energy (e.g. 20 kJ/mole if diffusion is rate controlling, see *Nakashima* [1995]) of these processes compared with solid state processes. Accordingly, increasing temperature will generally increase in the contribution of dislocation creep processes to the observed behaviour, inhibiting the study of the effect of fluid-assisted processes alone. To avoid these problems, fluid-assisted deformation processes have often been studied using rock analogue materials with high solubility and rapid interface reaction and diffusion kinetics [*Pharr and Ashby*, 1983; *Gratier*, 1993; *Spiers and Brzesowsky*, 1993; *Hickman and Evans*, 1995]. Using this methodology, the elementary processes of neck growth and pressure solution have been studied, but their effect on fault strength is largely unexplored.

The present study attempts to investigate the mechanisms of fluid-assisted fault healing and transient friction effects in a rock analogue system where fluid-rock interaction processes are extremely rapid. The system used in this study is halite + brine. The mechanisms and rates of solution transfer processes in halite are relatively well constrained [*Spiers et al.*, 1990; *Hickman and Evans*, 1995], making it an attractive candidate for the study of basic mechanistic aspects of fluid-assisted fault healing. We aim to characterize healing behaviour and identify the microscale mechanisms responsible for the observed behaviour. Also, the observed behaviour will be compared to the behaviour generally observed in quartzo-feldspathic gouges at room temperature and described by the RSF laws, to assess their applicability in systems and under conditions where solution transfer processes are rapid.

5.2 Experimental method

5.2.1 Apparatus and sample assembly

We performed a series of so-called slide-hold-slide experiments on simulated faults containing halite gouge. The experiments were conducted at room temperature and atmospheric pore fluid pressure (drained conditions) using a rotary shear apparatus illustrated schematically in Figure 5.2 and described more fully in Chapter 3. The annular sample assembly consists of two roughened stainless steel "wall rock" rings 10 cm in outer diameter and 1 cm in width, sandwiching a 1 mm thick layer of synthetic gouge. The sample assembly is sealed by means of a pair of inner and outer stainless steel sealing rings, fitted with O-rings. Two diametrically mounted tubes in the outer sealing ring allowed evacuation of the sample and addition of pore fluid. O-ring friction was measured in sliding experiments performed with water trapped between the wall rock rings, and found to be lower than 0.005 MPa at 2.5 MPa fluid pressure. The wallrock rings are gripped between two cylindrical forcing blocks. The lower of these is rotated at controlled angular velocity by a motor plus gearbox, while the upper block is maintained stationary, thus shearing the fault. Normal stress is applied and servo-controlled to within 0.01 MPa using an Instron 1362 loading frame and is measured using a 100 kN Instron load cell. The shear stress is measured using two force gauges mounted in a torque couple which provides the reaction needed to hold the upper forcing block stationary (resolution ~ 5 kPa). The resulting resolution in friction coefficient is 0.002.

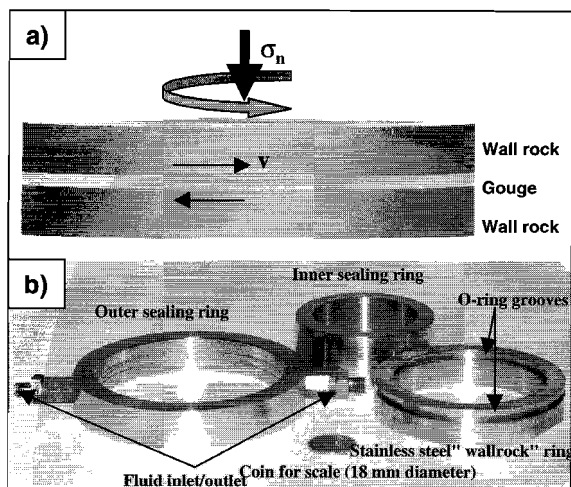


Figure 5.2. a) Schematic diagram of the ring-shear configuration used in this study. Granular fault gouge is sheared between annular stainless steel wall rock rings at controlled velocity v and normal stress σ_n . b) Photograph of the wall-rock rings and the sealing rings. See Chapter 3 for further details of the apparatus.

5.2.2 Experimental procedure

Prior to beginning individual shearing experiments, the granular gouge samples were pre-compacted under vacuum for ~5 minutes at 2.5 MPa normal stress, in order to ensure a reproducible starting microstructure. The samples were then flooded with the appropriate pore fluid, and the desired sliding velocity and normal stress were applied. All experiments are listed in Table 5.1, with the order of the various slide/hold steps performed. During sliding, the sliding velocity was 2 $\mu\text{m/s}$ in all experiments, except in experiment Heal4 (in which the effect of varying sliding velocity was explored). The normal stress imposed during sliding was 2.5 MPa in all experiments. The effect of hold time on fault strength was investigated by performing slide-hold-slide tests with hold periods of 60, 600 and 6000 seconds. Between hold steps, samples were slid for at least 2 mm. In several experiments, hold steps were repeated to constrain the effect of total strain on healing.

In order to investigate whether healing was related to time- or to slip-dependent effects [see e.g. *Beeler et al.*, 1994], the effect of shear creep during hold was examined. In experiments Heal1, Heal3 and Heal4 the hold steps were started by simply switching off the shear drive motor, allowing shear stress relaxation. In this case, elastic strain in the sample and the deformation apparatus is taken up by shear creep of the gouge. In contrast, in experiment Heal2, shear stress was rapidly reduced to zero by reversing the shear drive motor, so the sample was subjected only to normal stress during healing. In this way, no shear creep could occur during the hold period. These experiments are termed "zero shear stress" in this paper.

The effect of pore fluid chemistry on healing was investigated by performing one experiment (Heal3) using decane as pore fluid instead of brine. For this experiment, the halite gouge was dried for 24 hours at 100°C, and the sample was assembled in a dry room (relative humidity ~15%). However, the presence of trace amounts of adsorbed water on the (strongly hygroscopic) halite cannot be excluded.

Displacement normal to the fault surface (i.e. gouge compaction/dilatation) is measured using a Linear Variable Differential Transformer (LVDT, 1 mm full scale, 0.01% resolution) located inside the upper forcing block. Angular and hence linear fault displacement is measured using a potentiometer geared to the rotation of the lower forcing block.

As already mentioned, the experiments were performed using sieved synthetic granular halite (supplied by Merck) as simulated fault gouge. Samples were prepared at ambient humidity. The grain size distribution of the halite was determined using a Malvern particle sizer. This showed the median grain size to be 104 μm , with 90% of the grains in the range 57-110 μm . For pore fluid, we used either brine, which was pre-saturated with respect to the starting material, or decane, which is inert with respect to halite

Experiment	Gouge composition + pore fluid	Normal stress (MPa)	Sliding velocity ($\mu\text{m/s}$)	Hold times (s)	Shear stress during hold
Heal1	NaCl + brine	2.5	2	60 600 6000 600	allowed to relax
Heal2	NaCl + brine	2.5	2	60 600 6000 600	reduced to zero
Heal3	NaCl + decane	2.5	2	60 600 6000 600	allowed to relax
Heal4	NaCl + brine	2.5	2, 0.5, 2, 6, 2, 8, 2, 12, 2, 0.2	600	allowed to relax

Table 5.1. List of experiments and conditions

Finally, the effect of sliding velocity on healing after shear stress relaxation was investigated in experiment Heal4. Sliding velocity was stepped in the order 2, 0.5, 2, 6, 2, 12, 2, 8, 2, 0.2 $\mu\text{m/s}$. At each velocity, a hold step of 600 seconds duration was performed.

After the experiments, samples were flushed with hexane while still sealed to remove the brine from the pore space. The samples were then carefully removed from the forcing blocks and pieces were impregnated with blue-stained epoxy resin to allow sectioning. Subsequently, standard thin sections were prepared.

5.3 Results

5.3.1 General

Figure 5.3 shows shear stress and compaction data obtained in our experiments. Figure 5.3a shows results of experiment Heal1, in which shear stress was allowed to relax during hold periods, whereas Figure 5.3b shows results of experiment Heal2 in which shear stress was reduced to zero during at the start of the hold period. Figure 5.3c shows results of the relaxation experiment performed using decane as pore fluid (Heal3). Finally, Figure 5.3d shows experiment Heal4, in which the effect of varying sliding velocity was investigated.

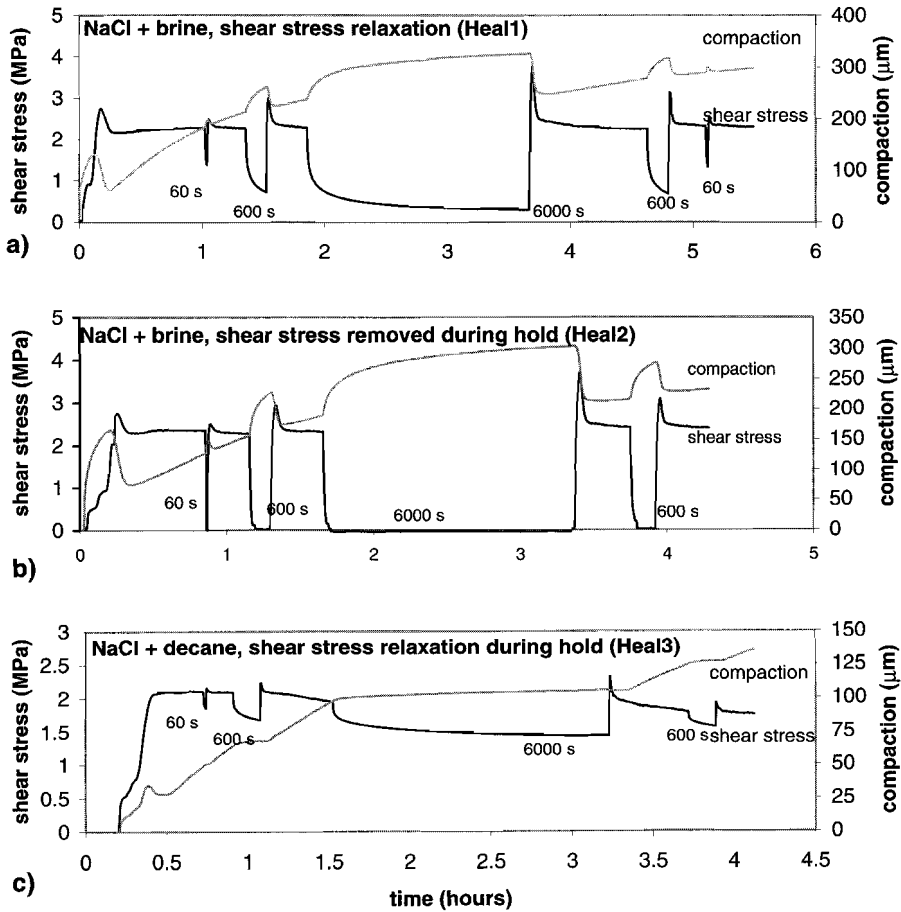


Figure 5.3. Plots of shear stress (black lines) and compaction (gray lines) versus time (5.3a,b,c) or displacement (5.3d, next page). Hold times and sliding velocities as indicated, in $\mu\text{m/s}$.

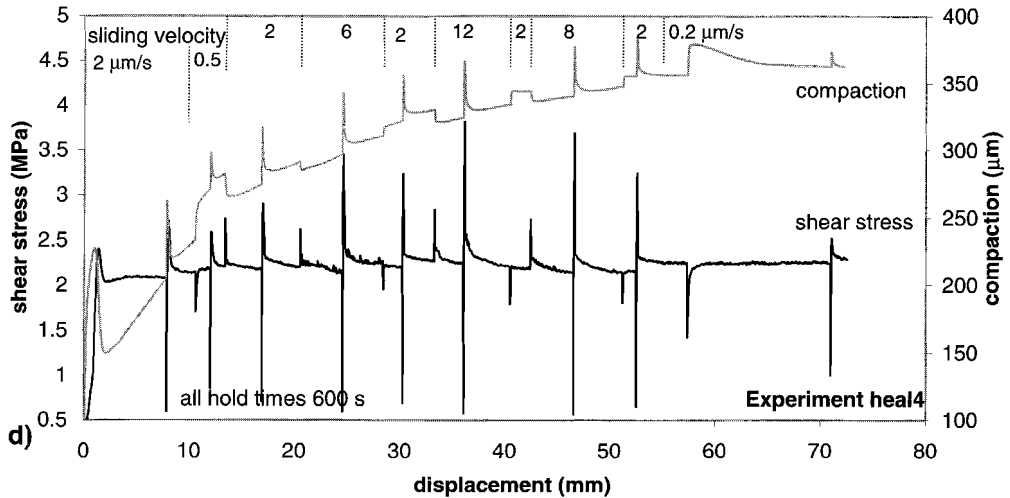


Figure 5.3 (continued)

The brine-saturated experiments (Heal1, Heal2 and Heal4) showed initial loading towards a stress peak, beyond which the shear stress gradually decreased to a roughly steady state value. The initial loading was accompanied by rapid compaction, followed by a period of dilatation around the stress peak. Upon reaching a steady state shear stress level, compaction had resumed. No significant dependence of steady state shear stress on gouge porosity was observed, even though the porosity reduction occurring during the experiments was quite high (up to 20%). In the experiments where shear stress was allowed to relax during hold periods (Heal1 and Heal4), rapid shear stress relaxation was indeed observed. Also, all brine-saturated experiments showed significantly increased compaction rates during hold periods. Upon re-shear, brine-saturated experiments showed a rapid increase in shear stress reaching a peak strength which systematically increased with hold time. Beyond each strength peak friction gradually decayed towards the original steady state value. Re-shear was in all cases accompanied by sharp dilatation, with compaction resuming as soon as steady state strength was reached. Note that in all brine saturated experiments, not all of the porosity that was lost during the hold period was recovered upon re-shear. Instead,

gouge porosity generally returned to the background compaction trend observed in the sliding portions of the experiments, rather than to the porosity at which the hold period started.

In the experiment using decane as pore fluid (experiment Heal3), the shear stress increased at the start of the experiment, then reaching a steady state level without a stress peak. During the hold periods, some stress relaxation was observed, though the amount of relaxation for a given hold time was much lower than in the brine-saturated samples. Upon re-shear, a stress peak and subsequent decay to steady state was observed, as in the brine-saturated experiments, but the stress peaks were much lower. In contrast to the brine-saturated experiments, only minor compaction was observed during the hold periods. Moreover, the compaction rate was much lower during the hold periods than during steady sliding.

Figure 5.3d shows shear stress and compaction as a function of displacement for the velocity stepping experiment (Heal4). The magnitudes of the stress peaks occurring after hold periods, as well as the amount of compaction and stress relaxation during the hold periods increased with increasing pre-hold sliding velocity. In general, the steady state shear stress curves did not have a smooth appearance, but instead tended to be "noisy" in appearance. The amplitude of this noise was

sliding velocity-dependent, increasing from 0.008 at a sliding velocity of 0.2 $\mu\text{m/s}$ to 0.024 at 6 $\mu\text{m/s}$, and decreasing again for higher sliding velocities.

Details of the velocity steps are shown in Figures 5.4, for velocity stepping from 2 to 8 $\mu\text{m/s}$ and back (Figures 5.4a and 5.4b) and from 0.5 to 2 $\mu\text{m/s}$ and back (Figures 5.4c and 5.4d). Stepping up in velocity was followed by a friction peak and significant dilatation, stepping down in velocity was followed by a friction drop and significant compaction. Note that the response upon stepping is not symmetrical, i.e. stepping up in velocity consistently produced a higher direct effect on friction of a than stepping down the same amount. In the case of stepping up in velocity, we calculated τ_x using equation (5.2). Stepping from 2 to 8 $\mu\text{m/s}$, τ_x first slightly increased and then dropped suddenly to a value below the steady state strength. Similar behaviour was observed when stepping from 2 to 12 $\mu\text{m/s}$ (not shown). Stepping from 0.5 to 2 $\mu\text{m/s}$ also produced an increase in τ_x followed by a stress drop, but here the value of τ_x did not fall below the steady state strength.

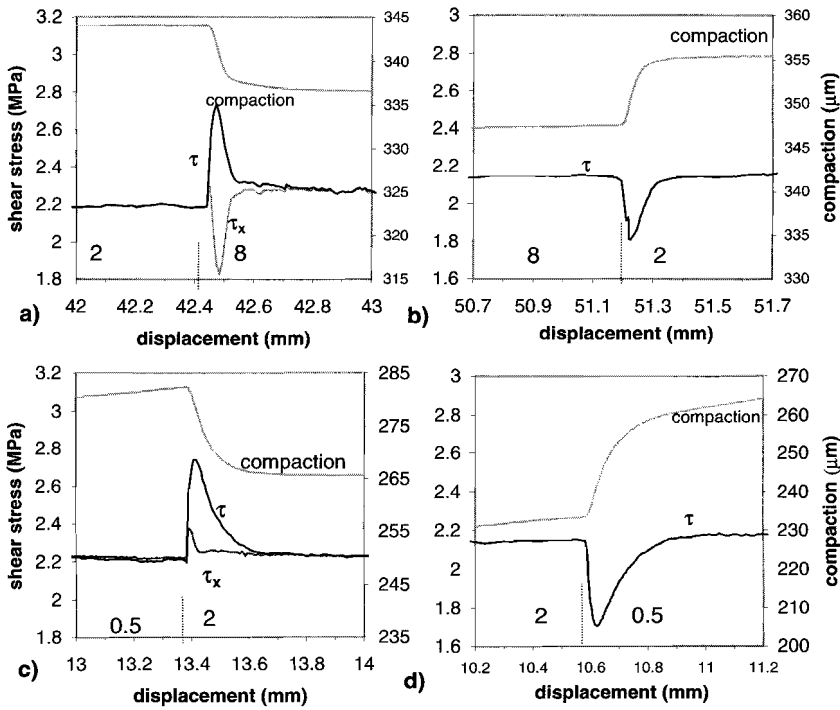


Figure 5.4. Plots of behaviour during velocity steps, showing shear stress τ , τ_x and compaction versus displacement. Sliding velocities as indicated, in $\mu\text{m/s}$.

The volumetric strain effects observed upon stepping the velocity in experiment Heal4 were only minor effects superimposed on a long term compaction trend (Figure 5.3d). No unique relation between sliding velocity and gouge porosity was observed. As in experiments Heal1 and Heal2, the long term compaction did not have a significant influence on frictional strength.

5.3.2 Stress relaxation behaviour

Figure 5.5 shows various parameters characterizing the hold periods of the relaxation experiments. The relaxation of shear stress with time is shown in Figure 5.5a, for the various hold periods employed in the experiments performed with brine and with decane as pore fluid. In the brine-saturated sample, shear stress relaxed roughly logarithmically with time. During relaxation, significant shear creep and gouge compaction occurred, as shown in Figures 5.5b and 5.5c, respectively. During a single hold period, the absolute magnitudes of fault normal displacement and shear displacement were roughly equal.

In samples saturated with decane, minor stress relaxation was observed (Figure 5.5a), but the rates were and order of magnitude lower than in the brine-saturated experiment. The amount of compaction and shear creep observed in the decane-saturated experiment were also roughly one order of magnitude lower than in the brine-saturated samples.

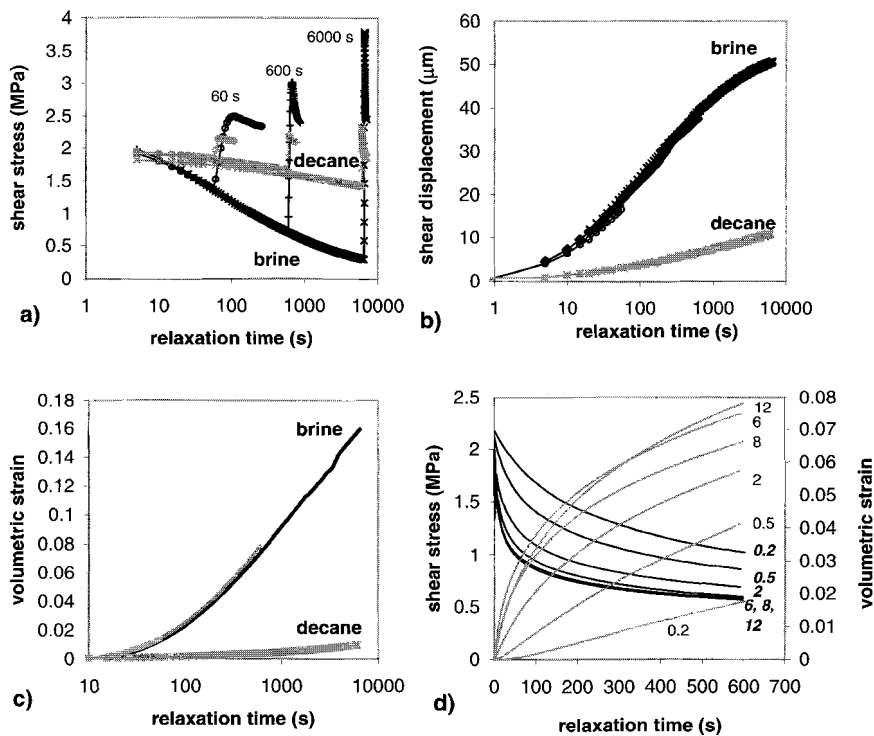


Figure 5.5. Parameters during relaxation, for both brine-saturated and decane-saturated samples. a) Shear stress vs. relaxation time. Hold times as indicated. For clarity, the start of the re-shear periods are also shown. b) Shear displacement versus relaxation time. c) Compaction strain versus relaxation time. d) Shear stress and compaction strain versus relaxation time, for various pre-hold sliding velocities. Sliding velocities as indicated, in $\mu\text{m/s}$.

Figure 5.5d shows stress relaxation and volumetric strain behaviour observed during hold periods following sliding at different velocities (experiment Heal4). Recall that in the steady sliding portions, dilatation was observed upon stepping up in velocity (Figures 5.4), but these were

deviations superposed on a general compaction trend. Nevertheless, as shown in Figure 5.5d both the stress relaxation rate and the compaction rate increased with increasing previous sliding velocity, the effect being largest at lower velocities (0.2-2 $\mu\text{m/s}$) and times and diminishing towards higher velocities (Figure 5.5d).

5.3.3 Re-shear behaviour

Detailed data of experiment Heal1 obtained in the re-shear periods are shown in Figure 5.6a, for different hold times. Apart from measured shear stress, data are also shown of $-\text{d}\epsilon/\text{d}\gamma$ (i.e. the dilatation per unit shear strain) τ_x as calculated using equation (5.1). The shear stress vs. displacement curves show a steep increase with displacement, after which the rate of strengthening decelerated until a friction peak was reached. Beyond this peak, shear strength decayed towards a steady state value over a characteristic displacement interval D_c . Both the peak stress height and D_c increased with increasing hold time. The dilatation rate $-\text{d}\epsilon/\text{d}\gamma$ similarly showed a peak, the height of which increased with increasing hold time. Note that the peak in measured shear stress consistently preceded the peak in dilatation rate. The peak in τ_x in turn preceded the peak in measured friction.

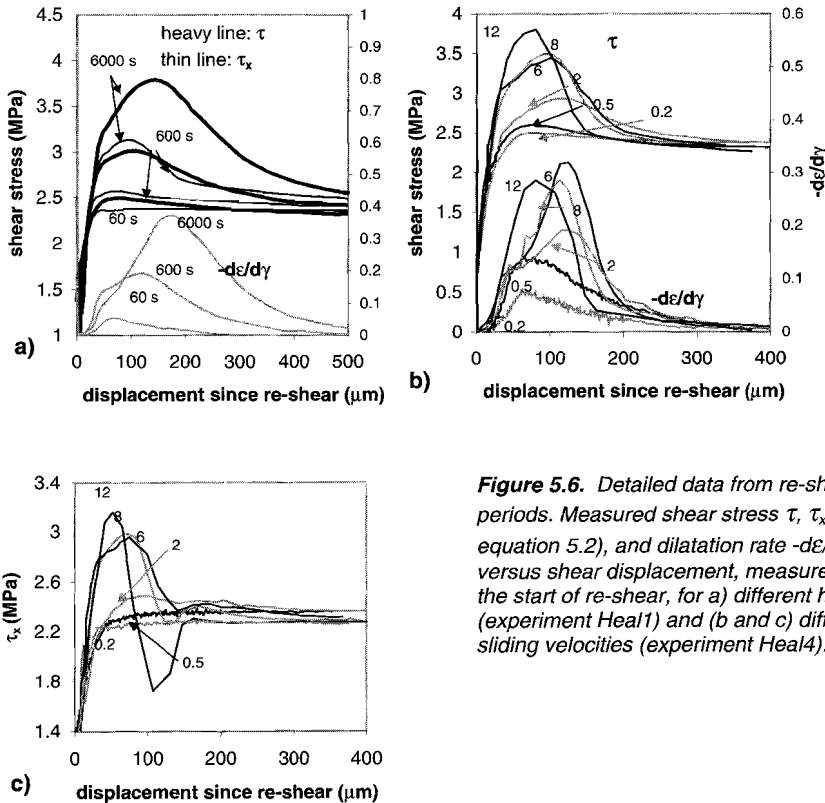


Figure 5.6. Detailed data from re-shear periods. Measured shear stress τ , τ_x (see equation 5.2), and dilatation rate $-\text{d}\epsilon/\text{d}\gamma$ versus shear displacement, measured since the start of re-shear, for a) different hold times (experiment Heal1) and (b and c) different sliding velocities (experiment Heal4).

In Figure 5.6b, shear stress and $-\text{d}\epsilon/\text{d}\gamma$ are shown as a function of displacement for different sliding velocities. The height of the peak stress increased with increasing sliding velocity. The amount of displacement preceding the shear stress peak, as well as the characteristic displacement,

decreased with increasing sliding velocity. Figure 5.6c shows τ_x versus displacement at different sliding velocities. At high sliding velocities (8 and 12.8 $\mu\text{m/s}$), τ_x friction first increased, and then dropped rapidly to a value below the subsequent steady state value. After this τ_x rose more gradually towards the steady state level. At lower sliding velocities, friction gradually decayed towards the steady state value after the friction peak, without dropping below the steady state value first. At the lower velocities (0.5 and 0.2 $\mu\text{m/s}$), no clear peak in τ_x was observed.

From each re-shearing step performed, we determined the friction increase $\Delta\mu$, defined as the difference between the peak shear stress and the previously resolved steady state sliding stress normalized by the normal stress, as well as the peak dilatation rate $(-d\epsilon/d\gamma)_{\text{max}}$. In addition, we calculated $\Delta\mu_x$, defined similar to $\Delta\mu$ but using τ_x instead of the measured shear stress τ . These parameters are plotted versus the logarithm of preceding hold time in Figures 5.7a-c. In the brine-saturated samples, $\Delta\mu$ increased strongly with hold time. The healing rate was about the same in all brine-saturated samples, although the increase in μ for a given hold time was slightly higher in relaxation experiments than in the zero shear stress experiment. In decane-saturated samples, the healing rate was about an order of magnitude lower than in the brine-saturated samples.

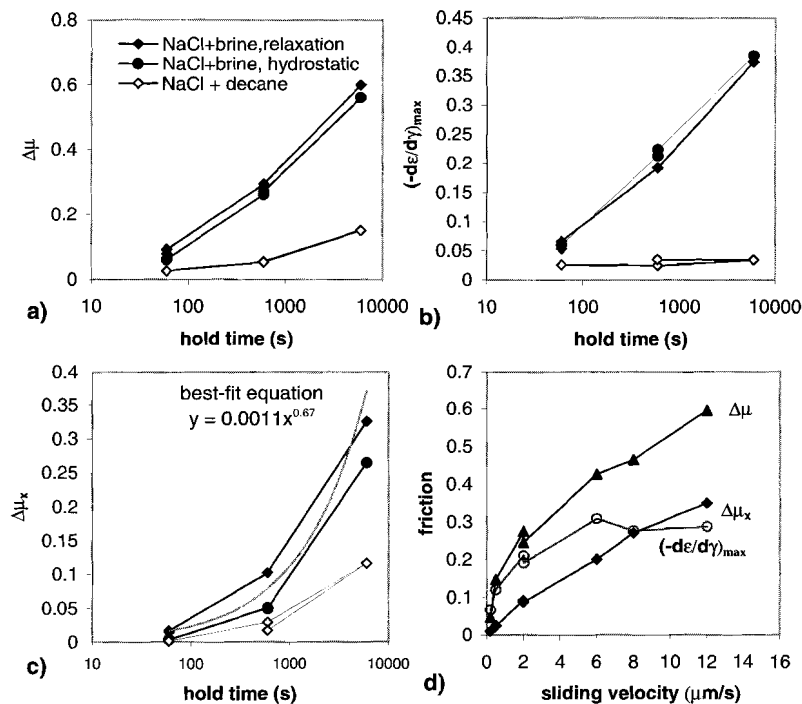


Figure 5.7. Normalised shear stress increase $\Delta\mu$ (a) $\Delta\mu_x$ (b) and peak dilatation rate (c) versus hold time, for experiments Heal1, Heal2 and Heal3. The gray line in Figure 5.7b indicates a best fit line through the data. The line shows healing increases with $t^{2/3}$, although the fit to our data is poor. d) $\Delta\mu$, $\Delta\mu_x$ and peak dilatation rate versus sliding velocity.

As shown in Figure 5.7b, $(-d\epsilon/d\gamma)_{\text{max}}$ increased with hold time for the brine-saturated samples, but no increase with hold time was observed in the decane-saturated samples. From Figure 5.7c it is clear that for both brine-saturated and decane-saturated samples $\Delta\mu_x$ increased in a

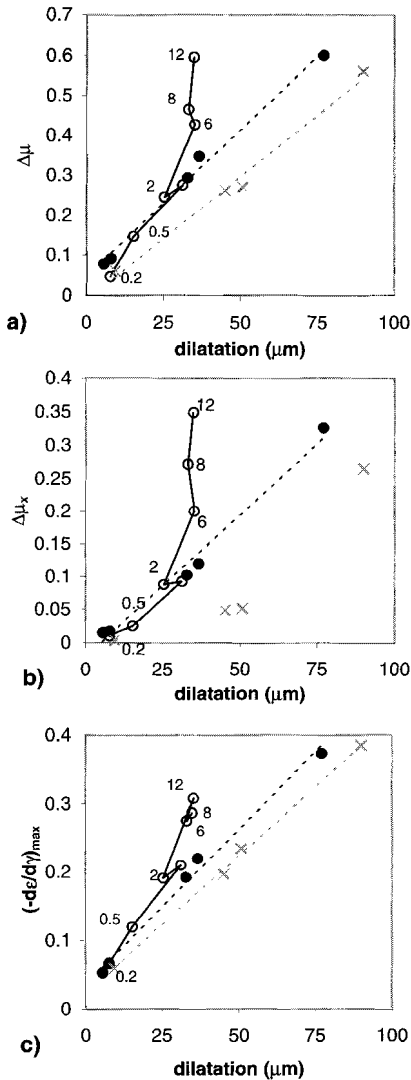


Figure 5.8. $\Delta\mu$ (5.8a), $\Delta\mu_x$ (5.8b), and peak dilatation rate (5.8c) plotted versus total dilatation upon re-shear, i.e. versus the portion of compaction during heal that was recovered upon re-shear. Data are shown for relaxation experiments (circles) as well as for zero shear stress experiments (crosses). Data from experiment Heal4 at different sliding velocities are shown as open circles, with sliding velocity indicated, in $\mu\text{m/s}$. Dotted lines indicate log-linear best-fit relations.

strongly non-linear way with the logarithm of time. As shown by the gray best-fit curve, $\Delta\mu$ increases linearly with $t^{2/3}$, although the fit to our data is poor. For decane-saturated samples, the hold time-dependence of $\Delta\mu_x$ was much lower than for brine-saturated samples. The effect of sliding velocity on healing in our experiments is shown in Figure 5.7d, which shows $\Delta\mu$, $\Delta\mu_x$ and $(-d\varepsilon/d\gamma)_{\text{max}}$ as a function of sliding velocity, after 600 s hold time. Both $\Delta\mu$ and $\Delta\mu_x$ increased strongly with increasing sliding velocity. In contrast, while $(-d\varepsilon/d\gamma)_{\text{max}}$ increased rapidly in the range 0.2-0.5 $\mu\text{m/s}$, it increased only slightly with velocity for sliding velocities higher than 0.5 $\mu\text{m/s}$.

In conclusion to presenting data on re-shearing behaviour, we consider how the peak stresses and peak $d\varepsilon/d\gamma$ may be related to total volume changes upon re-shear. Figure 5.8 thus plots $\Delta\mu$, $\Delta\mu_x$ and $(-d\varepsilon/d\gamma)_{\text{max}}$ as a function of the total dilatation occurring upon re-shear (i.e. the portion of the porosity loss during hold periods that was restored upon re-shear). Data are shown for experiments in which shear stress was removed prior to hold periods (crosses) as well as for experiments in which shear stress was allowed to relax (circles). The data from the experiment at different sliding velocities are shown as open circles, with sliding velocities indicated. The data show a good correlation between shear stress and volume change at velocities of 2 $\mu\text{m/s}$ and lower. Data from higher sliding velocities plot significantly higher than the trend. The data obtained from experiments where shear stress was removed during hold show a lower peak τ , τ_x and $-d\varepsilon/d\gamma$ for a given amount of volume change.

5.3.4 Microstructural observations

Figure 5.9a shows a transmitted light micrograph of a gouge layer after an experiment. Along strike, R₁ Riedel (R) shears surrounded by more porous zones (a), alternate with areas of much lower porosity (d). No through-going Y-shears were observed. A detail of the gouge is shown in Figure 5.9b. Note the low porosity, and evidence for pressure solution in the form of grain-to-grain indentations (i) and grain truncations (t).

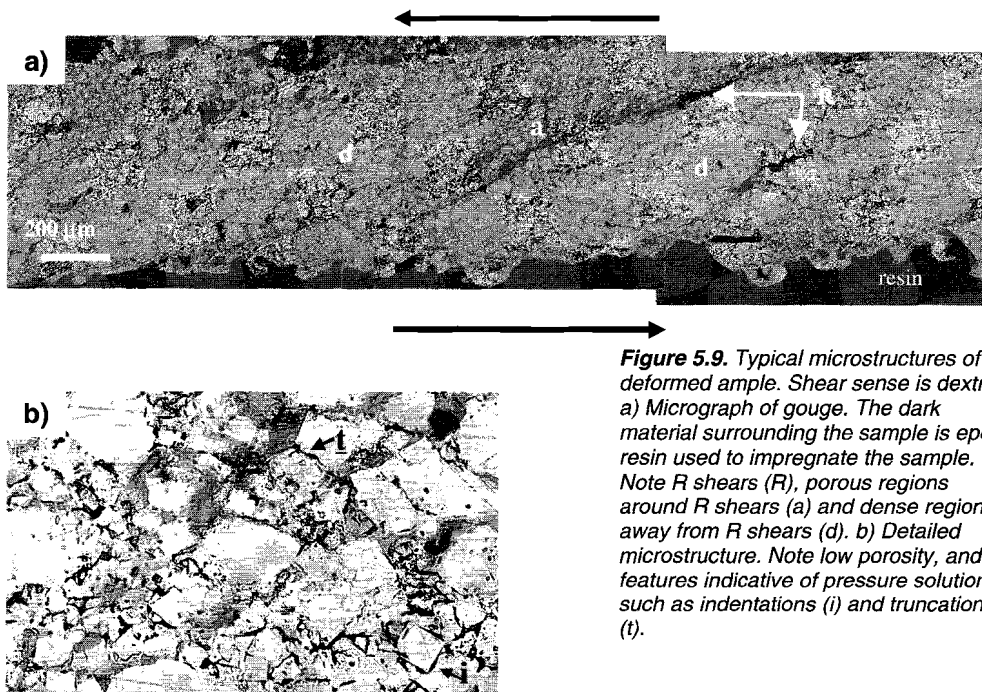


Figure 5.9. Typical microstructures of deformed sample. Shear sense is dextral. a) Micrograph of gouge. The dark material surrounding the sample is epoxy resin used to impregnate the sample. Note R shears (R), porous regions around R shears (a) and dense regions away from R shears (d). b) Detailed microstructure. Note low porosity, and features indicative of pressure solution such as indentations (i) and truncations (t).

5.4. Discussion

5.4.1 Mechanisms leading to observed behaviour

5.4.1.1 Mechanisms during steady state sliding

The microstructures suggests that, in accordance with previous experiments on granular halite under similar conditions (see Chapter 2 of this thesis), shear deformation of wet granular halite under the conditions of our experiments occurred by gouge faulting along R shears, accommodated by distributed cataclasis in the regions between the R shears. This implies that at any instant in time, only a limited part of the fault gouge is active in accommodating fault slip, namely the active R shears and their immediate surroundings. The compaction observed in the experiments could have been caused by cataclasis (at higher porosities) and/or by pressure solution. Both the very low porosities observed, in particular in the regions away from the R shears (see Figure 5.9a), and the observation that brine-saturated samples showed much more compaction than decane-saturated samples suggest that a significant portion of the compaction was due to pressure solution.

During steady sliding the measured friction was insensitive to gouge porosity, even though the total porosity reduction during the sliding parts of experiments was more than 20%. This may seem surprising, since decreasing porosity amounts to increasing the average contact area in the gouge. However, the measured compaction data involve the entire gouge, whereas, as argued above, only a small part of the gouge is active in shear at any moment. It seems likely that fault strength will be controlled by the average contact strength in these active zones. We propose that during

shear the total amount of porosity in the active zones (instead of total gouge porosity) is roughly constant. This can be accomplished due to the balancing effects of time-dependent compaction and shear-induced dilatation in a single active zone, as well as by an increasing number of R shears with displacement. This is consistent with the compaction behaviour upon velocity steps: upon increasing velocity (and hence increasing the rate of dilatation with respect to compaction), transient dilatation was observed, whereas decreasing sliding velocity lead to increased compaction (see Figure 5.5). The observation that total porosity continuously decreased during slip is then attributed to on-going compaction of the inactive zones of the gouge.

5.4.1.2 Mechanisms during hold periods

Upon halting sliding, significant compaction creep was observed all brine-saturated samples. In addition, shear creep was observed in the relaxation experiments. This time-dependent deformation could have involved crystal plasticity, stress corrosion cracking or pressure solution. The observation that the creep rates of the brine-saturated samples were an order of magnitude higher than those of the decane-saturated sample suggests that the creep effects in the brine-saturated samples were principally caused by a fluid-assisted deformation mechanism, with only a minor role played by crystal plasticity. Moreover, our microstructural observations show grain interpenetrations and zones of very low porosity, indicative of pressure solution compaction. On this basis, we infer that stress relaxation in our experiments occurred mostly by pressure solution-controlled deviatoric compaction creep of gouge, with possibly also a role played by stress corrosion cracking. This is consistent with previous work on granular halite, which shows rapid pressure solution compaction under the conditions of our experiments [Raj, 1982; Spiers *et al.*, 1990]. Our data further suggest that fluid-assisted neck growth is of minor or no importance, since this process would inhibit compaction and stress relaxation by pressure solution. The stress relaxation observed in the decane-saturated sample may be due to local plasticity at highly stressed grain contacts. Alternatively, the effect may be due to trace amounts of water adsorbed on the halite grains or present in the decane.

As shown in Figure 5.5d, the total amount compaction during hold periods was higher for higher sliding velocities. As argued above, the porosity in the actively deforming zones is determined by the contributions of time-dependent compaction and slip-dependent dilatation. Hence, at higher velocities the porosity is expected to be higher. Since the rate of pressure solution compaction is strongly dependent on porosity, we believe the variation in hold time compaction rate pre-hold sliding velocity is caused by higher local porosity in the active deformation zones at higher sliding velocities.

5.4.1.3 Mechanisms during re-shear

During re-shear, the contact strength distribution that developed as a result of pressure solution shear and compaction creep during the hold period is replaced by a distribution which in the new steady state will presumably be similar to the distribution pertaining before healing. This process likely involves grain fracture and dilatation, allowing reactivation of the old R shears and/or formation of new R shears. As shown in Figure 5.3, the compaction occurring during hold periods was not entirely restored in the dilatation following re-shear. This may reflect the fact that at any time shear deformation (and associated dilatation) is localised around the R shears, whereas compaction can occur throughout the gouge. Thus, the inactive bulk of the gouge continued to compact during the hold period, but was not involved in dilatation during re-shear, which is limited to the active zones.

Reactivation of the present R shear population, or alternatively localisation of deformation in new R shears, requires grain contact failure as well as dilatation. Hence, the peak strength observed upon re-shear will be determined by the healed contact strength as well as by the required

dilatation rate. Since the principal processes occurring during re-shear are dilatation and grain contact failure/sliding, the physical meaning of τ_x in this case is the total dissipation rate by contact sliding and fracture per unit shear strain. τ_x is thus a measure of total average gouge contact strength. Now, the sequence of events upon re-shear in our experiments involves elastic loading up to the yield point, followed by contact fracture, the maximum intensity of which is indicated by the maximum in τ_x . This contact fracture is then followed by a peak in dilatation rate, after which dilatation rate decreased again. It was argued by *Marone et al.* [1990] that decreasing dilatation rate with strain is favours localisation of deformation in the gouge because parts of the gouge that have accommodated more shear strain have lower local dilatation rates, and hence lower shear strength. We propose that in our samples dilatation eventually allowed localisation of deformation into R_1 -shears, and the subsequent re-establishment of a steady state friction level. This is consistent with our microstructures, as well as with previous work showing a relation between decreasing dilatation rate and localisation of deformation [*Marone et al.*, 1990]. The measured shear stress is the sum of the contribution from grain contact fracture and dilatation, and the shear stress maximum occurs at the point where the sum of these contributions is at a maximum.

After the shear stress peak, healing processes compete with contact destruction processes to re-establish a steady state contact population. Contact healing by pressure solution is a time-dependent process, and is hence expected to be less rapid relative to contact disruption processes, which are slip-dependent. The effect of time-dependent healing during decay towards steady state is evident from τ_x during re-shear (See Figure 5.6c): At high velocities, where time-dependent healing is relatively less important, τ_x drops after the peak to a value significantly below the steady state value. Similar behaviour was observed upon stepping up in sliding velocity (see Figure 5.4a). This behaviour can be explained by realizing that after contact rupture contact strength is essentially zero until significant (time-dependent) contact restrengthening has taken place. At high velocities, when many contacts break per unit time, the rate of contact fracture may transiently outweigh the healing rate, and contact strength may drop transiently below the steady state value. This type of behaviour has also been observed in dry friction experiments (see e.g. *Marone* [1998a]). We propose that the general mechanism is the same in these, but in our experiments the effect is only seen in τ_x (and not in the measured shear stress) because the concurrent dilatation rate is much higher in our experiments. At lower sliding velocities, where healing is relatively more rapid, healing can keep up with fracture and the integrated contact friction decays gradually towards the steady state value.

5.4.1.4 Healing data

The measured healing rate (i.e. the amount of increase in peak shear stress per order of magnitude hold time) was much higher for the brine-saturated samples than for the decane-saturated samples, which suggests that strengthening has occurred mostly by the fluid-assisted process occurring during the heal period. Both $\Delta\mu_x$ and $(-d\epsilon/d\gamma)_{\max}$ exhibited strong hold time dependence, showing that both contact strength increase and dilatation upon re-shear contributed to the observed healing. Indeed, the strong correlation that is observed between $\Delta\mu$ and the amount of volumetric strain during heal (see Figure 5.8) strongly suggests that healing is due to the processes leading to compaction.

Overall, there is not much difference in healing rate between the relaxation experiments and the zero shear stress experiments. This shows that healing is mostly time- (and not slip-) dependent. Nevertheless, the amount of healing for relaxation holds is slightly higher, which would suggest the presence of a small contribution of slip to healing. The main difference between the experiments with and without shear stress during hold is in the total average contact strength τ_x , which is consistently higher for experiments with shear stress relaxation during hold. This can be understood if contact strengthening is driven by contact normal stress during hold. Re-shear will necessarily

involve fracture of and slip along antithetically oriented grain contacts, since this is needed for the dilatation required to allow localisation into R_1 -shears. Since antithetic planes are planes oriented roughly perpendicular to σ_1 during shear, their frictional/fracture strength will contribute most to measured fault strength. During stress relaxation, contacts oriented in an antithetic orientation will experience a higher average contact normal stress than contacts oriented in a synthetic direction because of the contribution of macroscopic shear stress to local contact normal stress. Contact growth by pressure solution (or by any ductile mechanism) is normal stress-dependent, so the antithetically oriented contacts will grow more rapidly during a hold period where macroscopic shear stress is allowed to relax than during hold periods where macroscopic shear stress is removed completely. It is important to note here that in this situation healing does not occur as a consequence of shear creep. Rather, healing is caused by time-dependent processes (namely pressure solution), which also allow macroscopic shear creep of the gouge.

Our data show a significant loading rate dependence of $\Delta\mu$, consistent with dry friction experiments. The data also show that the source of this dependence is both in τ_x and in the dilatation rate, although the velocity dependence of τ_x is largest. If τ_x is interpreted as representing integral contact strength, our data imply that contact strength is time-dependent. This points towards a strong contribution of subcritical crack growth to the observed fracture behaviour. The increase of $(-d\varepsilon/d\gamma)_{\max}$ with velocity, especially at lower velocities, can be explained by the dependence of compaction rate during hold on pre-hold sliding velocity, which was particularly strong at low sliding velocities.

The time-dependence of contact strengthening observed in our experiments is different from the logarithmic dependence generally observed in room-temperature experiments on quartzo-feldspathic gouge. Rather, our data are more consistent with a power law dependence, with contact strength increasing as $t^{2/3}$, although more data are needed to constrain the relationship better. Theoretical models for compaction of porous aggregates by pressure solution which include the effect of volumetric strain on compaction rate [Spiers and Schutjens, 1990; Spiers and Brzesowsky, 1993] predict that contact area should increase as $t^{1/2-2/3}$, depending on the model geometry taken. This is in good agreement with our data. Also, Hickman and Evans [1992] observed an increase in contact area as $t^{1/2-2/3}$ in halite-halite contacts undergoing fluid-assisted neck growth. Hence, under conditions where fluid-assisted processes dominate contact healing, the logarithmic dependence of healing on time may not generally apply.

5.4.2 Comparison to experiments on quartzo-feldspathic gouge: transient effects under conditions favouring pressure solution

5.4.2.1 Comparison to experiments on quartzo-feldspathic gouge

The sliding behaviour observed in our experiments resembles the generally observed behaviour in friction studies on quartzo-feldspathic gouge in the sense that upon changing sliding velocity a direct effect on sliding strength is observed, followed by a gradual evolution to a new steady state. Detailed fitting of our data to the RSF equations is beyond the scope of this paper, but rough estimates for the typical RSF parameters (see Figure 5.10) give values for the direct effect upon changing velocity \mathbf{a} in the range 0.17-0.40 and values for $\mathbf{a-b}$ of 0.03-0.08. These values are roughly one order of magnitude higher than values typically observed in quartzo-feldspathic gouge under fluid-absent conditions. Furthermore, the direct effect after stepping up in velocity is ~25-35% larger than after stepping down. In the following we will discuss the mechanisms leading to the observed behaviour upon velocity stepping. We will attempt to explain the reason for the differences between our results and dry friction experiments, and assess implication for the applicability of RSF laws under conditions favouring pressure solution.

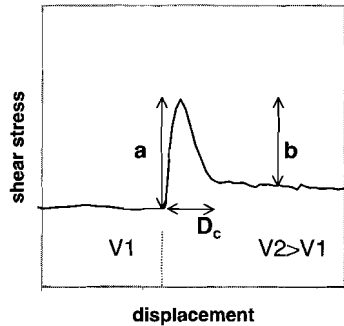


Figure 5.10. Typical shear stress vs. displacement data of velocity step, illustrating the RSF parameters a , b and D_c . V_1 and V_2 denote sliding velocities.

be affected: pressure solution allows rapid contact growth, thus increasing the sliding velocity dependence of steady state contact area, but fluids may also enhance stress corrosion cracking, increasing the velocity dependence of contact strength. Furthermore, when compaction by solution transfer processes is possible the gouge porosity will generally be lower than in dry gouges, which in turn increases $d\epsilon/d\gamma$ (which, after all, is simply a microstructural parameter reflecting the average sliding plane orientation in the gouge). Prediction of the value of a - b could in principle be done by detailed assessment of the above factors, but in practice we believe this is hampered by incomplete knowledge of basic aspects of these processes, as well as by the impossibility of characterising the microstructure (which determines the dilatation rate $d\epsilon/d\gamma$) of in particular natural faults in sufficient detail. It should be mentioned, however, that neither of these effects necessarily has a logarithmic velocity dependence, and any fit of experimental data to a logarithmic law could be fortuitous due to the small range of velocities/conditions studied.

We now move attention to the direct effect on shear strength upon velocity changes. On a bare surface this effect can be due to the fact that finite time or slip is needed to establish a new steady state contact area, so the fault initially slips at the steady state contact area of the previous sliding velocity. Also, the velocity dependence of contact strength may contribute to the direct effect. In a gouge-bearing fault, an additional contribution is expected from the volume change required to establish the new steady state porosity. When solution transfer processes are rapid, all these factors will increase with respect to dry gouge: the velocity dependence of steady state contact area will be higher due to increased contact growth rate, the velocity dependence of contact strength will increase due to an increased contribution of stress corrosion cracking, and the volume change required to establish a new steady state porosity will increase as well, as shown in our data. It is important to note here that in the presence of time-dependent compaction mechanisms such as pressure solution, the direct effect is expected to be asymmetric with respect to velocity changes, because the dilatation that is needed to establish a new steady state porosity upon a velocity increase occurs by a very different mechanism than the compaction occurring upon velocity decrease: contact disruption is an essentially brittle processes, whereas contact growth occurs by pressure solution. Indeed, our data show that the direct effect upon a velocity increase is larger than upon a velocity decrease. This is not incorporated in the rate- and state-dependent friction equations, but it may be important in natural situations. The issue of the contribution of volumetric strain to measured frictional strength is discussed more fully below.

Finally, the distance required to re-establish steady state strength after a velocity step is shown by our data to be directly related to volume change, i.e., steady state shear stress is reestablished at the point where dilatation has stopped. The sliding distance required to establish a

new steady state local porosity is expected to be asymmetrical with respect to velocity steps for the same reason as the direct effect: compaction occurs by an essentially time-dependent process, whereas dilatation is shear-dependent. Indeed, our data show significant asymmetry in the approach to steady state after velocity steps, in particular at higher displacements (see Figure 5.3d).

Summarizing, we believe that the higher magnitudes of the various transient effects compared to dry experiments, as well as the asymmetry with respect to sliding velocity, can be explained by an increased rate of time-dependent compaction and healing by pressure solution in our samples. It should be noted here that different time-dependent processes can act at the same time: as argued above, at least three different processes contribute to the various RSF parameters. The fact that these factors are not easily isolated in the RSF laws but are hidden in a few empirical parameters without clear physical meaning constitutes, we believe, a principal weakness of the RSF equations, which hampers the understanding of frictional phenomena from the basic microphysical processes operating, and thus the applicability of laboratory-derived friction data to natural situations.

5.4.2.2 On the contribution of volumetric strain to measured friction

Equations similar to our equation (5.1) have been applied to granular media undergoing shear, in which case τ_x is assumed to be essentially a constant, being the contribution to measured friction of frictional sliding of grains past each other. Indeed, *Marone et al.* [1990] used his volume change data from experiments on quartz gouge-bearing faults to calculate a predicted transient strength increase upon increasing sliding velocity, to test whether the observed transient strength increase could be explained by transient gouge dilatation. For this calculation they assumed τ_x to be the (velocity-dependent) frictional strength as measured in sliding experiments on bare surfaces, i.e. the type of data that led to the formulation of the RSF laws. *Marone et al.* [1990] found that the calculated values for μ due to the transiently increased dilatation rate overestimated his measured friction data. In a later paper, *Beeler and Tullis* [1997] argued that the data presented by *Marone et al.* [1990], as well as their own data, showed a contradiction between (5.1) and the RSF laws, because the overprediction of the shear stress peak upon a velocity increase by the version of (5.1) used by *Marone et al.* [1990] implies that upon increasing sliding velocity τ_x should transiently *decrease*, whereas friction data on bare surfaces consistently show an *increase* in shear stress in this case. However, the apparent discrepancy between (5.1) and the data described by the RSF relies on the assumption that τ_x in (5.1) equals the frictional strength as given by rate- and state friction data for bare surfaces. This assumption implies that no shear-dependent volume changes occur in sliding a bare surface. In view of the fact that frictional sliding of rock materials is an essentially brittle process, it is highly unlikely that this occurs without local volume changes. On bare surfaces these may be too small to measure, but, as implied by (5.1), it is the ratio of volumetric strain to shear strain that determines the behaviour. Since transient effects in bare surface experiments generally occur over very short displacement intervals, the concurrent dilatation need only be very small to produce a significant effect on measured friction. Thus, it is clear that τ_x in (5.1) cannot simply be equalled to the sliding strength of bare surfaces. If instead, as argued above, τ_x is viewed as a measure of average contact strength in the gouge, it is very well possible for τ_x to show a transient drop upon a velocity increase when the contact fracture rate transiently outweighs the contact healing rate (recall section 5.4.1.3). In conclusion, then, when the microphysical processes occurring in gouge-bearing processes are kept in mind, it is clear that τ_x is not simply equal to the sliding friction on a bare surface, and the apparent contradiction between equation (5.1) and friction data on gouge bearing faults vanishes.

Beeler and Tullis [1997] argue correctly that only the shear-dependent part of volume changes during sliding contribute to measured friction. They presented experimental data

suggesting that during fault healing compaction strain is almost completely time-dependent, and from this they concluded that in general the measured friction τ represents the friction leading to shear heating, and no corrections need to be made for volume change since volume change is mostly time-dependent. Their argument is that contributions to τ through time-dependent volumetric strain are balanced by dissipation contributing to τ_x . For a compacting gouge, this is easily understood; referring to equation (5.1), if all volumetric strain is assumed time-dependent the positive contribution of compaction to the left hand side of equation (5.1) through $\sigma_n \dot{\epsilon}$ is balanced by the (again positive) contribution of the dissipative processes allowing compaction to the right hand side of (5.1). However, in a dilating gouge this argument does not hold. Dilatation is not simply the reverse of time-dependent compaction, since, in contrast to compaction, dilatation cannot occur without shear. Whereas the contributions of time-dependent compaction to the left- and right-hand term of equation (5.1) are of the same sign, in the case of dilatation they are of opposite sign. Referring to equation (5.2), it can be seen that this means that both volume increase and the dissipative process allowing volume increase (e.g. frictional sliding along grain contacts) add up to the measured τ , even if the dissipative process leading to dilatation is time-dependent. Mathematically, the flaw in Beeler and Tullis' argument shows up in the assumption that the time- and slip dependent parts of volumetric strain are independent (see their appendix, equation A6). For a compacting gouge this may be true, but for dilating gouge it is physically impossible, because dilatation cannot occur without shear.

It is concluded then that Beeler and Tullis' conclusion that volume changes need not be accounted for in determining the frictional stress that leads to shear heating only applies to a gouge undergoing compaction, and is incorrect for a dilating fault gouge. In most friction experiments, the re-shear after hold periods (which can be viewed as an earthquake analogue) is usually accompanied by significant dilatation, especially in high strain faults. Hence, the case of a dilating fault gouge seems most relevant to natural earthquakes.

5.4.3 Implications for strength recovery along natural faults

Our data show that when solution transfer processes are active in an analogue system they lead to significant fault strengthening during periods of no (or little) slip. Natural faults contain abundant evidence for the operation of solution transfer processes [Chester *et al.*, 1993; Bruhn *et al.*, 1994; Hadizadeh, 1994; Caine *et al.*, 1996], so solution transfer processes are indeed likely to be of significant importance in determining the healing behaviour of natural faults at depth. Experiments on quartz gouges, under conditions where solution transfer processes are of negligible importance, generally show a roughly log-linear relation between healing and time (see Marone [1998b] for review), as also implied by the RSF equations. In contrast, our data show that when solution transfer processes are rapid this log-linear relation does not apply, especially where the contribution of contact strength (i.e. τ_x) is concerned. Note that the log-linear healing rate implied by the RSF equations has no microphysical basis: it is simply a best-fit to experimental data of room-temperature friction experiments. In contrast, microphysical models of fluid-assisted contact growth predict contact growth rate to scale with $t^{1/2-2/3}$, for contact growth by pressure solution [Visser, 1999] as well as for the case of contact growth by fluid-assisted neck growth [Hickman and Evans, 1992]. This is similar to our data on the time-dependence of τ_x . It follows that the log-linear relation between healing and time may not be applicable under the hydrothermal conditions pertaining in much of the seismogenic zone. The healing times and compaction strains reached in the typical healing experiments on natural gouge used to calibrate the log-linear relation are generally at least an order of magnitude lower than those expected on natural faults during interseismic periods [Lockner and Evans, 1995]. Therefore, healing rates from experiments that are

based on a log-linear relationship will generally underestimate the rate of fault healing in nature if healing is due to pressure solution, especially for longer interseismic intervals.

For a quantitative, mechanism-based assessment of healing rates of natural faults under seismogenic conditions, a detailed knowledge of the evolution of contact area, the evolution of contact strength (i.e. the time-dependence of adhesive properties), as well as of the way in which these grain contact scale parameters control macroscopic fault strength during the seismic cycle is required. Our data present a first step in this direction, but are no more than exploratory in nature. A severe limitation is posed by the fact that our study considers only monomineralic fault gouge, whereas natural fault gouges are generally polymineralic. Natural faults often contain a significant proportion of phyllosilicates [Wu *et al.*, 1975; Rutter *et al.*, 1986; Chester *et al.*, 1993; Bruhn *et al.*, 1994; Wintsch *et al.*, 1995], either inherited from the host rock or produced as alteration products, which may strongly influence fault healing. On the one hand phyllosilicates are known to increase the rate of compaction by pressure solution [Tada and Siever, 1989; Rutter and Wanten, 2000]. However, on the other hand phyllosilicates are believed to inhibit contact healing [Hickman and Evans, 1995], in this way possibly inhibiting fault strengthening. Hence, whereas experiments on monomineralic fault gouge are instructive for studying basic mechanistic aspects of fault healing, the actual rates observed may be of little relevance to natural faults.

5.5 Conclusions

We performed slide-hold-slide experiments on simulated fault gouge in the system NaCl + brine in order to assess the effect of fluid-assisted processes on fault healing. The following conclusions can be drawn:

1. During hold periods, pressure solution compaction and shear creep of gouge occurred, possibly accompanied by some subcritical cacking, allowing stress relaxation and leading to time-dependent fault healing through both packing density increase and contact area/strength increase. Upon re-shear, contact fracture occurred, followed by rapid dilatation, both of which contributed to the measured shear stress.
2. Our data broadly resemble the conventional rate- and state- dependent friction behaviour as observed in experiments on quartzo-feldspathic gouge, but the magnitudes of the various parameters are much larger than observed in quartzo-feldspathic gouge. This can be explained by a higher relative rate of time-dependent contact growth and compaction due to the operation of pressure solution.
3. Fluid-assisted healing by pressure solution does not show the log-linear time-dependence exhibited by quartzo-feldspathic gouges under conditions where solution transfer processes are unimportant. Rather, healing increases with $t^{2/3}$, similar to predictions of contact area growth by solution transfer processes. If pressure solution-induced healing is important in natural faults, applying a log-linear relation may lead to underestimation of natural fault healing rates.
4. Our data deviate from the behaviour predicted by the rate-and state-dependent friction laws in that the shear stress response upon changing sliding velocity is strongly different after stepping up in velocity compared to stepping down. This can be explained the fact that the dilatation occurring upon velocity increase occurs by a fundamentally different process than the compaction occurring upon a velocity decrease.

Chapter 6

Effect of clays on fluid-assisted fault healing

Accepted for publication in Earth and Planetary Science Letters as: B. Bos and C.J. Spiers, Effect of phyllosilicates on fluid-assisted healing of gouge-bearing faults

Abstract. On the basis of both experimental and field studies, it is widely accepted that solution transfer processes are important in controlling fault strength recovery (healing) in the hydrothermal reaches of the seismogenic zone. Fluid-assisted healing of fault gouge may be strongly influenced by phyllosilicate content and spatial arrangement, but little is known about such effects. To study these effects, we have performed slide-hold-slide experiments using simulated faults containing gouges of halite + kaolinite saturated with brine. In this system, solution transfer processes are extremely fast. The results show rapid healing in the case of pure halite gouge, whereas almost no such effects were observed in foliated, clay-bearing gouge under otherwise identical conditions. This raises questions regarding recent application of laboratory-derived healing data for monomineralic gouge to natural faults, since these generally contain significant amounts of phyllosilicates. Our results highlight the need to account for realistic fault gouge compositions and microstructures to further improve our understanding of fault strength and seismicity.

6.1 Introduction

It is well established that both natural and experimental faults show strength recovery (healing) during interseismic periods [Dieterich, 1972; Marone *et al.*, 1995], and that an understanding the mechanisms and kinetics of fault healing is important for understanding fault behaviour and the seismic cycle. Indeed, fault healing is the cornerstone of the often-used rate- and state-dependent friction laws based on dry, room temperature experiments [Dieterich, 1979; Ruina, 1983; Marone, 1998; Scholz, 1998], applied in theoretical models of seismic fault behaviour (e.g. [Cao and Aki, 1986; Rice, 1993]). Increased healing rates observed in experiments under hydrothermal conditions [Fredrich and Evans, 1992; Karner *et al.*, 1997; Olsen *et al.*, 1998] suggest that fluid-rock interaction processes such as surface energy driven neck growth, gouge cementation and pressure solution compaction (with associated contact area increase) are likely to be important mechanisms of fault healing in large parts of the seismogenic zone. However, the basic mechanisms of fluid-assisted strengthening are poorly understood.

From a consideration of the energy balance in a deforming fault zone (see Chapter 5.1), the measured shear stress τ of a gouge-bearing fault can be written

$$\tau = \tau_x - \frac{d\varepsilon}{d\gamma} \sigma_n \quad (6.1)$$

where $d\varepsilon$ is incremental volumetric strain (compaction taken positive), $d\gamma$ is incremental shear strain and σ_n is normal stress (compression positive), and τ_x represents the contribution to measured shear stress of dissipative processes in the gouge (such as fracture/ frictional sliding of grain contacts, crystal plasticity, or pressure solution). Following (6.1) strength increase after periods of no-slip can occur as a consequence of two basic effects: On the one hand, contact area/strength may increase during periods of no slip via processes such as pressure solution, requiring increased stress for contact sliding/disruption and thus leading to strengthening through the first right-hand side term in (6.1). On the other hand, gouge packing density may increase as a result of pressure solution, requiring dilatation and hence work against normal stress upon re-shear and thus contributing to the measured shear stress through the second right-hand side term in (6.1).

Field studies of exhumed faults have shown that most mature faults contain significant amounts of phyllosilicates [Wu *et al.*, 1975; Wu, 1978; Rutter *et al.*, 1986; Chester *et al.*, 1993;

Wintsch *et al.* 1995], derived either from the protolith or formed as a product of retrograde mineral reactions. These phyllosilicates may significantly influence the above-mentioned fluid-assisted healing mechanisms. For example, clays are known to inhibit neck growth, and increase the rate of pressure solution compaction [Dewers and Ortoleva, 1991; Hickman and Evans, 1995; Renard *et al.*, 1997; Rutter and Wanten, 2000]. Furthermore, clay-rich fault zones are often foliated, the phyllosilicates forming planes of weakness that may be less prone to healing than monomineralic grain boundaries. Hence, the presence and spatial arrangement of phyllosilicates can be expected to have a significant influence on fluid-assisted fault healing.

In this chapter we report so-called slide-hold-slide experiments designed to investigate the effect of kaolinite on fluid-assisted fault healing in the halite-brine system. Halite was chosen as a fault gouge analogue because solution transfer processes are well characterized and known to be extremely rapid in halite, making it a suitable material to study basic mechanistic aspects of fluid-assisted fault healing. It was shown previously (see Chapter 4) that halite/kaolinite gouges undergo significant microstructural evolution when sheared to high strain, evolving from a non-foliated, cataclastic microstructure to a strongly foliated mylonitic appearance. We explore not only the effect of the presence of clay but also the influence of this microstructural evolution on fluid-assisted healing in these gouges. The results show that healing is strongly retarded by the presence of phyllosilicates, and that the effect is most pronounced in foliated gouge. Also, the degree of healing in clay-bearing gouges was observed to decrease with progressive shear strain, in contrast to clay-free gouges, which showed an increase of healing with shear strain.

6.2 Experimental method

We performed room temperature, slide-hold-slide, rotary shear experiments on brine-saturated simulated gouges of pure halite and halite + 25 mass% kaolinite composition. In slide-hold-slide experiments, the sample is first sheared for a given period at constant sliding velocity, after which sliding is halted (the "hold" period) and shear stress allowed to relax. After a prescribed time, sliding is resumed ("re-shear"). For details regarding our deformation apparatus the reader is referred to section 5.2. In brief, the sample assembly consists of two annular, roughened, stainless steel "wall rock" rings (10 cm external diameter and 1 cm width) sandwiching a 1 mm thick layer of simulated gouge. The gouge is confined at the sides by stainless steel supporting rings, fitted with low-friction O-rings. Pore fluid was drained to atmospheric pressure. Normal stress was applied and controlled using an Instron 1362 loading frame, and maintained at 2.5 MPa during the experiments. An LVDT located at the center of the annular sample assembly allowed measurement of displacement normal to the simulated fault, i.e., gouge compaction/dilatation (resolution 0.1 μm). Rotary sliding was imposed at a constant velocity of 2 $\mu\text{m/s}$. The resolution in measured shear stress was ~ 0.01 MPa.

The experiments reported are listed in Table 6.1. Two types of experiments were done. In the first, the time-dependence of healing was studied in faults containing pure halite gouge (Heal1) as well as clay-bearing gouge (Heal1 and Heal2). Two microstructural types of clay-bearing gouge were investigated. Gouge with a non-foliated microstructure was produced by sliding for 12 mm at 2 $\mu\text{m/s}$ prior to the hold steps (Heal1). Strongly foliated gouge was created by sliding to similar displacement, but at lower velocity (0.2 $\mu\text{m/s}$) prior to healing (Heal2). Representative microstructures of the materials used are shown in Figures 6.1. In all experiments, hold periods were initiated by halting the rotary drive system, allowing shear stress relaxation. The degree of healing ($\Delta\mu$), defined as the difference between the peak shear stress upon re-shear and the foregoing steady state shear stress, normalized by the normal stress was investigated as a function of healing time (60, 600 and 6000 seconds).

Experiment	Gouge composition	Sequence of hold times (s)	Shear displacement before first hold (mm)
Heal1*	halite	60 600 6000 600 60	7.725
Healc1	halite + 25% kaolinite, "non-foliated"	60 600 6000	12.096
Healc2	halite + 25% kaolinite, "foliated"	600 6000 60	12.872
Healc3	halite + 25% kaolinite	600 (8x)	4.888
Heal6	halite	600 (8x)	6.486

*data also reported in Chapter 5

Table 6.1. List of experiments

In the second type of experiment, two runs were performed to investigate the effect of strain on fault healing (experiments Heal6 and Healc3). To this end, pure halite and halite + 25 mass% kaolinite gouge was sheared to ~45 mm displacement at 2 $\mu\text{m/s}$ sliding velocity and 2.5 MPa normal stress, interrupted at regular (5-7 mm) displacement intervals by hold periods of 600 seconds duration. It is known (see Figures 4.8) that significant microstructural change with progressive strain takes place under these conditions, although at this sliding velocity the microstructural evolution in the clay-bearing sample is not as pronounced as at the lower velocities used to create the above-mentioned, strongly foliated sample (Healc2).

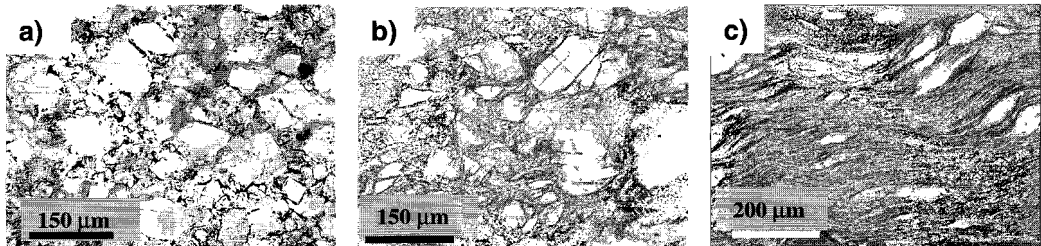


Figure 6.1. Microstructures of samples before healing. White material is halite, light grey material is epoxy resin, dark material is kaolinite. Shear sense dextral. a) Pure halite gouge. b) Non-foliated halite/kaolinite mixture. c) Foliated halite/kaolinite mixture.

6.3 Results

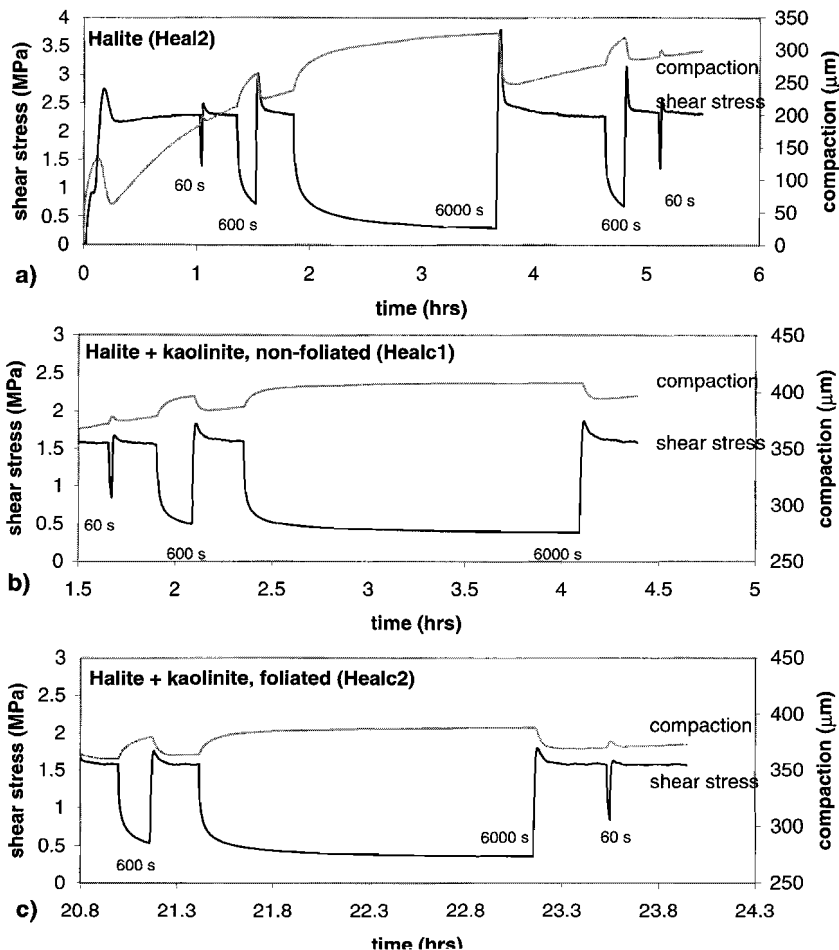


Figure 6.2. Shear stress and compaction data of healing experiments using (a) pure halite (experiment Heal1), (b) non-foliated halite + kaolinite (Healc1) and (c) foliated halite + kaolinite gouge (Healc2). Hold times as indicated. Note rapid shear stress relaxation and significant hold-time dependence of peak strength upon re-shear.

Figure 6.2 shows shear stress and compaction vs. time for the experiments reported (Heal1, Healc1 and Healc2). Note that the experimental data are shown only after the run-in stage, in which the desired "starting" microstructure was formed. The behaviour prior to the healing steps consisted of steady state sliding at constant shear stress for experiment Healc1, whereas significant strain weakening was observed in experiment Healc2 (see Chapter 4). After sliding was halted, rapid shear stress relaxation was observed, accompanied by a significantly increased compaction rate. Upon re-shear, shear stress rapidly reached a peak, thereafter falling gradually to a new quasi-steady state level. This was accompanied by significant dilatation. In general, the clay-bearing gouges

show lower amounts of stress relaxation and compaction for a given hold time than the pure halite gouge.

The behaviour typically observed during hold periods is illustrated in Figures 6.3a-c, which show stress relaxation, shear displacement and volumetric strain, respectively, as a function of time during a 600 seconds hold period for experiments Heal1, Healc1 and Healc2. The pure halite gouge showed higher rates of stress relaxation, shear displacement and compaction compared to the clay-bearing gouges. Of the clay-bearing gouges, the foliated gouge showed lower rates of shear displacement and compaction, but a similar stress relaxation rate compared to the non-foliated gouge.

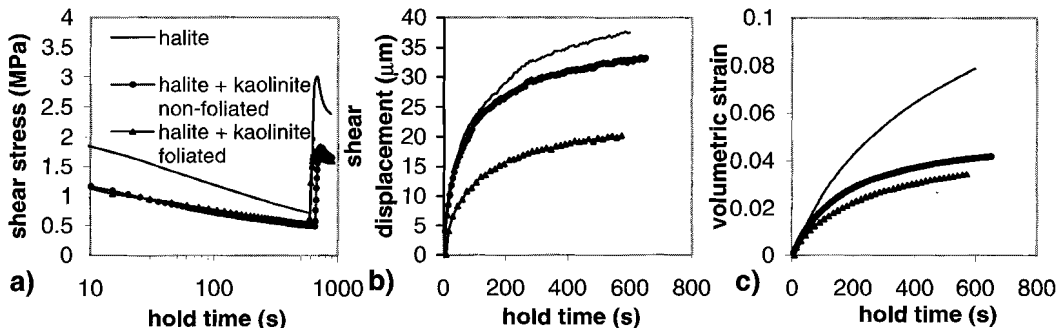


Figure 6.3. Data obtained during hold periods, for the same experiments as shown in Figure 6.2. a) Shear stress relaxation, b) Shear displacement and c) volumetric strain versus hold time. Solid line is pure halite, closed circles denote non-foliated halite/kaolinite gouge, and open triangles denote foliated halite/kaolinite gouge.

In Figures 6.4, we show τ , τ_x and the dilatation rate ($-d\varepsilon/d\gamma$) as a function of displacement after re-shear, for re-shear after 6000 seconds hold. Whereas in the pure halite gouge significant peaks were observed in both τ and τ_x , in the clay-bearing gouges the peak in τ_x and was hardly discernable. Furthermore, in the pure halite gouge, the peak in measured friction preceded the peak in $-d\varepsilon/d\gamma$ by $\sim 25 \mu\text{m}$, whereas in the case of clay-bearing gouges the peaks in measured friction and dilatation rate were closer together for the non-foliated gouge and exactly coincided for the foliated gouge.

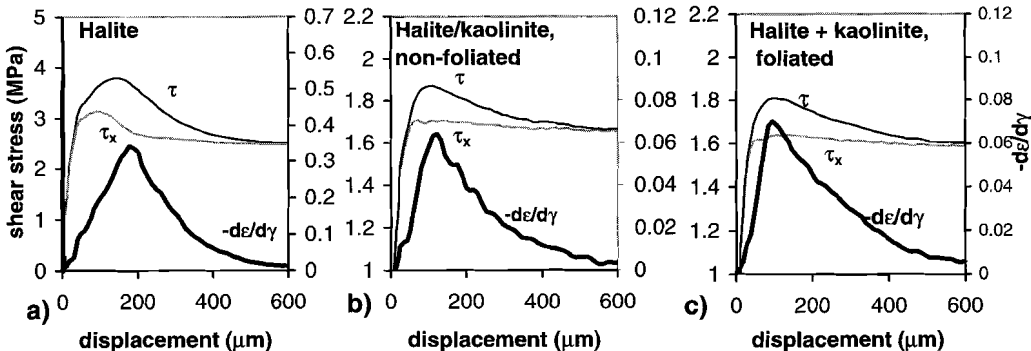


Figure 6.4. Measured shear stress τ , as well as τ_x and dilatation rate $-d\varepsilon/d\gamma$ plotted against displacement after re-shear, for re-shear after 6000 seconds hold time. a) Pure halite gouge (Heal1). b) Non-foliated halite/kaolinite mixture (Healc1). c) Foliated halite/kaolinite mixture (Healc2).

Figure 6.5a shows the degree of healing $\Delta\mu$, defined as the difference between the peak in τ_x and the previously resolved sliding friction normalized by the normal stress, as a function of hold time. The healing rate (change in μ per order of magnitude of healing time) is also indicated. In the clay-bearing gouges, the healing rate was ~ 1 order of magnitude lower than in the clay-free gouge, the total amount of healing also being lower for the foliated gouge. The dependence of $\Delta\mu_x$, defined as the difference between peak and steady state τ_x normalized by the normal stress, on hold time duration is shown in Figure 6.5b. On average, the non-foliated, clay-bearing gouge showed an ~ 8 times lower rate of increase of $\Delta\mu_x$ than the pure halite gouge, but no increase in $\Delta\mu_x$ was observed between the 600 and 6000 seconds hold periods. The healing rate in the foliated, clay-bearing gouge was insignificant within the resolution of our experiments, but at least 36 times lower than the healing rate of the pure halite gouge. Finally, the maximum dilatation rate after re-shear is shown as a function of hold time in Figure 6.5c. The maximum dilatation rates of the clay-bearing gouges were identical for a given hold time, and much lower than the maximum dilatation rates of the halite gouge.

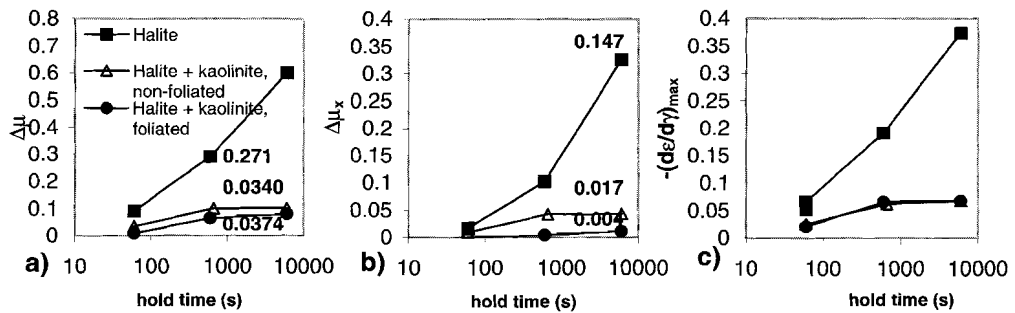


Figure 6.5. $\Delta\mu$ (a) $\Delta\mu_x$ (b) and $(-d\varepsilon/d\gamma)_{max}$ (c) as a function of healing time. $\Delta\mu_x$ was calculated from equation (1) using measured friction and compaction data. Indicated in boxes are average healing rates, i.e. slopes of linear best fits through the stress versus log time data.

Figures 6.6a and 6.6b show shear stress and compaction versus displacement for the experiments investigating the effect of strain on healing (experiments Healc3 and Heal6). In the clay-free sample, the peak stress upon re-shear increased with increasing shear displacement, especially in the first half of the experiment. The critical slip distance required to re-establish steady state shear stress decreased with increasing displacement. Exact determination of the parameter D_c as defined in rate- and state-dependent friction laws [Dieterich, 1979; Ruina, 1983] requires numerical modeling because of the finite stiffness of the deformation apparatus, and is outside the scope of this paper. We estimate that in our experiments D_c has a magnitude in the order of a few hundred microns. In contrast, the clay-bearing sample showed a decrease in re-shear peak stress with increasing displacement, and an increase of the critical slip distance with increasing displacement. In both experiments, a continuous background compaction trend was observed. Superposed on this, additional compaction occurred during heal periods, which was partly restored by dilatation during re-shear. In Figure 6.7a and 6.7b we show $\Delta\mu$, $\Delta\mu_x$ and $(-d\varepsilon/d\gamma)_{max}$ as a function of total shear displacement, for the pure halite and halite + kaolinite gouge, respectively. For the pure halite gouge $\Delta\mu$, $\Delta\mu_x$ and $(-d\varepsilon/d\gamma)_{max}$ all increased with displacement in the first 25 mm, after which they remained roughly constant. In contrast, in the clay-bearing sample $\Delta\mu$ and $(-d\varepsilon/d\gamma)_{max}$ decreased with increasing displacement, whereas $\Delta\mu_x$ first decreased in the initial 10 mm, then increased with increasing displacement up to 30 mm, after which it slightly dropped again.

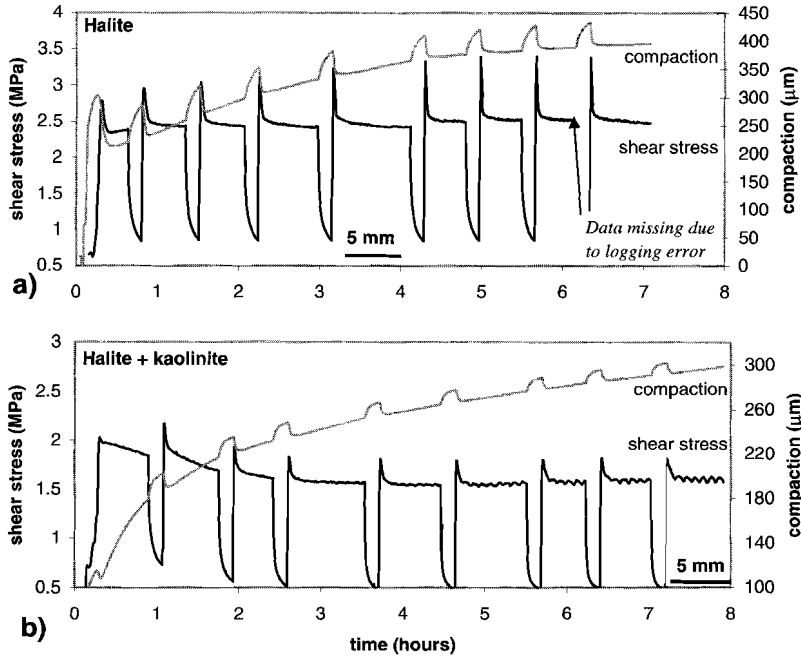


Figure 6.6. Shear stress and compaction versus time, showing the effect of total shear displacement on healing behaviour. a) Data for pure halite gouge (experiment Heal6). Note that in the last hold period data are missing due to a logging error. b) Data for halite + 25% kaolinite gouge (experiment Heal3).

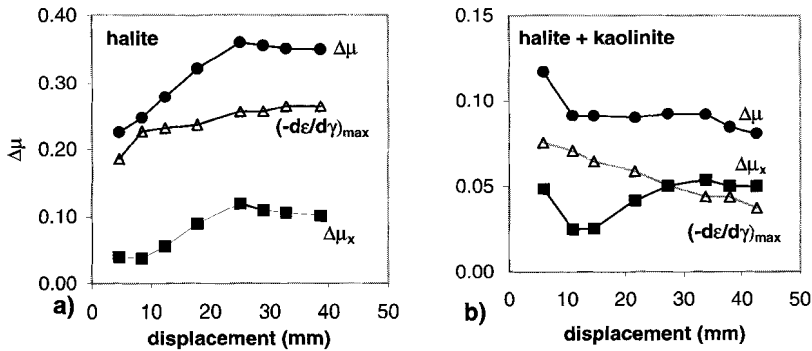


Figure 6.7. $\Delta\mu$, $\Delta\mu_x$ and $(-d\epsilon/d\gamma)_{\text{max}}$ plotted versus displacement for (a) pure halite gouge (experiment Heal6) and (b) halite + 25% kaolinite gouge (experiment Heal3).

6.4 Discussion

6.4.1 Healing mechanisms: monomineralic versus clay-bearing gouge

As shown previously (see Chapter 5), healing in pure halite gouges under the conditions of our experiments occurs as a consequence of compaction and shear creep by intergranular pressure solution during hold periods. This leads to strength increase because on the one hand packing density increase requires dilatation and hence work against normal stress upon re-shear (contributing to $\Delta\mu$ through $d\varepsilon/d\gamma$), and on the other hand because of increased average contact area after hold periods, thus contributing to $\Delta\mu$ through $\Delta\mu_x$. The data on pure halite show that the peak values of τ_x and $-d\varepsilon/d\gamma$ were of similar magnitude (see Figure 6.5), suggesting that contact strength and dilatation contributed roughly equally to the measured peak strength.

The clay-bearing gouges showed strongly reduced healing compared to the pure halite gouge. In the non-foliated halite + kaolinite gouge, both τ_x and $d\varepsilon/d\gamma$ contributed significantly to the measured healing (see Figure 6.5), which again suggests that both contact strength/area increase and dilatation contributed to the observed peak stress. In contrast, the foliated gouge showed no significant increase in τ_x with hold time, so that the peak shear stress must have been caused entirely by dilatation during re-shear, with little or no intergranular contact strengthening occurring during the hold periods. This is confirmed by the observation that the peak in measured shear stress exactly coincides with the peak in dilatation rate (see Figure 6.4c). The key microstructural feature distinguishing the foliated gouge from the others is the absence of halite-halite grain contacts: all halite grains in the foliated gouge are separated by kaolinite layers. In the non-foliated clay-bearing gouge, both clay-free and clay-filled halite-halite contacts are observed to be present, whereas the monomineralic gouge only contains halite-halite contacts, of course. Clay films at grain contacts presumably prevent grain contact strengthening by inhibiting contact adhesion and neck growth [Hickman and Evans, 1995]. We accordingly suggest that the reduced healing in our clay-bearing gouges is a direct reflection of the reduced proportion of healing-prone halite-halite grain contacts in these materials.

Turning to the compaction behaviour, significant compaction was observed in the clay-bearing gouges during individual hold times, but the amount of compaction was lower in the clay-bearing samples. This may seem surprising at first, since phyllosilicates are expected to increase the rate of pressure solution compaction. Note, however, that the total amount of gouge compaction early in the experiment (i.e. before the hold periods) was higher for the clay-bearing samples, so that these samples had lower porosity when the hold periods started. Since compaction rate is strongly porosity dependent, this may have contributed to the lower amounts of compaction in a given time in the clay-bearing samples.

The pure halite and clay-bearing gouges show striking differences in the evolution of healing with progressive fault strain. Overall, the magnitude of healing increases with progressive displacement in pure halite gouge whereas the opposite was observed in clay-bearing gouge. In the pure halite gouge, $\Delta\mu$ increased with strain in the first 25 mm displacement. Most of this increase can be attributed to increased average contact strength upon healing, since $\Delta\mu_x$ increased strongly over this interval whereas $(d\varepsilon/d\gamma)_{\max}$ only showed a slight increase. The reason for this increase in $\Delta\mu$ is not completely clear. Note also that the width of the peak upon re-shear (i.e. the critical slip distance required to re-establish steady state shear stress) progressively decreased with increasing strain. This trend was also noted for quartz gouge sheared under hydrothermal conditions [Nakatani and Scholz, 1999] as well as under room temperature conditions [Marone and Kilgore, 1993]. Marone and Kilgore [1993] interpreted the critical slip distance as being controlled by the thickness of the zone of localised shear strain in their samples. As discussed in Chapter 5, shear in our halite

gouges involves localised slip along R-shears, accommodated by dilatation and cataclasis in the surrounding regions. Applying the interpretation of *Marone and Kilgore* [1993] to our situation, this would imply that in our samples the average width of the active zones around the Riedel shears would decrease with increasing shear. Although we can not measure the thickness of the active zones directly, the amount of dilatation occurring upon re-shear is likely to be an indirect measure of the active zone thickness since, as argued in the previous chapter, it is this active zone that is undergoing active dilatation upon re-shear. This implies that if *Marone and Kilgore* [1993]'s interpretation of the critical slip distance applies to our samples the amount of dilatation upon re-shear should decrease with increasing displacement. Our data show that this is indeed the case. Hence, the decrease in critical slip distance observed in our experiments may reflect an increase in degree of localisation in the gouge.

The increase in the degree of healing with progressive shear strain can be explained in at least two ways, depending on the exact process reflected by the shear stress peak. First, the peak may reflect reactivation of a previously existing R-shear or set of R-shears. In this case, the increase in degree of healing with strain may be due to a decreasing average grain size around the R-shears with ongoing displacement, which would enhance fluid-assisted healing processes. Alternatively, the existing R-shear population may have healed to a strength exceeding the failure strength of the wall rock, and the peak stress may reflect formation of a new set of R-shears. In this case, increased healing with increasing shear displacement is expected because of the decreasing bulk porosity with ongoing shear strain. We cannot determine from our experiments which of these possibilities is the correct explanation: this would require either viewing the deformation process during the experiments (i.e. see-through experiments), or extremely precise acoustic emission event location, neither of which were possible in the current experimental set-up.

In contrast to pure halite samples, healing in the clay-bearing gouge decreased in magnitude with progressive strain, mostly due to a decrease in $(-d\varepsilon/d\gamma)_{\max}$. This can be explained by the formation of a progressively shallower foliation in these samples, although, as shown in Chapter 4, at these sliding velocities the foliation development is not very strong. The drop in $\Delta\mu_{\text{diss}}$ at displacements up to 10 mm may be caused by the elimination of halite-halite contacts with progressive strain in the initial part of the experiment. The subsequent increase with strain may be caused by an increase in the average area of contact due to decreasing gouge porosity. In clay-bearing samples, the critical slip distance progressively increased with shear strain. Following the argument outlined above, this may reflect more distributed flow of gouge with increasing shear strain, consistent with the microstructural evolution as described in Chapter 4 of this thesis.

In summary, clay-bearing gouges showed significantly reduced fluid-assisted healing compared to monomineralic gouge, due to the decreased proportion of healing-prone halite-halite contacts. The development of a foliation with progressive strain as reported for clay-bearing gouges in Chapter 4, is accompanied by a significant further decrease in the degree of healing because of a further reduction in the proportion of halite-halite contacts.

6.4.2 Implications for fluid-assisted healing of natural faults.

In most of the seismogenic zone temperatures are high enough to allow fluid-assisted processes like pressure solution to operate at significant rate, and such processes can therefore be expected to be prominent healing mechanisms in natural faults. Our data suggest that fluid-assisted healing may be retarded significantly due to the presence of phyllosilicates, and that this effect is even more pronounced when the phyllosilicates define a foliation. In view of the fact that many mature natural faults contain significant amounts of phyllosilicates, and are often foliated to some extent [*Wu et al.*, 1975; *Chester et al.*, 1993; *Snoke et al.*, 1999], our results raise questions regarding the validity of applying healing data obtained from experiments on monomineralic quartz gouge [*Fredrich and Evans*, 1992; *Karner et al.*, 1997; *Nakatani and Scholz*, 1999], and the

associated rate- and state- dependent friction parameters, to modelling seismic behaviour on natural faults. Our data suggest that for a foliated, phyllosilicate-rich fault gouge the general form of transient effects following velocity changes (as described by the rate- and state- dependent friction equations) will be similar to that observed in monomineralic gouge, but the associated healing rates will be much lower, since fluid-assisted healing is inhibited by the presence of phyllosilicates. Also, the transient peaks will be determined mostly by the dilatation behaviour occurring upon sliding, and not by gouge grain contact strength. As a next step towards a better understanding of fault behaviour, systematic experiments on foliated quartz plus phyllosilicate gouge under hydrothermal conditions are needed.

In addition, our data show that for clay-bearing faults the critical slip distance increased with progressive shear strain. A larger critical slip distance implies that larger displacements are needed to effectuate a given change in friction, which implies a greater tendency for stable sliding since instability is enhanced by rapid changes in friction. Hence our data suggest that large faults should become increasingly more stable with accumulating shear strain. In addition, the foliation intensity, and hence the degree of inhibition of fluid-assisted healing, is expected to increase with increasing shear strain in a fault gouge, again leading to increasingly stable behaviour with progressive shear strain. This may provide an explanation for the often-quoted decrease in seismicity with increasing fault offset [see e.g. *Wesnowsky, 1990*].

6.5 Conclusions

We performed slide-hold-slide experiments on brine-saturated simulated gouges of a) pure halite and b) halite + 25% kaolinite composition, with the aim of addressing the effect of phyllosilicates on fault healing. The following conclusions were reached:

1. Fluid-assisted fault healing is significantly retarded by the presence of phyllosilicates at halite grain boundaries. The effect is likely due to phyllosilicates inhibiting halite-halite grain contact healing, which accounts for much of the strengthening observed in pure halite gouge.
2. Whereas clay-free gouges show an increasing degree of healing with increasing shear displacement, clay-bearing gouges show the opposite: healing decreases with increasing shear strain. This can be explained by the progressive formation of a foliation with strain
3. We observed large differences in healing rates between clay-bearing and clay-free samples. Since natural faults contain significant amounts of phyllosilicates, our results raise questions regarding the usage of healing rates obtained from experiments on monomineralic gouge, and the application of rate- and state friction parameters obtained from these, to natural faults.

Chapter 7

A microphysical model for frictional-viscous flow at the brittle-ductile transition, with implications for crustal strength profiles

Submitted to Journal of Geophysical Research as: *B. Bos and C.J. Spiers, Frictional-viscous flow of phyllosilicate-bearing fault rock: Microphysical model and implications for crustal strength profiles*

Abstract. It is widely believed that around the brittle-ductile transition crustal faults can be significantly weaker than predicted by conventional two-mechanism brittle-ductile strength envelopes. Factors contributing to this weakness include the polyphase nature of natural rocks, foliation development, and the action of fluid-assisted processes such as pressure solution. Recently, experiments using halite/kaolinite mixtures as a rock analogue for the first time showed frictional-viscous behaviour (i.e. both normal stress and strain rate sensitive behaviour) involving the combined effects of pressure solution and phyllosilicates. This behaviour was accompanied by the development of a mylonitic microstructure. A quantitative assessment of the implications of this for the strength of natural faults has hitherto been hampered by the absence of a microphysical model. In this paper, a microphysical model for shear deformation of foliated, phyllosilicate-bearing fault rock by pressure solution-accommodated sliding along phyllosilicate foliae is developed. The model predicts purely frictional behaviour at low and high shear strain rates, and frictional-viscous behaviour at intermediate shear strain rates. The mechanical data on wet halite + kaolinite gouge compare favourably with the model. When applied to crustal materials, the model predicts major weakening with respect to conventional brittle-ductile strength envelopes, in particular around the brittle-ductile transition. The predicted strength profiles suggest that in numerical models of crustal deformation the strength of high strain regions could be approximated by an apparent friction coefficient of 0.25-0.35 down to depths of 15-20 km.

7.1 Introduction

Field observations show that crustal deformation is mostly localised into narrow fault zones. In numerical modeling of crustal dynamics, crustal rheology is generally modelled using a two-mechanism strength profile. The upper parts of the crust are modeled using a brittle-frictional faulting rheology, whereas the lower parts are described using a dislocation creep law for the relevant material, usually quartz or feldspar [Goetze and Evans, 1979; Govers and Wortel, 1995; Kohlstedt *et al.*, 1995; Ranalli, 1997]. This approach leads to a crustal or fault zone strength profile of the type shown schematically in Figure 7.1.

Though widely used, it has long been realized that this two-mechanism description of crustal rheology is drastically oversimplified, notably regarding the transition between brittle-frictional and ductile behaviour (loosely termed the brittle-ductile transition here). Firstly, such strength profiles are based on flow laws for monomineralic materials obtained from relatively low strain experiments. However, natural fault/shear zones are polymineralic, with individual minerals going through a brittle-ductile transition at different depths [Scholz, 1988; Handy, 1990; Handy *et al.*, 1999], and with mineral reactions progressively producing significant

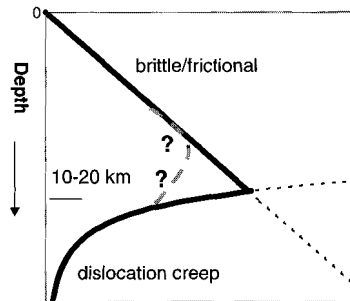


Figure 7.1. Schematic diagram showing the crustal strength profile defined by relations describing brittle/frictional behaviour (Byerlee's law) and dislocation creep (black lines). The hypothesized weakening around the brittle-ductile transition is shown by the dashed gray line. The profile is drawn for a single uniform strain rate and can be viewed applying to bulk crust or to fault zones.

portions of weak phyllosilicates [e.g. *Wintsch et al.* 1995]. Furthermore, with increasing strain, fault rocks often become foliated, allowing alignment and interconnection of weaker phases, in particular phyllosilicates, with associated effect on bulk rheology [*Shea and Kronenberg*, 1992; *Shea and Kronenberg*, 1993]. In addition, under the hydrothermal conditions pertaining around the brittle-ductile transition, where frictional sliding is inhibited by high confining pressures and crystal plastic flow by low-to-moderate temperatures, fluid-assisted deformation processes such as pressure solution are operative [*Rutter*, 1983; *Schwarz and Stoeckert*, 1996; *Stewart et al.*, 2000], and may significantly reduce long-term fault strength [*Sibson*, 1977; *Sibson*, 1983; *Lehner and Bataille*, 1984/85; *Chester and Higgs*, 1992; *Hickman et al.*, 1995]. Taken together, the above phenomena are expected to lead to truncation of the strength maximum at the brittle-ductile transition predicted by "classical" two-mechanism strength profiles, as qualitatively indicated in Figure 7.1 [*Sibson*, 1983; *Chester*, 1995; *Hickman et al.*, 1995]. Such a truncation of the strength profile can be expected to have a strong influence on the results of numerical modelling work on crustal dynamics, since the brittle-ductile transition region is the main load-bearing region of the crust. Moreover, a realistic description of the mechanical behaviour of fault zones at depths up to the brittle-ductile transition is imperative for understanding the seismic cycle. Despite the importance of the anticipated weakening effects in the brittle-ductile transitional region, very little quantitative information is available on these effects, in particular regarding the effects of fluid-assisted deformation processes.

In Chapters 3 and 4 of this thesis, we reported experiments showing frictional-viscous flow behaviour of simulated fault gouge (halite + kaolinite) sheared under conditions where pressure solution and cataclasis dominate over dislocation creep. By frictional-viscous behaviour we mean shear deformation behaviour in which the shear stress shows a significant dependence on both normal stress and strain rate. In our experiments, a transition was observed from purely frictional behaviour at low strain to frictional-viscous behaviour at high strain. This transition was accompanied by the development of an anastomosing, foliated microstructure, strongly reminiscent of natural S-C mylonites [*White et al.*, 1980; *Lister and Snoke*, 1984; *Passchier and Trouw*, 1996]. It was inferred that the observed rate-dependent behaviour occurred by a mechanism involving frictional sliding of the elongate halite clasts on the intervening kaolinite-rich foliae, with geometrical incompatibilities accommodated by pressure solution. The experiments provided, for the first time, experimental evidence of steady state fault creep accommodated by pressure solution, an idea that has been hypothesized for more than two decades [*Sibson*, 1977; *Rutter and Mainprice*, 1979; *Lehner and Bataille*, 1984/85]. The experiments also provide evidence that such a mechanism is strongly enhanced by, or maybe even critically dependent upon the presence of phyllosilicates. This is supported by recent field studies, which suggest that solution transfer processes may play an important role in allowing low stress, ductile deformation of phyllosilicate strands in major shear zones [*Wintsch et al.*, 1995; *Schwarz and Stoeckert*, 1996; *Stewart et al.*, 2000] under conditions where non-foliated or phyllosilicate-poor fault rocks do not deform.

However, to assess quantitatively the importance of the frictional-viscous behaviour reported in Chapters 3 and 4 for the long-term strength of natural phyllosilicate-bearing fault zones, and thus the implications of pressure solution controlled fault creep for crustal strength profiles, a microphysically-based model describing such behaviour is needed. Consequently, the aim of this paper is to develop a model for fault rock deformation by frictional sliding along phyllosilicate foliae, with accommodation of geometrical incompatibilities by pressure solution. Subsequently, the model predictions will be compared with our observations on halite/kaolinite gouge. Finally, the model will be applied to quartz-mica rocks, in order to estimate the effect of pressure solution controlled frictional-viscous behaviour on the strength of faults in the continental crust.

7.2 Previous data on frictional-viscous flow behaviour

In our previous experiments on simulated fault gouge (Chapters 3 and 4), brine-saturated mixtures of halite and kaolinite were sheared to high strains (shear strains up to 1000) in a rotary shear apparatus at room temperature, under conditions favouring pressure solution in wet halite, with negligible dislocation creep. The data showed a transition from frictional behaviour at small displacement to quasi-steady state frictional-viscous behaviour at large (>20 mm, shear strain ~35) displacement, accompanied by significant strain weakening. The mechanical behaviour observed at high strains, where steady state strength was reached, is illustrated in Figures 7.2a and 7.2b. These data show that halite/kaolinite gouge exhibited strongly rate-dependent steady state sliding behaviour at low (<1 $\mu\text{m/s}$) sliding velocities. In contrast, purely frictional behaviour (shear strength linearly dependent on normal stress and insensitive to sliding rate) was observed in pure kaolinite and pure halite gouge, showing that the rate-dependent behaviour requires the presence of both halite and kaolinite. Furthermore, it was observed that halite/kaolinite gouges saturated with an inert pore fluid also behave in a purely frictional manner, demonstrating that the rate-sensitive behaviour must be due to a fluid-assisted deformation mechanism.

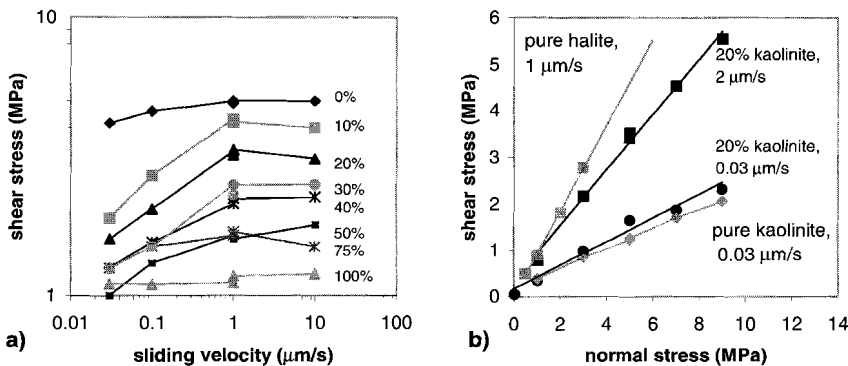


Figure 7.2. Data obtained from experiments on brine-saturated halite/kaolinite mixtures (see Chapter 3). For comparison, data on brine-saturated pure halite and pure kaolinite gouge are shown as well. a) Shear stress versus sliding velocity. Normal stress is 5 MPa, kaolinite content as indicated. b) Shear stress versus normal stress. Kaolinite content and sliding velocity as indicated. Note frictional-viscous flow behaviour in halite + kaolinite mixtures at velocities below 1 $\mu\text{m/s}$, and sliding velocity dependence of apparent friction coefficient (the slope of the line through the data in Figure 7.2b).

The microstructure of halite/kaolinite mixtures at mechanical steady state is shown in Figure 7.3a. Typically, the deformed gouge consists of isolated, augen-like clasts embedded in a contiguous, fine-grained halite/kaolinite matrix. The matrix consists of elongate, ribbon-shaped halite grains, surrounded by an anastomosing network of kaolinite. The material shows a wavy foliation, with regions displaying an oblique foliation alternating laterally with shear band-like zones, with subhorizontal- to synthetically oriented foliation. On average, the foliation is near-horizontal. Experiments performed to study the microstructural evolution of these gouges with shear (see Chapter 4) showed that the establishment of a contiguous network of matrix material coincides with the onset of a mechanical steady state. This suggests that steady state strength is controlled mostly by the rheology of the fine-grained matrix. Figure 7.3b shows a detail of the matrix. Neither grain shape nor foliation orientation track the finite strain ellipse, since in that case the foliation would be horizontal everywhere and the grains much more elongate. This implies that shear deformation within the matrix was inhomogeneous. It was proposed in Chapters 3 and 4 that

deformation occurred by a mechanism involving sliding of halite grains along anastomosing, phyllosilicate-rich foliae, with accommodation by pressure solution of the halite clasts and matrix grains. Deformation in the regions with oblique foliation and deformation within the shear bands were likely coupled, such that volume changes were minimal. A component of subcritical crack growth may also have contributed to the observed rate-dependent behaviour, but the lack of significant grain size reduction in the matrix with progressive strain (see Chapter 4) implies that cataclasis due to this process is of little importance. In the following, a microphysical model describing shear deformation by pressure solution-accommodated sliding will be developed. For this purpose, we assume that the average foliation orientation is horizontal. In the case of halite, the constitutive kinetic parameters for pressure solution are well-constrained [Spiers *et al.*, 1990]. Hence, our model can be tested by comparing its predictions with the mechanical behaviour observed in our previous experiments on halite/kaolinite gouge.

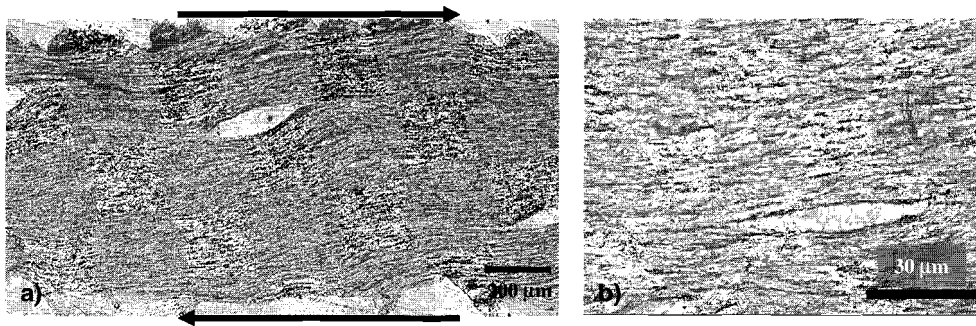


Figure 7.3. a) Typical microstructure of material deformed in the rate-sensitive regime, at sliding velocity $0.2 \mu\text{m/s}$ and 5 MPa normal stress. The microstructure shows elongated clasts embedded in fine-grained, foliated matrix. Shear sense is dextral. Total shear strain in this sample is 100. b) Detailed microstructure of matrix.

7.3 Model development

7.3.1 Model geometry and kinematics

Figure 7.4a shows a schematic diagram of our model microstructure. A contiguous, anastomosing network of phyllosilicate foliae surrounds elongated grains of a soluble solid. The phyllosilicates define a foliation that is horizontal on average. Figure 7.4b shows a volume of gouge material containing one wavelength of phyllosilicate-covered grain boundary (thick line). The amplitude of the foliation "waves" is denoted as h , the wavelength is $2d$, and the leading edge of the grains is inclined at an angle α to the shear plane.

We now assume that shear deformation occurs at constant volume by frictional sliding along or within the horizontal, phyllosilicate-coated grain boundaries, with accommodation by pressure solution, i.e., by diffusive mass transfer through the grain boundaries (dashed arrow) from the highly stressed "source" sites to the less stressed "sink" sites (see Figure 7.4b). The shear process envisaged is thus similar to diffusion-controlled sliding along a sinusoidal surface as modelled by *Raj and Ashby* [1971], but includes frictional sliding on the phyllosilicate foliae as an additional dissipative process. In the framework of the assumed microstructure and kinematics, the sliding process and pressure solution are clearly serial processes: matter must be dissolved at the

leading edge of grains for sliding to occur on the horizontal phyllosilicate foliae. Hence, the slowest or most difficult step controls the overall behaviour. This can be represented in terms of the mechanical analogue system drawn in Figure 7.5a. Here, a frictional slider (A, representing frictional sliding along phyllosilicate foliae) and a dashpot (B, representing the time-dependent pressure solution process) are connected in such a way that the strongest controls the overall strength. This rheological model will predict frictional behaviour at low shear strain rates, where pressure solution is relatively easy. At higher shear strain rates, however, pressure solution will take over as the strength-determining mechanism, leading to increasing shear stress with increasing shear strain rate.

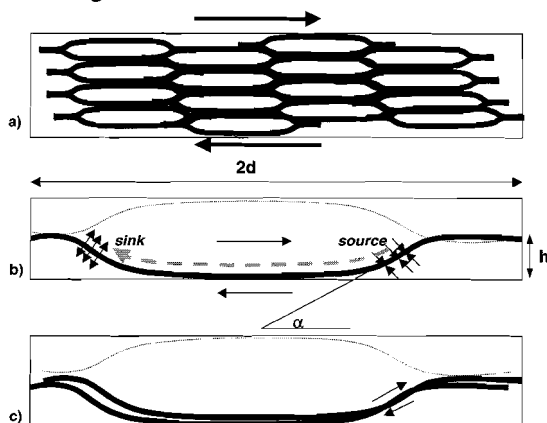


Figure 7.4. a) Schematic diagram of model microstructure, showing contiguous, anastomosing network of phyllosilicates separating elongate grains of a soluble solid. b) Schematic drawing of representative grain element of matrix, showing an active sliding surface in black. Shear sense is dextral. The diffusive mass flux from source to sink regions is indicated by a dashed arrow. The foliation waves have amplitude h , the grains have long axis d . The leading edge of the grain is inclined at angle α to the horizontal c) Schematic diagram illustrating behaviour at high velocities, where sliding along the leading edge of the grains leads to dilatation.

In this situation, on-going shear deformation can occur at zero porosity only if the macroscopic shear stress is below a critical value such that accommodation of horizontal intergranular sliding by pressure solution is favoured over sliding on the leading edge surfaces of the solid grains. If the shear strain rate is increased such that the shear stress attains this critical value, sliding along the leading edge planes will occur, producing dilatation (see Figure 7.4c) and thus creating porosity. Time-dependent compaction due to pressure solution will then tend to occur, in competition with shear-induced dilatation due to sliding up the leading edge. In general, the rate of compaction is expected to increase with increasing porosity. Therefore, the material will dilate only until a "steady state" porosity is reached at which the rates of compaction and dilatation balance. Shear deformation at this steady state porosity involves coupled sliding along the clay-coated grain boundaries plus pressure solution. In this scenario, the resolved shear stress due to pressure solution at the leading edges is constrained to lie on the criterion for the onset of dilatation for any given shear strain rate above that at which the critical shear stress for dilatation is first reached. The strengthening with increasing sliding rate due to pressure solution is balanced by the weakening due to decreased contact area (increased steady state porosity) with increasing sliding rate. Accordingly, the shear stress is independent of sliding velocity and linearly dependent on normal stress. Purely frictional behaviour is therefore expected in this case.

The behaviour around the critical shear stress at which dilatation starts may be incorporated in the mechanical analogue description by inserting an additional frictional slider C, as shown in Figure 7.5b. This slider does not actually represent a frictional sliding process in the gouge, but a limiting shear stress representing the stress needed for dilatation to occur. As explained above, at steady state, dilatation is balanced by pressure solution compaction, so C represents the "virtual work of dilatation" that is dissipated in driving the compaction by pressure solution needed to maintain constant volume. Element C acts in parallel with the dashpot representing pressure solution leading to shear (element B), thus limiting the stress on the dashpot to be at or below the dilatation criterion.

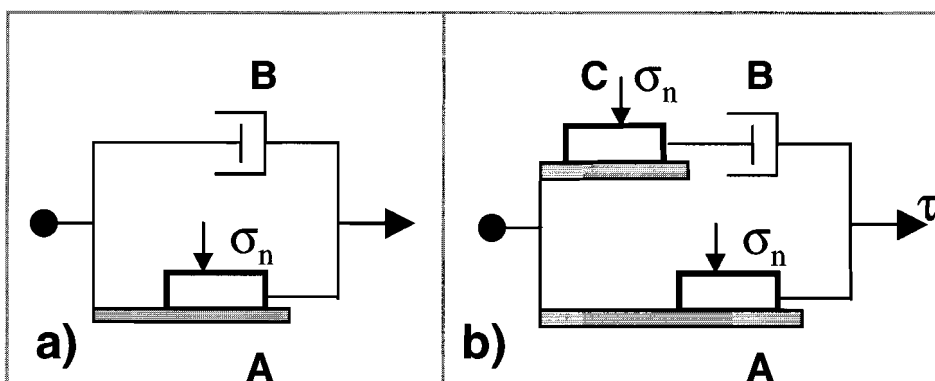


Figure 7.5. a) Mechanical analogue diagram for the postulated shear deformation process at zero porosity. Element A represents frictional sliding along phyllosilicate foliae, element B represents pressure solution. b) Mechanical analogue diagram including effect of dilatation by sliding along grain leading edges at high velocities (element C).

Strictly speaking, the frictional sliding accommodating pressure solution in the non-zero porosity scenario can only be approximated by element A, since this element represents sliding on the horizontal foliae. At shear strains above the critical value, however, sliding occurs on the leading edge of the grains and the horizontal boundaries will simply dilate (see Figure 7.4c). Also, the diffusion path in the pressure solution process will be modified due to dilatation. However, these effects are partly due to the choice of a simplified microstructure. In real situations, small amounts of dilatation will presumably lead to opening of grain boundary voids spanning only a small part of the grain boundary, and a large part of the horizontal surfaces will remain in contact. In the following, we will assume that the grain boundary area occupied by such grain boundary voids roughly equals the area of the corresponding leading edge, so that the effective sliding areas in the zero-porosity and non-zero porosity case are roughly equal. Also, we assume that the pressure solution process accommodating shear is not significantly influenced by the presence of small grain boundary voids. In this case, frictional sliding and pressure solution leading to shear can be represented by slider A and B, respectively, both at and below the critical stress.

Now, in the situation depicted in Figure 7.5b, at low velocities grain contact sliding (element A) is accompanied by pressure solution (element B), and element C is inactive. The total stress will be dominated by element A at the lowest velocities, leading to frictional behaviour, and by element B at higher velocities, leading to viscous behaviour. At even higher velocities, the shear stress becomes high enough for the strength of C (the dilatation criterion) to be exceeded. At this point, the stress in the upper branch of Figure 7.5b is constrained to remain at the level dictated by element C, i.e. to remain at the threshold of dilatation.

In the following section, we will develop a rheological model based on Figure 7.5b. A necessary condition for the high stress, rate-insensitive scenario of sliding at the critical stress is that during steady state sliding, the competing effects of dilatation and compaction can indeed balance, so that steady state deformation occurs at constant volume. Our compaction data (cf. Figure 3.6) suggest that in our rotary shear experiments on halite + kaolinite this is indeed the case: upon increasing the shear velocity only transient dilatation was observed, after which the sample deformed at roughly constant volume again.

It should be noted that the kinematic scenario of steady state shear at non-zero porosity as described above is expected to be valid only at low porosity, i.e. at shear strain rates just above the

critical value mentioned above. At higher shear strain rates, dilatation will proceed to such an extent that grains start "hopping over" each other before the contact area has decreased enough for pressure solution to take over as the shear-accommodation mechanism again. Such dilatation may lead to microstructural modifications such as localisation, or possibly cataclasis, in which case our model microstructure breaks down. The mechanical behaviour displayed in these cases will be of frictional nature. Since the present work is concerned mainly with modelling the rate-sensitive behaviour due to pressure solution, these cataclastic processes will not be modelled in detail.

7.3.2 Model formulation

From Figure 7.5b, during fault shear at constant strain rate, it follows from mechanical analogue theory [e.g. *Ranalli, 1995*] that the shear stress contributions of the different processes to the total shear stress τ are related via the equation

$$\tau = \tau_A + \left(\frac{I}{\tau_B} + \frac{I}{\tau_C} \right)^{-1} \quad (7.1)$$

where τ_A , represents the shear stress contribution due to frictional sliding along the phyllosilicate foliae, τ_B is the shear stress contribution due to pressure solution and τ_C represents the shear stress corresponding to the dilatancy criterion mentioned above. In the following, we will derive expressions for the three contributions τ_A , τ_B and τ_C .

First, the shear stress contribution due to frictional sliding along the phyllosilicate foliae, τ_A , can be written

$$\tau_A = P \mu_{gb} \sigma_n \quad (7.2)$$

where P is a factor expressing the proportion of the grain boundary area undergoing sliding (which is of order $\frac{3}{4}$ in our model microstructure) and μ_{gb} is an apparent grain boundary friction coefficient. Note that in general the apparent grain boundary friction coefficient may represent sliding of clasts along phyllosilicate layers, but also sliding within the phyllosilicate layers. Grain boundary cohesion is assumed to be negligibly small, since phyllosilicates are thought to inhibit contact adhesion [*Hickman and Evans, 1995*]. Instead of frictional intergranular sliding, a creep relation for basal dislocation glide within the phyllosilicates could also be inserted here.

From our preceding considerations it follows that τ_C equals the shear stress that would be needed to dilate the sample. This can be written

$$\tau_C = \tan \alpha \sigma_n \quad (7.3)$$

where α is defined in Figure 7.4b. Note that α is different from the friction angle used in granular mechanics, since this includes grain boundary friction next to grain packing, whereas in our case α is purely a microstructural parameter, and frictional sliding along the leading edge is represented by element A in Figure 7.5b.

For the case of pressure solution (element B in Figure 7.5), we consider the volume represented in Figure 7.4b. The process of pressure solution involves the series-sequential steps of dissolution at source sites (i.e. the top right region of the grains), diffusion through the grain boundary zone (phyllosilicate foliae), and precipitation at the sink sites (lower left region of the grains). The phyllosilicate foliae at grain boundaries are assumed to contain a fluid phase, either in

the form of an adsorbed thin film [Rutter, 1976; Renard and Ortoleva, 1997] or in the form of a dynamically stable island-channel structure at the boundary between phyllosilicates and halite [Raj and Chyung, 1981; Raj, 1982; Lehner, 1990; Spiers and Schutjens, 1990]. The grain boundary zone is characterized by an effective thickness δ and an effective diffusion coefficient D . To derive a relation between the shear stress contribution due to pressure solution and the shear strain rate, we follow Lehner and Bataille [1984/85] and Spiers and Schutjens [1990] in treating pressure solution as a non-equilibrium, dissipative process.

Assuming no increase in internal energy or entropy during deformation, the first law of thermodynamics requires that the rate of external work done on the fault zone per unit volume equals the rate of dissipation ($\dot{\Delta}$) due to pressure solution [De Groot and Mazur, 1962; Prigogine, 1967; Lehner and Bataille, 1984/85]. For isovolumetric, steady state conditions this can be written

$$\tau\dot{\gamma} = \dot{\Delta} \quad (7.4)$$

where τ is shear stress, and $\dot{\gamma}$ is shear strain rate. Now, the rate of energy dissipation due to pressure solution can be written as the product of a mass flux and a thermodynamic force, [Lehner and Bataille, 1984/85; Spiers and Schutjens, 1990], that is as

$$\dot{\Delta} = \dot{M}\Delta\Pi \quad (7.5)$$

Here the flux \dot{M} is the mass transfer rate per unit volume of fault zone ($\text{kg}/\text{m}^3\text{s}$) and the force $\Delta\Pi$ is the average chemical potential difference between source and sink sites (J/kg) driving pressure solution. The expression for the dissipation due to steady state pressure solution is dependent on which of the serial processes of dissolution, diffusion and precipitation is slowest, and hence rate-controlling. For the case of pressure solution in halite, diffusion is known to be the rate-controlling mechanism [Spiers *et al.*, 1990; Spiers and Brzesowsky, 1993]. To extend the applicability of our model to other materials, we will nevertheless derive expressions for the dissipation rate for both the diffusion controlled and the interface reaction controlled cases.

Pressure solution: diffusion controlled case. Grain boundary diffusion along the phyllosilicate foliae is governed by Fick's law, which can be written:

$$J = \rho_f D \text{grad}C \quad (7.6)$$

where J is the mass flux, ρ_f is fluid density and $\text{grad}C$ is the (stress-induced) concentration gradient along the contact (concentration in units of mass fraction). At each grain contact, this flux acts through a diffusion window $w\delta$, where w is the width of the contact. The rate of mass transfer per contact (kg/s) is then

$$J^* = w\rho_f D\delta \text{grad}C \quad (7.7)$$

Furthermore, using

$$\text{grad}C = \frac{C_s M_s}{RT} \text{grad}\Pi \quad (7.8)$$

where C_s and M_s are the solubility and molar mass of the solid, respectively, R is the gas constant and T is absolute temperature, and assuming the potential difference acts over an average diffusion distance d , the total mass flux per contact (kg/s) becomes

$$\dot{m} = \frac{\rho_f w D \delta C_s M_s}{RTd} \Delta \Pi \quad (7.9)$$

Now, the number of grains actively undergoing pressure solution in unit volume of fault zone is $N=A/(hwd)$, where A is a constant reflecting the proportion of grain contacts actively dissolving at any instant of time. The total rate of mass transfer per unit volume of fault zone ($\text{kg/m}^3\text{s}$) is then

$$\dot{M} = \frac{A \rho_f D \delta C_s M_s}{RThd^2} \Delta \Pi \quad (7.10)$$

Equation (7.10) constitutes the above mentioned microscale relation between force and flux in the case of diffusion controlled pressure solution creep. Substituting for $\Delta \Pi$ from (7.5) yields

$$\dot{\Delta}_d = \frac{RThd^2}{A \rho_f D \delta C_s M_s} \dot{M}^2 \quad (7.11)$$

We now proceed to derive an equation relating the rate of mass transfer per unit volume of fault zone to the imposed shear strain rate. On the scale of our representative grain (see Figure 7.4b), the shear strain rate can be written

$$\dot{\gamma} = v_{diss} / h \quad (7.12)$$

where v_{diss} is the average dissolution velocity of the contact in the direction of fault slip. Moreover, the mass transfer rate per contact can be related to v_{diss} by

$$\dot{m} = hw \rho_s v_{diss} \quad (7.13)$$

where ρ_s is the solid density, the angle α is defined in Figure 7.4b, and it is assumed that the area of dissolving contact is $hw/\sin\alpha$. Using $\dot{M} = \dot{m}/(hwd)$, and substituting for v_{diss} from (7.12) into (7.13), the mass transfer rate per unit volume of gouge can be expressed as a function of strain rate by

$$\dot{M} = \frac{Ah\rho_s}{d} \dot{\gamma} \quad (7.14)$$

Equation (7.14) can now be substituted into (7.11) to yield the final expression for the rate of dissipation due to diffusion controlled pressure solution. Also making use of

$$\frac{\rho_s}{M_s} = \frac{1}{\Omega_s}, \quad (7.15)$$

where Ω_s is the molar volume of the solid, the result is

$$\dot{\Delta}_d = \frac{A \alpha \rho_s RTh^3}{\rho_f D \delta C_s \Omega_s} \dot{\gamma}^2 \quad (7.16)$$

Combining this with (7.4) and using $d=Bh$, where B is the aspect ratio (length/width) of the grains, yields the following expression for the shear stress contribution due to diffusion controlled pressure solution:

$$\tau_d = \frac{A\rho_s RTd^3}{B^3 \rho_f D\delta C_s \Omega_s} \dot{\gamma} . \quad (7.17)$$

Pressure solution: interface reaction controlled case. For the kinetics of dissolution or precipitation, a phenomenological relationship of the form

$$v_{s,p} = k_{s,p} M_s \left(\frac{\Delta\Pi}{RT} \right)^n \quad (7.18)$$

can be postulated [Lehner and Bataille, 1984/85], in accordance with experimental data on dissolution/growth kinetics. Here, k is phenomenological rate coefficient, which may differ for dissolution (subscript s) and precipitation (subscript p). Following Lehner and Bataille [1984/85], the exponent n is taken to be unity here, although this need not always be the case (cf. De Meer and Spiers [1997]). Since the surface areas of dissolution and precipitation are roughly equal in our model geometry the two processes must proceed at equal rates under closed system conditions. Therefore, the analysis for the dissolution- and precipitation controlled cases are essentially equivalent. As in the foregoing case of diffusion control, the mass transfer rate is written as a function of driving force using equation (7.13) and (7.18). This yields

$$\dot{m} = \frac{k_{s,p} M_s h w \rho_s}{RT} \Delta\Pi \quad (7.19)$$

Again using $\dot{M} = \dot{m}A/hwd$ and substituting for $\Delta\Pi$ from (7.5), the rate of dissipation due to dissolution or precipitation reactions can be written in terms of the mass transfer rate per unit volume of fault zone as

$$\dot{\Delta}_{s,p} = \frac{RTd}{A k_{s,p} \rho_s M_s} \dot{M}^2 \quad (7.20)$$

Again using (7.14) and (7.15) and combining with (7.4), the relation between shear stress and strain rate for the interface-reaction controlled pressure solution can be written

$$\tau_{s,p} = \frac{ARTd}{B^2 k_{s,p} \Omega_s} \dot{\gamma} . \quad (7.21)$$

Final model. We now use the above expressions for the shear stresses τ_A , τ_C and $\tau_B = \tau_{d,s,p}$ to obtain the complete model for shear deformation of phyllosilicate-rich fault rock under conditions favouring pressure solution. To do this, we substitute (7.2), (7.3) and either (7.17) or (7.21) into (7.1). This yields

$$\tau = P\mu_{gb}\sigma_n + \frac{\sigma_n \tan \alpha K_d \dot{\gamma}}{\sigma_n \tan \alpha + K_d \dot{\gamma}} \quad (7.22)$$

for the case of diffusion controlled pressure solution, where K_d is a kinetic factor, defined

$$K_d = \frac{A\rho_s RTd^3}{B^3 \rho_f D\delta C_s \Omega_s} . \quad (7.23)$$

For the case of interface reaction controlled pressure solution the expression is

$$\tau = P\mu_{gb}\sigma_n + \frac{\sigma_n \tan \alpha K_{s,p} \dot{\gamma}}{\sigma_n \tan \alpha + K_{s,p} \dot{\gamma}} , \quad (7.24)$$

where $K_{s,p}$ is defined as

$$K_{s,p} = \frac{ARTd}{B^2 k_{s,p} \Omega_s} . \quad (7.25)$$

7.4 Application to the system halite + kaolinite

In this section, we will illustrate the general behaviour predicted by the model. We will then compare the model predictions with our experimental data on halite + kaolinite gouge. For the value of the grain boundary friction coefficient μ_{gb} we use our previously measured friction coefficient for wet kaolinite gouge, i.e., 0.2 (see Chapter 3). This value is low compared to other experiments on wet kaolinite gouge, performed at higher pressures, in which values of 0.4-0.6 were measured [Rutter, 1979; Rutter and Maddock, 1992; Morrow *et al.*, 2000]. However, it should be noted that the friction coefficient measured in experiments on gouge layers is not necessarily equal to the solid/phyllsilicate or phyllsilicate-phyllsilicate grain boundary friction coefficient, since the measured friction coefficient of gouge may be determined by grain boundary friction as well as by gouge microstructure. The kaolinite-rich gouges that yielded friction values of 0.4-0.6 show distributed deformation and the formation of a steep foliation and R-shears [Rutter, 1979; Rutter *et al.*, 1986]. Unfortunately, Morrow *et al.* [2000] did not show any microstructures of their deformed samples. In our pure kaolinite experiments, deformation was localised on a horizontal Y-shear. This could explain our lower friction coefficient, since sliding along the foliation in an obliquely foliated gouge requires dilatation in addition to overcoming grain boundary friction, both contributing to the measured shear stress. This implies that our measured value of kaolinite friction is probably more close to the grain boundary friction coefficient of kaolinite than obtained in studies showing distributed deformation. The experiments of Morrow *et al.* [2000] showed a significant lubrication effect of water in various phyllsilicate minerals. The weakening/lubrication effect on kaolinite due to the presence of water measured in our experiments (see Chapter 3) is similar in magnitude to that reported by Morrow *et al.* (i.e., a reduction in μ of 0.2). Since it is the grain boundary friction coefficient and not the microstructure that is likely to be instantaneously influenced by the presence of fluid, this observation again suggests that the difference between our friction values and other findings can be attributed to microstructural factors.

Pressure solution in halite is known to be diffusion controlled. The effective diffusion factor $D\delta$ was determined by *Spiers et al.* [1990] for halite-halite interphase boundaries and by *Hickman and Evans* [1995] halite-silica interphase boundaries. Both studies obtained a value of the order of $4 \times 10^{-19} \text{ m}^3/\text{s}$. Experimental data indicate that the presence of clays at halite grain contacts causes a fivefold increase in the rate of pressure solution [*Hickman and Evans*, 1995]. Assuming that this effect is due to enhanced grain boundary diffusion, we multiplied the diffusion factor mentioned above by a factor 5. We chose a value for d of $20 \mu\text{m}$, representative of the average grain size in the matrix of our sheared samples (see Figure 7.3b), and we took the average aspect ratio B to be 5. Finally, the proportion of actively dissolving grain boundaries A was assumed to be 0.5.

The general behaviour predicted by our model at room temperature is illustrated in Figures 7.6. Figure 7.6a shows shear stress versus sliding velocity, using various dilatation angles α and grain sizes d . Three regimes of behaviour can be identified, as already anticipated qualitatively. At high slip rates (regime 3 in Figure 7.6a), shear stress is insensitive to shear strain rate. This is the region where in our model shear strength is controlled by elements A and C (see Figure 7.5b), and the predicted strength is simply the sum of the grain boundary friction coefficient and $\tan\alpha$, multiplied by the normal stress. We will refer to this value as the maximum shear strength. With decreasing sliding velocity a regime is entered where the shear strength is strongly strain rate sensitive (regime 2). This is the region where shear stress is controlled by pressure solution (element B), and to some extent by sliding friction (element A). Note that, although a linear shear stress versus strain rate relation was inserted for the pressure solution process, the shear stress predicted by the

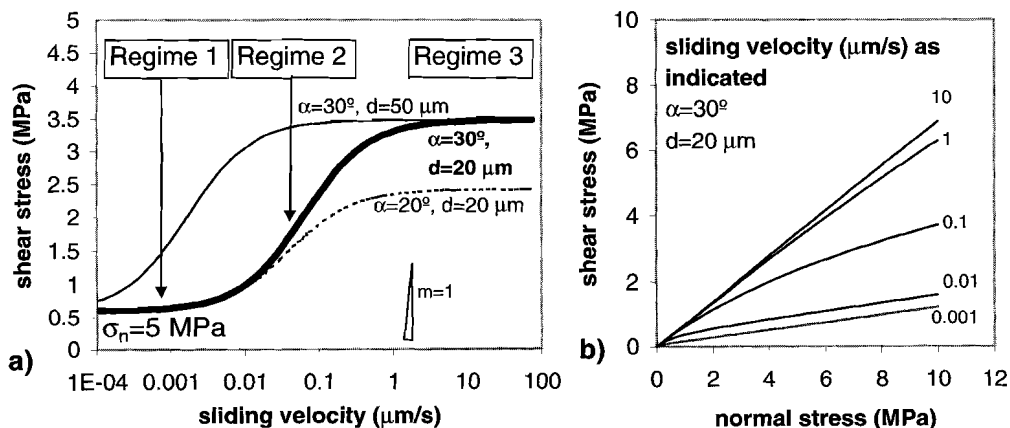


Figure 7.6. Model predictions for halite/kaolinite gouge, at 5 MPa normal stress. Values for α and grain size d used are indicated. Slope $m=1$ indicates a strain rate sensitivity of shear stress corresponding to a linear viscous material. Three regimes of behaviour can be identified. With reference to Figure 7.5, at high velocities a frictional regime (regime 3) is predicted, with strength dominated by elements A and C. At intermediate velocities a strongly rate-dependent regime (regime 2) is predicted, dominated by element B, and at low velocities a frictional regime (regime 1) dominated by element A. b) Predicted shear stress versus normal stress behaviour. Note strong rate-sensitivity of apparent friction coefficient (i.e., the slope of the lines), in particular at sliding velocities between 1 and $0.01 \mu\text{m/s}$.

model does not show linear viscous behaviour (see Figure 7.6a) in any strain rate interval: instead the maximum predicted value of the strain rate sensitivity m is ~ 0.3 , rather than the value of 1

expected for linear viscous behaviour. Finally, at low velocities (regime 1) the model predicts shear strength to be independent of sliding velocity, like at high velocities, but the strength is much lower. In this region, pressure solution is relatively fast and shear stress is determined mainly by the grain boundary friction coefficient. We will refer to this value as the "minimum shear strength".

It can be seen from Figure 7.6a that the value of the maximum shear stress, as well as the maximum strain rate sensitivity reached, is strongly dependent on the chosen dilatation angle α . Increasing the grain size does not change the values of maximum and minimum shear stress, but shifts the transition between them to lower strain rates. Figure 7.6b shows the predicted shear stress versus normal stress behaviour. The apparent friction coefficient (i.e. the slope of the plot) is predicted to be strongly strain rate sensitive, in particular at velocities corresponding to regime 2 in Figure 7.6a.

The model predictions will now be compared to our data on halite + kaolinite gouge. A complication now arises, since in the experiments different clay contents were used, whereas clay content was not incorporated as a parameter in our model. However, from the gouge microstructures (see Figure 3.10 of this thesis) it can be seen that the average foliation angle α decreases with increasing clay content. Figure 7.7 shows shear stress versus sliding velocity, with our data points for gouges containing 10, 30 and 50% kaolinite. The dashed lines are model predictions for the dilatation angles of 30, 20 and 10°, which are considered roughly representative of the microstructure of gouges with kaolinite contents of 10, 30 and 50%. It can be seen from Figure 7.7 that reasonable agreement is obtained between the model and our experimental data. The strength values predicted by the model fall in the range of the observed values. Moreover, the velocity range of rate dependent behaviour (regime 2) predicted by the model is similar to that observed in our data. The model fits the data particularly well for low-to-intermediate clay contents (10 and 30%), where the rate-sensitivity of strength was strongest.

At velocities above 1 $\mu\text{m/s}$ the model tends to overestimate the measured strength. This may be due to the fact that deformation at high velocities involves cataclasis and/or faulting, as discussed in section 7.3.1. In addition, the fit of the model to our data is not particularly good for high clay contents. A feature of the model that is not observed in the data is the low velocity

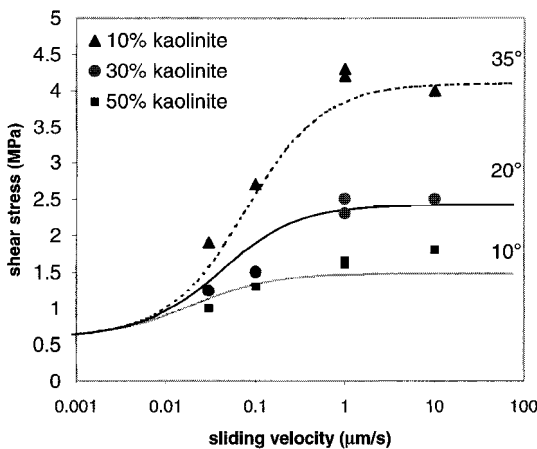


Figure 7.7. Comparison of model to data obtained from experiments on halite + kaolinite samples (cf. Chapter 3). Model curves are shown for values of α of 10, 20 and 30°. Experimental data are shown for kaolinite contents of 10, 30 and 50%, which showed similar values for α .

regime of rate-independent strength. This may be due to the fact that the imposed sliding velocities were not low enough. To verify this, experiments are needed on an apparatus with which even slower sliding rates can be attained. Alternatively, a smaller initial grain size could be used. Lastly we note that the fit

of our model to the data, though seemingly reasonable, should be viewed with some caution: As demonstrated by Figure 7.7, the model is strongly sensitive to the chosen values for dilatation angle α and grain size d , parameters which show considerable spread and are spatially inhomogeneous in our samples. Nevertheless, we believe that the rough agreement between the

model and our data strongly supports our inference that deformation in our samples indeed occurred by a mixed grain boundary sliding plus pressure solution mechanism, at least at sliding velocities of 1 $\mu\text{m/s}$ and lower and at clay contents <50%.

7.5 Application to natural faults: a strength profile for zones of high strain

7.5.1 Model parameters

In this section, our model will be applied to natural materials, in order to provide a quantitative estimate of the effect of the pressure solution controlled creep process on the strength of crustal shear zones. The model will be applied to four different tectonic settings: (1) a transcrustal strike slip fault zone (such as the San Andreas fault zone), (2) a normal fault zone accommodating crustal extension, (3) a thrust fault zone deforming under high pressure, low temperature conditions, typical of a subduction setting, and (4) a thrust fault zone deforming under intermediate conditions typical of continent-continent collision zones. The strength profiles shown are not meant to be applied directly to a particular region, but rather are illustrative in nature. The geothermal gradients chosen for the models are 25°C/km for case (1), consistent with heat flow data from the San Andreas Fault Zone region [Lachenbruch and Sass, 1980; Sibson, 1983], 35°C/km for case (2), 15°C/km for case (3) [Schwarz and Stoeckert, 1996], and 25°C/km for case (4) [Spear, 1993]. For these examples, we assume hydrostatic pore pressure at all depths. Crustal density is taken to be 2.75 g/cm^3 . At upper crustal levels we will assume purely frictional behaviour. For this region, we used a coefficient of friction of 0.75, typical for a wide range of materials [Byerlee, 1978].

The frictional strength of a fault is a function of the type of fault, the effective pressure, and the coefficient of friction. For the case of a strike-slip fault, we assume that the effective overburden pressure, σ_v , is the intermediate principal effective stress, and is equal to the mean effective stress, i.e. $\sigma_v = \frac{1}{2}(\sigma_1 + \sigma_3)$, where σ_1 and σ_3 are the maximum and minimum principal effective stresses, respectively. In this case, the minimum differential stress ($\sigma_1 - \sigma_3$) to activate sliding is [Sibson, 1974; Ranalli, 1995]

$$\sigma_1 - \sigma_3 = 2\sigma_v(R' - 1)/(R' + 1), \quad (7.26)$$

where

$$R' = \sigma_1/\sigma_3 = \left[(1 + \mu^2)^{1/2} - \mu \right]^{-2}. \quad (7.27)$$

For the case of a normal fault and a thrust fault, σ_v equals σ_1 and σ_3 , respectively, and the minimum differential stress to activate sliding is

$$\sigma_1 - \sigma_3 = \sigma_v(R' - 1)/R' \quad (7.28)$$

for a normal fault, and

$$\sigma_1 - \sigma_3 = 2\sigma_v(R' - 1) \quad (7.29)$$

for a thrust fault. Effective overburden pressure is given by

$$\sigma_v = \rho_s g z (1 - \lambda) \quad (7.30)$$

where ρ_s is solid density, g is gravitational acceleration, z is depth and λ is the pore fluid factor, i.e., the ratio of pore fluid pressure to overburden pressure, which for our case takes the value 0.36. The minimum shear stress required to activate frictional sliding is

$$\tau = \frac{1}{2}(\sigma_1 - \sigma_3) \sin[\tan^{-1}(1/\mu)] \quad (7.31)$$

where $(\sigma_1 - \sigma_3)$ is given by (7.26), (7.28) or (7.29).

To describe crystal plastic flow at greater depth we use the creep equation for wet quartz of *Luan and Paterson* [1992], rewritten for the case of simple shear as

$$\dot{\gamma} = 3^{(n+1)/2} A^* \tau^n \exp\left(\frac{-Q}{RT}\right) \quad (7.32)$$

where $n=2.3$, $A=1.8 \times 10^{-18}$, and the activation energy Q is 150 kJ/mole.

For the frictional-viscous flow mechanism described above we assume a foliated quartz-mica mylonite. The dilatation angle is taken to be 20° , the grain size d is taken to be 25 μm and the grain aspect ratio is taken to be 4. As in the case of kaolinite, the appropriate value for the apparent grain boundary friction coefficient is not well constrained. Conventional friction experiments are again of little use, because these experiments typically measured the frictional strength of phyllosilicate gouge, whereas the local contact friction coefficient is required. From the tribology literature, it seems that the friction coefficient of a flat, ideally oriented mica grain may be as low as 0.01 in the presence of water [*Israelachvili*, 1992]. However, this value was measured at fairly low normal stress, and whether it is realistic for natural situations is not clear. An upper bound for the sliding strength of phyllosilicate foliae may be formed by the strength of micas undergoing basal glide. The strengths of mica single crystals oriented for glide are very low (< 10 MPa) at geologic deformation rates [*Shea and Kronenberg*, 1992; *Wintsch et al.*, 1995]. Deformation studies of basal dislocation glide in muscovite single crystals at 400°C show that strength is pressure sensitive up to 50 MPa normal stress, and can be approximated by an apparent friction coefficient of ~ 0.12 over pressures corresponding to the depth range 0-15 kilometers [*Mares and Kronenberg*, 1993]. In this study we take a value for the grain boundary friction coefficient of 0.2, but in actual fact it may be lower, and more detailed work is needed on this subject.

For the solubility of quartz the relation reported by [*Rimstidt*, 1997] was used, neglecting small effects of pressure [*Fournier and Potter*, 1982]. The interface reaction rate constants k_{diss} and k_{prec} for quartz were taken from [*Bird et al.*, 1986]. Here, the rate constant is referred to a standard system of 1 m^2 of surface area subjected to 1 kg of water. As pointed out by *Paterson* [1995], to express the values obtained by *Bird et al.* [1986] in m/s, the value for the dissolution coefficient must be divided by ρ_s , and the value of the precipitation coefficient was multiplied by the product $M_s \Omega_s C^{-1}$.

The diffusion coefficient of fluid-filled grain boundaries undergoing pressure solution is the subject of long-standing debate. Pressure solution compaction experiments indicate a grain boundary diffusion process similar to ionic diffusion in a static fluid, but the absolute value of the grain boundary diffusion coefficient may be 2 to 3 orders of magnitude lower than that of ionic diffusion in a bulk fluid [*Gratier and Guiget*, 1986; *Spiers et al.*, 1990]. On the other hand, grain boundary coefficients determined in novaculites by [*Farver and Yund*, 1991] at temperatures of $450\text{-}800^\circ\text{C}$ yield much lower diffusion coefficients, and an activation energy of ~ 113 kJ/mole, i.e.,

much higher than that for ionic diffusion. We have followed [Nakashima, 1995] in taking an activation energy characteristic of ionic diffusion (i.e. ~20 kJ/mole) and extrapolated the value for diffusivity obtained by [Gratier and Guiget, 1986]. However, it should be stressed here that the grain boundary diffusivity should be considered an ill-constrained parameter, and determination of grain boundary diffusivity during pressure solution in both synthetic and natural materials is an important future research goal.

The relation between depth and fault normal stress is more complicated in the case of frictional-viscous behaviour than in the frictional case because the apparent coefficient of friction itself, and hence the contribution of the differential stress to the normal stress on the fault, is expected to be a function of depth. The normal stress on the fault is given by

$$\sigma_n = \frac{1}{2}(\sigma_1 + \sigma_3) - \frac{1}{2}(\sigma_1 - \sigma_3) \cos[\tan^{-1}(1/\mu_{app})] \quad (7.33)$$

For the case of a strike slip fault, using the relation

$$\sigma_v = \frac{1}{2}(\sigma_1 + \sigma_3) \quad (7.34)$$

and

$$\tau = \frac{1}{2}(\sigma_1 - \sigma_3) \sin[\tan^{-1}(1/\mu_{app})] = \mu_{app} \sigma_n, \quad (7.35)$$

σ_n can be written in terms of the apparent friction coefficient μ_{app} and the overburden pressure σ_v as

$$\sigma_n = (1 + \mu_{app}^2)^{-1} \sigma_v \quad (7.36)$$

Similarly, for a normal fault, using $\sigma_v = \sigma_1$ and (7.28), the relation between normal stress and overburden pressure is

$$\sigma_n = \frac{1}{2} \sigma_v \left[\left(1 + \frac{1}{R'}\right) - \left(1 - \frac{1}{R'}\right) \cos(\tan^{-1} \mu_{app}^{-1}) \right], \quad (7.37)$$

and for a thrust fault, using $\sigma_v = \sigma_3$ the relation becomes

$$\sigma_n = \frac{1}{2} \sigma_v \left[(R' + 1) - (R' - 1) \cos(\tan^{-1} \mu_{app}^{-1}) \right]. \quad (7.38)$$

Note that in this case although an apparent friction coefficient is used a strictly linear relation between τ and σ_n , is not implied, since μ_{app} may vary with depth due to the increased contribution of pressure solution with increasing temperature. It follows from the above that the relation between σ_n and σ_v depends on the apparent friction coefficient. Hence, the exact relation between can only be obtained by iteration. However, our model dictates that the apparent friction coefficient always lies between the grain boundary friction coefficient μ_{gb} (the "minimum strength" mentioned in section 7.4) and the sum of μ_{gb} and $\tan\alpha$. (i.e., the "maximum strength" mentioned in 7.4). For the values assumed above this means that the apparent friction coefficient varies between 0.2 and 0.65. In the case of a strike-slip fault, then, the value of the term $(1 + \mu^2)^{-1}$ varies between 0.76 and 0.96. Taking an average value for μ_{app} of 0.40 throughout the crust results in only a limited error in the term $(1 + \mu^2)^{-1}$ (<8%). For the other geometries, the error is of similar

magnitude. This error is considered small enough for present purpose, considering the large uncertainties involved in the other parameters. However, it should be borne in mind that at shallow depths, where frictional sliding plus dilatation/cataclasis determines fault strength, our model slightly underestimates the normal stress on the fault whereas at greater depth the normal stress is slightly overestimated.

7.5.2 Crustal strength profiles incorporating pressure solution controlled frictional-viscous behaviour

Before presenting our model predictions, it should be noted that the quality of the model predictions is, as always, determined by the quality of the model assumptions and input data. In this case, the uncertainties in many of the input parameters, in particular grain boundary friction coefficient and diffusion coefficient, are considerable. Therefore, the strength profiles presented here should be viewed with caution. With these reservations, we nonetheless show crustal strength profiles for the four cases mentioned above in Figures 7.8a-d. In Figure 7.8, "Byerlee's law" friction is shown using a dashed line, whereas dislocation creep curves for different strain rates (as indicated) are shown using solid gray lines. The strength as predicted by our model is shown as black lines for strain rates of 10^{-10} and 10^{-12} s⁻¹. This corresponds to a fault zone sliding at ~30 mm/yr, such as the San Andreas Fault, where sliding is accommodated in a fault zone of 10 and 1000 m wide, respectively. Curves are shown for diffusion controlled pressure solution, since the model results indicate that diffusion is the rate-limiting step in pressure solution at all depths in our model. In natural fault zones, strain rate is not expected to be constant with depth; rather, shear zones are known to widen with increasing depth, leading to a decrease in average strain rate with depth. As a crude way of incorporating this in discussing our model results, we tentatively assume a strain rate of 10^{-12} s⁻¹ in the lower crust where dislocation creep dominates, and a strain rate of 10^{-10} s⁻¹ in phyllosilicate-rich shear zones in the middle-to-upper crust, so a crustal strength profile is outlined by the bold lines in Figures 7.8.

The model shows a transition from behaviour closely resembling Byerlee's law at shallow depths (corresponding to regime 3 in Figure 7.6) to behaviour where strength is controlled by grain boundary friction (regime 1 in Figure 7.6) at greater depths. The transition region is the pressure solution controlled regime (regime 2 in Figure 7.6), where mechanical behaviour is strongly rate-sensitive as well as normal stress sensitive. For the conditions and strain rates considered above, this regime dominates over the depth range 5-20 kilometers. Indeed, this is the depth range where solution transfer processes are expected to be active as inferred from microstructural observations [Groshong, 1975; McClay, 1977; Rutter, 1983; Schwarz and Stoeckhert, 1996]. The depth at which frictional-viscous behaviour is expected varies strongly with the geotherm and the type of fault. Nevertheless, in all cases the rate-sensitive behaviour occurs at depths where temperatures are too low for dislocation creep to be active at significant rate. Thus, our model predicts that a significant range of the crust should show mechanical behaviour that is both strain rate and normal stress dependent. At depths greater than 15-20 kilometer, the model predicts that dislocation creep takes over as the strength determining mechanism. Because of the lower stresses supported by the frictional-viscous mechanism, the depth at which dislocation creep becomes the strength determining mechanism is shifted to slightly deeper levels in our model compared to a classical two-mechanism strength profile.

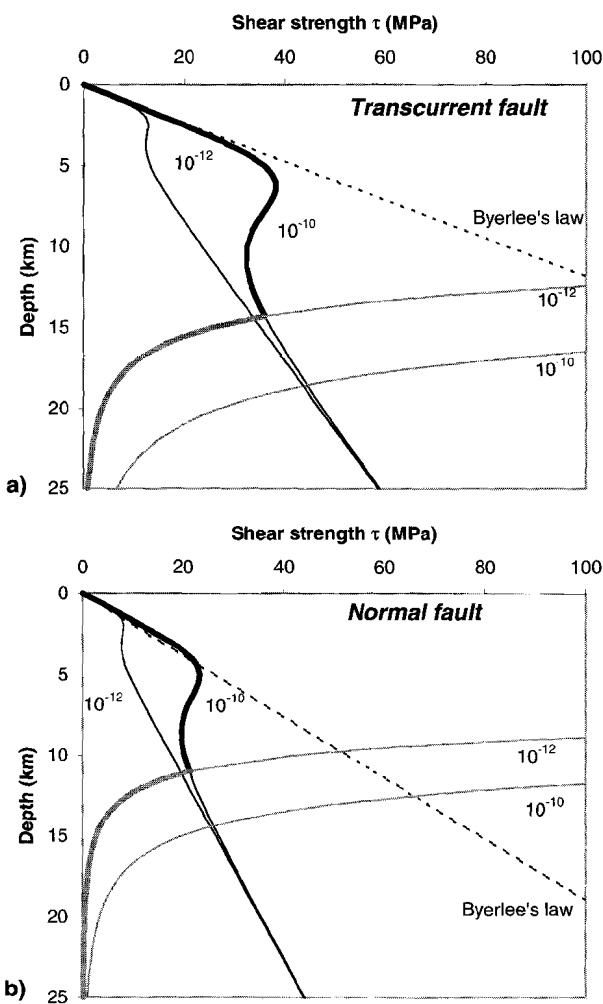


Figure 7.8. Model predictions of shear strength versus depth for different tectonic settings. Strength profiles are shown for (a) a transcrustal strike-slip fault zone, (b) a normal fault zone, in an extensional region, (c) a thrust fault zone in a subduction setting, and (d) a thrust fault zone in a typical continental collision zone. Temperature gradients used are 25, 35, 15 and 25°C/km, respectively. The dashed lines shows frictional "Byerlee's law" behaviour, with a friction coefficient μ of 0.75. The gray lines show flow laws for quartz dislocation creep for strain rates of 10^{-10} and 10^{-12} s^{-1} . The black lines show predictions of our model, for the case of diffusion controlled pressure solution, for strain rates of 10^{-10} and 10^{-12} s^{-1} . Crudely taking into account the widening of shear zones (and hence the decreasing strain rate) with depth, a typical crustal strength profile in high strain fault zones would be given by the bold lines, connecting the frictional-viscous flow curve for 10^{-10} s^{-1} and the dislocation creep curve for 10^{-12} s^{-1} . Note that our model predicts pressure solution controlled creep to dominate the rheology of high strain fault zones at depths ranging from 5-20 km. This leads to rheological weakening by up to a factor 4.5 with respect to conventional two-mechanism strength profile in phyllosilicate-bearing shear zones.

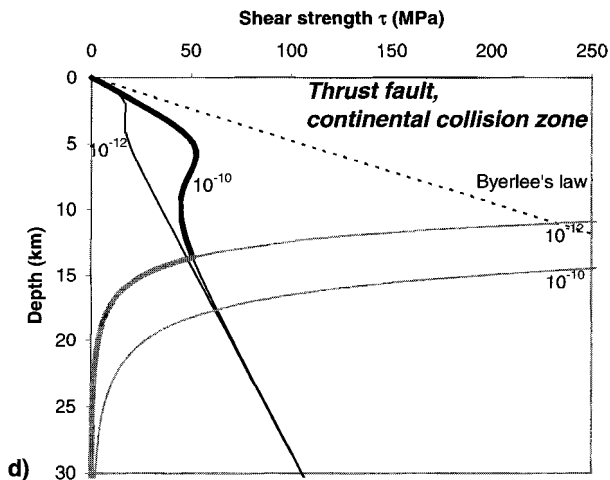
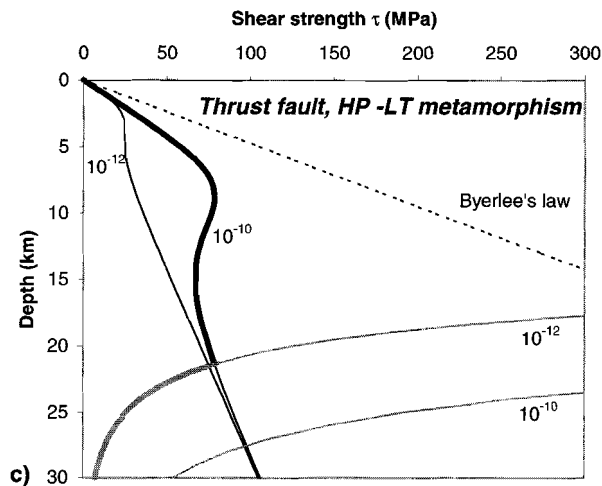


Figure 7.8 (continued)

The least well-constrained parameters in the model are the grain boundary diffusion coefficient and the grain boundary friction coefficient. The model sensitivity to the grain boundary diffusion coefficient can be estimated directly from the strain rate sensitivity in Figures 7.8, since an order of magnitude increase in strain rate has the same effect as an order of magnitude decrease in grain boundary diffusion coefficient (see equation 7.17). The value of the diffusion coefficient has a strong effect on the depth of the transition region between Byerlee's law behaviour and behaviour controlled by grain boundary friction. The grain boundary friction coefficient determines the slope of the strength versus depth line below the transition region, and hence has a strong influence on the total integrated strength of the crust. The depth of the transition, however, is not very sensitive to the grain boundary friction coefficient.

The model shows that the presence of foliated, fine-grained phyllosilicate-bearing shear zones, undergoing deformation by pressure solution-accommodated sliding, leads to significant modification of the crustal strength envelope, in particular in the region where classical two-mechanism strength profiles (as defined by the Byerlee's law line and the dislocation creep curves in Figure 7.8) predict a pronounced strength maximum. In the strength profile no pronounced peak is predicted by our model, and the increase of strength with depth is much more gradual than in two-mechanism strength profiles. In addition, significant weakening with respect to classical two-mechanism strength profiles is predicted in all tectonic regimes. The effect is strongest in a HP-LT "subduction" setting (Figure 7.8c), where our model predicts weakening by more than a factor 4 around the brittle-ductile transition, although in the other scenarios significant weakening, by a factor 2-3, is predicted as well. For finer grained fault rocks, or a lower value of the grain boundary friction coefficient, the weakening effect would be even larger. Deformation of quartz phyllonites at stress levels below those needed to activate dislocation creep has been inferred from field observations, in particular in HP-LT environments [Imber *et al.*, 1997; Stewart *et al.*, 2000; Schwarz and Stoeckhert, 1996]. Both the inferred depth range and the inferred deviatoric stress level is broadly consistent with our model predictions.

The importance of pressure solution controlled flow of fine-grained fault rock in allowing weakening with respect to Byerlee's law friction has been stressed for two decades [Sibson, 1977; Rutter and Mainprice, 1979; Sibson, 1983; Chester and Higgs, 1992; Hickman *et al.*, 1995]. The model developed here allows for the first time quantitative incorporation of this mechanism into geodynamic models for crustal tectonics. In geodynamic modelling studies, rheology is usually expressed in the simplest possible way, to avoid excessive numerical cost. While it would be preferable to incorporate the rheological laws developed here directly into numerical models of crustal tectonics, a low-cost alternative would be to tentatively assume an apparent friction coefficient for highly strained crust of $\sim 0.25-0.35$. This value could then apply to the crust up to depths where dislocation creep becomes active. A way to incorporate the evolution of mechanical behaviour with increasing strain (see also Chapter 4 of this thesis) would then be to allow the apparent friction coefficient to evolve from ~ 0.75 for unstrained rock to ~ 0.3 for highly strained material. This is likely to significantly influence tectonic modelling results, probably favouring strong localisation of deformation into strain-weakening shear zones, as observed in natural tectonic belts.

The weakening with respect to Byerlee's law for high strain fault zones predicted by our model may aid in explaining the low heat flow in the San Andreas Fault area. Here, the lack of a measurable heat flow anomaly in the vicinity of the fault is inferred to imply an average frictional traction on the fault of 20 MPa or lower [see e.g. Lachenbruch and Sass, 1980; Hickman, 1991], i.e. far higher than the 90-260 MPa predicted from Byerlee's law. For the strike slip case (Figure 7.8a) our model indeed predicts an average crustal strength of a few tens of MPa over the depth range 0-20 kilometers, based on an assumed 10 m wide shear zone at these depths. Note, however, that this value strongly depends on the assumed value for the grain boundary friction coefficient, which is a poorly constrained parameter.

7.6 Conclusions

1. A microphysical model for deformation of foliated, phyllosilicate-rich fault rock by a mechanism of sliding along phyllosilicate foliae accommodated by pressure solution predicts three regimes of rheological behaviour: a regime of frictional behaviour at high shear strain rates, a regime of frictional-viscous behaviour at intermediate shear strain rates, and again a regime of frictional behaviour at low sliding velocities. Fault strength is predicted to be normal stress dependent at all shear strain rates.
2. The model describes our experimental data on the system halite/kaolinite reasonably well, particularly at low (<50%) clay contents and sliding velocities of 1 $\mu\text{m/s}$ and lower. This supports earlier inferences that these materials deformed by pressure solution-accommodated sliding along kaolinite foliae.
3. When applied to the crust, the model predicts that in foliated, phyllosilicate-bearing fault zones strength is dominated by pressure solution controlled frictional-viscous behaviour at depths ranging from 5-20 km, depending on tectonic setting. This is broadly consistent with inferences from field observations on natural, phyllosilicate-rich fault zones.
4. The model predicts that the development of foliated, phyllosilicate-bearing shear zones may lead to significant rheological weakening, by up to a factor 4.5 with respect to conventional crustal strength envelopes. Since crustal strength is known to be strongly controlled by the presence of major shear zones, our results question the applicability of conventional strength profiles for modelling crustal tectonic processes.
5. The crustal strength profiles predicted by our model suggest that in numerical models for geodynamic processes the strength of highly deformed regions should be approximated using our equation for frictional-viscous behaviour instead of using conventional strength profiles, since the latter may significantly overestimate crustal strength. Alternatively, and numerically cheaper, the usage of an apparent friction coefficient of 0.25-0.35 for the frictional part of the strength envelope is suggested.
6. The quantitative predictions of our model rely heavily on grain contact scale parameters such as grain boundary diffusion and friction coefficients. However, the underlying processes are poorly understood, and the corresponding coefficients are not well constrained. Future work should be aimed at obtaining more reliable data on contact parameters.

Chapter 8

General conclusions and suggestions for further research

8.1 Conclusions of this research

This thesis has investigated the role of solution transfer processes in influencing sliding behaviour of simulated, gouge bearing faults. In relation to the aims stipulated in the introduction, the following general conclusions were reached:

1. *On the possibility of pressure solution controlled fault slip*

Our experiments have shown that in porous, monomineralic fault gouge the action of pressure solution does not lead to steady state fault creep behaviour. Instead, pressure solution compaction and healing effects dominate, leading to frictional behaviour. The results show that existing models for pressure solution controlled fault slip may not be applicable to monomineralic, porous gouge under drained conditions, where compaction and healing effects are rapid.

2. *Effect of phyllosilicates*

In contrast to monomineralic halite gouge, wet halite/kaolinite gouges showed a transition from purely frictional behaviour at low strains to frictional-viscous flow behaviour (i.e., behaviour in which shear strength is strongly dependent on both sliding rate and normal stress) at high strains. This transition was accompanied by an evolution from a cataclastic microstructure at low strains to a microstructure consisting of augen-like halite grains embedded in a fine-grained, foliated halite/kaolinite matrix at high strains. It was inferred that both phyllosilicates and pressure solution are required for the frictional-viscous behaviour observed: The presence of phyllosilicates at grain boundaries prevented grain contact healing, allowing deformation of the gouge by a mechanism of frictional sliding along anastomosing kaolinite foliae, with accommodation of geometrical incompatibilities by pressure solution.

3. *Microphysical model*

A microphysical model for frictional-viscous flow behaviour of phyllosilicate-bearing fault rock based on the deformation process mentioned under 2) was developed, and applied to the quartz-muscovite system. The model predicts that foliated, phyllosilicate-bearing shear zones can deform by pressure solution-accommodated sliding along phyllosilicate foliae under conditions where dislocation creep is not yet active (5-20 kilometer depending on tectonic setting). The predicted flow strengths for such shear zones are up to a factor 4 lower than those predicted by classical, two-mechanism strength profiles. Hence, the development of hydrated, phyllosilicate-bearing shear zones can be expected to lead to significant crustal weakening, in particular around the brittle-ductile transition.

4. *Effect of fluids on fault strength recovery (healing) behaviour.*

The action of pressure solution strongly enhances fault healing rates. This effect is due to pressure solution compaction of gouge, causing an increase in both packing density and contact area/strength. The behaviour observed was broadly similar to that described by the rate- and state-dependent friction (RSF) laws, but the increase of static friction with time was stronger than the log-linear increase predicted by the RSF laws. This suggests that in situations where pressure solution is an important healing mechanism, strength recovery models based on the RSF laws may underestimate fault strength recovery rates.

5. Effect of clays on healing

The presence of clays at grain contacts strongly retards fluid-assisted fault healing processes. This effect is particularly strong in foliated gouge, where healing rates are more than an order of magnitude lower than in monomineralic gouge at similar conditions. The retardation is due to phyllosilicate preventing grain contact healing. This strong retardation raises questions regarding the application of healing rates derived from experiments on monomineralic gouge to natural faults, since these often contain significant amounts of phyllosilicates.

8.2 Suggestions for further research

The research described in this thesis has brought up a number of unsolved questions and further research topics.

1. The application of the model developed in Chapter 7 relies heavily on grain contact properties such as grain contact friction coefficients and grain contact diffusion coefficients. Unfortunately, such parameters are very poorly constrained. There is accordingly an urgent need for experimental research on grain contact properties and processes. Data should preferably be obtained in very basic experiments so the data can be interpreted with as little ambiguity as possible. Lack of reliable contact property data constitutes one of the greatest problems in extrapolating laboratory deformation data, and microphysical models derived from these, to natural situations.
2. Following up on this work, there is obviously a need for experimental verification of the possibility of frictional-viscous flow behaviour such as reported in Chapters 2 and 3 for natural materials (for example on quartz/mica mixtures), in spite of the difficulties inherent in using high stresses and temperatures outlined in Chapter 1.5. These experiments should be done in a high-pressure and high-temperature hydrothermal rotary shear configuration, since this is the only configuration in which high enough shear strains can be reached to allow the grain size reduction and foliation development necessary to activate the frictional-viscous flow mechanism.
3. The model developed in Chapter 7 was tested only in a very crude, exploratory manner. Although it was clearly shown that a the transition from purely frictional to rate-sensitive behaviour predicted by the model fits the data well, no experimental evidence was obtained for the existence of the low velocity, frictional regime (regime 3 in Figure 7.6) in the present experiments. The reason for this may be that the sliding rates that could be achieved in the ring-shear apparatus were too high to reach the low velocity frictional regime. A way of solving this problem may be to use gouge with a significantly smaller starting grain size, although this is not straightforward since the gouge grain size evolves during the initial stages of the experiments. Also, the effect of phyllosilicate type and grain size on rheology and microstructural evolution requires further study.
4. The interpretation of the mechanical behaviour observed in both steady state sliding and fault healing experiments would be greatly facilitated by performing see-through experiments on halite/kaolinite gouges. This would allow visual inspection of, for example, the order of formation of the mylonitic S-foliation and the C' shear bands as described in Chapter 4 as well as the detailed kinematics of the steady state deformation process observed at high strains in our halite/kaolinite experiments. In addition, performing see-through slide-hold-slide experiments will allow a detailed assessment of the processes occurring during the peak strength and the

subsequent decay to steady state after hold periods, greatly facilitating the interpretation of the mechanical data obtained in these experiments.

5. The model for frictional flow behaviour developed in Chapter 7 is oversimplified in the sense that it only applies to constant volume deformation, and is therefore only applicable to steady state deformation. The model could be extended to incorporate transient effects by incorporating volume changes due to dilatation and pressure solution directly into the model. In this way, the type of behaviour described by the RSF laws may be predicted from a microphysically based model. Related to this is the development of a microphysical model for frictional slip of monomineralic gouge incorporating the effect of pressure solution. In such a model, deformation may be described as involving localised frictional slip along R-shears, accommodated by volume change (compaction or dilatation) in areas between R-shears.
6. Recently, granular flow of gouge has been simulated using so-called particle based "lattice solid" models [Mora and Place, 1999] or molecular dynamics models [Aharonov and Sparks, 1999; Sparks and Aharonov, 1999]. These models allow simulation of the behaviour of large numbers of grains, and provide a potentially very powerful tool for investigating sample-scale behaviour resulting from the input of prescribed grain contact scale mechanical properties, and hence for testing inferences regarding sample-scale mechanical behaviour from grain scale microstructural observations. Using this type of simulations may aid in extrapolating laboratory results to more complex geometries. To date, these models include only grain rolling and frictional sliding. An important further improvement could be to include processes such as pressure solution and associated time-dependent porosity and contact strength evolution.
7. An important question for fault and sealing studies of seismogenic faults, but also in hydrocarbon reservoir research, is the dependence of healing (i.e. strengthening) rate and sealing (i.e. permeability reduction) rate on gouge grain size. Grain size effects were only explored to a very limited extent in this thesis, partly due to the fact that grain size is an evolving parameter during cataclasis. Grain size is likely to affect healing and sealing due to an increased pressure solution compaction rate. However, at smaller grain sizes surface energy related effects such as neck growth become increasingly important, leading to fault strengthening but inhibiting compaction and thus fault gouge permeability decrease. Clearly, there is a need for experimental work on the effect of grain size on static frictional strength as well as permeability.
8. The last suggestions concern scaling of laboratory results to nature. Currently, flow laws are developed and calibrated with laboratory samples, which have dimensions typically in the order of centimeters, and are as homogeneous as possible. In numerical models of lithospheric dynamics, these flow laws are then applied assuming a more-or-less homogeneous lithosphere. However, field studies show that lithospheric deformation is in general strongly inhomogeneous, and often localised in networks of shear zones with mechanical properties very different from their surroundings. In order to meaningfully apply laboratory results to nature, one must understand how these networks of weak shear zones determine the mechanical behaviour of the crust on a larger scale. A way to do this is by combining detailed mapping of the geometry of such shear zone networks with numerical modelling of the mechanical behaviour of a region containing such a shear zone network. Work of this kind is done on brittle fault systems in basins, mapping out the 3-D structure of a fault network using seismics and subsequently modelling the mechanical behaviour. Extension of the approach used in such models to deeper crustal levels may greatly enhance our understanding of the mechanical behaviour of a heterogeneous lithosphere.

References

- Aharonov, E., and D. Sparks, Rigidity phase transition in granular packings, *Phys. Rev. E*, **60**, 6890-6897, 1999.
- Angevine, C.L., D.L. Turcotte, and M.D. Furnish, Pressure solution lithification as a mechanism for the stick-slip behavior of faults, *Tectonics*, **1**, 151-160, 1982.
- Atkinson, B.K., and P.G. Meredith, The theory of subcritical crack growth with applications to minerals and rocks, in *Fracture Mechanics of Rock*, edited by B.K. Atkinson, pp. 111-166, Academic Press, London, 1989.
- Baykara, T., and G.M. Pharr, Effects of liquid phases on intrinsic interfacial sliding of alkali halide crystals, *Acta Metall. Mater.*, **39**, 1141-1150, 1991.
- Beeler, N.M., and T.E. Tullis, The roles of time and displacement in velocity-dependent volumetric strain of fault zones, *J. Geophys. Res.*, **102**, 22,595-22,609, 1997.
- Beeler, N.M., T.E. Tullis, M.L. Blanpied, and J.D. Weeks, Frictional behavior of large displacement experimental faults, *J. Geophys. Res.*, **101**, 8697-8715, 1996.
- Beeler, N.M., T.E. Tullis, and J.D. Weeks, The roles of time and displacement in the evolution effect in rock friction, *Geophys. Res. Lett.*, **21**, 1987-1990, 1994.
- Ben-Zion, Y., and D.J. Andrews, Properties and implications of dynamic rupture along a material interface, *Bull. Seismol. Soc. Am.*, **88**, 1085-1094, 1998.
- Biegel, R.L., C.G. Sammis, and J.H. Dieterich, The frictional properties of a simulated gouge having a fractal particle distribution, *J. Struct. Geol.*, **11**, 827-846, 1989.
- Bird, G., J. Boon, and T. Stone, Silica transport during steam injection into oil sands I. Dissolution and precipitation kinetics of quartz: New results and review of existing data, *Chem. Geol.*, **54**, 69-80, 1986.
- Bird, P., Hydration-phase diagrams and friction of montmorillonite under laboratory and geologic conditions, with implications for shale compaction, slope stability, and strength of fault gouge, *Tectonophysics*, **107**, 235-260, 1984.
- Blanpied, M.L., D.A. Lockner, and J.D. Byerlee, Fault stability inferred from granite sliding experiments at hydrothermal conditions, *Geophys. Res. Lett.*, **18**, 609-612, 1991.
- Blanpied, M.L., D.A. Lockner, and J.D. Byerlee, An earthquake mechanisms based on rapid sealing of faults, *Nature*, **358**, 574-576, 1992.
- Blanpied, M.L., D.A. Lockner, and J.D. Byerlee, Frictional slip of granite at hydrothermal conditions, *J. Geophys. Res.*, **100**, 13,045-13,064, 1995.
- Blanpied, M.L., C.J. Marone, D.A. Lockner, J.D. Byerlee, and D.P. King, Quantitative measure of the variation in fault rheology due to fluid-rock interactions, *J. Geophys. Res.*, **103**, 9691-9712, 1998.
- Bos, B., C.J. Peach, and C.J. Spiers, Slip behavior of simulated gouge-bearing faults under conditions favoring pressure solution, *J. Geophys. Res.*, **105**, 16699-16717, 2000.
- Brace, W.F., and J.D. Byerlee, Stick-slip as a mechanism for earthquakes, *Science*, **153**, 990, 1966.
- Braun, J., J. Chéry, A. Poliakov, D. Mainprice, A. Vauchez, A. Tomassi, and M. Daignières, A simple parameterization of strain localization in the ductile regime due to grain size reduction: A case study for olivine, *J. Geophys. Res.*, **104**, 25,167-25,181, 1999.
- Brudy, M., M.D. Zoback, K. Fuchs, F. Rummel, and J. Baumgärtner, Estimation of the complete stress tensor to 8 km depth in the KTB scientific drill holes: Implications for crustal strength, *J. Geophys. Res.*, **102**, 18,453-18,475, 1997.
- Bruhn, R.L., W.T. Parry, W.A. Yonkee, and T. Thompson, Fracturing and hydrothermal alteration in normal fault zones, *Pure Appl. Geophys.*, **142**, 609-644, 1994.
- Brune, J.N., S. Brown, and P.A. Johnson, Rupture mechanism and interface separation in foam rubber models of earthquakes: A possible solution to the heat flow paradox and the paradox of large overthrusts, *Tectonophysics*, **218**, 59-67, 1993.
- Brzesowsky, R.H., Micromechanics of sand grain failure and sand compaction, PhD thesis, University of Utrecht, 1995.
- Byerlee, J., Friction of rocks, *Pure Appl. Geophys.*, **116**, 615-627, 1978.
- Byerlee, J., Friction, overpressure and fault normal compression, *Geophys. Res. Lett.*, **17**, 2109-2112, 1990.
- Byerlee, J., Model for episodic flow of high-pressure water in fault zones before earthquakes, *Geology*, **21**, 303-306, 1993.
- Caine, J.S., J.P. Evans, and C.B. Forster, Fault zone architecture and permeability structure, *Geology*, **24**, 1025-1028, 1996.
- Cao, T., and K. Aki, Seismicity simulation with a rate- and state-dependent friction law, *Pure Appl. Geophys.*, **124**, 487-513, 1986.
- Carter, N.L., S.T. Horseman, J.E. Russell, and J. Handin, Rheology of rocksalt, *J. Struct. Geol.*, **15**, 1257-1271, 1993.
- Chester, F.M., A rheologic model for wet crust applied to strike-slip faults, *J. Geophys. Res.*, **100**, 13,033-13,044, 1995.
- Chester, F.M., J.P. Evans, and R.L. Biegel, Internal structure and weakening mechanisms of the San Andreas fault, *J. Geophys. Res.*, **98**, 771-786, 1993.
- Chester, F.M., and N.G. Higgs, Multimechanism friction constitutive model for ultrafine quartz gouge at hypocentral conditions, *J. Geophys. Res.*, **97**, 1859-1870, 1992.
- Chester, F.M., and J.M. Logan, Implications for mechanical properties of brittle faults from observations of the Punchbowl Fault Zone, California, *Pure Appl. Geophys.*, **124**, 79-106, 1986.
- Chester, F.M., and J.M. Logan, Frictional faulting in polycrystalline halite: correlation of microstructure, mechanisms of slip, and constitutive behaviour, in *The brittle-ductile transition in rocks: the Heard volume*, edited by A.G. Duba, Durham, W.B., Handin, J.W. and Wang, H.F., pp. 49-65, 1990.
- Cox, S.F., and M.S. Paterson, Experimental dissolution-precipitation creep in quartz aggregates at high temperatures, *Geophys. Res. Lett.*, **18**, 1401-1404, 1991.
- David, C., B. Menéndez, and Y. Bernabé, The mechanical behaviour of synthetic sandstone with varying brittle cement content, *In. J. Rock Mech. Min. Sci.*, **35**, 759-770, 1998.
- De Bresser, J.H.P., C.J. Peach, J.P.J. Reijts, and C.J. Spiers, On dynamic recrystallization during solid state flow: Effects of stress and temperature, *Geophys. Res. Lett.*, **25**, 3457-3460, 1998.
- De Meer, S., and C.J. Spiers, Creep of wet gypsum aggregates under hydrostatic loading conditions, *Tectonophysics*, **245**, 171-183, 1995.
- De Meer, S., and C.J. Spiers, Uniaxial compaction creep of wet gypsum aggregates, *J. Geophys. Res.*, **102**, 875-891, 1997.
- De Meer, S., and C.J. Spiers, On mechanisms and kinetics of creep by intergranular pressure solution, in *Growth, Dissolution and Pattern Formation in Geo-Systems*, edited

- by B. Jamtveit, and P. Meakin, pp. 345-366, Kluwer Academic Publishers, 1999.
- Dell' Angelo, L.N., and J. Tullis, Textural and mechanical evolution with progressive strain in experimentally deformed aplites, *Tectonophysics*, 256, 57-82, 1996.
- Den Brok, B., M. Zahid, and C. Passchier. Cataclastic solution creep of very soluble brittle salt as a rock analogue, *Earth Planet. Sci. Lett.*, 163, 83-95, 1998.
- Dennis, S.M., and B.K. Atkinson, The influence of water on the stress supported by experimentally faulted Westerly granite, *Geophys. J. R. astr. Soc.*, 71, 285-294, 1982.
- Dewers, T., and A. Hajash, Rate laws for water-assisted compaction and stress-induced water-rock interaction in sandstones, *J. Geophys. Res.*, 100, 13,093-13,112, 1995.
- Dewers, T., and P. Ortoleva, Influences of clay minerals on sandstone cementation and pressure solution, *Geology*, 19, 1045-1048, 1991.
- Dieterich, J.H., Time-dependent friction in rocks, *J. Geophys. Res.*, 77, 3690-3697, 1972.
- Dieterich, J.H., Modeling of rock friction I. Experimental results and constitutive equations, *J. Geophys. Res.*, 84, 2162-2168, 1979.
- Dieterich, J.H., and G. Conrad, Effect of Humidity on Time- and Velocity-Dependent Friction in Rocks, *J. Geophys. Res.*, 89, 4196-4202, 1984.
- Dunning, J., B. Douglas, M. Miller, and S. McDonald, The role of the chemical environment in frictional deformation: Stress corrosion cracking and comminution. *Pure Appl. Geophys.*, 143, 151-178, 1994.
- Etheridge, M.A., and J.C. Wilkie, Grain size reduction, grain boundary sliding and the flow strength of mylonites, *Tectonophysics*, 58, 159-178, 1979.
- Farver, J.R., and R.A. Yund, Measurement of oxygen grain boundary diffusion in natural, fine grained, quartz aggregates, *Geochim. Cosmochim. Acta*, 55, 1597-1607, 1991.
- Farver, J.R., and R.A. Yund, Oxygen bulk diffusion measurements and TEM characterization of a natural ultramylonite: implications for fluid transport in mica-bearing rocks, *J. Metamorphic Geol.*, 17, 669-683, 1999.
- Fournier, R.O., and R.W. Potter. An equation correlating the solubility of quartz in water from 25° to 900°C at pressure up to 10,000 bars, *Geochim. Cosmochim. Acta*, 46, 1969-1973, 1982.
- Fredrich, J.T., and B. Evans, Strength recovery along simulated faults by solution transfer processes, in *Proc. 33rd U.S. Symp. Rock Mech.*, pp. 121-130, 1992.
- Goetze, C., and B. Evans, Stress and temperature in the bending lithosphere as constrained by experimental rock mechanics, *Geophys. J. R. astr. Soc.*, 59, 463-478, 1979.
- Govers, R., and M.J.R. Wortel, Extension of stable continental lithosphere and the initiation of lithosphere scale faults, *Tectonics*, 14, 1041-1055, 1995.
- Gratier, J.-P., Experimental pressure solution of halite by an indenter technique, *Geophys. Res. Lett.*, 20, 1647-1650, 1993.
- Gratier, J.P., and R. Guiget, Experimental pressure solution-deposition on quartz grains: the crucial effect of the nature of the fluid, *J. Struct. Geol.*, 8, 845-856, 1986.
- Groshong, R.H., Fractures and pressure solution in natural single-layer folds, *Geol. Soc. Am. Bull.*, 86, 1363-1376, 1975.
- Hadizadeh, J., Interaction of cataclasis and pressure solution in a low-temperature carbonate shear zone, *Pure Appl. Geophys.*, 143, 255-280, 1994.
- Handy, M.R., Deformation regimes and the rheological evolution of fault zones in the lithosphere: the effects of pressure, temperature, grain size and time, *Tectonophysics*, 163, 119-152, 1989.
- Handy, M.R., The solid-state flow of polymineralic rock, *J. Geophys. Res.*, 95, 8647-8661, 1990.
- Handy, M.R., S.B. Wissing, and L.E. Streit, Frictional-viscous flow in mylonite with varied binomeric composition and its effect on lithospheric strength, *Tectonophysics*, 303, 175-191, 1999.
- Heald, M.T., Significance of stylolites in permeable sandstones, *J. Sediment. Petrol.*, 29, 251-253, 1959.
- Heaton, T.H., Evidence for and implications of self-healing pulses of slip in earthquake rupture, *Phys. Earth Planet. Inter.*, 64, 1-20, 1990.
- Hickman, S., R. Sibson, and R. Bruhn, Introduction to special section: Mechanical involvement of fluids in faulting, *J. Geophys. Res.*, 100, 12,831-12,840, 1995.
- Hickman, S.H., Stress in the Lithosphere and the Strength of Active Faults, *U.S. Nat. Rep. Int. Union Geod. Geophys. 1987-1990, Rev. Geophys.*, 29, 759-775, 1991.
- Hickman, S.H., C.A. Barton, M.D. Zoback, R. Morin, J. Sass, and R. Benoit, In situ stress and fracture permeability along the stillwater fault zone, Dixie Valley, Nevada, *Int. J. Rock Mech. Min. Sci.*, 34, 414, 1997.
- Hickman, S.H., and B. Evans, Growth of grain contacts in halite by solution-transfer: Implications for diagenesis, lithification, and strength recovery, in *Fault Mechanics and Transport Properties of Rocks*, edited by B. Evans, and T.-f. Wong, pp. 253-280, Academic Press, 1992.
- Hickman, S.H., and B. Evans, Kinetics of pressure solution at halite-silica interfaces and intergranular clay films, *J. Geophys. Res.*, 100, 13,113-13,132, 1995.
- Holdsworth, R.E., C.A. Butler, and A.M. Roberts, The recognition of reactivation during continental deformation, *J. Geol. Soc. London*, 154, 73-78, 1997.
- Imber, J., R.E. Holdsworth, C.A. Butler, and G. Lloyd, Fault-zone weakening processes along the reactivated Outer Hebrides Fault Zone, Scotland, *J. Geol. Soc. London*, 154, 105-109, 1997.
- Israelachvili, J.N., Adhesion forces between surfaces in liquids and condensable vapours, *Surf. Sci. Rep.*, 14, 109-159, 1992.
- Jordan, P., The deformational behaviour of bimimneral limestone-halite aggregates, *Tectonophysics*, 135, 185-197, 1987.
- Kanagawa, K., S.H. Cox, and S. Zhang, Effects of dissolution-precipitation processes on the strength and mechanical behavior of quartz gouge at high-temperature hydrothermal conditions, *J. Geophys. Res.*, 105, 11,115-11,126, 2000.
- Kanamori, H., and C.R. Allen, Earthquake repeat time and average stress drop, in *Earthquake Source Mechanics. AGU Geophys. mono. 37*, edited by S. Das, J. Boatwright, and C.H. Scholz, pp. 227-236, 1986.
- Karner, S.L., C. Marone, and B. Evans, Laboratory study of fault healing and lithification in simulated fault gouge under hydrothermal conditions, *Tectonophysics*, 277, 41-55, 1997.
- Kawamoto, E., and T. Shimamoto, Mechanical behavior of halite and calcite shear zones from brittle to fully-plastic deformation and a revised fault model, *Proc. 30th Intern. Congr.*, 14, 89-105, 1997.
- Kawamoto, E., and T. Shimamoto, The strength profile for bimimneral shear zones: an insight from high-temperature shearing experiments on calcite-halite mixtures, *Tectonophysics*, 295, 1-14, 1998.
- Kirby, S.H., Tectonic stresses in the lithosphere: Constraints provided by the experimental deformation of rocks, *J. Geophys. Res.*, 85, 6353-6363, 1980.
- Kirby, S.H., Rheology of the lithosphere, *Rev. Geophys. Space Phys.*, 21, 1458-1487, 1983.
- Kohlstedt, D.L., B. Evans, and S.J. Mackwell, Strength of the lithosphere: Constraints imposed by laboratory experiments, *J. Geophys. Res.*, 100, 17,587-17,602, 1995.

- Kronenberg, A.K., S.H. Kirby, and J. Pinkston, Basal slip and mechanical anisotropy of biotite, *J. Geophys. Res.*, *95*, 19,257-19,278, 1990.
- Lachenbruch, A.H., and J.H. Sass, Heat flow and energetics of the San Andreas fault zone, *J. Geophys. Res.*, *85*, 8185-6222, 1980.
- Lachenbruch, A.H., and J.H. Sass, Heat flow from Cajon Pass, fault strength, and tectonic implications, *J. Geophys. Res.*, *97*, 4995-5015, 1992.
- Lachenbruch, A.H., and G.A. Thompson, Oceanic ridges and transform faults: Their intersection angles and resistance to plate motion, *Earth Planet. Sci. Lett.*, *15*, 116-122, 1972.
- Lehner, F.K., Thermodynamics of rock deformation by pressure solution, in *Deformation Processes in Minerals, Ceramics and Rocks*, edited by D.J. Barber, and P.D. Meredith, pp. 296-333, Unwin Hyman, London, 1990.
- Lehner, F.K., and J. Bataille, Nonequilibrium thermodynamics of pressure solution, *Pure Appl. Geoph.*, *122*, 53-85, 1984/85.
- Lister, G.S., and A.W. Snoke, S-C Mylonites, *J. Struct. Geol.*, *6*, 617-638, 1984.
- Lockner, D., and B. Evans, Densification of quartz powder and reduction of conductivity at 700°C, *J. Geophys. Res.*, *100*, 13,081-13,092, 1995.
- Logan, J.M., C.M. Dengo, N.G. Higgs, and Z.Z. Wang, Fabrics of experimental fault zones: their development and relationship to mechanical behaviour, in *Fault mechanics and transport properties of rocks*, edited by B. Evans, and Wong, T.-f., pp. 33-67, Academic Press, 1992.
- Logan, J.M., and K.A. Rauenzahn, Frictional dependence of gouge mixtures of quartz and montmorillonite on velocity, composition and fabric, *Tectonophysics*, *144*, 87-108, 1987.
- Luan, F.C., and M.S. Paterson, Preparation and deformation of synthetic aggregates of quartz, *J. Geophys. Res.*, *97*, 301-320, 1992.
- Lund, B., and M.D. Zoback, Orientation and magnitude of in situ stress to 6.5 km depth in the Baltic Shield, *Int. J. Rock Mech. Min. Sci.*, *36*, 169-190, 1999.
- Magee, M.E., and M.D. Zoback, Evidence for a weak interplate thrust fault along the northern Japan subduction zone and implications for the mechanics of thrust faulting and fluid expulsion, *Geology*, *21*, 809-812, 1993.
- Mandl, G., L.N.J. de Jong, and A. Maltha, Shear zones in granular material, *Rock Mechanics*, *9*, 95-144, 1977.
- Mares, V.M., and A.K. Kronenberg, Experimental deformation of muscovite, *J. Struct. Geol.*, *15*, 1061-1075, 1993.
- Marone, C., Laboratory-derived friction laws and their application to seismic faulting., *Ann. Rev. Earth Planet. Science*, *26*, 643-696, 1998.
- Marone, C., The effect of loading rate on static friction and the rate of fault healing during the earthquake cycle, *Nature*, *391*, 69-72, 1998.
- Marone, C., and B. Kilgore, Scaling of the critical slip distance for seismic faulting with shear strain in fault zones, *Nature*, *362*, 618-621, 1993.
- Marone, C., C.B. Raleigh, and C.H. Scholz, Frictional behaviour and constitutive modeling of simulated fault gouge, *J. Geophys. Res.*, *95*, 7007-7025, 1990.
- Marone, C., and C.H. Scholz, Particle-size distribution and microstructures within simulated fault gouge, *J. Struct. Geol.*, *11*, 799-814, 1989.
- Marone, C., J.E. Vidale, and W.E. Ellsworth, Fault healing inferred from repeating earthquakes, *Geophys. Res. Lett.*, *22*, 3095-3098, 1995.
- Maskara, A., and D.M. Smith, Agglomeration during the drying of fine silica powders, part II: The role of particle solubility, *J. Am. Ceram. Soc.*, *80*, 1715-1722, 1997.
- McClay, K.R., Pressure solution and Coble creep in rocks and minerals: a review, *J. Geol. Soc., London*, *134*, 57-70, 1977.
- Means, W.D., and P.F. Williams, Crenulation cleavage and faulting in an artificial salt-mica schist, *J. Geol.*, *80*, 569-591, 1972.
- Melosh, H.J., Dynamical weakening of faults by acoustic fluidization, *Nature*, *379*, 601-606, 1996.
- Miller, S.A., A. Nur, and D.L. Olgaard, Earthquakes as a coupled shear stress-high pore pressure dynamical system, *Geophys. Res. Lett.*, *23*, 197-200, 1996.
- Moore, D.E., D.A. Lockner, M. Shengli, R. Summers, and J.D. Byerlee, Strengths of serpentinite gouges at elevated temperatures, *J. Geophys. Res.*, *102*, 14,787-14,801, 1997.
- Moore, D.E., D.A. Lockner, R. Summers, M. Shengli, and J.D. Byerlee, Strength of chrysotile-serpentinite gouge under hydrothermal conditions: Can it explain a weak San Andreas fault?, *Geology*, *24*, 1041-1044, 1996.
- Mora, P., and D. Place, Simulation of the frictional stick-slip instability, *Pure Appl. Geophys.*, *143*, 61-87, 1994.
- Mora, P., and D. Place, The weakness of earthquake faults, *Geophys. Res. Lett.*, *26*, 123-126, 1999.
- Morrow, C., B. Radney, and J.D. Byerlee, Frictional strength and the effective pressure law of montmorillonite and illite clays, in *Fault mechanics and transport properties of rocks*, edited by B. Evans, and Wong, T.-f., pp. 69-88, Academic Press, 1992.
- Morrow, C.A., D.E. Moore, and D.A. Lockner, The effect of mineral bond strength and adsorbed water on fault gouge frictional strength, *Geophys. Res. Lett.*, *27*, 815-818, 2000.
- Mount, V.S., and J. Suppe, State of stress near the San Andreas fault: Implications for wrench tectonics, *Geology*, *15*, 1143-1146, 1987.
- Mount, V.S., and J. Suppe, Present-day stress orientations adjacent to active strike-slip faults: California and Sumatra, *J. Geophys. Res.*, *97*, 11,995-12,013, 1992.
- Nakashima, S., Diffusivity of ions in pore water as a quantitative basis for rock deformation rate estimates, *Tectonophysics*, *245*, 185-203, 1995.
- Nakatani, M., and C.H. Scholz, Hydrothermal healing of quartz gouge at 200°C. (due to pressure solution?) (Abstract), *EOS Transactions AGU*, *80*, 1015, 1999.
- Okubo, P.G., Dynamic rupture modeling with laboratory-derived constitutive relations, *J. Geophys. Res.*, *94*, 12,321-12,335, 1989.
- Oldenburg, D.W., and J. Brune, An explanation for the orthogonality of ocean ridges and transform faults, *J. Geophys. Res.*, *93*, 9007-9026, 1975.
- Olgaard, D.L., and B. Evans, Grain growth in synthetic marbles with added mica and water, *Contrib. Mineral. Petrol.*, *100*, 246-260, 1988.
- Olsen, M.P., C.H. Scholz, and A. Léger, Healing and sealing of a simulated fault gouge under hydrothermal conditions: Implications for fault healing, *J. Geophys. Res.*, *103*, 7421-7430, 1998.
- Passchier, C.W., and R.A.J. Trouw, *Microtectonics*, 289 pp., Springer Verlag, 1996.
- Paterson, M.S., A theory for granular flow accommodated by material transfer via an intergranular fluid, *Tectonophysics*, *245*, 135-151, 1995.
- Pharr, G.M., and M.F. Ashby, On creep enhanced by a liquid phase, *Acta metall.*, *31*, 129-138, 1983.
- Platt, J.P., Secondary cleavages in ductile shear zones, *J. Struct. Geol.*, *6*, 439-442, 1984.
- Platt, J.P., and R.L.M. Vissers, Extensional structures in anisotropic rocks, *J. Struct. Geol.*, *2*, 397-410, 1980.
- Poirier, J.-P., *Creep of Crystals*, 260 pp., Cambridge University Press, 1985.
- Power, W.L., and T.E. Tullis, The relationship between slickenside surfaces in fine-grained quartz and the seismic cycle, *J. Struct. Geol.*, *11*, 879-893, 1989.

- Price, R.H., Effects of anhydrite and pressure on the mechanical behaviour of synthetic rocksalt, *Geophys. Res. Lett.*, 9, 1029-1032, 1982.
- Raj, R., Creep in polycrystalline aggregates by matter transport through a liquid phase. *J. Geophys. Res.*, 87, 4731-4739, 1982.
- Raj, R., and M.F. Ashby, On grain boundary sliding and diffusional creep, *Metal. Trans.*, 2, 1113-1126, 1971.
- Raj, R., and C.K. Chyung, Solution-precipitation creep in glass ceramics, *Acta Metall.*, 29, 159-166, 1981.
- Ranalli, G., *Rheology of the earth*, 413 pp., Chapman & Hall, 1995.
- Ranalli, G., Rheology of the lithosphere in space and time, in *Orogeny through time*, edited by J.-P. Burg, and M. Ford, pp. 19-38, Geological Society Special Publication 54, London, 1997.
- Renard, F., and P. Ortoleva, Water films at grain-grain contacts: Debye-Hückel, osmotic model of stress, salinity, and mineralogy dependence, *Geochim. Cosmochim. Acta*, 61, 1963-1970, 1997.
- Renard, F., P. Ortoleva, and J.P. Gratier, Pressure solution in sandstones: influence of clays and dependence on temperature and stress, *Tectonophysics*, 280, 257-266, 1997.
- Rice, J.R., Fault stress states, pore pressure redistributions, and the weakness of the San Andreas fault, in *Fault Mechanics and Transport Properties of Rocks*, edited by B. Evans, and Wong, T.-f., pp. 476-503, Academic Press, 1992.
- Rice, J.R., Spatio-temporal complexity of slip on a fault, *J. Geophys. Res.*, 98, 9885-9907, 1993.
- Rimstidt, J.D., Quartz solubility at low temperatures, *Geochim. Cosmochim. Acta*, 61, 2553-2558, 1997.
- Ross, J.V., and S.J. Bauer, Semi-brittle deformation of anhydrite-halite shear zones simulating mylonite formation, *Tectonophysics*, 213, 303-320, 1992.
- Ross, J.V., S.J. Bauer, and F. Hansen, Textural evolution of synthetic anhydrite-halite mixtures, *Tectonophysics*, 140, 307-326, 1987.
- Ross, J.V., and K.R. Wilks, Microstructure development in an experimentally sheared orthopyroxene granulite, *Tectonophysics*, 256, 83-100, 1996.
- Rubie, D.C., Mechanisms of reaction-enhanced deformability in minerals and rocks, in *Deformation Processes in Minerals, Ceramics and Rocks*, edited by D.J. Barber, and Meredith, P.G., pp. 262-295, Unwin Hyman, London, 1990.
- Ruina, A., Slip instability and state variable friction laws, *J. Geophys. Res.*, 88, 10,359-10,370, 1983.
- Rutter, E.H., The kinetics of rock deformation by pressure solution, *Phil. Trans. R. Soc. London A*, 283, 203-219, 1976.
- Rutter, E.H., The mechanical properties of kaolinite fault "gouge" at moderate confining pressure, 20 °C, *Int. J. Rock Mech. Min. Sci. & Geomech. Abstr.*, 16, 407-410, 1979.
- Rutter, E.H., Pressure solution in nature, theory and experiment, *J. geol. Soc. London*, 140, 725-740, 1983.
- Rutter, E.H., and K.H. Brodie, The role of tectonic grain size reduction in the rheological stratification of the lithosphere, *Geol. Rundschau*, 77, 295-308, 1988.
- Rutter, E.H., and K.H. Brodie, Lithosphere rheology - a note of caution, *J. Struct. Geol.*, 13, 363-367, 1991.
- Rutter, E.H., R.H. Maddock, S.H. Hall, and S.H. White, Comparative microstructures of natural and experimentally produced clay-bearing fault gouges, *Pure Appl. Geophys.*, 124, 3-30, 1986.
- Rutter, E.H., and R.H.I. Maddock, On the mechanical properties of synthetic kaolinite/quartz fault gouge, *Terra Nova*, 4, 489-500, 1992.
- Rutter, E.H., and D.H. Mainprice, The effect of water on stress relaxation of faulted and unfaulted sandstone, *Pure Appl. Geophys.*, 116, 634-654, 1978.
- Rutter, E.H., and D.H. Mainprice, On the possibility of slow fault slip controlled by a diffusive mass transfer process, *Gerlands Beitr. Geophysik*, 88, 154-162, 1979.
- Rutter, E.H., and P.H. Wanten, Experimental study of the compaction of phyllosilicate-bearing sand at elevated temperature and with controlled pore water pressure, *J. Sedimentary Res.*, 70, 107-116, 2000.
- Rutter, E.H., and S.H. White, The microstructures and rheology of fault gouges produced experimentally under wet and dry conditions at temperatures up to 400 °C., *Bull. Mineral.*, 102, 101-109, 1979.
- Sammis, C.G., and S.J. Steacy, The micromechanics of friction in a granular layer, *Pure Appl. Geophys.*, 142, 777-794, 1994.
- Schmid, S.M., and M.R. Handy, Towards a genetic classification of fault rocks: Geological usage and tectonophysical implications, in *Controversies in Modern Geology*, edited by D.W. Müller, J. McKenzie, and H. Weissert, pp. 339-361, Academic Press, New York, 1991.
- Scholz, C.H., The brittle-plastic transition and the depth of seismic faulting, *Geol. Rundschau*, 77, 319-328, 1988.
- Scholz, C.H., *The mechanics of earthquakes and faulting*, 439 pp., Cambridge University Press, 1990.
- Scholz, C.H., Earthquakes and friction laws, *Nature*, 391, 37-42, 1998.
- Scholz, C.H., Evidence for a strong San Andreas fault, *Geology*, 28, 163-166, 2000.
- Schutjens, P.M.T.M., Experimental compaction of quartz sand at low effective stress and temperature conditions, *J. Geol. Soc. London*, 148, 527-539, 1991.
- Schutjens, P.M.T.M., and C.J. Spiers, Intergranular pressure solution in NaCl: Grain-to-grain contact experiments under the optical microscope, *Oil & Gas Science and Technology - Rev. IFP*, 54, 729-750, 1999.
- Schwarz, S., and B. Stoeckert, Pressure solution in siliciclastic HP-LT metamorphic rocks - constraints on the state of stress in deep levels of accretionary complexes, *Tectonophysics*, 255, 203-209, 1996.
- Seront, B., T.-f. Wong, J.S. Caine, C.B. Forster, R.L. Bruhn, and J.T. Fredrich, Laboratory characterization of hydromechanical properties of a seismogenic normal fault system, *J. Struct. Geol.*, 20, 865-881, 1998.
- Shea, W.T., and A.K. Kronenberg, Rheology and deformation mechanisms of an isotropic mica schist, *J. Geophys. Res.*, 97, 15,201-15,237, 1992.
- Shea, W.T., and A.K. Kronenberg, Strength and anisotropy of foliated rocks with varied mica contents, *J. Struct. Geol.*, 15, 1097-1121, 1993.
- Shimamoto, T., Transition between frictional slip and ductile flow for halite shear zones at room temperature, *Science*, 231, 711-714, 1986.
- Shimamoto, T., The origin of S-C mylonites and a new fault-zone model, *J. Struct. Geol.*, 11, 51-64, 1989.
- Shimamoto, T., and J.M. Logan, Effects of simulated clay gouges on the sliding behavior of Tennessee sandstone, *Tectonophysics*, 75, 243-255, 1981.
- Shimamoto, T., and J.M. Logan, Velocity-dependent behavior of simulated halite shear zones: an analog for silicates, in *Earthquake Source Mechanics*, edited by S. Das, Boatwright, J. and Scholz, C.H., pp. 49-63, 1986.
- Sibson, R.H., Frictional constraints on thrust, wrench and normal faults, *Nature, Phys. Sci.*, 249, 542-543, 1974.
- Sibson, R.H., Fault rocks and fault mechanisms, *J. Geol. Soc. London*, 133, 191-213, 1977.
- Sibson, R.H., Power dissipation and stress levels on faults in the upper crust, *J. Geophys. Res.*, 85, 6239-6247, 1980.

- Sibson, R.H., Continental fault structure and the shallow earthquake source, *J. Geol. Soc. London*, 140, 741-767, 1983.
- Sibson, R.H., Roughness at the base of the seismogenic zone: Contributing factors, *J. Geophys. Res.*, 89, 5791-5799, 1984.
- Sleep, N.H., Ductile creep, compaction, and rate and state dependent friction within major fault zones, *J. Geophys. Res.*, 100, 13,065-13,080, 1995.
- Sleep, N.H., Application of a unified rate and state friction theory to the mechanics of fault zones with strain localization, *J. Geophys. Res.*, 102, 2875-2895, 1997.
- Sleep, N.H., and M.L. Blanpied, Creep, compaction and the weak rheology of major faults, *Nature*, 359, 687-692, 1992.
- Smith, D.L., and B. Evans, Diffusional crack healing in quartz, *J. Geophys. Res.*, 89, 4125-4135, 1984.
- Snoke, A.W., J. Tullis, and V.R. Todd, *Fault-related rocks: A photographic atlas*, Princeton University Press, New Jersey, 1999.
- Sparks, D.W., and E. Aharonov, Dynamics of stick-slip motion in granular materials, *EOS, Transaction AGU*, 80, 1036, 1999.
- Spiers, C.J., and R.H. Brzesowsky, Densification behaviour of wet granular salt: Theory versus experiment, in *Seventh Symposium on Salt*, pp. 83-92, Elsevier, 1993.
- Spiers, C.J., and N.L. Carter, Microphysics of rocksalt flow in nature, in *Fourth conference on the mechanical behavior of salt*, edited by M. Aubertin, and H.R. Hardy, Jr., pp. 115-128, Trans Tech Publications, 1998.
- Spiers, C.J., and P.M.T.M. Schutjens, Densification of crystalline aggregates by fluid phase diffusional creep, in *Deformation Processes in Minerals, Ceramics and Rocks*, edited by D.J. Barber, and Meredith, P.G., pp. 334-353, Unwin Hyman, London, 1990.
- Spiers, C.J., P.M.T.M. Schutjens, R.H. Brzesowsky, C.J. Peach, J.L. Liezenberg, and H.J. Zwart, Experimental determination of constitutive parameters governing creep of rocksalt by pressure solution, in *Deformation Mechanisms, Rheology and Tectonics*, Geol. Soc. Sp. Publ. 54, 215-227, 1990.
- Stewart, M., R.E. Holdsworth, and R.A. Strachan, Deformation processes and weakening mechanisms within the frictional-viscous transition zone of major crustal-scale faults: insights from the Great Glen Fault Zone, Scotland, *J. Struct. Geol.*, 22, 543-560, 2000.
- Tada, R., and R. Siever, Experimental knife-edge pressure solution of halite, *Geochim. Cosmochim. Acta*, 50, 29-36, 1986.
- Tada, R., and R. Siever, Pressure solution during diagenesis, *Ann. Rev. Earth Planet. Sci.*, 17, 89-118, 1989.
- Tenthorey, E., C.H. Scholz, E. Aharonov, and A. Léger, Precipitation sealing and diagenesis I. Experimental results, *J. Geophys. Res.*, 103, 23,951-23,967, 1998.
- Ter Heege, J.H., J.H.P. De Bresser, and C.J. Spiers, The role of microstructure in determining rheology, *Geophys. Res. Abstracts*, 1, 69, 1999.
- Townend, J., and M.D. Zoback, How faulting keeps the crust strong, *Geology*, 28, 399-402, 2000.
- Tse, S.T., and J.R. Rice, Crustal earthquake instability in relation to the depth variation of frictional slip properties, *J. Geophys. Res.*, 91, 9452-9472, 1986.
- Visser, H.J.M., Mass transfer processes in crystalline aggregates containing a fluid phase, PhD thesis, Utrecht University, 1999.
- Wang, K., T. Mulder, G. Rogers, and R. Hyndman, Case for very low coupling stress on the Cascadia subduction fault, *J. Geophys. Res.*, 100, 12,907-12,918, 1995.
- Weertman, J., Unstable slippage across a fault that separates elastic media of different elastic constants, *J. Geophys. Res.*, 85, 1455-1461, 1980.
- Wesnousky, S.G., Seismicity as a function of cumulative geologic offset: some observations from southern California, *Bull. Seismol. Soc. Am.*, 80, 1374-1381, 1990.
- White, S.H., P.G. Bretan, and E.H. Rutter, Fault-zone reactivation: kinematics and mechanisms, *Phil. Trans. R. Soc. Lond.*, A317, 81-97, 1986.
- White, S.H., S.E. Burrows, J. Carreras, N.D. Shaw, and F.J. Humphreys, On mylonites in ductile shear zones, *J. Struct. Geol.*, 2, 175-187, 1980.
- Wilcock, W.S.D., G.M. Purdy, and S.C. Solomon, Microearthquake evidence for extension across the Kane transform fault, *J. Geophys. Res.*, 95, 15439-15462, 1990.
- Wintsch, R.P., R. Christoffersen, and A.K. Kronenberg, Fluid-rock reaction weakening of fault zones, *J. Geophys. Res.*, 100, 13,021-13,032, 1995.
- Wojtal, S., and G. Mitra, Strain Hardening and Strain Softening in Fault Zones from Foreland Thrusts, *Geol. Soc. Am. Bull.*, 97, 674-687, 1986.
- Wong, T.-f., and L.-C. Wu, Tensile stress concentration and compressive failure in cemented granular material, *Geophys. Res. Lett.*, 22, 1649-1652, 1995.
- Wood, D.M., *Soil behaviour and critical state soil mechanics*, 462 pp., Cambridge University Press, 1990.
- Wu, F.T., Mineralogy and physical nature of clay gouge, *Pure Appl. Geophys.*, 116, 655-689, 1978.
- Wu, F.T., L. Blatter, and H. Robertson, Clay gouges in the San Andreas Fault System and their possible implications, *Pure Appl. Geophys.*, 113, 87-95, 1975.
- Yund, R.A., M.L. Blanpied, T.E. Tullis, and J.D. Weeks, Amorphous material in high strain experimental fault gouges, *J. Geophys. Res.*, 95, 15,589-15,602, 1990.
- Zhang, S., T.E. Tullis, and V.J. Scruggs, Permeability anisotropy and pressure dependency of permeability in experimentally sheared gouge materials, *J. Struct. Geol.*, 21, 795-806, 1999.
- Zoback, M.D., and J.H. Healy, In situ stress measurements to 3.5 km depth in the Cajon Pass scientific research borehole: Implications for the mechanics of crustal faulting, *J. Geophys. Res.*, 102, 18,477-18,491, 1992.
- Zoback, M.D., M.L. Zoback, V.S. Mount, J. Suppe, J.P. Eaton, J.H. Healy, D. Oppenheimer, P. Reasenber, L. Jones, C.B. Raleigh, I.G. Wong, O. Scotti, and C. Wentworth, New evidence on the state of stress of the San Andreas fault system, *Science*, 238, 1105-1111, 1987.

Nederlandse samenvatting

Aardbevingen zijn de meest destructieve natuurrampen die de mensheid teisteren. Het begrijpen van de processen die tot aardbevingen leiden is van groot wetenschappelijk en maatschappelijk belang. De meeste aardbevingen vinden plaats langs breukzones, zones waar de rigide platen waaruit de aardkorst bestaat ten opzichte van elkaar bewegen. Op sommige plaatsen schuiven de platen langs elkaar, zoals bij de San Andreas breuk in California of de Noord-Anatolische breuk in Turkije (denk aan de Izmit aardbeving van augustus 1999). Op andere plaatsen schuift de ene plaat onder de andere in zogenaamde subductiezones, zoals bij het Andesgebergte of Japan. Op sommige plaatsen botsen continentale landmassa's op elkaar, zoals in de Alpen of de Himalaya. Deze breukzones zijn geen discrete breuken, maar zones van meters tot enige kilometers breed, waar het gesteente (breukgesteente genoemd) door de relatieve bewegingen van de platen zwaar vervormd is. De mechanische processen in breukzones staan centraal in dit proefschrift. Het onderzoek levert een bijdrage aan het begrip van de mechanische eigenschappen van deze breukzones en aan het inzicht in de processen die tot aardbevingen leiden. Met dit inzicht zijn aarbevingsrisico's beter in te schatten. De resultaten zijn daarnaast van belang voor het numeriek modelleren van grootschalige deformatie processen in de korst, zoals bijvoorbeeld gebergtevorming.

Wetenschappers beschrijven de processen die de mechanische eigenschappen van breukzones bepalen met behulp van zogenaamde sterkteprofielen van de aardkorst. Deze sterkteprofielen zijn in de afgelopen decennia ontwikkeld op basis van vergelijkingen tussen veldgeologische waarnemingen en laboratoriumexperimenten. De sterkte van het bovenste deel van de aardkorst wordt volgens deze profielen bepaald door bros breukgedrag of wrijving langs breukvlakken. De sterkte neemt hier toe met de diepte omdat door de toename van druk met de diepte de normaalkracht op de breukvlakken toeneemt. Aardbevingen ontstaan hoofdzakelijk als gevolg van breukprocessen in het brosse deel van de korst. Op grotere diepte wordt de sterkte van de korst bepaald door ductiel- of vloeigedrag. Door de toename van de temperatuur met de diepte treden intrakristallijne processen (ook wel dislocatiekruip genoemd) op, waardoor het gesteente ductiel wordt, i.e. kan vloeien. In dit deel neemt de sterkte af met de diepte, doordat het gesteente minder visceus wordt bij hogere temperatuur. Sterkteprofielen voorspellen een overgang van bros naar ductiel gedrag op een diepte van 10-20 kilometer. In deze overgangszone is de sterkte van de korst het hoogst. Sterkteprofielen worden regelmatig toegepast in numerieke modelleringsstudies van tectonische processen zoals bijvoorbeeld gebergtevorming.

Toch is er al decennia lang kritiek op deze sterkteprofielen. Deze zouden de sterkte van de korst sterk overschatten, omdat ze de natuurlijke situatie sterk simplificeren. Een bevestiging hiervan geven spanningsmetingen, met name op de San Andreas breuk, die aangeven dat deze breukzone significant zwakker is dan voorspeld door simpele bros-ductiele sterkteprofielen. Mogelijke oorzaken hiervan zijn:

- Sterkteprofielen negeren de effecten van de aanwezigheid van zwakkere, plaatvormige mineralen zoals mica's en kleien in breukzones, terwijl deze mineralen juist in verhoogde concentraties voorkomen in breukzones. Deze mineralen hebben met name een groot effect als ze een foliatie vormen in het breukgesteente. Foliatie houdt in dat de mineralen bij een toenemende vervorming van het breukgesteente de oriëntatie van de schuifrichting aanemen.
- Sterkteprofielen negeren de effecten van water. Veldstudies hebben aangetoond dat er vrijwel altijd water in breukzones aanwezig is. Water kan leiden tot verzwakking van de breukzone door het optreden van vloeistof-geassisteerde deformatieprocessen zoals drukoplossing. Drukoplossing houdt in dat materiaal oplost op plaatsen waar de spanning hoog is, gevolgd door neerslag op plaatsen waar de spanning laag is. Hierdoor wordt ductiel gedrag mogelijk op een diepte waar zonder water alleen bros gedrag mogelijk is. Veldstudies laten zien dat

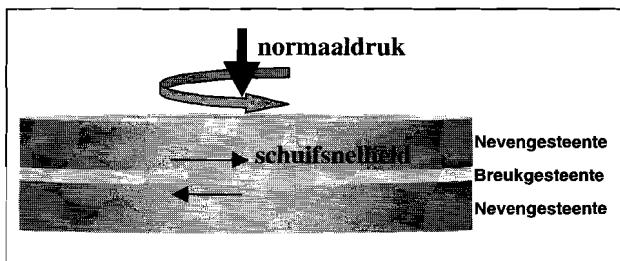
deformatie van breukgesteente door drukoplossing met name optreedt in de overgangszone tussen bros en ductiel gedrag.

Hoewel het idee van een zwakkere korst door bovengenoemde factoren al meer dan twee decennia geleden geopperd werd is er weinig experimenteel bewijs voor vloeigedrag van breukgesteente door deze processen, en zijn er geen kwantitatieve modellen ontwikkeld die dergelijk gedrag beschrijven.

Oplos- en neerslagreacties hebben, naast een effect op de vloeisterkte van breukgesteente, ook invloed op het herstel van sterkte van breuken na aardbevingen. Gedacht wordt dat, na een aardbeving, water in de loop der tijd compactie en verkitting van breukgesteenten mogelijk maakt, zodat op dezelfde breuk nieuwe aardbevingen mogelijk zijn. Hoewel modellen voor tijdsafhankelijk sterkteherstel van breuken wijdverbreid zijn in het modelleren van seismisch gedrag zijn de achterliggende mechanismen nog vrij slecht begrepen.

Dit proefschrift karakteriseert en geeft een kwantitatieve beschrijving van de effecten van vloeistofgeassisteerde deformatieprocessen in breukgesteenten. Het gaat in op de effecten in zowel monomineralische systemen als in klei- of mica-houdende gesteenten en beschrijft naast vloeigedrag ook de mechanismen die leiden tot sterkteherstel na aardbevingen.

Het onderzoek is gebaseerd op deformatie-experimenten aan gesimuleerde breukgesteenten. De experimenten zijn gedaan in een zogenaamd "ring-shear" apparaat (zie nevenstaand figuur). Doordat met dit apparaat de mogelijkheid bestaat een grote vervorming van het breukgesteente te bereiken, is deze bij uitstek geschikt om de invloed van microstructurele evolutie, zoals de vorming van foliatie, op mechanisch gedrag te bestuderen.



Schematisch diagram van de "ring-shear" deformatieconfiguratie, waarin een ringvormig monster breukgesteente vervormd wordt doordat de "nevangesteente" ringen ten opzichte van elkaar gedraaid worden.

Als breukgesteente zijn geen natuurlijke gesteenten maar gesteenteanalogen gebruikt, te weten mengsels van keukenzout (Haliet, NaCl) en kaoliniet (een kleimineraal). Vervormingsprocessen in natuurlijke gesteenten opereren over tijdsschalen van honderden jaren (typisch tijdsinterval tussen aardbevingen op dezelfde breuk) tot miljoenen jaren (typische tijdschaal voor gebergtevormingsprocessen), veel te langzaam om in een laboratorium te kunnen bestuderen dus. Door gesteenteanalogen te kiezen waarin de snelheid van deformatieprocessen aanmerkelijk hoger is dan in natuurlijke materialen wordt het mogelijk de effecten van vloeistofgeassisteerde deformatieprocessen op het mechanisch gedrag van breukgesteenten systematisch te bestuderen in het laboratorium. De fysisch-mathematische beschrijving die hierdoor verkregen wordt kan vervolgens op andere, meer realistische materialen en tijdsschalen toegepast worden.

In de experimenten worden twee vlakken (de breuk), gescheiden door een laag monstermateriaal (het breukgesteente), met gecontroleerde snelheid en normaaldruk langs elkaar geschoven terwijl de schuifspanning gemeten wordt. Er zijn twee typen experimenten uitgevoerd. In het eerste type is, om het vloeigedrag van het breukgesteente te karakteriseren, het breukgesteente tot hoge vervormingen gedeformeerd bij verschillende schuifsnelheden. Bij het tweede type experiment is het sterkteherstel na aardbevingen gesimuleerd door de deformatie voor gecontroleerde tijd stil te zetten en vervolgens weer op te starten, waardoor de sterkte-toename tijdens de "rustperiode" gemeten kan worden. Na experimenten zijn dunne doorsneden van het breukgesteente

gemaakt, om -met behulp van een microscoop- de microstructuur te kunnen bestuderen. Uit de microstructuur is af te leiden welke deformatieprocessen operatief waren tijdens het experimenten.

De resultaten in dit proefschrift laten zien dat puur keukenzout slechts bros gedrag (en dus geen vloeigedrag) te zien geeft, hoewel in de microstructuren duidelijke aanwijzingen gevonden zijn dat drukoplossing optrad (zie hoofdstuk 2). Daarnaast blijkt in monomineralische systemen dat, in tegenstelling tot wat algemeen werd aangenomen, de verkitting van het breukgesteente door oplossen neerslagprocessen domineert over verzwakking door water geassisteerd vloeigedrag.

Als de gesimuleerde breuk gevuld is met een mengsel van haliet en kaoliniet is heel ander gedrag te zien (zie hoofdstuk 3 en 4). Met toenemende vervorming is een overgang te zien van puur bros gedrag naar ductiel vloeigedrag. Dit gaat gepaard met korrelgroottereductie en de ontwikkeling van een sterke foliatie, gedefinieerd door de kleimineralen. De microstructuren laten zien dat dit vloeigedrag veroorzaakt wordt door het glijden van korrels over de kleimineralen in de foliatievlakken. Obstakels worden overwonnen door plaatselijk oplossen van zoutkorrels. De resultaten laten voor het eerst experimenteel bewijs zien van vloeigedrag van breukgesteente door een mechanisme van drukoplossing, een proces dat tot nu toe alleen als hypothese geopperd was.

Op basis van het laatstgenoemde deformatieproces is vervolgens een theoretisch model opgesteld voor deformatie van klei- of mica-houdend breukgesteente (zie hoofdstuk 7). Dit model is toegepast op natuurlijke materialen om de invloed van water-geassisteerde deformatieprocessen op de sterkte van breukzones in de aardkorst te bepalen.

De modelresultaten laten zien dat de aanwezigheid van gefolieerde, klei- of mica-houdende breukzones leidt tot een verzwakking van meer dan een factor 4 in vergelijking met de momenteel gebruikte sterkteprofielen gebaseerd op bros gedrag en dislocatiekruip. Dit impliceert dat de aardkorst in deformerende zones waarschijnlijk significant zwakker is dan tot nu toe gedacht, gezien het feit dat het overgrote deel van de deformatie in de aardkorst geacommodeerd wordt in gefolieerde, mica-houdende schuifzones. Daarnaast laten de modelresultaten zien dat ook het diepte-interval waarin ductiel vloeigedrag plaatsvindt (in plaats van bros gedrag) flink groter is dan gedacht. Deze resultaten worden ondersteund door waarneming in recente veldstudies van phylloniet schuifzones in, onder andere, Schotland en het Egeïsch gebied.

Tot slot zijn twee series experimenten uitgevoerd (hoofdstukken 5 en 6) met als doel het bestuderen van processen die leiden tot sterkteherstel na aardbevingen. In de eerste serie experimenten is puur haliet gebruikt. De resultaten bevestigen het alomtegenwoordige idee dat sterkteherstel versneld wordt door de aanwezigheid van water. Ze laten zien dat sterkteherstel veroorzaakt wordt door compactie van het poreuze breukgesteente, veroorzaakt door drukoplossing. Drukoplossing, -en de daarmee geassocieerde neerslag van materiaal in de poriën van het gesteente-, veroorzaakt verkitting. Hierdoor ontstaat een toename van de breuksterkte van het gesteente. Daarnaast moet, als gevolg van de compactie, het gecompacteerd breukgesteente uitzetten tijdens de aardbeving. Immers, de korrels moeten over elkaar kunnen rollen. Dit kost arbeid tegen de normaaldruk op de breuk, wat weer bijdraagt aan de breuksterkte.

In een tweede serie experimenten is het effect van klei op sterkteherstel bestudeerd. De resultaten tonen aan dat de snelheid van sterkteherstel met een orde van grootte afneemt door de aanwezigheid van klei of mica. Dit effect is nog sterker als de klei een foliatie vormt. Het effect wordt grotendeels veroorzaakt door de invloed van klei op de verkitting van breukgesteente: de aanwezigheid van klei in de de korrelcontacten blijkt verkitting van breukgesteenten grotendeels te voorkomen. Dit verklaart ook dat de snelheid van sterkteherstel het laagst is in gefolieerde gesteenten: hier is op vrijwel alle korrelcontacten klei aanwezig.

De resultaten van bovenstaande experimenten vergroten het inzicht in de processen die leiden tot sterkteherstel na aardbevingen, en de relatieve rollen van volumeverandering (compactie) en verkitting, aanzienlijk. Zo laten ze zien dat het voor het modelleren van sterkteherstel aan

natuurlijke breuken data van experimenten aan klei-houdende gesteenten gebruikt moeten worden, aangezien natuurlijke breukgesteenten vrijwel altijd klei of mica bevatten. Het gebruik van data van monomeralische experimenten, wat tegenwoordig nog veel gedaan wordt, leidt tot significante overschatting van de snelheid van sterkteherstel op natuurlijke breuken.

Daarnaast zijn de resultaten van belang voor het begrijpen van de oorzaken en mechanismen van reactivatie van grote breukzones door de geologische tijd heen. Uit veldstudies blijkt dat bestaande breukzones door de geologische tijd heen meerdere malen gereactiveerd worden terwijl het gebied waar ze zich bevinden door verschillende gebergtevormingsfasen heen gaat. Het blijkt gemakkelijker te zijn om een oude breukzone te reactiveren dan om een nieuwe te vormen, zelfs als de oude breukzone een minder gunstige orientatie heeft voor de nieuwe deformatiefase. Dit onderzoek laat zien dat de vorming van foliaties in breukzones het sterkteherstel van het breukgesteente -waardoor het weer de sterkte van het nevengeesteente zou krijgen- aanzienlijk vertraagt en soms zelfs geheel voorkomt. Dit verklaart waarom deze breukzones zo vaak gereactiveerd worden. De resultaten impliceren dat voor het modelleren van gebergtevormingsprocessen de aanwezigheid van oude breukzones als beginconditie moet worden meegenomen.

Concluderend heeft dit proefschrift geleid tot een beter begrip van processen die leiden tot verzwakking en sterkteherstel in de aardkorst door effecten van water en mica's. Bovendien zijn deze effecten voor het eerst gekwantificeerd in een fysisch-mathematisch model, wat gebruikt kan worden in numerieke modelleringsstudies van tectonische processen in de korst.

Dankwoord

Na vier jaar promoveren besef ik dat ik een gezegend mens ben, onder andere omdat ik de second year dip, de "third year despair", de laatste-fase stress, de holle ogen, het slechte eten, het jaar zonder vakantie, de continue stroom zweet en tranen en al die andere zaken die promoveren tot zo'n ongezonde bezigheid kunnen maken een beetje ben misgelopen. Ik heb van begin tot eind genoten van het promoveren en alles wat daarbij kwam kijken. In ben blij dat ik de kans heb om hier alle mensen te bedanken die de afgelopen jaren op wat voor manier dan ook hebben bijgedragen aan de totstandkoming van dit proefschrift. Het wordt een lekker lang dankwoord! De afgelopen vier jaar waren op veel manieren bewogener dan ik vooraf ooit had kunnen denken, maar met de hulp van velen heb ik me er (vind ik zelf) redelijk doorheengeslagen.

Als eerste wil ik noemen mijn directe familie: Pap, Jan, Anouk, Hanneke, Dick. Wat jullie voor mij betekenen is niet in woorden te vatten. Mama zou trots op jullie zijn! Jan ook nog bedankt voor het redigeren van de Nederlandse samenvatting.

Uitgebreide dank gaat ook uit naar al mijn vrienden, voor het bieden van gezelligheid, een luisterend oor, een stevige schouder, zinloze gesprekken, zinvolle gesprekken, gezelschap op bergtochten, kampeerweekenden, concerten, en vooral ook veel lol. Als eerste wil ik hier Jelmer en Fraukje noemen, maar verder ook Sietse, Erik, Saskia, Magdeleen, Monique, Maartje, Severina, Ingrid, Wim, Willem, Wouter, Marcel en Julien. Jullie zijn helden.

Op het Iva waren met name de vrijdagmiddagborrels met de collega's van de Structurele Geologie en HPT groepen een bron van plezier en ontspanning, en een uitlaatklep tijdens wat stressvollere periodes. Ultiem hoogtepunt was natuurlijk het bijschrijven van mijn naam op de Ratsropfen-trofee, na het winnen van de blaasvoetbalcompetitie samen met Andor! Regelmatig aanwezig waren mijn medepromovendi Fraukje, Armelle, Arjan, Andor, Marga, René, Kike, Marije, Jan en postdocs Siese, Rob, Paul, Pat en Julie, maar ook stafleden Martyn Drury, Stan White, Herman van Roermund en Bernard de Jong. Naast de vrijdagmiddagborrels was ieder jaar de HPT "all-weather" barbecue ("loads of food and drink!") een hoogtepunt, en dan met name het schoonkrabben van de barbecueroosters op de dag na de barbecue, samen met eerst Rob en later Jan, met elk jaar weer zo'n gruwelijke houten kop dat je je voorneemt de volgende barbecue niets te drinken.

Heel veel dank ben ik verschuldigd aan Chris Spiers, mijn promotor en begeleider. Chris heeft me vanaf het eerste moment dat ik hem zag altijd weten te motiveren met zijn enthousiasme en met zijn nadruk op een precieze, exacte benadering in het woud van vage bla-bla die de Geologie vaak is. Chris liet me altijd m'n eigen gang gaan (of dit mede door tijdgebrek kwam wil ik niet eens weten) zonder dat dat ten koste ging van zijn betrokkenheid en z'n vermogen enthousiasme over te brengen. In het laatste jaar las hij geconcentreerd en nauwgezet mijn artikelen en proefschrift hoofdstukken, zelfs in periodes waarin hij zelf omkwam in het werk. Ik heb onnoemelijk veel geleerd van zijn opbouwend-kritische houding, zijn oog voor detail, zijn nadruk op heldere argumentatie, en zijn perfectionisme. Chris, we're a great team! Met Colin Peach heb ik tijdens mijn afstuderen meer samengewerkt dan tijdens mijn promotie. Desalniettemin heeft Colin met name in het beginstadium van mijn onderzoek veel laboratoriumproblemen opgelost, en zijn deur stond altijd open voor vragen van allerlei aard. Colin, thank you for being one of the nicest persons I've ever met. Hans de Bresser leek altijd tijd te hebben voor een discussie over deformatiemechanismen of microstructuren; een leuke sport was Hans met een vraag onderscheppen als-ie voorbij kwam lopen, en vervolgens kijken hoe lang je hem aan de praat kon houden. Als het studentenonderwijs hieronder geleden heeft spijt me dat oprecht. Siese de Meer was altijd bereid mij niet te geloven, en wist iedereen daarnaast met zijn onuitputtelijke energie altijd te motiveren voor een bezoek aan Pandje, diep in de nacht. Martyn Drury stelde altijd moeilijke vragen na praatjes, en heeft geholpen met de EBSD metingen die gerapporteerd zijn in hoofdstuk 4.

Dan nog mijn kamergenoot Jan, met wie het nooit moeilijk was om onderzoek te relativieren. Het is voor promovendi erg belangrijk om een kamergenoot te hebben om tegen te klagen, om Britney Spears mee te zingen ("crazy!"), voorbijgangers uit te schelden, op konijnen en merels te schieten en wat dies meer zij. Veel succes met je eigen proefschrift.

A number of people from outside our university contributed to this thesis through discussions at conferences and during visits. Sandy Steacy is thanked for comments regarding the importance of wall rock surface roughness at a conference in Southern Italy in 1997. Chris Scholz, Masao Nakatani, Einat Aharonov and Kul Karcz, all from Lamont-Doherty Earth Observatory in New York, are thanked for hospitality and discussions during my stop-over at LDEO in December 1999. Brian Evans (MIT) is thanked for discussions during his visit in the context of our Ph.D. student education programme in November 1999. Steve Hickman (USGS), Amotz Agnon (Hebrew University of Jerusalem), Dan Faulkner (University of Manchester), Terry Tullis (Brown University) and Diane Moore (USGS) provided thorough and constructive reviews of manuscripts based on Chapters 2, 3 and 6. Finally, the dissertation committee, consisting of Terry Tullis (Brown University), Mark Handy (Freie Universität Berlin), Fred Chester (Texas A&M University), Rinus Wortel (Tectonophysics, Utrecht University) and Stan White (Structural Geology, Utrecht University) are thanked for judging of and commenting on the thesis.

Peter van Krieken, Gert Kastelein en Eimert de Graaff, de technici van het HPT-team, stonden altijd klaar om te helpen bij experimentele problemen of vragen, en waren gezellige collega's tijdens koffiepauzes, dagelijkse praatjes enzovoort. Gert was betrokken bij de ontwikkeling en de bouw van het ring-shear apparaat, samen met Tony van der Gon Netscher van de werkplaats. Gert was altijd bereid om op dubbele snelheid dingen te maken. Eimert bouwde de akoestische emissie set-up. Peter hielp met van alles en nog wat. Ik heb veel spijt van alle tijd die ik heb verspild door Peter te vragen waar dingen lagen zonder zelf eerst goed te kijken. Verder was onze secretaresse Magda Martens altijd goed voor het oplossen van ieder mogelijk probleem, met nog een gratis glimlach erbij ook. Paul van Oudenallen, Isaak Santoe en Jacco Bergenhenegouwen van de audio-visuele dienst hebben geholpen met het maken van posters en met de omslag van dit proefschrift. Boudewijn 't Hart regelde menig vliegreisje, en wilde ook altijd z'n vakantiefoto's graag laten zien.

Voor de broodnodige activiteit naast mijn promotie heb ik mijn werk voor de VMSG Opleidingscommissie altijd met veel plezier gedaan, niet in het minst dankzij mijn mede-opcomers Ron Noomen, Kabir Roy-Chowdury, Marleen Nyst, Hans de Bresser, Andre van der Hoeven, Ildiko Csikos, en later ook nog even mijn twee-vrouws vervangingsteam Kike Beintema en Annemarie Bos. Ik weet zeker dat OPCOM in de komende jaren met afstand het succesvolste onderdeel van de VMSG blijft.

Tot slot nog een wijze les, voor wie er behoefte aan heeft:

"There are two ways to live: one is as if nothing is a miracle;
the other as if everything is."

(Albert Einstein)

Curriculum Vitae

Ik ben geboren op 27 april 1973 in Hoogeveen. Na het halen van het examen VWO aan het Menso Alting College te Hoogeveen in de zomer van 1991 begon ik in hetzelfde jaar aan de studie Geologie aan de (toenmalige) Rijksuniversiteit Utrecht. Ik koos daarin de afstudeerrichting "Aardse Materialen". In de zomer van 1996 werd het doctoraalexamen Geologie behaald. In hetzelfde jaar begon ik aan een promotieonderzoek in het HPT Laboratorium van de faculteit Aardwetenschappen van de Universiteit Utrecht. Dit proefschrift beschrijft de resultaten van dit onderzoek.